M. E.

JOURNAL OF THE

AEROSPACE SCIENCES

VOLUME 28 MAY 1961 NUMBER 5

PURDUE UNIVERSITY
MAY 17 1961
LIBRARY

MECHANICAL ENGINEERING
MAY 20 1961
LIBRARY

CONTENTS

Boundary-Layer Displacement and Leading-Edge Bluntness Effects in High-Temperature Hypersonic Flow ..... H. K. CHENG, J. GORDON HALL, T. C. GOLIAN, AND A. HERTZBERG 353

Transient and Periodic Response of a Loaded Sandwich Panel ..... CHIEH C. CHANG AND BERTRAND T. FANG 382

Some Considerations on the Laminar Stability of Time-Dependent Basic Flows ..... S. F. SHEN 397

Influence of Transverse Shear on Nonlinear Vibrations of Sandwich Beams With Honeycomb Cores ..... HU-NAN CHU 405

A Study of Cotangential, Elliptical Transfer Orbits in Space Flight ..... WILLIAM LI-SHU WEN 411

Readers' Forum 418

Published by
INSTITUTE OF THE AEROSPACE SCIENCES, INC.

JOURNAL OF THE AEROSPACE SCIENCES

Editor: W. R. SEARS
Director, Graduate School of Aeronautical Engineering, Cornell University

Associate Editor: ROBERT R. DEXTER *Managing Editor:* RITA J. TURINO

Editorial Assistant: CHARLOTTE C. ROBB

IAS Aerospace Technology Panels

Paul J. Burr, Technical Services Director, Coordinator

The members of the IAS Aerospace Technology Panels shown here are to be available, collectively or as individuals, to assist and advise IAS committees, Sections, and staff members as to currently interesting and important technical topics related to their specialties and as to people most qualified to speak or write on such topics. The panels will also stimulate thought and scientific papers of potential value for the future, and they should be sensitive to technical activity of other professional groups, seeking through joint action the enlightenment of all having professional aerospace interests. Panel chairmen are indicated with an asterisk (*).

Aerodynamics and Fluid Mechanics

Lester Lees*
Seymour M. Bogdonoff
Dean R. Chapman
Antonio Ferri
Paul Germain
Wayland C. Griffith
Hans W. Liepmann
C. C. Lin
Henry T. Nagamatsu
W. R. Sears
John R. Sellars
R. T. Whitcomb
Hideo Yoshihara

Aeroelasticity

R. L. Bisplinghoff*
Y. C. Fung
I. E. Garrick
Martin Goland
Kurt H. Hohenemser
J. C. Houbolt
W. P. Jones
W. J. Mykytow
Robert F. Speaker

Biomedical Sciences

Brig. Gen. D. Flickinger, USAF*
W. Ross Adey
Capt. Wm. Augerson, USA
Hilding Bjurstedt
Stuart Bondurant
A. Scott Crossfield
Cdr. J. H. Ebersole, USN
W. R. Lovelace, II
Capt. Bruce Pine, USAF
Stanley Roscoe

Communication

P. C. Sandretto*
K. C. Black
James M. Bridges
Leonard Jaffe
David S. Little
Cdr. D. O. Mann, USN
Paul Rosenberg
William Sen
Arnold Shostack
Teck A. Wilson

Control, Guidance, and Navigation

C. S. Draper*
R. C. Berendsen
B. Paul Blasingame
Robert N. Brown
S. F. Eyestone
Percy Halpert
B. J. O'Connor
Robert L. Roderick
S. F. Schmidt
O. Hugo Schuck
H. Philip Whitaker

Energy Conversion

David Altman*
Robert Bromberg
M. U. Clauser
J. Preston Layton
Frank Marble
G. H. Markstein
A. M. Rothrock
Milton M. Slawsky
Martin Summerfield
T. Y. Toong

Flight Mechanics

H. J. Kelley*
Malcolm J. Abzug
H. Julian Allen
A. E. Bryson, Jr.

Flight Mechanics (Cont.)

T. N. Edelbaum
William C. House
Bernard Maggin
Angelo Miele
John D. Nicolaides
Charles B. Westbrook

Instrumentation

R. H. Tripp*
Paul F. Bechberger
J. M. Hungerford
Mac Lowy
Walter McKay
M. David Prince
Charles P. Sonett
George I. Toumanoff
William A. Wildhack

Meteorology

Thomas F. Malone*
Robert D. Fletcher
Henry T. Harrison
Joseph Kaplan
Donald T. Perkins
Herbert Riehl
Morris Tepper
Clayton Van Thullenar
Harry Wexler

Nuclear Applications

J. Donald Rauth*
Jack L. Armstrong
Robert W. Bussard
H. M. Dieckamp
Capt. R. L. Duncan, USN
Harold B. Finger
Donald J. Keirn
Frank E. Rom
Raymer E. Schreiber
D. Roy Shoults
T. B. Taylor

Operations

Benjamin S. Kelsey*
Maj. Gen. Otis Benson, USAF (MC)
Ernest A. Cutrell
Capt. E. E. Fawkes, USN
Melvin N. Gough
Franklin W. Kolk
Col. J. L. Marinelli, USA
Richard V. Rhode
W. E. Rhodes
M. B. Spaulding, Jr.
Maj. Gen. D. Yates, USAF

Propulsion Systems

Bruce T. Lundin*
Robert H. Boden
George W. Brady
David Cochran
Elliot Mitchell
Perry W. Pratt
C. C. Ross
John G. Wilder, Jr.
Maurice J. Zucrow

Space Physics

John C. Evvard*
Herbert Friedmann
Leo Goldberg
C. F. Hansen
Arthur Kantrowitz
Bruno Rossi
S. F. Singer
Leo Steg
Fred L. Whipple

Structures and Materials

Nicholas J. Hoff*
Samuel B. Batdorf
Bruno A. Boley
Pol Duwez
R. R. Heldenfels
Samuel Levy
George N. Mangurian
S. S. Manson
Nathan E. Promisel
Ernest E. Sechler

Support

Ernest G. Stout*
Albert D. Brown
Edward I. Brown
Col. Paul T. Cooper, USAF
P. J. Daniel
Paul Hartline
Donald R. Hill
Capt. N. D. Hodson, USN
Lt. Col. George L. Lovett
R. R. Malik
John McKenna
Gilbert Rolan
Richard A. Schmidt
William R. Owens

Vehicle Design

C. E. Pappas*
Ralph Alex
Adolph Burstein
C. H. Christenson
A. J. Eggers, Jr.
E. V. Marshall
Rene H. Miller
John R. Ragazzini
George S. Schairer
George S. Trimble, Jr.

SUBSCRIPTION RATES

JOURNAL OF THE AEROSPACE SCIENCES, Published Monthly. United States and Possessions: 1 Year, $15.00; Single Copies, $1.50. Foreign Countries Including Canada (American Currency Rates): 1 Year, $16.00; Single Copies, $1.50.

AEROSPACE ENGINEERING, Published Monthly. United States and Possessions: 1 Year, $5.00; Single Copies, $0.50. Foreign Countries Including Canada (American Currency Rates): 1 Year, $6.00; Single Copies, $0.50.

Notices of change of address, which should be sent at least 30 days prior to actual change of address, and correspondence regarding subscriptions should be sent to the Circulation Department, JOURNAL OF THE AEROSPACE SCIENCES, 2 East 64th Street, New York 21, N.Y.

Manuscripts for publication, proofs, and all correspondence should be addressed to the Editorial Office of the JOURNAL.

© *Copyright, 1961, by the Institute of the Aerospace Sciences, Inc.*

Publication Office, 20th and Northampton Sts., Easton, Pa. Second-Class Mail Privileges Authorized at Easton, Pa. Acceptance for mailing at a special rate of postage provided for in Section 1103, Act of October 3, 1917, authorized April 29, 1937.

JOURNAL OF THE AEROSPACE SCIENCES

VOLUME 28 MAY 1961 NUMBER 5

Boundary-Layer Displacement and Leading-Edge Bluntness Effects in High-Temperature Hypersonic Flow†

H. K. CHENG,* J. GORDON HALL,* T. C. GOLIAN,** AND A. HERTZBERG***

Cornell Aeronautical Laboratory, Inc.

Summary

Two important features of hypersonic flow over slender or thin bodies are the displacement effect of the boundary layer and the large downstream influence of leading-edge bluntness. The present paper contributes new theoretical and experimental results on this problem.

The interaction of the two effects is treated theoretically by extending the basic shock-layer concept. In the outer inviscid flow, a model consisting of a detached shock layer and an entropy layer is introduced to account for bluntness. In the boundary layer, the approximate solution is found to be governed by a local flat-plate similarity. Under the assumption of a strong bow shock and a specific heat ratio close to unity, a theory is developed for an arbitrary thin body. For flat-plate afterbodies, the theory yields a solution agreeing with blast-wave theory at one limit and strong-interaction theory at the other. Within the framework of the present theory, the problems involving angle of attack are also analyzed. Complementary to the above study, a hypersonic similitude involving strong shocks, but not requiring γ close to one, is given. The solutions obtained in the leading approximation provide a natural comparison with experimental data correlated on the basis of this similitude.

Flat-plate experiments in air, conducted in the C.A.L. 11 × 15-in. hypersonic shock tunnel under cold-wall conditions, included measurement of surface heat-transfer distributions and schlieren studies for zero and nonzero angle of attack. Steady laminar heat-transfer rates were measured by means of thin-film resistance thermometers at air test-flow Mach numbers around 12, free-stream Reynolds numbers from 1.4×10^4 to 1.8×10^6 per in., and leading-edge Reynolds numbers from 3 to 1.5×10^4. For most of the experiments, airflow stagnation temperatures ranged from 1,900°K to 2,000°K, giving wall-to-stagnation temperature ratios of about 0.15. The range of test conditions at this stagnation temperature encompassed the limiting cases of dominant bluntness and dominant viscous-interaction effects. Heat-transfer distributions were also measured on a sharp plate for air stagnation temperatures ranging from 2,000°K up to 4,000°K.

The experimental data are quite well correlated in terms of the foregoing theoretical similitude variables characterizing combined effects of boundary-layer displacement and bluntness. The correlations obtained suggest that for the present experimental conditions, at least, the hypersonic viscous similitude is valid even with leading-edge bluntness. Quantitative agreement with the zero-order theory, discussed in detail in the paper, is generally fair.

Symbols

a_∞ = speed of sound in the free stream

A, B = constants

C_f = $(\mu\, \partial u/\partial y)_w/(1/2)\rho_\infty U^2$, the skin-friction coefficient

C_H = $(\kappa\, \partial T/\partial y)_w/\rho_\infty U(H_\infty - H_w) = q/\rho_\infty U(H_\infty - H_w)$, the surface heat-transfer coefficient

C_p, C_v = specific heats of the gas at constant pressure and at constant volume, respectively

C = the constant of proportionality in the linear viscosity-temperature relation $\mu/\mu_\infty = CT/T_\infty$

C_* = $[\mu(T_*)/\mu(T_\infty)](T_\infty/T_*)$

D_N = the drag of the blunt leading-edge or nose

e = the specific internal energy of the gas

f, F = symbols representing certain functions of the variables involved

h = the specific enthalpy

H = $h + (1/2)(u^2 + v^2)$, the total specific enthalpy

J_ν, Y_ν = νth-order Bessel's functions of the first and second kind, respectively

k = $D_N/(1/2)\rho_\infty U^2 t$, the leading-edge (nose) drag coefficient

Presented at the Hypersonic Phenomena Session, IAS 28th Annual Meeting, N. Y. Jan. 25–27, 1960. Revised and received August 23, 1960.

† The experimental phase of this research was sponsored by the U.S. Air Force through the Office of Scientific Research, Contract No. AF 18(603)-10. The theoretical study was sponsored by the U.S. Navy through the Office of Naval Research, Contract No. Nonr-2653(00). Technical monitoring was done by Milton Rogers, Chief, Mechanics Division, AFOSR, and by Ralph D. Cooper, Chief Fluid Dynamics Branch, ONR.

* Principal Aerodynamicists.

** Associate Mechanical Engineer.

*** Head, Aerodynamic Research Dept.

K_ϵ = $M^3 k_\epsilon (t/x)$, a parameter controlling inviscid tip-bluntness effect
L = a reference length
m = a constant associated with the streamline in the entropy layer
M = U/a_∞, the free-stream Mach number
p = the pressure
Pr = Prandtl number $\mu C_p/\kappa$
q = local surface heat-transfer rate
R = the gas constant in the equation of state $p = \rho RT$
Re_x = the Reynolds number $\rho_\infty Ux/\mu_\infty$
t = the thickness of the blunt leading-edge or nose
T = the temperature
T_* = $T_0[1 + 3(T_w/T_0)]/6$, a reference temperature for defining C
u, v = the velocity components parallel to the x and y axes, respectively
U = the value of u in the free stream
Δu = $u - U$, the streamwise perturbation velocity
x, y = rectangular coordinates in directions parallel and normal, respectively, to the free-stream velocity, with the origin at the nose
Y_b, Y_e, Y_s, Y_w = the y ordinates of the inner edge of the entropy layer, the outer edge of the entropy layer, the shock, and the body surface, respectively
z, ζ = the variables related to Y_e and x, respectively; the relations between z and Y_e, and between ζ and x, are different for different cases
α = the angle of attack of the flat plate; positive α refers to compression or wedge flow over the surface in question
β = the variable $\chi_\epsilon K_\epsilon^{-2/3}$
γ = C_p/C_v, the specific-heat ratio
Γ = $K_\epsilon M\alpha/2\chi_\epsilon^2$, a parameter governing the bluntness-displacement-incidence interactive effect
δ, δ_* = the boundary-layer thickness and displacement thickness, respectively
$\epsilon, \epsilon_\infty$ = $(\gamma - 1)/(\gamma + 1)$, $(\gamma_\infty - 1)/(\gamma_\infty + 1)$, respectively
θ = a typical flow-deflection angle which may be taken as dY_s/dx
Θ = $(H - H_w)/(H_\infty - H_w)$
Φ = a function whose derivative $\partial\Phi/\partial\eta$ is u/U
κ = thermal conductivity of the gas
μ = the viscosity of the gas
λ, ϕ = certain variables
ξ, η = two spatial variables used in the boundary-layer analysis, see Eq. (2.1)
ρ = the gas density
τ = a body-thickness parameter used in the similitude consideration
$\bar{\chi}, \bar{\chi}_L$ = $M^3\sqrt{C/Re_x}, M^3\sqrt{C/Re_L}$
χ_ϵ = $\epsilon[0.664 + 1.73(H_w/H_\infty)]\bar{\chi}$, a parameter governing the boundary-layer displacement effect
ω = the constant exponent in the relation $\mu \propto T^\omega$

Subscripts

b pertaining to the inner edge of the entropy layer
B pertaining to the Blasius solution
e at the outer edge of the entropy layer
L based on the reference length ($x = L$)
N pertaining to the condition behind the strongest part of the shock at the nose
s behind the shock (at x)
t based on the nose thickness ($x = t$)
w at the body surface or wall
δ at the outer edge of the boundary layer
0 pertaining to the free-stream stagnation condition (for the temperature)
∞ pertaining to the free-stream condition
$*$ based on the reference temperature T_*

(1) INTRODUCTION

THE EFFECTS OF leading-edge or nose bluntness and boundary-layer displacement are important in the hypersonic flight of thin bodies at high altitude. In recent years, these phenomena have received considerable attention in both theoretical and experimental studies. Theoretical studies to date have considered only limiting cases where either one or the other effect is dominant. Thus, on one hand we have the so-called blast-wave theory,[1–8] for dominant leading-edge bluntness effect, which has been criticized on various grounds.[9,10] In many cases the blast-wave phenomena appear to be subject to the influence of viscous effects in an obscure way, tending to discredit the theory. On the other hand, for dominant boundary-layer displacement effect we have the rather well-established theories of strong and weak interactions for a flat plate, as well as treatments of related problems.[11–26]

Experimentally, studies of hypersonic flow over flat plates with bluntness[12,45–58] have been carried out mainly for adiabatic-wall conditions, in which case boundary-layer displacement effects are considerably larger than expected for the cold-wall conditions of hypersonic flight. Most of the experimental investigations have been concerned with measurement of shock-wave shapes and/or surface-pressure distribution (the studies of references 51, 53, 55, and 57 are exceptions). Test Mach numbers in helium have ranged from about 10 to 24, and in air from about 5 to 9.6. Generally speaking, the experiments have provided useful insight into leading-edge bluntness and boundary-layer displacement phenomena and have served to assess the limitations of theory.

The present paper gives the results of a theoretical and experimental study of leading-edge bluntness and boundary-layer displacement effects for the general situation in hypersonic thin-body flow where both phenomena may be equally important. In Section 2, a theoretical approach to the general problem is developed using the concept of a detached shock layer for the inviscid flow and local similarity for the boundary layer. The leading approximation for the flow model adopted is developed in detail; its simplicity permits solutions to numerous cases of interest. The solutions obtained reveal the combined effects of bluntness, viscous interaction, and body angle in hypersonic flows over thin bodies. In addition, the classical hypersonic similitude of Tsien and Hayes is extended to include bluntness and displacement effects.

On the experimental side, Section 3 describes studies in the C.A.L. 11 × 15-in. shock tunnel of hypersonic airflows at Mach numbers around 12 over sharp and blunt leading-edge flat plates. For most of these studies, the stagnation temperature was close to 2,000°K. The corresponding ratio of wall-to-stagnation temperature was about 0.15, giving highly cooled, laminar boundary layers. Shock-wave shapes were determined by schlieren photography, and detailed, surface-heat-transfer distributions were measured by

thin-film thermometry. Leading-edge Reynolds numbers were varied from 3 to 1.5×10^4 for stream Reynolds numbers from 1.4×10^4 to 1.8×10^5 per inch. The results at zero angle of attack encompass the limiting cases of dominant bluntness and dominant viscous-interaction effects. Angle-of-attack effects were studied at low and high leading-edge Reynolds numbers. Heat transfer was also measured on a sharp plate for stagnation temperatures up to 4,000°K.

In Section 4, correlations of the experimental data are made in terms of the extended viscous similitude for bluntness, and the degree of correlation obtained is discussed. In addition, the experimental data are compared with predictions from the theoretical solutions developed in Section 2.

(2) THEORY*

(2.1) Scope and Assumptions

In this study, a continuum flow model consisting of a laminar boundary layer adjacent to the body and an inviscid outer flow field will be assumed. Since the Mach numbers considered are high, and the bodies thin, the lateral extent of the flow field bounded by the bow shock is small. Our analysis may therefore be carried out within the scope of the boundary-layer theory[14,16] and the (inviscid) hypersonic small-disturbance theory.[34–36] Within this framework, two complementary studies are made. First, and the major part of our analysis, is the development of an approach which includes the interaction of boundary-layer displacement, tip bluntness, as well as body thickness effects. To achieve this end, certain approximations and simplifications will be introduced. The second study is concerned with hypersonic similitude when both boundary-layer and tip-bluntness effects are present, and with simplification of the similarity law for flows with strong shock waves. For this similitude consideration, a number of the assumptions introduced in the first study are not required.

Underlying the present approach are the two basic concepts of local boundary-layer similarity and a detached shock layer. Both of these concepts are desirable for a development consistent with the so-called Newtonian shock-layer approximation.[28–33] The consistency between local similarity and the shock-layer approximation has, in fact, been discussed earlier.[10] The concept of a detached shock layer, which includes the so-called "free layers"[9,32] as special cases, is a necessary modification of the shock-layer theory to allow treatment of tip bluntness.

A similar treatment of the tip-bluntness effect has been given previously by Chernyi.[4,5] The essential idea of a detached shock layer is implicit in his integral method for hypersonic inviscid flows. While Chernyi's method and the present analysis are equivalent in the idealized limit $\gamma \to 1$, they differ, however, in the higher-order approximation for γ not close to unity. It may also be pointed out that the inviscid tip-bluntness effect has been considered recently by Guiraud.[7,66] The idea of a detached shock layer is employed, and certain equations obtained are very similar to ours.* Guiraud's study does not lead to explicit solution of the problem, however.

Throughout the present analysis an ideal gas with constant specific heats will be assumed ahead of and behind the shock, although γ may change across the

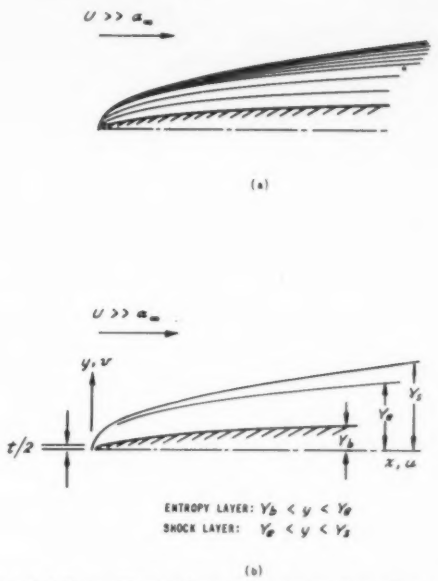

FIG. 2.1. (a) *Top:* Illustrations of the stream-line pattern of the flow field around a slender body with small blunt nose. (b) *Bottom:* Division of the inviscid-flow region about a slender afterbody into a shock layer and an entropy layer.

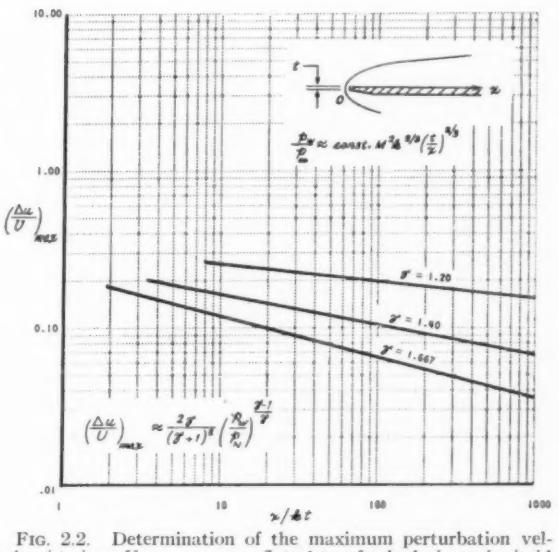

FIG. 2.2. Determination of the maximum perturbation velocity $|\Delta u| \equiv U_\infty - u$ over a flat-plate afterbody in an inviscid hypersonic flow.

* Most of the detailed analysis in this section was done by Mrs. Angela Chang of the Aerodynamic Research Dept.

* We thank Mr. Guiraud for calling our attention to reference 66 in a recent private communication.

shock. In order to arrive at a simple form of the local similarity for the boundary layer, the Prandtl number is taken to be unity, the body temperature is assumed to be uniform, and a linear viscosity-temperature relation is adopted. The analysis presented in this paper will deal mainly with steady, plane flows.

The three requirements which control the accuracy of the analysis may be expressed as follows:

(*a*) The disturbance velocity $\Delta u/U \equiv [(u/U) - 1]$, as well as the square of the flow angle, in the inviscid flow field must be negligibly small in comparison to unity.

(*b*) The bow shock wave must be sufficiently strong.

(*c*) The specific heat ratio γ must be sufficiently close to unity.

The first requirement implies exclusion of the blunt-nose region itself from the present enquiry, and we will deal only with its downstream effect. The consistency of these requirements with the degree of approximations involved will be examined later. The zero-order theory, which is to be studied in detail, pertains to the leading approximation under the last two requirements cited, and may therefore be compared with the classical (Newtonian-plus-centrifugal-force) result of Busemann for slender bodies.[28–33]

(2.2) An Approach to the Problem of Tip Bluntness and Boundary-Layer Displacement

In the following, the local similarity and its consistency with the shock-layer approximation will be discussed first. Then the theory of a detached shock layer will be considered. Finally, the zero-order theory for the complete problem will be developed and applied to particular cases of interest.

The Local Similarity and the Shock-Layer Theory

The idea of assuming a local similarity as a means of estimating heat-transfer rates on blunt bodies at high speed was first proposed by Lees[37] and later utilized by a number of workers.[38,39] Lees observed that the thermal boundary layer is rather insensitive to pressure gradient, particularly if the boundry layer is cooled. For most engineering applications it suffices to ignore the pressure-gradient term in the equation of motion, in which case the problem is reducible to that of a flat plate.* For the latter problem, a self-similar solution exists if the wall-to-stagnation temperature ratio is constant along the plate.

It is essential to recognize that in the present study, where only thin bodies are considered, the direct pressure-gradient effect is unimportant not primarily because of a cold wall, but because the direct effect of pressure gradient on the hypersonic boundary layer under consideration is at most of the order

$$\epsilon \equiv (\gamma - 1)/(\gamma + 1)$$

The condition of small ϵ is a requirement in existing shock-layer theories for inviscid hypersonic flows.[28–33] It is natural to treat the present boundary-layer problem by an analogous perturbation procedure which uses ϵ as a controlling parameter. The argument used for the local-similarity method in blunt-body applications is avoided in the present study.

The foregoing considerations become evident if the variables x,y in the boundary layer are transformed as follows:

$$\xi = \int_0^x C \frac{p}{p_\infty} \frac{dx}{L}$$

$$\eta = \sqrt{Re_L} \left(\int_0^y \frac{\rho}{\rho_\infty} \frac{dy}{L} \right) \left(\int_0^x C \frac{p}{p_\infty} \frac{dx}{L} \right)^{-1/2}$$

where $$Re_L \equiv \rho_\infty U L/\mu_\infty$$

Assuming a linear viscosity-temperature relation

$$\mu/\mu_\infty = C\, T/T_\infty$$

and a unit Prandtl number, the system of differential equations is reduced to

$$\left.\begin{aligned} &2\Phi_{\eta\eta\eta} + \Phi\Phi_{\eta\eta} - 2\xi[\Phi_\eta\Phi_{\xi\eta} - \Phi_\xi\Phi_{\eta\eta}] = \\ &\qquad \epsilon\left[\left(2\,\frac{dp}{dx}\int_0^x p\,dx\right)\Big/ p^2\right]\left[\frac{T_w}{T_0} + \left(1 - \frac{T_w}{T_0}\right)\Theta - \Phi_\eta{}^2\right] \\ &2\Theta_{\eta\eta} + f\Theta_\eta - 2\xi\left[\Phi_\eta\Theta_\xi - \Phi_\xi\Theta_\eta + \Phi_\eta\Theta\,\frac{d}{d\xi}\ln\left(1 - \frac{T_w}{T_0}\right)\right] = 0 \end{aligned}\right\} \quad (2.1)$$

and the boundary conditions to

$$\left.\begin{aligned} \Phi &= \Phi_\eta = \Theta = 0 \quad \text{at} \quad \eta = 0 \\ \Phi_\eta &= \Theta = 1 \quad \text{at} \quad \eta = \infty \end{aligned}\right\} \quad (2.1a)$$

where

$$\Phi_\eta = u/U \qquad \Theta = (H - H_w)/(H_\infty - H_w)$$

In arriving at these equations, quantities of the order of $1/\epsilon M^2$ and $\Delta u_\delta/U$ higher than the remaining terms have been neglected. From the above formulation, it is quite clear that the leading approximation solution for small ϵ will be independent of ξ, and is therefore governed by the Blasius equation

$$\left.\begin{aligned} &2\Phi_B''' + \Phi_B\Phi_B'' = 0 \\ &\Phi_B = \Phi_B'(0) = \Phi_B'(\infty) - 1 = 0 \end{aligned}\right\} \quad (2.2)$$

with $\Theta_B = \Phi_B'$. The problem of determining the higher-order approximation is equivalent to finding a correction to the classical flat-plate solution for a slight nonuniformity of the outer inviscid flow. The nonhomogeneous term appearing on the right in the first of Eqs. (2.1) reveals clearly the role of the wall-to-stagnation temperature ratio in controlling the degree

* The similarity under consideration may be more appropriately termed the "local flat-plate similarity."

of approximation of local boundary-layer similarity. Changing T_w/T_0 from unity to zero may typically reduce the correction term by 75 percent.

Neglect of the pressure-gradient term in the boundary-layer momentum equation has also been employed by Lees[16] to simplify the problem of strong-shock boundary-layer interaction. For this problem, however, a self-similar solution exists even with the pressure gradient retained. The theoretical justification for neglecting the pressure gradient in cases involving arbitrary pressure distribution on the basis of the shock-layer theories has been pointed out only quite recently.[10]

In the leading approximation for small ϵ, the surface heat-transfer rate, the skin friction, and the displacement thickness of the boundary layer are determined explicitly from the pressure distribution. For plane flows,

$$\left.\begin{aligned} M^3 C_H &\approx 0.332 \bar{\chi}_L \left(\frac{p}{p_\infty}\right)\left(\int_0^x \frac{p}{p_\infty}\frac{dx}{L}\right)^{-1/2} \\ C_f &\approx 2C_H \\ M\frac{\delta_*}{L} &\approx \epsilon\left(0.664 + 1.73\frac{T_w}{T_0}\right)\bar{\chi}_L \times \\ &\qquad \left(\int_0^x \frac{p}{p_\infty}\frac{dx}{L}\right)^{1/2}\left(\frac{p}{p_\infty}\right)^{-1} \end{aligned}\right\} \quad (2.3)$$

where $$\bar{\chi}_L \equiv M^3\sqrt{C/Re_L}$$

These results, in view of the approximations involved, will be subject to errors of order ϵ and $\Delta u_\delta/U$. The usual errors inherent in the boundary-layer equations as well as errors from possible slip, temperature-jump, and vorticity-interaction effects, will presumably be no larger than those incurred by the approximation $u_\delta \simeq U$.[9,10,23,26] The magnitude of $\Delta u_\delta/U$ will be examined later.

Before proceeding to the analysis of the inviscid flow region, the choice of a reference temperature for the determination of the constant in the linear viscosity-temperature relation will be discussed. The assumption of such a viscosity law may seem to be unrealistic since the temperature variation within the hypersonic boundary layer is quite large. The approximation may be improved considerably by choosing the constant C to represent correctly the value of viscosity at an appropriate reference temperature. Instead of choosing the wall temperature as a reference, as was proposed earlier by Chapman and Rubesin[40] and adopted later by others for hypersonic applications, we recommend, for the present study involving boundary layer over slender bodies, a reference temperature T_* defined by

$$T_* \equiv T_e[1 + 3(T_w/T_0)]/6 \quad (2.4)$$

whence $$C = C_* \equiv [\mu(T_*)/\mu(T_\infty)](T_\infty/T_*)$$

This choice of T_* is particularly meaningful when local flat-plate similarity holds, as in the present problem. For then we may apply Crocco's integral relation, and the reference temperature T_* given above is seen to be simply an average temperature across the hypersonic boundary layer over a thin body, i.e.,

$$T_* = \int_0^1 T\frac{du}{u_\infty} \approx \int_0^1 T\frac{du}{u_\delta}$$

The skin friction and the heat-transfer rate on a flat plate under uniform pressure based on T_* of Eq. (2.4) agree exceedingly well with results based on the Young formula[63] at the higher Mach number range, provided the Prandtl number is not far from unity

The Bluntness Effect and Detached Shock Layer

The necessity for allowing the shock layer to detach from the afterbody of a blunt leading edge is evidenced by the breakdown of the standard shock-layer theory around the shoulder region where the pressure would accordingly fall below zero and the shock-layer thickness would become infinite. The essence of our analysis is that the pressure at the base of the detached layer will not be put equal to zero, a priori, as was done for a "free layer,"[32] but is to be determined as part of the solution to the problem.

It is essential to realize that, within the inviscid, hypersonic-flow region bounded by the shock and the body surface or the outer edge of the boundary layer downstream of a small blunt nose, there is an inner core of considerable extent containing gas particles which have come through the comparatively forward, and hence stronger, portion of the shock (see Fig. 2.1). It is appropriate to term this region the "entropy layer," since its specific entropy is much higher than that prevailing near the shock above. The temperature within this layer is accordingly much higher, and the density much lower, than the corresponding values near the shock; the gas within the entropy layer has been heated, so to speak, by the strong forward portion of the curved shock. It is natural to consider the remaining, and relatively thin, high-density part of the flow field behind the shock as a shock layer in the usual sense, except for the fact that it is no longer attached to a rigid body. The equivalent body surface for this shock layer can be taken, over the relatively slender, downstream portion of the flow field, to coincide with the outer edge of the entropy layer, $y = Y_e(x)$, which, in view of the particle-isentropic condition, must also be a streamline [see Fig. 2.1(b)]. Across this streamline boundary, the pressure must be continuous.

The flow structure within a hypersonic shock layer has been treated quite extensively by Freeman[30] and others.[31–33] Our present inquiry will deal with the entropy layer, the outer edge of which is the base of the shock layer. To investigate this, we need a knowledge of the pressure at the base of the shock layer in terms of Y_e. The leading approximation for this relation, according to shock-layer analysis for a plane flow, is simply

$$p_e \approx \rho_\infty U^2(Y_e'^2 + Y_eY_e'') \quad (2.5)$$

which represents the Newtonian-plus-centrifugal (Busemann) pressure formula simplified for thin bodies.

In view of the high temperatures attained within the entropy layer, the local velocity u could be reduced considerably from its free-stream value U. Since the assumption of $u_\delta \approx U$ has been made in the boundary-layer analysis, and will be used later in the treatment of the entropy layer, an assessment of the magnitude of $\Delta u/U$ is important and will be made prior to further development.

For the purpose of examining the magnitude of $\Delta u/U$ in the entropy layer, we consider first the particular case of a flat plate under the influence of the strong blast-wave effect produced by its blunt tip. For this case, the surface pressure distribution is known[3,6] and we can determine the maximum value of the perturbation velocity (for arbitrary x) from the particle-isentropic condition and the Bernoulli relation. Maximum values of $|\Delta u/U|$ for $\gamma = 1.20$, 1.40, and 1.667 are presented in Fig. 2.2 as a function of x/kt. The results indicate that sufficiently far downstream of a blunt nose ($x/kt \gtrsim 10$), $\Delta u/U$ remains sufficiently small to permit the approximation $u \approx U$.

Since in most cases

$$p_b < p_s \approx [2\gamma/(\gamma + 1)]M^2\theta^2$$

where θ is the local shock angle (which gives also the typical local flow angle), from the entropy behind the normal shock and by the Bernoulli equation, a conservative estimate for the perturbation velocity may in the general case be taken as

$$|\Delta u/U| \lesssim (1/2)\theta^{2(\gamma-1)/\gamma}$$

where the exponent $2(\gamma - 1)/\gamma$ has the values 1/3, 4/7, and 4/5 for $\gamma = 1.20$, 1.40, and 1.667, respectively.

We may now state in more explicit terms the requirements which will control the degree of accuracy of our analysis:

(a) $(1/2)(\theta)^{2(\gamma-1)/\gamma}$ must be negligible in comparison with unity.

(b) $1/M^2\theta^2$ must be sufficiently small in comparison with unity.

(c) ϵ must be sufficiently small in comparison with unity.

Obviously, condition (a) is essential for the assumption $u = U$ at the outer edge of the boundary layer and within the entropy layer as well. Condition (b) calls for a sufficiently strong shock, and (c) and (b) together will permit treatment by the shock-layer concept. By these requirements, the admissible ranges of the shock (and flow) angle θ, and ϵ, are necessarily restricted: To satisfy the small-perturbation assumption, θ must be small, but not so small that the shock cannot remain strong. In addition, the shock-layer approximation requires ϵ to be close to unity, but not so close that the small-perturbation assumption will be violated. The ranges for θ and ϵ can, of course, be enlarged by increasing M and by including (consistently) terms of higher orders in ϵ and $1/M^2\theta^2$.

Our analysis will be based on the fact that the density within the entropy layer is low compared to that in the free stream, i.e., $\rho \ll \rho_\infty$. It is essential to examine the compatibility of this fact with the requirements set forth above. Since the density depends not only on the pressure but also on the entropy, we should distinguish two situations. In one, the streamlines over most of, or at least a considerable part of, the entropy layer come from the immediate vicinity of the blunt nose. In other situations, the streamlines from the blunt-nose region reach only a small fraction of the entropy layer. The rest of the streamlines come from the slender but still the more forward and stronger portion of the curved shock. In the first situation, the specific entropy is at the same level as that prevailing at the nose, and the order of magnitude of the density may therefore be represented for particle-isentropic flow by

$$\frac{\rho}{\rho_\infty} \approx \frac{\gamma + 1}{\gamma - 1}\left(\frac{p}{p_N}\right)^{1/\gamma} = 0\left[\frac{1}{\epsilon}(\theta)^{2/\gamma}\right]$$

Comparing this with requirement (a) which implies that $\theta^{2/\gamma} \ll \epsilon$ for $\epsilon \ll 1$, we see that the local density is indeed small in comparison with the free-stream value when (a) is satisfied. In the second situation, the density distribution given by the strong blast-wave theory[1-3,41,42] should be valid, since streamlines over most parts of the entropy layer now come from the slender portion of the shock. The fact that the blast-wave solutions reveal the structure of a detached shock layer and a low-density entropy layer is well known, and the ratio ρ/ρ_∞ in this situation may, in fact, be represented (assuming a flat-plate afterbody) by

$$\rho/\rho_\infty = 0[(1/\epsilon)e^{-1/\epsilon}]$$

which is small for all practical purposes. Presumably, the second situation may be realized only for an extremely small blunt nose (hence large x/t) together with an extremely high Mach number. In either situation, the supposition

$$\rho/\rho_\infty \ll 1 \tag{2.6}$$

within the entropy layer can be well justified. Its error is presumably no larger than that incurred by the assumption $u \approx U$, that is, requirement (a).

An immediate consequence of the low density in the entropy layer is that the variation of pressure across it is small and negligible. We can examine this from the equation of motion governing the momentum component in the direction transverse to the layer. The fractional variation in pressure across the entropy layer is readily seen to be

$$\left|\frac{p - p_e}{p_e}\right| = 0\left[\frac{\rho}{\rho_\infty}\left(\frac{Y_e - Y_b}{Y_e}\right)\right] = 0\left(\frac{\rho}{\rho_\infty}\right) \ll 1 \tag{2.7}$$

and is therefore negligible according to our requirements.

In view of the above conclusion, we can now employ the simplification

$$u \approx U \qquad p \approx p_e(x) \tag{2.8}$$

for study of the flow pattern within the entropy layer. The equations stating continuity and particle-isentropy are

$$\left(u\frac{\partial}{\partial x}+v\frac{\partial}{\partial y}\right)\rho=-\rho\frac{\partial v}{\partial y}$$

$$\left(u\frac{\partial}{\partial x}+v\frac{\partial}{\partial y}\right)\ln\rho=\frac{1}{\gamma}\left(u\frac{\partial}{\partial x}+v\frac{\partial}{\partial y}\right)\ln p$$

Eliminating the density ρ and making use of the simplification on u and p, these two equations give an equation for v, or v/u. This equation can be integrated to yield

$$\frac{v}{u}=Y_b'(x)+\frac{(Y_b-y)}{\gamma}\frac{d}{dx}\ln p_e \tag{2.9}$$

for which the boundary condition at the inner edge of the entropy layer (also the outer edge of the boundary layer), i.e., $v/u = Y_b'(x)$ at $y = Y_b(x)$, has been satisfied. Putting dy/dx for v/u, we can integrate Eq. (2.9) once again and obtain an equation for the streamline

$$[y-Y_b(x)]^\gamma p_e(x)=m \tag{2.10}$$

where m is a constant differing for each streamline. This equation should hold throughout the entropy layer. Applying it at the streamline boundary $y = Y_e(x)$, we arrive at

$$[Y_e(x)-Y_b(x)]^\gamma p_e(x)=\text{constant} \tag{2.11}$$

This simple integral relation between the pressure and the cross-sectional area of the entropy layer is basic to our subsequent development.

The pressure p_e is that at the base of the shock layer, $Y = Y_e$, and is given by shock-layer theory once $Y_e(x)$ is specified. This relation for p_e from shock-layer theory can be used to eliminate p_e in Eq. (2.11), and we can write down, at least in principle, an ordinary differential equation involving only Y_e. The shock-layer theory gives the Busemann formula, Eq. (2.5), as a leading approximation. The pressure-area relation consistent with this approximation is therefore [from Eq. (2.11)] reducible to

$$(Y_e-Y_b)(Y_eY_e')'=\text{constant}$$

In carrying out a higher order analysis (in ϵ and $1/M^2\theta^2$), we should not only employ a pressure formula correct to the order desired, but also work consistently with a more accurate pressure-area relation based on Eq. (2.11). The first-order ϵ correction to the Busemann formula has been given explicitly by Freeman in reference 30.

The constant on the right-hand side of Eq. (2.11) is evidently related to the drag of the small blunt nose which produces the downstream blast-wave effect. Consider the balance of momentum change in the streamwise direction, assuming a supersonic flow. With the help of the equation of continuity and making use of the requirement (*a*), i.e., $u \approx U$, we can write

$$\frac{D_N}{2}+\int_{+0}^{x}p_bY_b'dx=\int_{Y_b}^{Y_e}\frac{p}{\gamma-1}dy+\int_{Y_b}^{Y}\frac{\rho v^2}{2}dy-\frac{p_\infty}{\gamma-1}Y_e \tag{2.12}$$

where D_N is the drag contributed by the pressure distribution around the small blunt nose excluded from the range of integration for the integral on the left.* The second terms on both sides of Eq. (2.12), as well as the third term on the right, belong to the orders ϵ and $1/M^2\theta^2$ higher than the others, and can be dropped in the leading approximation (a more detailed discussion is given in reference 65). To the same degree of approximation, we can replace the location of the shock front by the base of the shock layer. We can now put $p = p_e(x)$ under the integral sign of the first integral on the right, and reduce Eq. (2.12) to

$$D_N/2=[p_e/(\gamma-1)](Y_e-Y_b)$$

that is,

$$(Y_e-Y_b)(Y_eY_e')'=\epsilon D_N/\rho_\infty U^2 \tag{2.13}$$

This is the pressure-area relation pertaining to the zero-order theory previously given, but with the constant now determined.† To this approximation it seems that consideration of the momentum-integral relation not only determines the constant of Eq. (2.11), but also furnishes an alternative, and apparently simpler, derivation of the pressure-area relation. For the higher approximation, however, we may find it convenient to use Eq. (2.12) strictly as a subsidiary condition. The constant in the pressure-area relation, Eq. (2.11), can be determined by passing to the limit $x \to 0$ in Eq. (2.12).

We may note that, on the basis of Eq. (2.13), the pressure p_e, i.e., $(Y_eY_e')'$, can never become negative. This is to be expected since the shock layer in our treatment is no longer required to follow the body surface. However, Eq. (2.13), as well as Eq. (2.11), have not excluded the possibility of an attached shock layer, and also contain the free layer as a limiting solution. We can see this readily by examining Eq. (2.13) for the nearly limiting situation of an extremely small nose. The constant on the right of Eq. (2.13) in this case then reduces to a very small but positive number. Now, for p_e to be finite, it is clear that the shock layer must remain essentially attached to the body, i.e., $Y_e \approx Y_b$. As soon as p_e approaches zero, the entropy layer will, accordingly, begin to thicken and the shock layer will detach to form a free layer.

---

* The nose drag D_N has been defined as the total drag of a symmetrical nose, namely, $y = \pm Y_0(x)$. In the case without top-bottom symmetry, $D_N/2$ should be taken as the contribution of one part of the surface which begins at the apex, or the stagnation point, of the nose.

† For the axisymmetric case, the relations corresponding to Eq. (2.11) and Eq. (2.13) are, respectively, $[Y_e^2-Y_b^2]^\gamma p_e = \text{constant}$, and $[Y_e^2-Y_b^2][Y_e'^2+(Y_eY_e''/2)]=2\epsilon D_N/\pi\rho_\infty U^2$.

Our general approach to the inviscid leading-edge problem is also similar to a treatment given previously by Chernyi,[4,5] as pointed out earlier. In Chernyi's treatment, which is essentially a momentum-integral method, use is made of $u \approx U$ and $p \approx p_e(x)$. The basic equations employed, written here for steady plane flows, are

$$\left.\begin{aligned} \frac{D_N}{2} + \int_{+0}^{x} p_b Y_b' dx &= \frac{p_b}{\gamma - 1}(Y_s - Y_b) + \frac{\rho_\infty}{2} U^2 Y_s (Y_s')^2 \\ p_b &= \rho_\infty U^2 (Y_s'^2 + Y_s Y_s'') \end{aligned}\right\} \quad (2.14)$$

It is evident that, as far as the leading approximation for small ϵ and $1/M^2\theta^2$ is concerned, the above equation and Eq. (2.13) obtained by us are essentially equivalent. When the higher order approximations are considered, we must compare Chernyi's equation, i.e., Eq. (2.14), with our Eq. (2.11). We may note, in Eq. (2.14), that implicitly the outer edge of the entropy layer has been taken to be the shock itself, and the Busemann pressure formula has been used. Hence, it is doubtful that Eq. (2.14) would yield a valid correction to the leading approximation. At any rate, the two treatments will be seen to be quite different when higher order approximations are considered.

The entropy layer has also been studied recently by Guiraud in references 7 and 66 in which an equation quite similar to our pressure-area relation, Eq. (2.11), has been given. To determine the term corresponding to the constant on the right of our Eq. (2.11), certain knowledge of the entropy distribution near the nose seems necessary, according to Guiraud's analysis. Hence, this term cannot be determined until the complete problem is solved. In our analysis, however, the constant is found with the momentum-integral relation, Eq. (2.12), as an auxiliary condition, and is thus determined by the nose drag (further discussions are given in reference 65).

In what follows, we shall apply the results of the above analysis to the problem involving both tip bluntness and boundary-layer displacement effects. The zero-order theory for small ϵ and large $M^2\theta^2$ will be developed in detail.

The Zero-Order Theory

For small ϵ, the boundary layer has been shown to be governed by a local similarity; assuming, in addition, that the shock wave involved is strong, the simple pressure-area relation Eq. (2.13) for the entropy layer should also hold. Combining these results, the leading-edge problem of hypersonic flows subject to the tip-bluntness and boundary-layer displacement effects can be treated in a rather straightforward fashion.

To apply Eq. (2.13) to this problem, the inner edge of the entropy layer, $Y_b(x)$, will be taken as an equivalent body surface which should account for the displacement effect of the hypersonic boundary layer. Inasmuch as the assumption $u_\delta \approx U$ is valid,[14,16] the outer edge of the boundary layer may be represented approximately by the displacement thickness δ_* because of the extreme low density resulting from viscous

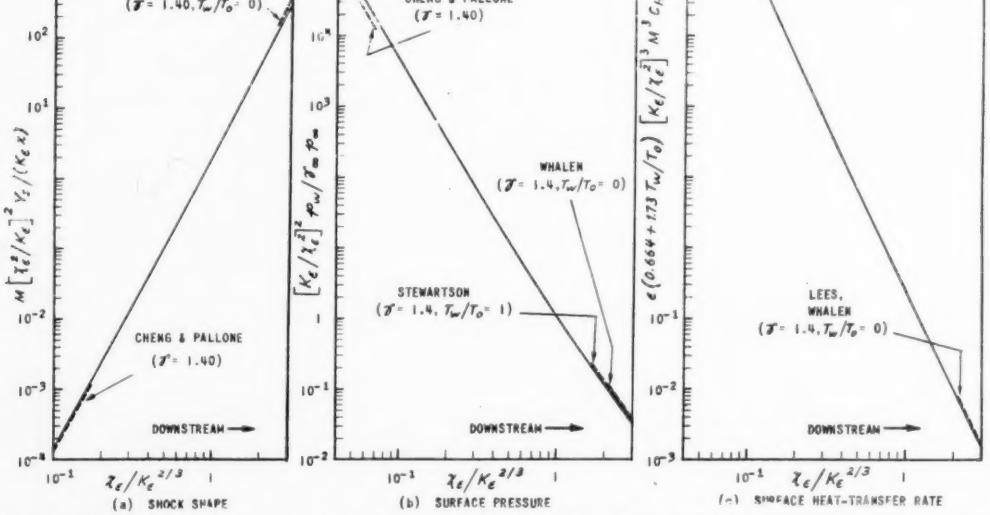

FIG. 2.3. Results based on the zero-order theory of a flat plate under the combined effect of tip bluntness and boundary-layer displacement.

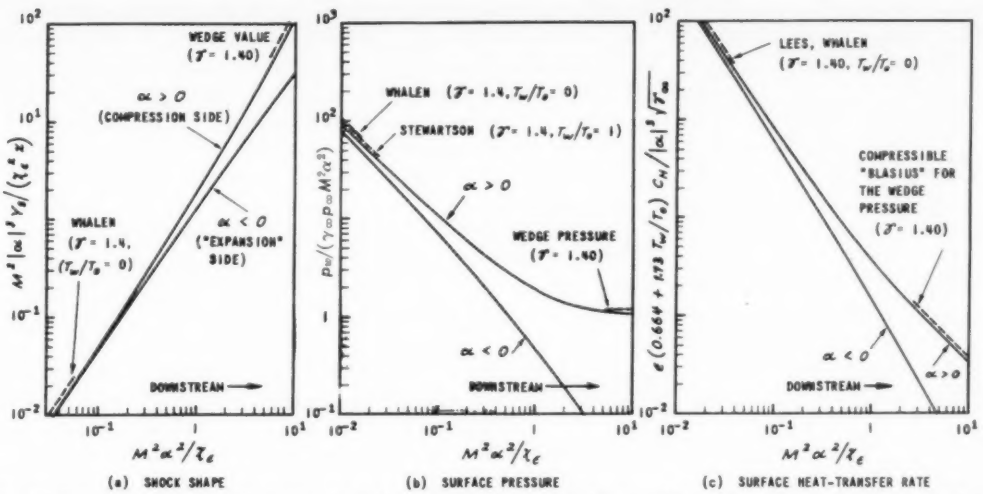

FIG. 2.4. Results based on the zero-order theory of a flat plate at incidence under the combined effect of boundary-layer displacement and angle of attack.

heating. In this instance, we can replace Y_b by $Y_w(x) + \delta_*(x)$. By local similarity, δ_* is given by Eq. (2.3) explicitly in terms of the pressure distribution, which is now provided by the Busemann formula.

The equation governing our zero-order theory is therefore

$$\left.\begin{aligned} &[Y_e - Y_w - \delta_*](Y_eY_e')' = \epsilon k t/2 \\ &\delta_* = \epsilon\left(0.664 + 1.73\,\frac{T_w}{T_0}\right)\frac{\tilde{\chi}_L\sqrt{L}}{M^2}\,\frac{\sqrt{Y_eY_e'}}{(Y_eY_e')'} \end{aligned}\right\} \quad (2.15)$$

After solving Eq. (2.15) for Y_e, we can determine the pressure from the Busemann formula and the heat-transfer rate as well as the skin-friction from Eq. (2.3). The rudimentary manner in which the three flow regions—boundary layer, entropy layer, and shock layer—interact is contained in the ordinary differential equation given above. In the absence of tip bluntness, we have only the shock layer and the boundary layer. The first of the above equations then becomes

$$Y_e = Y_w + \delta_*$$

and Eqs. (2.15) reduce to

$$2(Y_e - Y_w)[\sqrt{Y_eY_e'}]' = \epsilon\left(0.664 + 1.73\,\frac{T_w}{T_0}\right)\frac{\tilde{\chi}_L\sqrt{L}}{M^2} \quad (2.15a)$$

The first of Eqs. (2.15) is singular at the origin and admits the solution $Y_e \sim x^{2/3}$. This is the correct behavior when the blast-wave effect of the leading edge is strong,[2,3] and confirms that near the leading edge the displacement effect of the boundary layer gives way to the more powerful effect of leading-edge bluntness. For cases which do not involve bluntness, Eq. (2.15a) reveals singular behavior of another type: as $x \to 0$, $Y_e \sim x^{3/4}$. This is the behavior to be expected when the displacement effect predominates.[15,16,19] With these singular solutions as leading terms, solutions to Eq. (2.15) can be obtained by a forward integration from the origin. These singular leading terms in the asymptotic solutions for Y_e, as well as the pressure and the heat transfer, will be examined subsequently for flat-plate afterbodies.

Implicit in the above discussion is the assumption that the afterbody shape is sufficiently regular at the leading edge except for its abrupt beginning. It may also be pointed out that the blast-wave solution $Y_e \sim x^{2/3}$ is not the only mathematical solution to Eq. (2.15) near the origin for $\epsilon k \neq 0$. For example, in the special case of $Y_w = \delta_* = 0$, a complete solution to Eq. (2.15) can readily be obtained. However, the only particular solution compatible with the small-distance requirement (*a*) turns out to be $Y_e \propto x^{2/3}$ (this point is discussed further in Appendix I of reference 65).*

As is obvious from the requirements (*a*)–(*c*), the error in the zero-order theory is

$$0\ [\epsilon + 1/M^2\theta^2 + (1/2)(\theta)^{2(\gamma-1)/\gamma}]$$

If terms of the next orders are consistently included in the analyses of the entropy layer and of the boundary layer, in the manner previously described, the first two error terms may presumably reduce to ϵ^2 and $1/M^4\theta^4$.

In view of their frequent occurrence in the later development, it is convenient to introduce two new variables

$$\left.\begin{aligned} K_e &\equiv M^3\epsilon k(t/x) \\ \chi_\epsilon &\equiv \epsilon[0.664 + 1.73(T_w/T_0)]M^3\sqrt{C/Re_x} \end{aligned}\right\} \quad (2.16)$$

where Re_x is a local Reynolds number based on the free-stream properties, namely, $\rho_\infty Ux/\mu_\infty$. Except for the factors ϵ and $\epsilon\ [0.664 + 1.73(T_w/T_0)]$, these two vari-

* The existence of a complete solution to Eq. (2.15) in the case of $Y_w = \delta_* = 0$ was called to the writer's attention by Mr. J. P. Guiraud of ONERA, France, in a private communication.

ables are those employed previously for the bluntness and the displacement problems.[1–27]

In what follows, the zero-order theory will be applied to the problem of a flat plate in hypersonic flow subject to the three effects of bluntness, displacement, and angle of attack. In order to see clearly the manner in which these effects will act in combination, the simpler problems involving only two simultaneous effects at a time will first be singled out.

The Flat Plate With Bluntness and Displacement

For this problem, Eq. (2.15) can be reduced to

$$z(zz')' - \sqrt{zz'} = 1 \tag{2.17}$$

where the new variables are

$$z = 8M(\chi_\epsilon^2/K_\epsilon)(Y_e/K_\epsilon x), \qquad \zeta = 16(\chi_\epsilon/K_\epsilon^{2/3})^6$$

Note that both $K_\epsilon x (= M^3\epsilon kt)$ and $\chi_\epsilon^2/K_\epsilon (= \epsilon[0.664 + 1.73(T_w/T_0)]^2M^3C/kRe_t)$ are independent of x, hence both z and ζ are proportional, respectively, to Y_e and x. Let $\phi = z^2/2$ and $\lambda = d\phi/d\zeta$. Eq. (2.17) may then be written

$$\sqrt{2\phi}\,\lambda(d\lambda/d\phi) - \sqrt{\lambda} = 1$$

which can be integrated by a separation of variables to give

$$\phi = 4[\sqrt{\lambda} - (\lambda/2) + (\lambda^{3/2}/3) - \ln(1 + \sqrt{\lambda})]^2$$

This result provides the correct behavior at the origin, namely, $Y_e \sim x^{2/3}$ as $x \to 0$. To obtain a relation between ζ and ϕ, we note that

$$d\zeta = (d\zeta/d\phi)d\phi = (1/\lambda)(d\phi/d\lambda)d\lambda$$

and the solution of Eq. (2.17) can finally be brought to the parametric form

$$\left.\begin{aligned} z &= 2\sqrt{2}[\sqrt{\lambda} - (\lambda/2) + (\lambda\sqrt{\lambda}/3) - \ln(1 + \sqrt{\lambda})] \\ \zeta &= (1 + \sqrt{\lambda})^4 - (22/9)(1 + \sqrt{\lambda})^3 + 9(1 + \sqrt{\lambda})^2 - (46/3)(1 + \sqrt{\lambda}) + (10/3)\ln(1 + \sqrt{\lambda}) - 4\sqrt{\lambda}\ln(1 + \sqrt{\lambda}) + 2[\ln(1 + \sqrt{\lambda})]^2 + (76/9) \end{aligned}\right\} \tag{2.18}$$

This result for Y_e, which may also be taken as the shock location Y_s, is presented in Fig. 2.3(a) as $M(\chi_\epsilon^2/K_\epsilon)^2(Y_e/K_\epsilon x)$ vs. $(\chi_\epsilon/K_\epsilon^{2/3})$. The corresponding surface pressure and the surface heat-transfer rate are given in Figs. 2.3(b) and 2.3(c) as $(K_\epsilon/\chi_\epsilon^2)^2(p_w/\gamma_\infty p_\infty)$ and $\epsilon[0.664 + 1.73(T_w/T_0)](K_\epsilon/\chi_\epsilon^2)^2(M^3C_H/\sqrt{\gamma_\infty})$. We can see that Y_e varies as $x^{3/4}$ as $x \to \infty$, and as $x^{2/3}$ as $x \to 0$. These two limits correspond to situations in which displacement and bluntness dominate, respectively, agreeing with strong-interaction theory in the first case and strong blast-wave theory in the second. One important feature here is that all parameters and spatial variables (including wall-to-stagnation temperature ratio and the specific-heat ratio) are grouped together to form one single variable $\chi_\epsilon/K_\epsilon^{2/3}$. An analogous variable, which controls the combined effect of bluntness and displacement, has been previously pointed out by Lees and Kubota in a discussion assuming a weak nose effect.[2] From Fig. 2.3 we see that transition from the strong-blast-wave to the strong-interaction regimes occurs in the range $10^{-1} < \chi_\epsilon/K_\epsilon^{2/3} < 2$.

The appearance of γ_∞ and $\sqrt{\gamma_\infty}$ in the nondimensional forms of pressure and heat-transfer rate introduced above result from the use of the dynamic pressure $\rho_\infty U^2 = \gamma_\infty p_\infty M^2$ in connection with the Busemann formula Eq. (2.5). Retaining the factor γ_∞, instead of replacing it by unity, is in keeping with the convention of existing shock-layer theories.[28–33] Furthermore, it permits ϵ to represent conditions behind the shock even when ϵ_∞ is not small.

It is of interest to examine more closely the asymptotic solutions. They can be written, for large and small $[\chi_\epsilon/K_\epsilon^{2/3}]$ respectively, as

$$\left.\begin{aligned} MY_s/x &= 1.21\chi_\epsilon^{1/2}, \quad 1.31K_\epsilon^{1/3} \\ p_w/\gamma_\infty p_\infty &= (\sqrt{3}/2)\chi_\epsilon, \quad (1/18)^{1/3}K_\epsilon^{2/3} \\ \epsilon[0.664 + 1.73(T_w/T_0)](M^3C_H/\sqrt{\gamma_\infty}\chi_\epsilon) &= 0.219\chi_\epsilon^{1/2}, \quad 0.119K_\epsilon^{1/3} \end{aligned}\right\} \tag{2.19}$$

The appearance of χ_ϵ in the above strong-interaction solutions indicates clearly the roles of ϵ and the wall-temperature level. In view of the factor $[0.664 + 1.73(T_w/T_0)]$ in χ_ϵ, the boundary-layer displacement effect will depend strongly on the wall temperature. An interesting observation is that if we simply add the two asymptotic solutions for p_w/p_∞, the sum differs from the exact solution in the transition region by less than 12 percent. This seems to lend support to the empirical linear-combination laws proposed previously by certain investigators,[47,53] at least when ϵ is small.

We may now compare the zero-order solution in the two limits, i.e., Eq. (2.19), with the corresponding self-similar solutions which do not assume γ close to unity.[3,16,19,27] Some of these results are shown in Fig. 2.3. We may conclude from these comparisons that as an approximation for the surface pressure and skin friction when $\gamma = 1.4$, the zero-order solution may not be adequate, and a higher order solution (in ϵ) appears desirable. For the surface heat-transfer rate as well as the shock shape, however, the zero-order theory works reasonably well, in spite of the fact that γ in this case is actually not too close to unity.

The Inclined Flat Plate with Displacement

For this problem without bluntness, Eq. (2.15a) can be transformed to

$$(z \mp \zeta)(\sqrt{zz'})' = 1 \tag{2.20}$$

where the variables z and ζ now stand for

$$z = 4M^4|\alpha|^3Y_e/\chi_\epsilon^2 x, \qquad \zeta = 4[M^2\alpha^2/\chi_\epsilon]^2$$

The angle of attack of the plate, α, is positive for compressive flow over the plate. The negative sign in

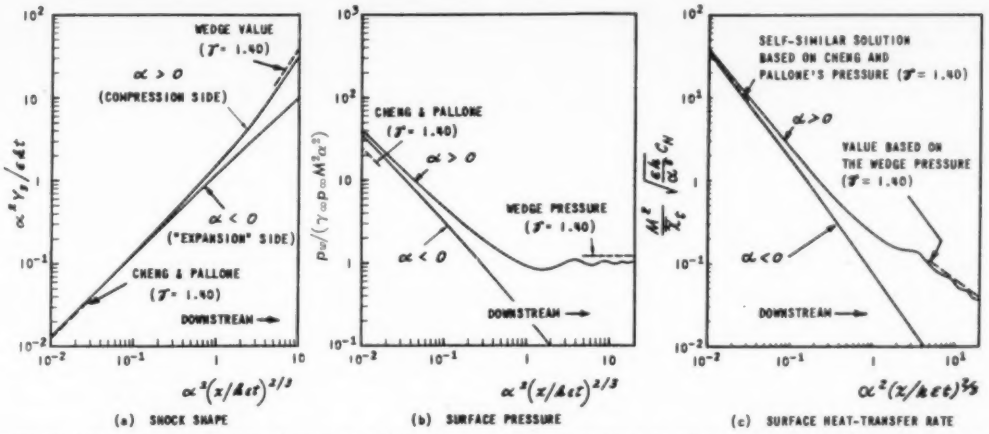

FIG. 2.5. Results based on the zero-order theory of a flat plate under the combined effect of leading-edge bluntness and angle of attack.

front of ζ in Eq. (2.20) applies to $\alpha > 0$. In view of the strong-shock requirement, our solution for $\alpha < 0$ pertains only to the situation when the boundary layer is thick enough to induce a strong bow shock. This implies that the region of validity is confined to certain upstream portions of the flow field, and to a rather small range of negative α. Again, there is only one variable governing the problem. In this case, it is $M^2\alpha^2/\chi_\epsilon$. Eq. (2.20) appears to be quite different from that underlying the analysis of Pai and Shen.[11,17,20] The difference arises perhaps mainly from the different flow models assumed for the outer flow.

For the case of $\alpha > 0$ the solution of Eq. (2.20) for large $M^2\alpha^2/\chi_\epsilon$, i.e., large x, will approach that for a wedge without displacement effect, i.e.,

$$Y_s = \alpha x + \ldots \tag{2.21}$$

For small argument of the variable, the strong-interaction solution results, as given previously in Eq. (2.19), and

$$Y_s = \frac{2}{(3)^{1/4}}\,\chi_\epsilon^{1/2}\frac{x}{M} + \frac{3}{10}\,\alpha x + \ldots \tag{2.22}$$

This development near the sharp leading edge is valid for both $\alpha > 0$ and $\alpha < 0$, and reveals a pattern of asymmetry. The curves for $\alpha > 0$ presented in Fig. 2.4* give a smooth transition from the regime of strong interaction to that of a usual hypersonic wedge flow. Curves for $\alpha < 0$ in the same figure show a gradual deviation from the Stewartson-Lees solution as we go downstream. For the shock shape and the pressure, the range of transition for $\alpha > 0$ appears to occur in $10^{-2} < M^2\alpha^2/\chi_\epsilon < 10$ whereas for the heat-transfer rate, the value corresponding to the pure wedge-flow solution is closely approached as early as $M^2\alpha^2/\chi_\epsilon = 2$. From the agreement of our zero-order solutions with the self-similar solution for $\gamma = 1.40$ in the two limits (see Fig. 2.4), we may anticipate the zero-order results to be reasonable for heat-transfer, pressure, and shock shape, provided the surface temperature is substantially lower than the stagnation temperature.

* The numerical results of Fig. 2.4 were obtained by digital-machine computation (IBM 704), using an interval of 100 points per unit of $(\zeta)^{1/4}$.

The Inclined Flat Plate With Tip Bluntness

For the inviscid problem of the blunted flat plate at incidence, we have from Eq. (2.15) the simple differential equation

$$(z \mp \zeta)(zz')' = 1 \tag{2.23}$$

where the variables z and ζ now stand for

$$z = 2\alpha^2 Y_e/\epsilon kt, \qquad \zeta = 2\,|\alpha|^3 x/\epsilon kt$$

In this case, we again use the same convention for α.

Near the leading edge, we find from Eq. (2.23) the result

$$Y_e/t = (3/2)^{2/3}(\epsilon k)^{1/3}(x/t)^{2/3} + (1/6)\,\alpha\,(x/t) + \ldots \tag{2.24}$$

which holds for both positive and negative α and reveals an asymmetrical perturbation of the blast-wave solution. At the far-downstream end, where the effect of the surface incidence dominates, we will develop the asymptotic solution only for $\alpha > 0$. Eq. (2.23) then yields for large ζ

$$\begin{aligned} z &= \zeta + 1 + (1/\sqrt{\zeta})[AJ_\nu(2\sqrt{\zeta}) + BY_\nu(2\sqrt{\zeta})] + \ldots \\ &= \zeta + 1 + (A/\zeta^{3/4})\cos(2\sqrt{\zeta} + B) \end{aligned} \tag{2.25}$$

In view of the first and second terms we see that the shock will tend to the wedge surface, but never quite reach it, as we go downstream. More interesting, however, is the oscillatory behavior of the solution. The corresponding behavior of the pressure is

$$\begin{aligned} p_w/(\gamma_\infty p_\infty M^2\alpha^2) &= (zz')' = \\ &1 - (A/\zeta^{3/4})\cos(2\sqrt{\zeta} + B) + \ldots \end{aligned} \tag{2.26}$$

Comparing Eqs. (2.25) and (2.26), the oscillatory decay of the tip-bluntness effect will be more readily revealed in the pressure distribution than in the shock shape. Some results obtained from numerical integration of Eq. (2.23) by digital machine computation are presented in Fig. 2.5.* The oscillatory decay of the tip-bluntness effect is indeed exhibited by the pressure distribution for $\alpha > 0$.

The physical reality of this decay is doubtful. The result of the zero-order solution in this respect is evidently connected with the passage to the mathematical limit, $\gamma \to 1$. Apparently, the oscillation represents a repeated reflection or skipping of the re-attaching shock layer as it reaches the vicinity of the surface of a very slender afterbody at infinite Mach number. The phenomena may hence be interpreted as a form of glancing reimpingement of the shock layer. From the fact that this oscillation is a decay phenomenon, its detail will probably be substantially altered by higher-order ϵ corrections. For $\gamma = 1.40$, we may not anticipate any oscillation in the pressure decay over a blunted wedge, since the amplitude of the fluctuation shown is never large.

The General Case of the Flat-Plate Problem and Similitude Based on Zero-Order Theory

For the flat-plate problem involving all three effects (χ_ϵ, K_ϵ, and $M\alpha$) we may choose to use, for example, the transformation

$$z = 8M(\chi_\epsilon^2/K_\epsilon)^2(Y_c/(K_\epsilon x), \qquad \zeta = 16(\chi_\epsilon/K_\epsilon^{2/3})^6$$

and Eq. (2.15) becomes

$$(z - \Gamma\zeta)(zz')' - \sqrt{zz'} = 1 \tag{2.27}$$

where Γ is the parameter (independent of x)

$$\Gamma \equiv K_\epsilon M\alpha/2\chi_\epsilon^2 \tag{2.28}$$

Fig. 2.6 gives the results of integration for the surface heat-transfer rate. Shown are curves corresponding to five positive values of Γ, namely, $\Gamma = 0$, 10^{-2}, 10^{-1}, 1, and 10. The curve for $\Gamma = 0$ has been previously given in Fig. 2.3(c). From these results we can see the role of the wedge angle in controlling the combined effect of bluntness and boundary-layer displacement. The slight oscillatory mode revealed in the curve at the upper left corner of the figure for $\Gamma = 10$ corresponds to the oscillatory pressure decay discussed previously for the inviscid wedge problem.

It may be pointed out that the zero-order theory has been applied thus far to problems involving the relatively simple case of the flat-plate afterbody. Eq. (2.15), meanwhile, is applicable to an arbitrary slender afterbody shape. In any case, a solution can be obtained by a "forward integration." With Eq. (2.15), an interesting aspect of the problems of optimization from the viewpoint of lift, drag, or heat transfer, which take into account both the bluntness and the displacement effects, may also be explored.

From the flat-plate problem, we see that the zero-order solution will be governed by only one variable and one parameter Γ. Viscous hypersonic flows over a blunted inclined plate will accordingly be similar for the same Γ. For thin bodies other than flat plates, inspection of Eq. (2.15) shows readily that the parameters governing the similitude are Γ and $(\chi_\epsilon/K_\epsilon^{2/3})_L$. The correlations based on this similitude will be subject, of course, to the same errors as Eq. (2.15). Implicit in the above results are also the assumptions of the linear viscosity-temperature relation, unit Prandtl number, as well as uniform T_w/T_0. Thus, for a more accurate correlation under more general conditions, the similitude based on our zero-order theory may not suffice. As a part of the study complementing the foregoing analysis, an examination of the hypersonic similitude under less restrictive conditions will be given in Section 2.3.

(2.3) Similarity of Hypersonic Flows Involving Leading-Edge Bluntness and Boundary Layers

For both experimental investigations and practical applications, laws of similitude for correlating flow-field properties under different free-stream conditions and body dimensions are desirable. The similitude arrived at previously in Section 2.2 is simple but restrictive. In the following, the more general viscosity-

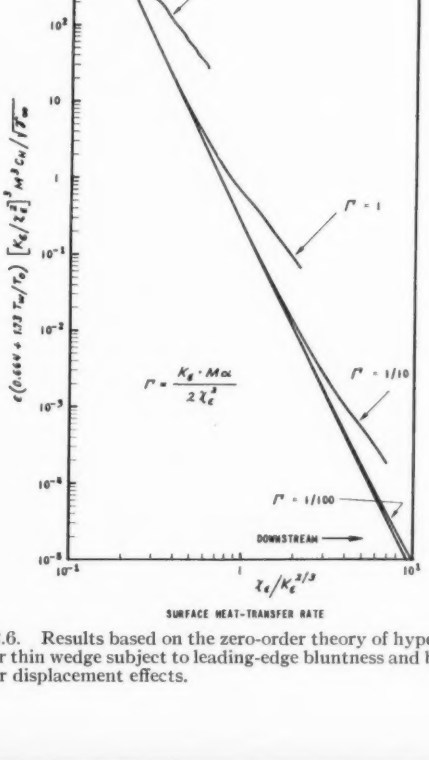

FIG. 2.6. Results based on the zero-order theory of hypersonic flow over thin wedge subject to leading-edge bluntness and boundary-layer displacement effects.

* An interval of 100 points per unit of $\zeta^{1/3}$ was used in the computation.

temperature relation $\mu \propto T^{\omega}$ is assumed, the Prandtl number is taken constant but otherwise arbitrary, and the body-surface temperature is not necessarily uniform. A perfect gas with constant specific heats is still employed but the specific-heat ratio is no longer required to be close to unity.

Basic Requirements for the Validity of Hypersonic Boundary-Layer Similitude Involving Leading Edge Bluntness

The (inviscid) hypersonic similitude which takes into account the effect of slight blunting has been given by one of us.[43] In a recent paper, Hayes and Probstein[44] considered the similitude involving boundary layers. From these two studies a viscous hypersonic similitude involving bluntness is not difficult to infer. Hayes and Probstein caution, however, that the similitude involving bluntness may *not* be extended to the viscous case, except under a condition so restrictive as to make the result uninteresting. In view of this, an examination of the basic requirements which underlie hypersonic similitude seems proper at this point.

Hayes and Probstein observe that the "equivalence principle," that is, the hypersonic small-disturbance theory, necessarily fails in the vicinity of the blunt nose itself, and it would appear that the layer of fluid of increased entropy nearest the body may not obey the law of similitude. It would also follow that the hypersonic boundary-layer similitude cannot exist. The major conclusion of our following discussion is that a full similitude capable of correlating the density and the temperature fields near the outer edge of the boundary layer is not possible, but for pressure and velocity fields, as well as for the density and the temperature within the boundary layer, the similarity laws do apply.

Let us first examine whether similitude can exist in the inviscid flow region. On the basis of our discussion in the earlier part of Section 2.2, we see that under requirement (a), the approximation $u \approx U$ holds throughout the inviscid flow region including the entropy layer. The applicability of the requirement (a), and the degree of approximation involved, have been examined. From the fact that $u \approx U$ we can conclude that the pressure p and the velocities v and u do obey the "equivalence principle"—hence, the hypersonic similitude.[35] For the density and temperature in the entropy layer, however, the "equivalence principle" may not be strictly applicable since these quantities may depend on the entropy determined upstream at the nose shock.

For the boundary layer, we observe that with the wall conditions specified the solution will be completely determined, in general, by the three quantities at its outer edge: the pressure p_δ, the total enthalpy H_δ $(=H_\infty)$, and the velocity u_δ. Now, all these quantities obey the law of similitude of the inviscid region; in particular, we have $u \approx U$, and these are exactly the conditions required for the similitude of the hypersonic boundary layers in the sense of reference 44. We may note that the actual magnitude of the error in the heat-transfer rate, the skin friction, and the displacement thickness incurred by the approximation $u_\delta \approx U$ will not differ a great deal from $|\Delta u_\delta/U|$. In fact, if we assume local similarity (which is appropriate for the present application) the corrections to these quantities will be, respectively, $-1/2$, $-3/2$, and $+1/2$ of $|\Delta u_\delta/U|$.

Therefore we conclude that with the exception of the density and temperature fields in the entropy layer, the classical hypersonic similitude of Tsien and Hayes can be extended to include both bluntness and boundary layer, so long as the flow regions immediately downstream of the leading edge are excluded and the flow Mach number is high, i.e.,

$$(1/2)(\theta)^{2(\gamma-1)/\gamma} \ll 1, \qquad M \gg 1 \tag{2.29}$$

In the absence of the tip bluntness, the first of these requirements may, of course, be replaced by a less restrictive condition related to the error due to slip, temperature-jump, or vorticity effect.

The inclusion of the tip-bluntness effect introduces an additional parameter M^3kt/L^* into the boundary-layer similitude discussed in reference 44. The similarity law correlating the flow quantities of interest in the experiments to be described may be written as

$$\left.\begin{array}{l} M(\chi_\epsilon^2/K_\epsilon)^2(Y_s/K_\epsilon x), \qquad (K_\epsilon/\chi_\epsilon^2)^2(p_w/\gamma_\infty p_\infty) \\ \epsilon\left(0.664 + 1.73\,\dfrac{T_w}{T_0}\right) \times \left[\dfrac{K_\epsilon}{\chi_\epsilon^2}\right]^3 (M^3C_H/\sqrt{\gamma_\infty}) \end{array}\right\} = f\left[\frac{x}{L};\ \left(\frac{\chi_\epsilon}{K_\epsilon^{2/3}}\right)_L,\ \Gamma,\ \frac{\chi_\epsilon^2}{K_\epsilon},\ \gamma,\ \omega,\ Pr\right] \tag{2.30}$$

with $\qquad Y_w/\tau L, \quad T_w/T_0 = f(x/L)$

This form may also be compared with the similitude reducible from Eq. (2.15) discussed previously. We see that the simplicity gained by the zero-order theory, which assumes a very strong shock and a very small ϵ, consists essentially in the elimination of the parameters γ, T_w/T_0, and $\chi_\epsilon^2/K_\epsilon$.

There are two important limiting cases of the similitude given above. One is the case of negligible boundary-layer displacement effect, the other that of a very strong shock wave. For the first, the interaction parameter $M^{2+\omega}/\sqrt{Re_L}$ will become merely a scaling factor, and we have

$$M\delta_*/L,\ M^3C_H,\ M^3C_f = (M^{2+\omega}/\sqrt{Re_L})f(x/L;\ M\tau,\ M^3kt/L,\ \gamma,\ \omega,\ Pr)$$

A discussion of the second case follows.

Hypersonic Similitude Involving Strong Bow Shocks

For this case, we require the shocks to be very strong

* For the axisymmetric case, it will be $M^3\sqrt{k}(t/L)$.

so that terms of order $1/M^2\theta^2$ are negligible in comparison with unity. From the viewpoint of practical application, consideration of this special form is not trivial. Since the essential difference in basic requirements between this similitude and the zero-order theory is the condition on γ, the zero-order theory furnishes a convenient basis for comparison with data correlated by this similitude.

Under the assumption of a strong shock the Rankine-Hugoniot shock conditions may be simplified. Using a suitable affine transformation, we arrive at a form of similitude comparable with Eqs. (2.29) and (2.30):

$$\left.\begin{matrix} M(\chi_\epsilon^2/K_\epsilon)^2(Y_s/K_\epsilon x), & (K_\epsilon/\chi_\epsilon^2)^2(p_w/\gamma_\infty p_\infty) \\ \epsilon\left[0.664 + 1.73\left(\frac{T_w}{T_0}\right)\frac{K_\epsilon}{\chi_\epsilon^2}\right]^3 (M^3C_H/\sqrt{\gamma_\infty}) \end{matrix}\right\} = f\left[\frac{x}{L}; \left(\frac{\chi_\epsilon}{K_\epsilon^{2/3}}\right)_L, \Gamma, \gamma, \omega, Pr\right] \tag{2.31}$$

with $\quad Y_w/\tau L, \quad T_w/T_0 = f(x/L)$

Comparing this with the more general similitude of Eq. (2.30), we see that in the above form of similitude the dependence on the parameter $(\chi_\epsilon^2/K_\epsilon)$ or, what amounts to the same thing, $kRe_t/M^{1+2\omega}$, becomes very weak as a result of the shock being very strong. On the other hand, comparison with the similitude based on the zero-order theory shows that as a consequence of relaxing conditions on Pr, ω, and ϵ, we have now to include as invariants the parameters Pr, ω, γ, as well as T_w/T_0. The dependence on γ and on T_w/T_0 in the strong-shock similitude cannot be too strong, however, since both are connected with the first-order ϵ effect.

(3) EXPERIMENTAL STUDIES OF FLATPLATE FLOWS

The foregoing theoretical study of Section 2 has treated the general problem of combined tip-bluntness, viscous-interaction, and body-angle effects in hypersonic flow about slender bodies. In particular, specific solutions have been given in Section 2.2 for the general flat-plate problem. In addition, hypersonic viscous similitude has been extended in Section 2.3 to include leading-edge bluntness effects. The present section will describe the accompanying experimental program which was designed to provide experimental data for assessment of the extended similitude of Section 2.3, and for comparison with predictions of the theoretical solutions of Section 2.2. Detailed results of the experiments are discussed in Section 4.

(3.1) Outline of Experiments

The experimental program involved the measurement of surface heat-transfer distributions and shock-wave shapes in hypersonic airflows about sharp and blunted flat plates under cold-wall conditions such that the (laminar) boundary layers were highly cooled. These studies were made in the C.A.L. 11 × 15-in. hypersonic shock tunnel at free-stream Mach numbers in the range 10.5 to 12.5. The range of leading-edge and unit free-stream Reynolds numbers employed was large enough to encompass the extremes of dominant bluntness and dominant viscous-interaction effects. Instrumentation has also been developed for measurement of surface-pressure distributions, and surface-pressure studies are currently underway.

Most of the experiments were conducted with air-stagnation temperatures in the range 2,000 ± 100°K, at Mach numbers in the range 11.3 to 12.5. With a plate surface temperature of close to 300°K, the corresponding wall-to-stagnation temperature ratios were within the range 0.15 ± 0.01. For these conditions, tests were made at zero angle of attack for leading-edge Reynolds numbers from about 3 to 15,000. Stream Reynolds numbers per inch here ranged from about 14,000 to 180,000, and leading-edge thicknesses from 0.0002 to 0.203 in.

Angle-of-attack effects were studied at low and high leading-edge Reynolds numbers over the incidence range −10 to +15°.

Heat-transfer measurements were also made over a range of air-stagnation temperatures from 2,000°K to 4,000°K for a sharp plate at zero angle of attack. The ratio of wall-to-stagnation temperatures in these tests ranged from 0.15 down to 0.075.

(3.2) Shock-Tunnel and Test Conditions

All experiments were conducted in the C.A.L. 11 × 15-in. hypersonic shock tunnel. A detailed description of this tunnel and the measurement techniques employed in its operation is given in reference 59. In the initial experiments of the present study, conducted with helium as the driver gas, 14 ft. of 3 in.-i.d., low-pressure-driven tube was used with a 14 ft., 3.5 in.-i.d. high-pressure driver. In the later stages of the program, an additional 14 ft. of driven tube was added, thereby doubling the total driven-tube length. The additional tube length served to increase the useful test time obtained with hydrogen as the driver gas. It may be noted here that doubling the driven-tube length resulted in no detectable change in measured heat-transfer rates or pressures in the tunnel test section with helium driver-gas operation. This fact indicated negligible effects on the test flow from possible mixing at the tailored interface.

The model tests were conducted in a two-stage nozzle described in reference 59, which was coupled to the end of the driven tube. The first stage of this nozzle is

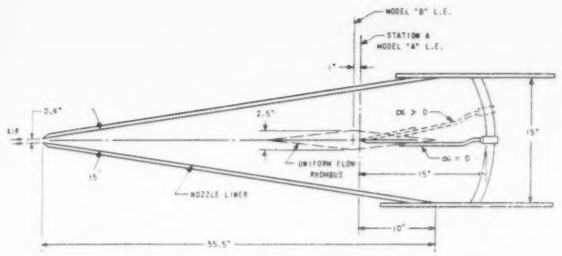

FIG. 3.1. Second-stage 15°-wedge nozzle used for tests.

convergent-divergent and expands the flow in a horizontal plane to a 1.5 × 12.25-in. cross section. Prior to entering the second stage, the flow is turned 10° upward by means of a deflection wedge in order to centrifuge out diaphragm particles. Final expansion in the vertical plane then takes place in a sharp-entrance, 15°-wedge nozzle which terminates in an 11 × 15-in. test section. Fig. 3.1 shows a schematic drawing of the 15°-wedge nozzle and illustrates the general test arrangement and model locations. Further details of model location are discussed in section 3.3.

The tunnel was operated under tailored-interface conditions with helium or hydrogen at room temperature used as the driver gas. With tailored-interface operation, the driver-gas initial conditions are adjusted to avoid shock reflection at the driver-driven gas interface. Theoretical tailoring with room-temperature helium and hydrogen results for shock Mach numbers in air of about 4 and 6.5, respectively. The corresponding (stagnation) temperatures behind the reflected shocks are close to 2,000 and 4,000°K. The range of stagnation pressure, p_0, behind the reflected shock employed in the experiments was from 1,000 to 10,000 psi. Experience has shown the quality of nozzle reservoir conditions attained behind the reflected shock to be negligibly affected by small departures from theoretical tailoring. With the 28-ft. driven tube, the duration of useful test flow was about 3 and 6 msec. for hydrogen and helium driver gases, respectively, following the initial period of 0.5 to 1 msec. required to attain steady, test-flow conditions.

Shock-tube conditions measured in each experiment included initial air pressure in the driven tube, initial shock-wave speed, and the nozzle reservoir pressure p_0 attained behind the reflected shock wave. The nozzle reservoir conditions, including stagnation enthalpy, pressure, and density, are calculated from measured shock speeds with the use of real-gas, equilibrium-flow, shock relations. The measured pressure p_0, obtained as a function of time by means of SLM piezoelectric and Norwood strain-gauge transducers, provides a positive and direct check on the calculated reservoir conditions. Over a range of values of p_0 from 1,000 to 10,000 psi, the average difference between measured and calculated values of p_0 is about 5 percent.

Calibration studies of the test flow in the 15°-wedge nozzle have included simultaneous measurement of static pressures at the tunnel sidewalls and flow pitot pressures across the tunnel by means of a multiple-probe rake, flow angularity studies with a multiple-wedge rake instrumented for heat transfer,[61] and measurement of surface pressures on a sharp-edged plate at large compressive incidence such that interaction effects are negligible. Static pressures at the sidewalls have been measured with Altec-Lansing microphones and also with barium-titanate piezoelectric transducers. The latter have also been employed in pitot-pressure rakes.* As regards test Mach number, the calibration studies for helium/air operation, $T_0 \sim 2{,}000$°K, indicate an average value on the tunnel centerline at station A (Fig. 3.1) of 12.6 ± 0.3 at a stagnation pressure p_0 of 10,000 psi, 12.3 ± 0.3 at 5,000 psi, and 11.3 ± 0.2 at 1,000 psi. Typical calibration results for Mach number variations with time at several positions along a diagonal in the plane of station A (Fig. 3.1) are shown in Fig. 3.2 for reservoir pressures of 1,030 and 4,350 psi. The open symbols indicate Mach numbers at the diagonal positions shown as calculated from the ratios of the measured pitot (p_0') to reservoir (p_0) pressures assuming isentropic, equilibrium flow. The local pitot pressures in this case were measured with a pitot rake

* Most of the pressure instrumentation employed for calibration studies was developed by the Hypersonic Wind Tunnel Department of the C.A.L. Experimental Facilities Division. Grateful acknowledgement is made to K. D. Bird and J. F. Martin, Head and Assistant Head, respectively, of that Department, for their cooperation in making this instrumentation available

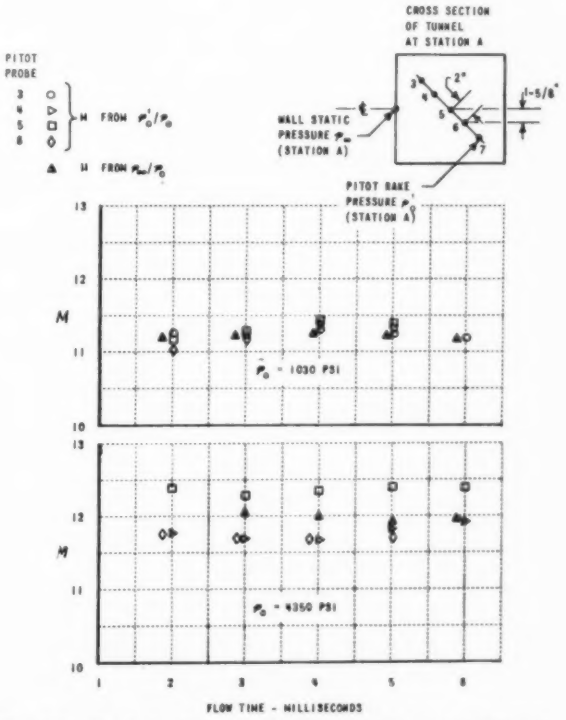

FIG. 3.2. Typical calibration results for Mach number (M) survey at Station A. Helium/air operation, $T_0 \sim 2{,}000$° K.

employing barium-titanate transducers. Also shown in Fig. 3.2 is the flow Mach number as calculated from the ratio of measured wall static pressure to reservoir pressure, the wall static pressure being obtained with a modified Altec-Lansing microphone located on the tunnel centerline at station A.

Measurements of local pitot pressure and flat-plate heat transfer at different longitudinal stations on the 15°-nozzle centerline have indicated very small longitudinal gradients over a distance of three to four inches at the test location used. Differences in heat transfer were not measurable over this distance. The maximum Mach-number gradient at the test location is estimated to be less than 0.1 per inch. It will be noted in Fig. 3.1 that the test location is included within the theoretical, uniform-flow test rhombus as calculated from the method of characteristics with allowance for boundary-layer development.

Information on the flow angularity with respect to the 15°-nozzle axis has been obtained from surveys with a multiple-wedge rake instrumented for heat-transfer measurement.[61] More recently, further information on the flow angularity has been obtained from the results of extensive heat-transfer studies with a yawed slender cone.[67] The results of these tests indicate the centerline flow at station A to have an angularity of −0.8 degrees in the pitch plane (downward in Fig. 3.1) and 0.6 degrees in the yaw plane.

For individual experiments, the test-flow properties at station A were calculated from the test Mach number M, the reservoir pressure p_0, and the stagnation enthalpy H_∞, assuming isentropic expansion with thermodynamic equilibrium maintained. At the stagnation temperature of 2,000°K and the relatively high stagnation pressures employed (exceeding 1,000 psi), oxygen dissociation is quite negligible and molecular vibration is the only inert degree of freedom excited. The assumption of a test flow in thermodynamic equilibrium for these conditions is considered valid on the basis of calculations of typical vibrational relaxation effects to be expected in the first expansion stage of the 11 × 15-in. tunnel nozzle. These calculations were carried out for pure nitrogen at a stagnation temperature of 2,000°K over a range of reservoir pressures appropriate to the present experiments. The nitrogen molecules were assumed to be harmonic oscillators initially in complete thermodynamic equilibrium at the reservoir conditions. In subsequent expansion through the nozzle, a Boltzmann population of vibrational states was assumed to persist, characterized by a lagging vibrational temperature. This model for relaxation from an initial Boltzmann distribution is consistent with the findings of Montroll and Shuler[64] for Landau-Teller collisional transition probabilities. For the particular geometry of the first expansion stage, the results of the calculations show vibration-relaxation effects to be relatively small and probably unimportant at reservoir pressures of 1,000 psi, and quite negligible at higher pressures.

At the stagnation temperature of 4,000°K and the lower stagnation pressures employed, an appreciable amount of oxygen is dissociated. Departure from equilibrium of oxygen dissociation in the nozzle expansion must be considered at these conditions, as the enthalpy involved is of the same order as that in nitrogen vibration. As part of a separate program of nonequilibrium-flow research underway at C.A.L., calculation studies of nonequilibrium nozzle airflows involving oxygen dissociation have been made on the basis of various simplified kinetic models of air.[68,69] For a stag-

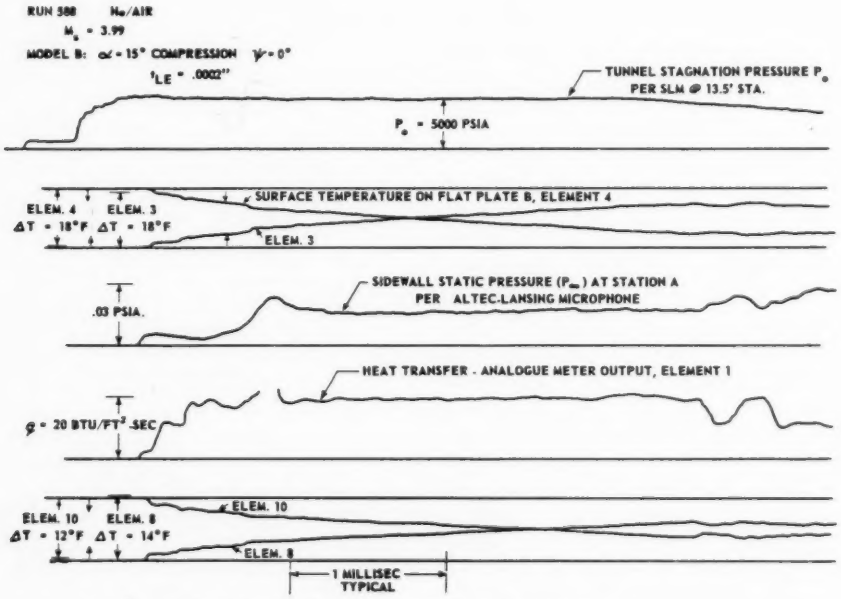
RUN 588 H_∞/AIR
M_∞ = 3.99
MODEL B: α = 15° COMPRESSION ψ = 0°
t_{LE} = .0002"
TUNNEL STAGNATION PRESSURE P_o PER SLM @ 13.5" STA.
P_o = 5000 PSIA
SURFACE TEMPERATURE ON FLAT PLATE B, ELEMENT 4
ELEM. 4
ELEM. 3
ΔT = 18°F
ΔT = 18°F
ELEM. 3
SIDEWALL STATIC PRESSURE (P_∞) AT STATION A PER ALTEC-LANSING MICROPHONE
.03 PSIA.
HEAT TRANSFER - ANALOGUE METER OUTPUT, ELEMENT 1
q = 20 BTU/FT^2-SEC
ELEM. 10
ELEM. 8
ΔT = 12°F
ΔT = 14°F
ELEM. 10
ELEM. 8
1 MILLISEC TYPICAL

FIG. 3.3. Typical drum-camera oscilloscope record.

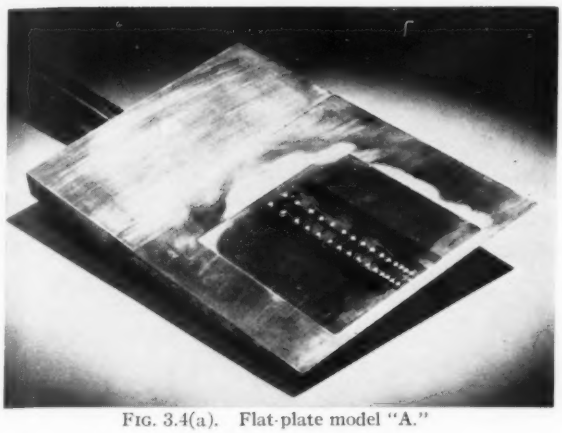

FIG. 3.4(a). Flat-plate model "A."

nation temperature of 4,000°K and the present pressure levels, these studies indicate the effects of dissociation nonequilibrium on test-section conditions to be relatively small. While some freezing of atomic oxygen may be expected to occur, the amount of enthalpy frozen in is not sufficiently large to substantially affect the thermodynamic and gasdynamic state of the flow. This is particularly true at the higher stagnation-pressure levels of the present tests, i.e., around 5,000 psi.

As regards the possibility of air liquefaction in the nozzle flow, the lowest static stream temperature at station A was around 70°K, attained with helium as the driver gas and a stagnation temperature of around 2,000°K. This static temperature was well above the equilibrium liquefaction limit at the pressures involved.

A typical drum-camera record from the multichannel Hathaway oscilloscope employed for recording is shown in Fig. 3.3. The record shows the time histories of reservoir pressure p_0 and sidewall static pressure p_∞ at station A, in addition to surface temperature change with time at various locations on a flat-plate model at station A.

(3.3) Heat-Transfer Models and Instrumentation

Two flat-plate models were employed in the experiments. Figs. 3.4 and 3.5 show the pertinent details of the two models which will henceforth be designated as A and B. Both models are made of steel. The leading-edge wedge angles are 30° for A and 20° for B. These relatively large angles permitted location of a heat-transfer gauge within $^3/_8$ in. of the leading edge (see below) and also facilitated honing of the leading edges to a thickness of 0.0002 in. for the sharp-edge tests.

For heat-transfer measurements, each model was fitted with thin-film resistance thermometers of platinum deposited by air spray on a thin Pyrex insert, as indicated in Figs. 3.4 and 3.5. The insert of Model A contains a central row of 15 elements. That of Model B contains elements at several spanwise stations as well as the central row in order to provide a check on spanwise effects. The Pyrex inserts and steel were mated very carefully, particularly at the leading edge, to minimize the step.

The heat capacity of such thin-film thermometers is sufficiently small that the films record instantaneous surface temperature change with time within very small errors.[62] Local heat-transfer rates were obtained

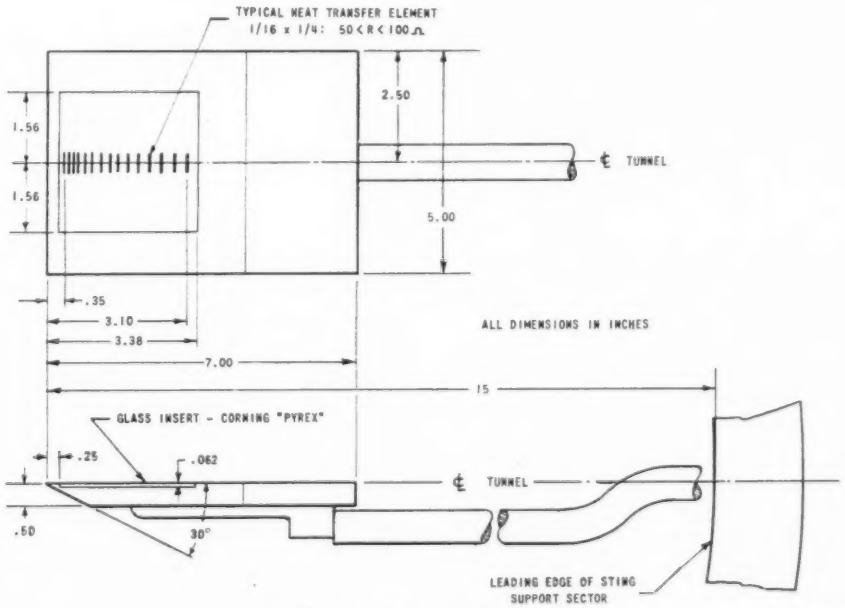

FIG. 3.4(b). Flat-plate model "A."

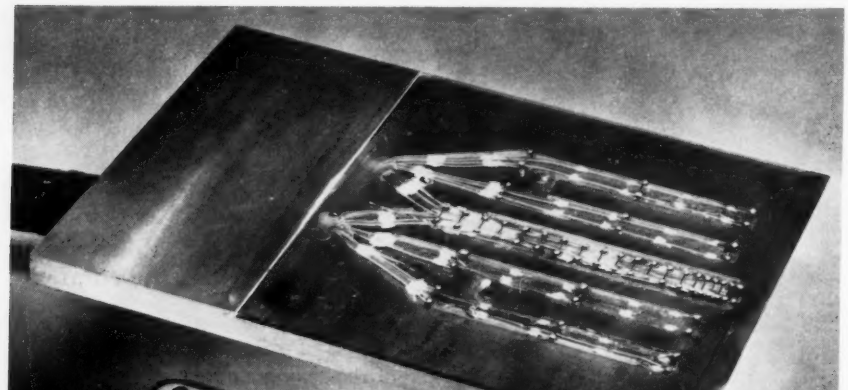

FIG. 3.5(a). Flat-plate model "B."

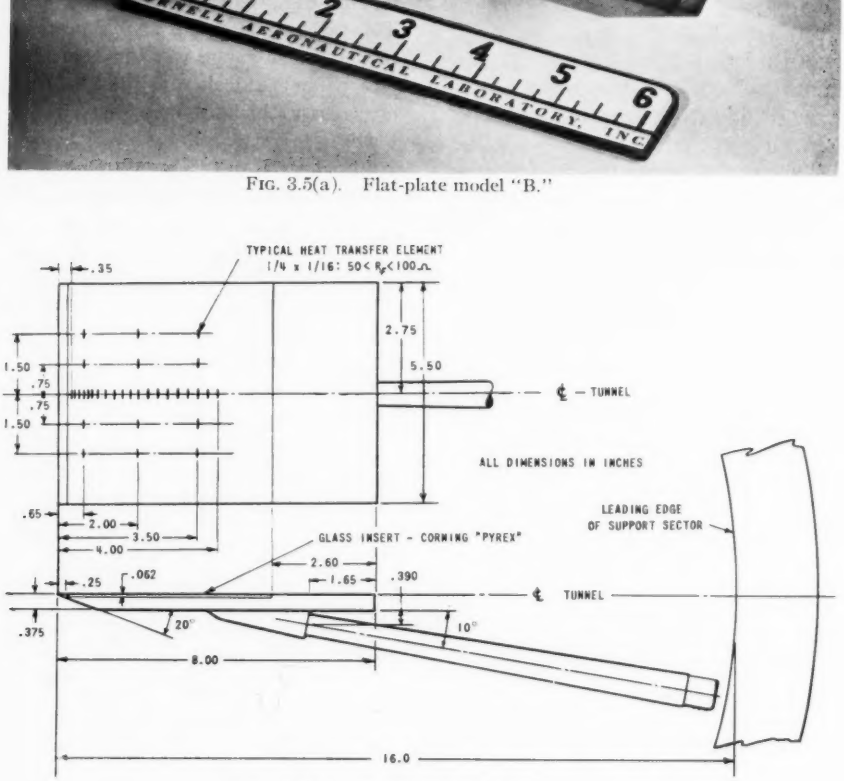

FIG. 3.5(b). Flat-plate model "B."

by numerical (IBM 704) solution of the one-dimensional heat-flow equation with the measured surface temperature-time histories as input data. Further detailed information on the thin-film circuitry and recording methods employed with the 11 × 15-in. C.A.L. shock tunnel is given in reference 60.

Model calibration included determination of the product $\rho C_p k$ for the Pyrex plate inserts, as well as determination of the resistance-temperature curve for each film. The product $\rho C_p k$ is required in the calculation of heat-transfer rate from measured, surface-temperature change. Calibration of $\rho C_p k$ with the electrical pulse method[62] gave values of $\sqrt{\rho C_p k}$ in close agreement with the value 0.0745 Btu/ft²—°F previously determined for Pyrex by Vidal.[62] This value was used in reduction of the data.

The resistance-temperature curve for each film was determined by a film resistance measurement at two temperatures with the assumption that the slope was constant. The assumption of constant slope has been shown to be good over a very wide range of film temperature change.[62] In the present tests, the surface temperature rise in the time period of interest did not usually exceed 10°F. Film resistance was checked at frequent intervals. Only the slope of the resistance temperature curve enters the determination of heat-transfer rate. Over a period of about a year the films were found to be exceedingly stable. With Model A,

for example, the maximum change during this time in the resistance-temperature curve slope of any one element was about 3 percent, and for most elements it was less than 1 percent.

Regarding film durability, the major loss of films occurred during the first few runs with the newly instrumented models. This experience is common with thin-film instrumentation. Model A proved very durable, with only one of 15 elements being lost. On Model B, however, 12 of the 20 central elements were eventually lost as well as several of the outboard elements.

Model A was employed for the initial, sharp leading-edge tests and for all bluntness tests. For the bluntness tests, the leading-edge material was progressively removed to a maximum leading-edge thickness of about 0.010 in. Further blunting up to 0.203 in. was done by cementing on thin slabs with sharp 90° and 120° corners maintained by subsequent light grinding and hand finishing [see Fig. 4.2(d)]. The leading edge of Model B was not blunted. Leading-edge thicknesses t were measured on an optical comparator. For the smallest thicknesses, 0.0002 to 0.0096 in., comparator measurements were made of impressions of the leading edge taken with soft solder across the model span. The thickness of 0.0002 in. represents the best estimate obtainable for the sharpest leading-edge condition and is to be considered as an upper limit on t.

Both models were supported by stings from a circular-arc sector as indicated in Figs. 3.1, 3.4, and 3.5. At zero angle of attack, the instrumented surface of both models lay in the tunnel centerplane. The leading edge of A was located at station A. The leading edge of B was about one inch upstream of station A. At angle of attack, the leading edge of A remained fixed in the tunnel centerplane while that of B moved a maximum distance of 0.5 in. off the centerplane at $\alpha = 15°$.

Angles of attack (α), roll (zero), and yaw (zero), were maintained to about ± 0.10 degrees to the geometric axes of the tunnel.

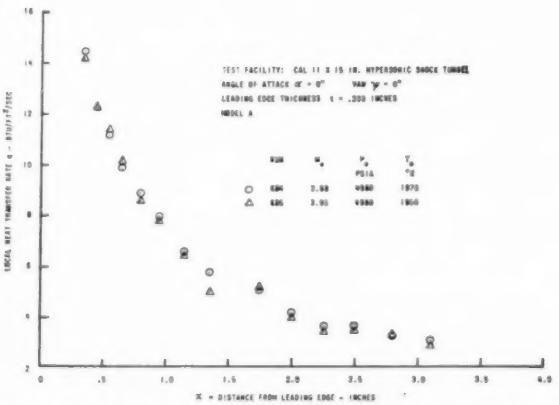
TEST FACILITY: CAL. I.I. X 15 IN. HYPERSONIC SHOCK TUNNEL
ANGLE OF ATTACK α = 0°
YAW ψ = 0°
LEADING EDGE THICKNESS t = .200 INCHES
MODEL A
RUN
M_∞
P_o PSIA
T_o °F
684 3.98 4980 1970
685 3.95 4980 1960
LOCAL HEAT TRANSFER RATE q - BTU/FT²/SEC
X - DISTANCE FROM LEADING EDGE - INCHES

FIG. 4.1. Typical variation and reproducibility of measured heat transfer.

Schlieren Apparatus

The schlieren system employed was the conventional, off-axis single-pass type with 12-ft focal length, 16-in. diameter, parabolic mirrors. A short-duration barium-titanate spark was the light source. A magnification somewhat greater than one was used to increase detail. The collimated schlieren beam was very carefully aligned with the model in roll and yaw with the aid of sighting wires located at extreme spanwise stations. Calibration photos which included a length calibration grid were taken prior to each run.

Shock-wave coordinates relative to the plate were measured from the photographic negatives on an optical comparator.

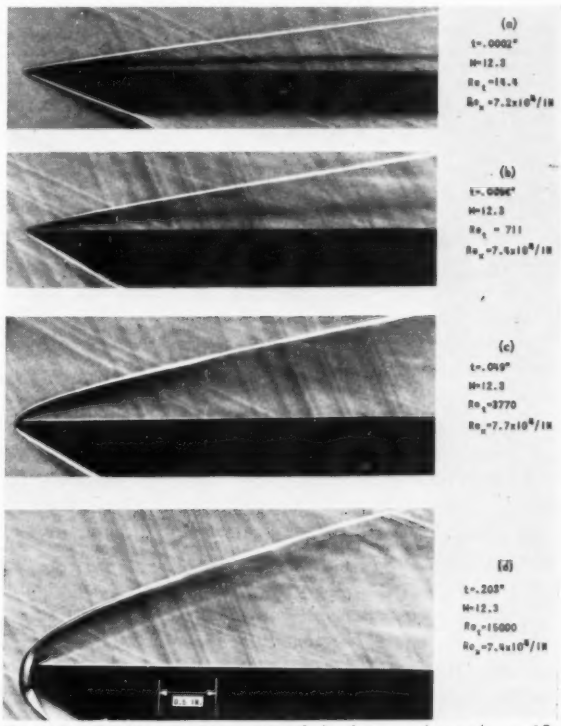

FIG. 4.2. Schlieren photographs of shock-wave shapes ($\alpha = 0°$, $T_0 \sim 2{,}000°\text{K}$).

(4) EXPERIMENTAL RESULTS

(4.1) General

Some general aspects of the experimental results will be discussed prior to considering the detailed findings.

Fig. 3.3 shows typical oscilloscope recordings of plate-surface temperatures. With constant surface heat-transfer rates, the temperature at any point increases as the square root of time. With the small ratio of wall-to-stagnation temperatures of the present tests, and the small rise of surface temperatures in the short test-flow period, the changes in surface temperature have negligible effect on the local heat-transfer rates.

Also shown in Fig. 3.3 is the output from a simple analog computer network which solves the one-dimensional heat-flow equation.[70] The input signal for the analog network is the output voltage from a thin-film element. The output signal of the computer, shown in Fig. 3.3, is the local heat-transfer rate q. Such analog networks have recently been incorporated into all recording channels.

(4.2) Schlieren Results

Schlieren studies were carried out at zero angle of attack for the nominal conditions described in Section 3.1. At the test Mach number of around 12 and $T_0 \sim 2{,}000°\text{K}$, the range of Re_t covered was such that $\beta = \chi_\epsilon K_\epsilon^{-2/3}$ varied from large values for which viscous-interaction effects would dominate down to small values

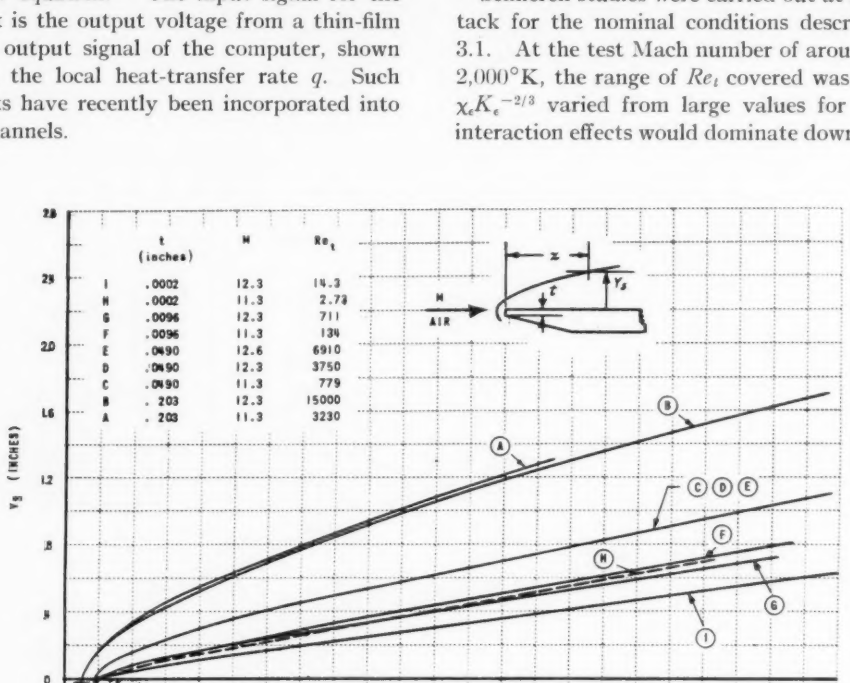

FIG. 4.3. Summary of shock-wave shapes ($\alpha = 0$, $T_0 \sim 2{,}000°\text{K}$).

In general, at least two tunnel runs were made for each set of experimental conditions. Fig. 4.1 shows a plot of local heat-transfer rate q versus distance downstream from the plate leading edge for two successive runs with closely equal stagnation temperatures and pressures. The reproducibility here is perhaps somewhat better than that usually obtained. The average scatter obtained in q was about ± 5 percent.

The distribution of q in Fig. 4.1 is typical for all conditions studied. The magnitude and distribution of q indicate a laminar boundary layer. Changes in q indicative of transition were not observed. Early experiments with Model A having a length of 4 in. showed somewhat high values of q at the most downstream elements, followed by a very rapid drop in q. It was suspected that these peculiarities were caused by some type of trailing-edge influence, and they were substantially eliminated on lengthening the model to 7 in.

Tests with Models A and B for the sharpest leading edges (0.0002 in.) under the same tunnel conditions gave the same results within the normal scatter. This indicated small effect due to the difference in the two wedge angles of 30 and 20 degrees, respectively. As regards spanwise variations of q, tests with Model B over a wide range of reservoir pressures showed no significant spanwise variations across the central 1.5 in. of the test surface.

for which inviscid bluntness effects would dominate. A valuable aspect of the schlieren studies was the direct assessment they provided of the degree to which the experimental flows met requirements (a) and (b) of the theory (Section 2.2) as expressed in terms of the local shock-wave angle.

Typical schlieren photographs for a range of Re_t at nearly constant Re_x per inch are shown in Fig. 4.2. The outer region of the boundary layer is evident in (a) and (b). With increased blunting, the density decreases adjacent to the surface. For sufficient blunting, the boundary layer is not detectable at the low-density levels obtained. The background striations in the photographs of Fig. 4.2 are caused by the relatively poor schlieren quality of the test-section windows employed. These windows produced negligible image distortion.

A comparative summary of typical shock-wave shapes deduced from photographic negatives is given in Fig. 4.3. Here the behavior of the shock shape is seen to be qualitatively similar to that observed by previous investigators (e.g., reference 49) for hypersonic flow with adiabatic-wall conditions. For sufficiently large Re_t, the flow is nearly inviscid and the shock shape becomes dependent only on K_ϵ. At sufficiently small values of Re_t the shape is determined essentially by mutual interaction of the shock wave and plate bound-

ary layer. The effect of the boundary layer for small Re_t may be seen by comparing shapes H and I in Fig. 4.3 which were obtained for the same leading-edge thickness t but for different free-stream Reynolds numbers per inch. With decreased Reynolds number the boundary-layer displacement thickness and hence, the effective body thickness is increased, which pushes out the shock wave. A significant difference between the present studies and previous adiabatic-wall investigations is the fact that in the present experiments the boundary layer was highly cooled. The large cooling thins the boundary layer in comparison with the adiabatic-wall case, and thereby reduces the displacement effect.

For sufficiently large values of Re_t the hypersonic similitude for inviscid, perfect-gas flows with bluntness[43] should apply. The similitude indicates that the shock shape should then correlate as

$$Y_s/t = kM^2 f(x/M^3kt, \gamma)$$

even for the weak-shock case. Correlations of this type have previously been observed for helium test gas results.[3] Fig. 4.4 shows correlation of the present air results in the form Y_s/t versus x/t at the three largest values of Re_t employed. Also shown for comparison is the limiting theoretical prediction from the present zero-order theory of Section 2.2 for small β, and a previously obtained strong blast-wave result.[3] The correlation of the experimental shock shapes is good. The agreement with the zero-order prediction, which assumes a strong shock wave and γ close to one, is within about 10 percent at best. At small x/t, the large flow deflections cause departure from the theory. At large x/t, departure results because of progressive deterioration of the strong shock condition required by the theory, i.e., $M^2(dY_s/dx)^2 \gg 1$.

A general correlation of all experimental shock shapes in terms of the variables $\chi_\epsilon{}^4 K_\epsilon{}^{-3} M Y_s/x$ and $\beta = \chi_\epsilon K_\epsilon{}^{-2/3}$ given by the strong shock similitude for a perfect gas (Section 2.2) is shown in Fig. 4.5. In reducing the schlieren data to this form, stream conditions were obtained as discussed in Section 3.2. Values assumed

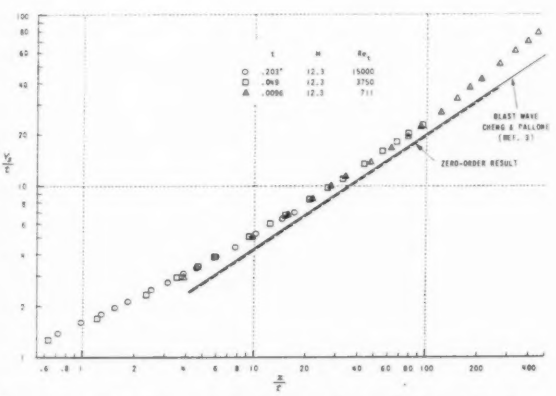

FIG. 4.4. Correlation of shock-wave shapes for large Re_t ($\alpha = 0°$, $T_0 \sim 2{,}000°$ K).

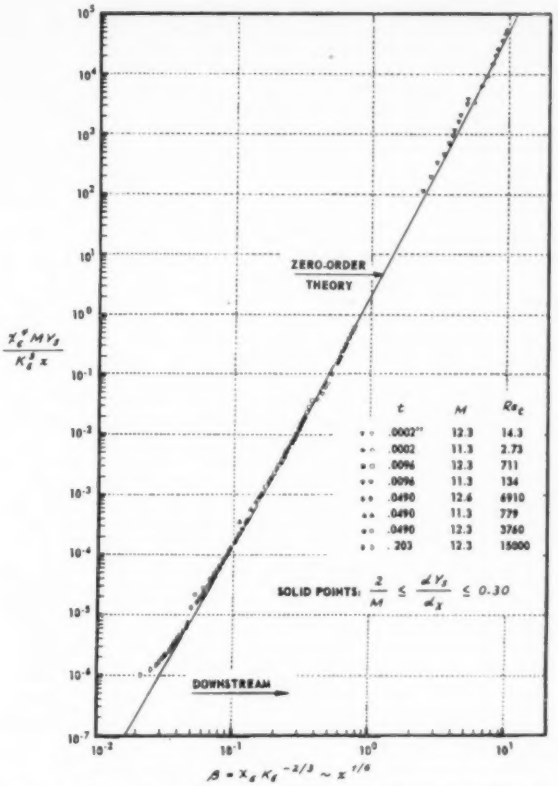

FIG. 4.5. General correlation of shock-wave shapes for arbitrary β ($\alpha = 0°$, $T_0 \sim 2{,}000°$K).

for γ and the leading-edge drag coefficient k were 1.40 and 2, respectively. The correlation is fairly insensitive to the value of k. The value of C used in evaluating χ_ϵ was based on the reference temperature T_* suggested in Section 2.2. Correlation of the data in terms of variables applicable for a perfect gas flow is reasonable in the present situation. With the large boundary-layer cooling present, the maximum temperature in the boundary layer was only of the order of 500 to 700°K ($T_0 \sim 2{,}000°$K). The inviscid flow field external to the boundary layer was several hundred degrees cooler than this except in the immediate stagnation-point region with large bluntness. Assuming equilibrium flow about the plate (no vibrational lag), real-gas effects would be quite small where flow deflections are sufficiently small to satisfy the requirement of the theory—i.e., away from the stagnation zone.

In addition to requiring the usual conditions for hypersonic small-perturbation theory, $M \gg 1$ and $\theta \ll 1$, a correlation in Fig. 4.5 also requires the condition of a strong shock wave. The lack of correlation of certain data points can, in general, be attributed to failure of the experiments to meet these conditions. In order to emphasize this aspect of the experimental data, the data points have been divided into two groups on the basis of whether or not they meet the criterion

$$2/M \leq dY_s/dx \leq 0.30$$

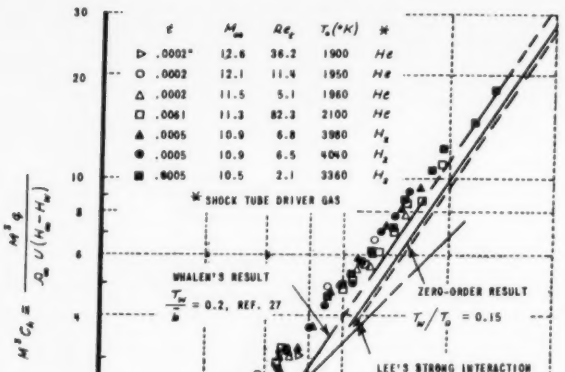

FIG. 4.6. Correlation of experimental heat transfer for small Re_t ($\alpha = 0$).

These arbitrary limits on dY_s/dx result from the conditions

$$(1/2)(dY_s/dx)^{2(\gamma-1)/\gamma} \leq 1/4 \qquad \text{(a)}$$

$$M^2(dY_s/dx)^2 \geq 4 \qquad \text{(b)}$$

considered to be reasonable minimum requirements corresponding to (*a*) and (*b*) in Section 2.2. The filled symbols in Fig. 4.5 are those for which dY_s/dx falls within the above bounds. It can be seen that these points correlate reasonably well. The remaining points violate condition (b) far downstream and condition (a) close to the leading edge. In particular, it will be noted that all the data points for the experiment with $t = 0.0002$ in. and $Re_t = 14.3$ fail to meet condition (b) above.

Also shown in Fig. 4.5 for comparison with the experimental data is the zero-order result of the present theory. In addition to requiring the above conditions to be satisfied, the zero-order result requires small ϵ, or γ close to unity. The agreement with the experimental data is seen to be fairly good over a wide range of β where the assumptions of the theory are most valid. In particular, the largest discrepancy between experiment and theory occurs for $t = 0.0002$ in. and $Re_t = 14.3$, where no data points satisfy the strong-shock limit (b) above.

(4.3) Heat-Transfer Results

For purposes of correlation and comparison with the present zero-order theory for a perfect gas, a local heat-transfer coefficient $C_H = q/\rho_\infty U(H_\infty - H_w)$ was used. Values of other parameters employed in reduction of the data were $\gamma = 1.4$, $k = 2$, and $C = C(T_*)$.

A general characteristic of the correlations to be discussed (and also of Fig. 4.5) is the fact that they are not too sensitive to the drag coefficient k, leading-edge thickness t, or to the stream Mach number M and the constant C for fixed stagnation conditions p_0 and H_∞. Changes in M at fixed p_0 and H_∞, of course, also produce corresponding changes in $\rho_\infty U$ and Re_x. This relative insensitivity also applies to a considerable degree to the measure of agreement between theory and experiment. The insensitivity results because changes in the parameters concerned generally affect both ordinate and abscissa in such a way as to displace points in a direction more parallel to the correlation curve than normal to it. As a consequence of this behavior, possible small errors in the test Mach number at given p_0 and H_∞ would have very little effect on the present correlations.

Small Re_t, $\alpha = 0$

The present similitude study (Section 2.3) indicates that for the strong shock-wave condition, M^3C_H for $\alpha = 0$ should correlate in terms of the usual viscous-interaction variable $\bar{\chi} = M^3\sqrt{C}/\sqrt{Re_x}$ at large values of $\beta = \chi_\epsilon K_\epsilon^{-2/3}$, for given values of γ, H_w/H_∞, etc. Correlation for a weaker shock will show an additional dependence on $K_\epsilon\chi_\epsilon^{-2}$. If $K_\epsilon\chi_\epsilon^{-2}$ is sufficiently small, however, even the weaker-shock case should correlate in terms of $\bar{\chi}$. In terms of the present experiments where the strong-shock condition is met only to a marginal degree, this means that a correlation of M^3C_H in terms of $\bar{\chi}$ could be expected only for the lowest values of Re_t.

Typical experimental results in the form M^3C_H versus $\bar{\chi}$ are plotted in Fig. 4.6 for a range of stagnation temperatures up to 4,000°K. The values of Re_t range from 2 to 200, approximately. Also shown are theoretical predictions for the strong-interaction region given by Lees,[16] Whalen,[27] and the present zero-order theory, as discussed in Section 2.2. The zero-pressure-gradient prediction of A. D. Young (reference 63, page 422) has been evaluated for the typical experimental conditions $M = 12.3$, $H_w/H_\infty = 0.14$, $Pr = 0.72$, and $\omega = 0.80$. The latter prediction is quite insensitive to this particular choice of conditions.

In general, the data of Fig. 4.6 for 2,000°K stagnation temperature correlate reasonably well. With the data scatter obtained, it was difficult to detect a positive influence of increasing Re_t for values of Re_t less than about 300. From the strong-shock similitude, the relative importance of viscous-interaction and bluntness effects depends only on the variable β, provided the shock is strong. For the highly cooled boundary layer, bluntness effects at a given station x are relatively larger than in the adiabatic-wall case, since large cooling thins the boundary layer and reduces the severity of viscous interaction. This was first pointed out by Lees and Kubota,[2] and is evident from examination of the effect of H_w/H_∞ on β as discussed in Section 2.2. If a value for Re_t of 300 is taken as that indicating a measurable

bluntness effect in the present experiments, the corresponding value of β at $x = 1$ in. downstream from the plate leading edge is about 0.4. For this value of β, the present zero-order theory predicts an increase in M^3C_H of about 10 percent due to leading-edge bluntness.

The data of Fig. 4.6 for stagnation temperatures between 2,000 and 4,000°K provide an extended check of the similitude as well as a check of possible real-gas effects. Equilibrium real-gas phenomena reduced the Mach number of these tests to the range 10.5 to 10.9. The high-temperature data correlate well with those for low temperature, indicating that the wall-to-stagnation temperature ratio and real-gas effects have small net influence on the heat transfer. This behavior is not unexpected, since in the similitude of the zero-order theory the dependence on H_w/H_∞ disappears completely. Further, real-gas effects in the flow about the plate are minimized for the sharp leading-edge condition. Such real-gas effects as occur may be expected to be correlated in terms of the heat-transfer coefficient used which is based on a total enthalpy rather than a total temperature difference.

As regards the agreement of theory and experiment in Fig. 4.6 for small Re_t, the present zero-order theory lies below the experimental data. The difference is attributed principally to failure of the experiments to meet adequately the strong shock condition required by the theory, and also to the fact that the experimental values of γ and Pr are not too close to 1. Effects due to velocity-slip, temperature-jump, and shock-wave heating, which are not accounted for in the theory, are considered to be small. The shock is strongest close to the plate leading edge where the slope is largest. In this region, the data points in the largest range of $\bar{\chi}$ (from 15 to 27) show the best agreement with theory, being some 15 to 20 percent high. This difference becomes larger with increasing distance downstream as $\bar{\chi}$ and the shock slope decrease. The agreement with Whalen's more exact calculation[27] based on the self-similar solution and $\gamma = 1.4$, $T_w/T_0 = 0.2$, and $Pr = 1$ is excellent at the largest values of $\bar{\chi}$.

Comparison of the data in Fig. 4.6 with the zero-pressure-gradient result of A. D. Young suggest that the data may lie in a transition region whereby M^3C_H tends from the variation proportional to $\bar{\chi}$ at low $\bar{\chi}$ (Young) to the variation proportional to $\bar{\chi}^{3/2}$ at high $\bar{\chi}$ (Lees, etc.). It was desired to obtain low Mach number (low $\bar{\chi}$) data to determine whether such data would fair in smoothly to the zero-pressure-gradient theory at sufficiently low $\bar{\chi}$. However, tests could not be carried out at sufficiently low Mach numbers for this purpose in the 11 × 15-in. tunnel. As an alternative, it was decided to reduce the data obtained for small t at large positive angle of attack (compressive flow), and high density, in terms of local M^3C_H and $\bar{\chi}$ values based on conditions behind the leading-edge shock wave as computed for inviscid flow. At sufficiently high density behind the shock, the viscous interaction effects are small and the zero-pressure-gradient result should apply.

The filled symbols of Fig. 4.7 are the positive angle-of-attack data ($T_0 \sim 2{,}000$°K) plotted in this form, i.e., $M_1{}^3C_{H_1}$ versus $\bar{\chi}_1$, where state (1) is that behind the leading-edge shock for inviscid flow. The data for $\alpha = 0$ and $T_0 \sim 2{,}000$°K of Fig. 4.6 are also included as the open, unflagged symbols. The local values of $\bar{\chi} = \bar{\chi}_1$ go down to about 0.4 for $\alpha = +15°$. At this end, the experimental results do appear to fair in quite well with the zero-pressure-gradient theory. Likewise, the data for $\alpha > 0$ blend quite smoothly with those for $\alpha = 0$, although at lower α, where interaction effects are present, a rigorous correlation on this basis is not

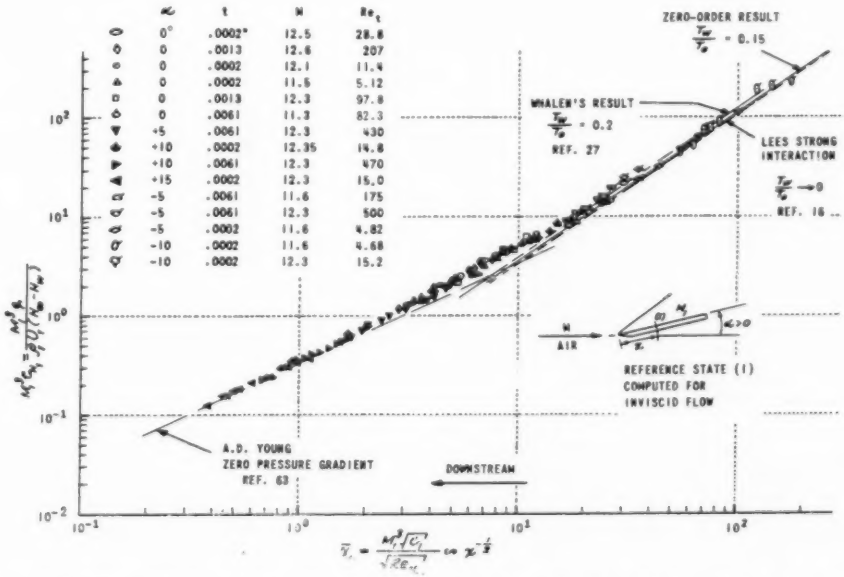

FIG. 4.7. Correlation of experimental heat transfer for small Re_t using local inviscid reference state (1). $T_0 \sim 2{,}000$°K.

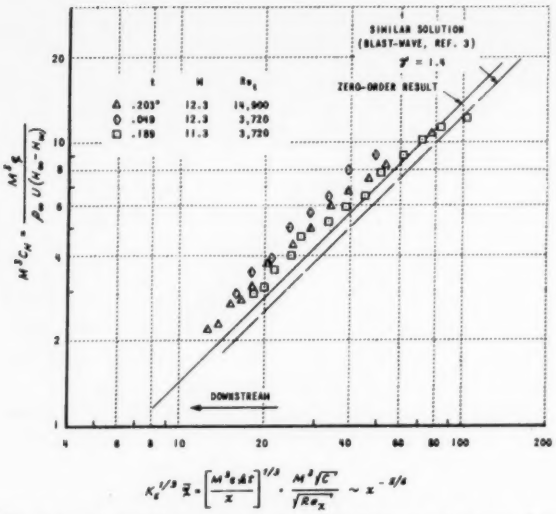

FIG. 4.8. Correlation of experimental heat transfer for large Re_t ($\alpha = 0°$, $T_0 \sim 2{,}000°K$).

to be expected. The good agreement of the experimental data with the classical, zero-pressure-gradient result for the smallest values of $\bar{\chi}_1$ affords a good check on the experimental technique.

Also shown in Fig. 4.7, by the flagged symbols, are data for negative angles of attack (expansion flow) reduced in the same manner—i.e., the reference state (1) is that behind the leading-edge Prandtl-Meyer expansion fan for inviscid flow over the plate. There appears to be no reason to expect $\bar{\chi}_1$ to correlate the data in this case, and the degree of correlation obtained is somewhat surprising.

Large Re_t, $\alpha = 0$

At the other limiting extreme of very large Re_t for $\alpha = 0$, the general similitude (Section 2.3) indicates that $M^3C_H/\bar{\chi}$ should depend only on K_ϵ (for given values of γ, Pr, H_w/H_∞) regardless of whether the shock is strong or not. In this case, $\bar{\chi}$ serves only as a scaling factor. For the strong shock wave and γ close to one, the zero-order result in this limit gives M^3C_H proportional to $K_\epsilon^{1/3}\bar{\chi}$ (Section 2.2).

Fig. 4.8 shows typical experimental data for 2,000°K stagnation temperature plotted in the form M^3C_H versus $K_\epsilon^{1/3}\bar{\chi}$. Results are given for the highest value of Re_t obtained, namely 15,000, as well as for the value 3,700 obtained at two different values of t differing by a factor of about 4. Also shown are the present zero-order result, and a self-similar solution employing the plane blast-wave pressure distribution[3] with $\gamma = 1.4$ and $Pr = 1$.

The correlation obtained in Fig. 4.8 is considered fairly good. The trend of the results for the higher density level, i.e., for the higher value of Re_x per inch, is to shift to the right with increasing Re_t, as expected. At a lower density level but the same value of $Re_t = 3{,}700$, however, the value of M^3C_H is reduced. A contributing factor here is that the strong shock condition is met best in the case of large leading-edge thickness.

Regarding comparison with the theory, the experimental values of M^3C_H for the highest values of Re_t are some 20 to 25 percent higher than the zero-order result, except in the leading edge vicinity where experiment and theory cross. Here the flow deflections become unduly large, and the heat transfer is presumably reduced by the associated shock-wave heating effect. Away from the leading-edge region the slope of the data points is quite close to the theoretical slope. At $Re_t = 15{,}000$, the shock slope is everywhere larger than the arbitrary limit of 0.30 previously discussed in connection with the schlieren results of Fig. 4.5. However, the resulting shock-wave heating from this effect would tend to reduce the heat transfer rather than increase it. The strong-shock-wave requirement of the theory is met reasonably well for $t = 0.203$ in. The error incurred in the zero-order theory from requiring γ close to one is such as to predict a heat-transfer level which is too high, as discussed in Section 2.2 and illustrated by the similar solution for the plane blast-wave pressure distribution, $\gamma = 1.4$, and $Pr = 1$, shown in Fig. 4.8. For the values of K_ϵ appropriate to the $Re_t = 15{,}000$ case, the plane blast-wave pressure distribution has been shown to be in very good agreement with that calculated exactly for inviscid flow from the method of

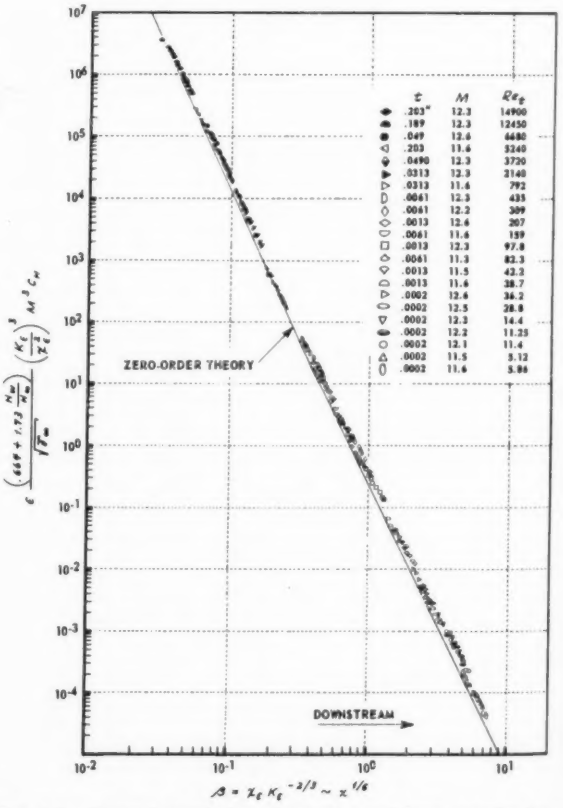

FIG. 4.9. General correlation of experimental heat transfer for arbitrary β ($\alpha = 0°$, $T_0 \sim 2{,}000°K$).

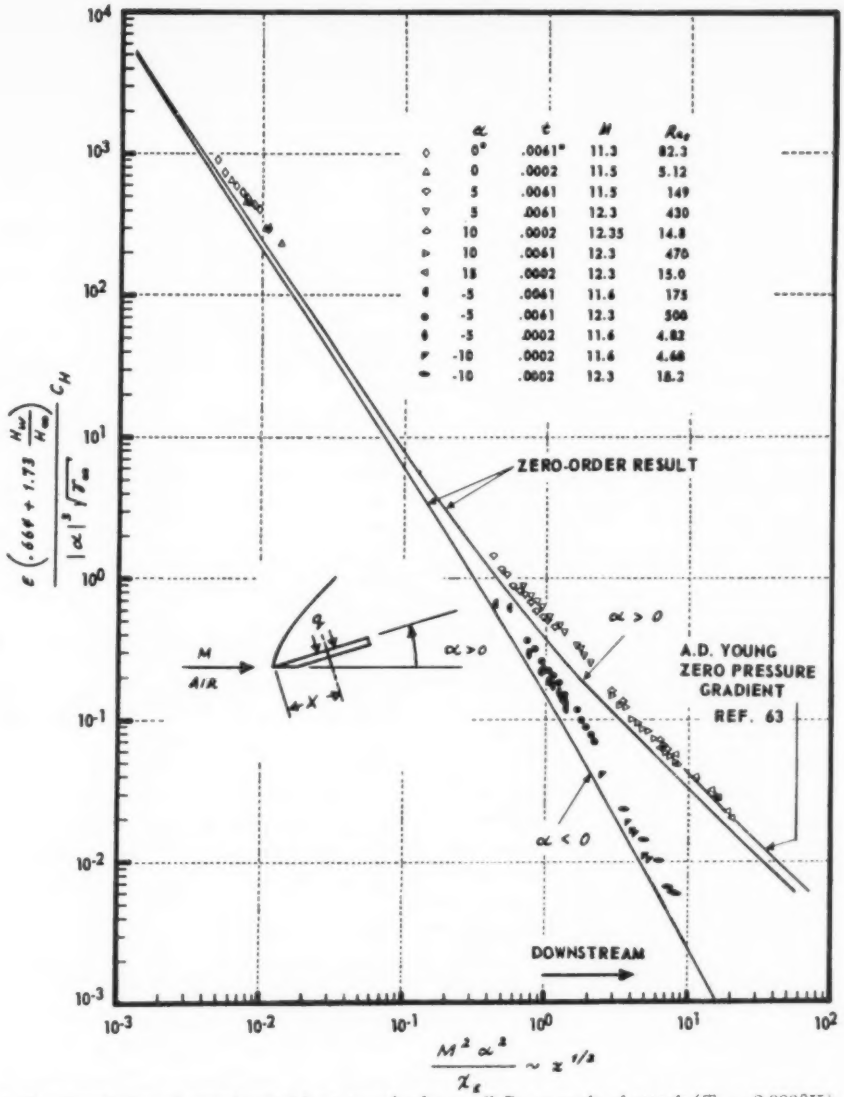

FIG. 4.10. Correlation of experimental heat transfer for small Re_t at angle of attack ($T_0 \sim 2{,}000°K$).

characteristics.[6,43] The discrepancy between theory and the correlated experimental data may be attributed in part to the assumption of $Pr = 1$ in the theories.

General Correlation for Arbitrary $\beta = \chi_\epsilon K_\epsilon^{-2/3}$, $\alpha = 0$

Provided that the strong shock-wave condition is satisfied, the simplified hypersonic similitude shows that for $\alpha = 0$, the quantity

$$\epsilon[0.664 + 1.73(H_w/H_\infty)]\gamma_\infty^{-1/2}(K_\epsilon/\chi_\epsilon^2)^3 M^3 C_H$$

should be correlated in terms of the variable $\beta = \chi_\epsilon K_\epsilon^{-2/3}$ (for given values of γ, Pr, H_w/H_0) when both bluntness and viscous-interaction effects are important. A general presentation of the experimental heat-transfer data for zero angle of attack and $T_0 \sim 2{,}000°K$ is given in this form in Fig. 4.9. The zero-order result applicable for a strong shock wave and γ close to one is also shown.

In general, the overall correlation obtained in Fig. 4.9 is considered to be reasonably good. The data appear to correlate somewhat better at the lower values of β (large bluntness effect) than at the higher values (large viscous interaction effect). As previously discussed, at the higher values of β the strong shock-wave condition is not well satisfied in the experiments. With weak shock-wave conditions, an additional dependence of the ordinate of Fig. 4.9 on $K_\epsilon \chi_\epsilon^{-2}$ is to be expected. This additional dependence on $K_\epsilon \chi_\epsilon^{-2}$ is observed in the data of Fig. 4.9 and generally accounts for the data separation at intermediate and large values of β.

As regards agreement with the zero-order theory, the experimental heat transfer is generally higher than predicted. At intermediate and large values of β this difference may be accounted for by failure of the experiments to meet the strong-shock condition, by the fact that the theory is subject to an error of order ϵ, and by

the fact that $Pr \simeq 0.71$ for the experiments. For the data points of any one experiment at intermediate and large values of β, it is seen that the best agreement with the theory is obtained closest to the leading edge where the strong-shock condition is best satisfied. The agreement here is typically in the range 10 to 15 percent. At low values of β, the experimental heat transfer is typically some 20 percent to 25 percent higher than the theory, as discussed in the previous section for large Re_t. For the largest values of t in this range of β, the experimental heat-transfer points cross the theoretical curve in the vicinity of the leading edge. As previously discussed, this behavior probably results because of the large flow-deflection angles at a fixed station x in the leading-edge region when t becomes large.

Small Re_t at Angle of Attack

For sufficiently small values of Re_t and a strong shock wave, the present viscous similitude predicts that the quantity

$$\epsilon \frac{[0.664 + 1.73(H_w/H_\infty)]C_H}{|\alpha|^3\sqrt{\gamma}}$$

should be correlated in terms of $M^2\alpha^2\chi_\epsilon^{-1}$ for small angles of attack α. Fig. 4.10 shows a plot of the experimental data for small Re_t, $T_0 \sim 2{,}000°$K, in this form along with the theoretical zero-order result for γ close to one. The angle-of-attack range includes data for $\alpha = +5, +10, +15, -5$, and $-10°$. In addition, data obtained at nominal zero angle of attack have been plotted for an arbitrary, small value of α of 0.01 radians.

The correlation obtained in Fig. 4.10 is fairly good. For a positive α of 5° there is a suggestion of bluntness effect at the higher value of Re_t. This is understandable in terms of the parameter $\Gamma = K_\epsilon M\alpha/2\chi_\epsilon^2 \sim Re_t\alpha/M^2$ (Section 2.2) which controls the viscous similitude for a blunted plate at incidence. The correlation of the negative angle-of-attack data is better than anticipated in view of the fact that the strong-shock condition is rather poorly met for expansion flow over the plate.

The experimental heat transfer in Fig. 4.10 is generally higher than predicted by the zero-order theory. The agreement with the theory is generally best for positions close to the plate leading edge where the strong-shock condition is best satisfied. It will be noted that at $\alpha = 15°$ the experimental data agree quite well, as expected, with the zero-pressure-gradient result of A. D. Young calculated for $Pr = 0.72$. Young's value is about 20 per cent higher than the limiting, zero-order result of Section 2.2 for large $M^2\alpha^2\chi_\epsilon^{-1}$.

Large Re_t at Angle of Attack

The data plot analogous to Fig. 4.10 for large Re_t and dominant bluntness effect at angle of attack is shown in Fig. 4.11 along with the zero-order prediction. The similitude indicates that the quantity $(M^2/\tilde{\chi}_t)\times\sqrt{\epsilon k/\gamma_\infty}|\alpha|^5\ C_H$ should be correlated in terms of $M^2\alpha^2K_\epsilon^{-2/3}$ in this case. The boundary-layer displacement parameter $\tilde{\chi}_t = M^3\sqrt{C}/\sqrt{Re_t}$ appears as a scaling factor in the ordinate.

A correlation in Fig. 4.11 requires small flow deflections as well as the strong-shock condition and large Re_t. The correlation obtained and the agreement with the zero-order theory are fairly good, particularly for $\alpha < 0$, in view of the experimental limitations. As in the case of small Re_t, the experimental heat transfer is greater than predicted. The marked falloff in heat transfer, relative to the theory, close to the plate leading edge for negative angle of attack is undoubtedly due to the large flow deflections in this region and local failure of the small perturbation assumption. This effect is evident at $\alpha = 0$, as illustrated in Fig. 4.9 for the smallest values of β. The falloff is increased for $\alpha < 0$ and decreased for $\alpha > 0$. This behavior results from change in the effective bluntness of the square leading edge due to change in the stagnation-region flow pattern with angle of attack. The effective bluntness decreases for $\alpha > 0$ and increases for $\alpha < 0$ because of shift of the flow stagnation line on the body.

(5) CONCLUDING REMARKS

A theoretical and experimental study has been carried out on combined leading-edge bluntness and boundary-layer displacement effects in hypersonic flow over thin bodies.

A theoretical approach has been developed based on a continuum flow model consisting of three adjoining regions: an inner laminar boundary layer, an outer (detached) shock layer, and between these two, an entropy layer. Solutions for this flow model have been obtained by considering the mutual interaction of these three regions under the requirements (*a*) to (*c*) stated in Section 2. In the boundary layer, a small perturbation procedure in $\epsilon = (\gamma - 1)/(\gamma + 1)$ is developed which yields the local flat-plate similarity as a leading approximation. In the entropy layer, the low density leads to the simple pressure-area relation Eq. (2.11). In the detached shock layer, the results of existing shock-layer theory are applicable. The zero-order theory in this approach corresponds to the classical result of Busemann.

The zero-order theory corresponding to the leading approximation under requirements (*b*) and (*c*) has been developed in detail; its simplicity permits solutions to numerous specific problems of interest. In general, the solutions reveal the combined effects of bluntness, viscous interaction, and angle of attack in hypersonic flows over thin bodies. Continuous transitions are exhibited between limiting solutions which agree with existing blast-wave, strong-viscous-interaction, and hypersonic-wedge theories. One interesting feature found for inviscid flow over a blunted wedge is an oscillatory pressure decay over the afterbody surface. This result may be interpreted as one limiting form of shock-layer reimpingement at glancing incidence.

Hypersonic similitude has been examined in Section

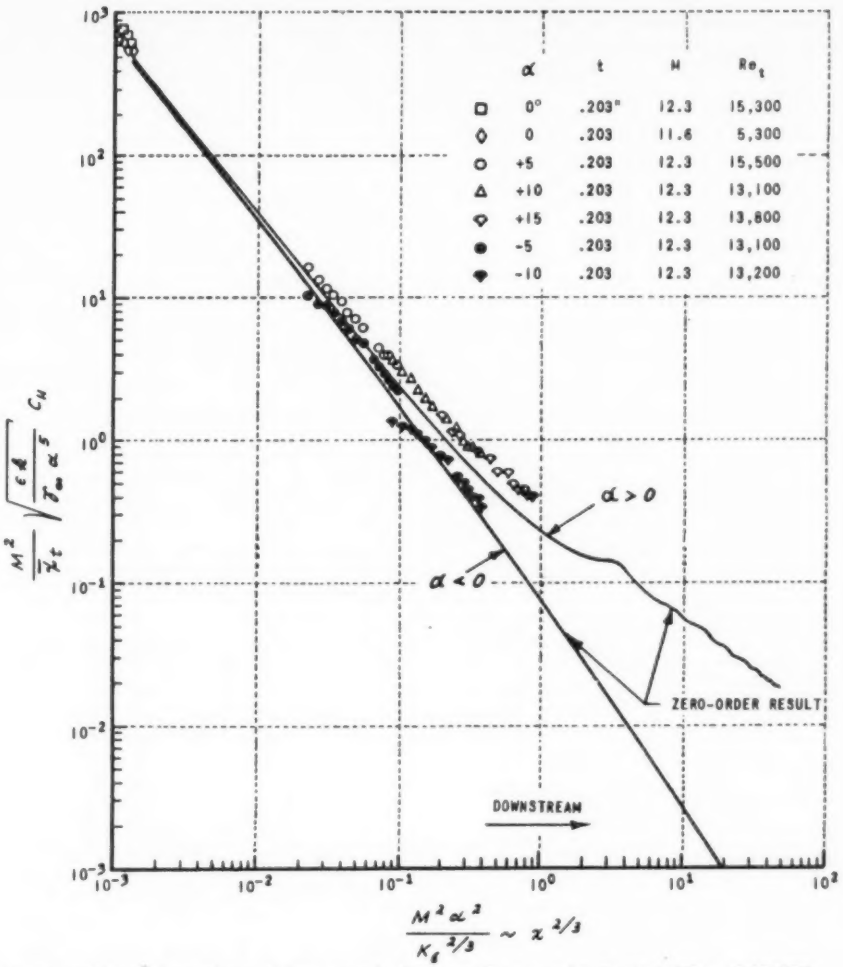

FIG. 4.11. Correlation of experimental heat transfer for large Re_t at angle of attack ($T_0 \sim 2{,}000°K$).

2.3 for the present problem where both bluntness and boundary-layer displacement effects are present. The classical similitude of Tsien and Hayes can be extended to include these effects for correlation of pressure and velocity fields, as well as flow quantities of interest within the boundary layer, provided the vicinity of the blunt leading edge or nose is excluded. For flows involving strong shock waves, a simplified similitude is obtained. The zero-order results, which require a strong shock and also small ϵ, may be readily compared with experimental data correlated in this similitude.

The theoretical results of the present paper pertain chiefly to the case of plane flows. Certain aspects of the treatment can readily be applied to flows with rotational symmetry, for example, flows about a blunted cone, and to three-dimensional boundary-layer flows over wing systems. Results from these applications of the theory are discussed in reference 65.

On the experimental side, studies have been made of hypersonic airflows at Mach numbers around 12 over sharp and blunt leading-edge flat plates for conditions of large boundary-layer cooling. These studies were made in the C.A.L. 11 × 15-in. hypersonic shock tunnel mainly at stagnation temperatures close to 2,000°K, giving wall-to-stagnation temperature ratios of the order of 0.15. Shock-wave shapes were obtained by schlieren photography, and surface heat-transfer distributions were measured by thin-film resistance thermometry. At zero angle of attack, the leading-edge thickness and stream Reynolds number were varied over a sufficient range to encompass the limiting cases of dominant bluntness and dominant viscous-interaction effects. Leading-edge Reynolds numbers varied from about 3 to 1.5×10^4 for stream Reynolds numbers varying from about 1.4×10^4 to 1.8×10^5 per inch. Angle-of-attack effects from +15 to −10° were studied at low and high leading-edge Reynolds numbers. Heat-transfer measurements were also made on a sharp plate at zero angle of attack for air stagnation temperatures up to 4,000°K.

The experimental data have been reduced and plotted in forms indicated by the general hypersonic similitude of Section 2.3 for viscous flow with leading-edge bluntness effects. In addition, comparisons have been made within this framework with the predictions of the zero-order theory given in Section 2.2.

The results of the schlieren studies of shock-wave shapes permit an assessment of the degree to which the experimental flows met the assumptions of the theory as expressed in terms of the local shock-wave angle. In particular, the similitude used for arbitrary bluntness and viscous interaction, and the zero-order theory, both require the condition of a strong shock wave in addition to small flow-deflection angles. For given stream Mach number, these conditions place upper and lower bounds on the local shock angle.

Generally speaking, when due allowance is made for local failure of the strong-shock or small-flow-deflection-angle conditions in the experiments for $\alpha = 0$, the schlieren and heat-transfer data for $T_0 \sim 2{,}000°\text{K}$ are found to be correlated reasonably well by the similitude forms of Section 2.3 over a very wide range of varying bluntness and viscous-interaction effects. For the present experimental conditions, at least, the correlation obtained suggests that the hypersonic viscous similitude is valid even with leading-edge bluntness. The general heat-transfer correlation in the bluntness-dominated region appears somewhat better than that in the displacement-dominated region, probably because the former meets the strong-shock condition best. The correlation of heat transfer for angle of attack is found to be quite good. Good correlation is also obtained for heat transfer on a sharp plate at stagnation temperatures from 2,000 to 4,000°K.

As regards agreement of the theoretical predictions of Section 2.2 with experiment, the zero-order theory for $\alpha = 0$ predicts heat-transfer rates generally lower than those measured. However, the discrepancies appear to be largely accounted for by the limitations of the experiments in meeting the condition of a strong shock wave, by the fact that the theory is subject to an error of order ϵ, and by the fact that $Pr \simeq 0.71$ for the experiments. Where the strong-shock condition is best satisfied, close to the leading edge, the zero-order result for heat transfer is typically some 10 to 15 percent low.

For the angle-of-attack results at small and large Re_t, the theoretical, zero-order heat transfer is typically some 15 or 20 percent below that measured. At large compressive inclination giving high-density flow over the plate, the measured heat transfer checks well, as expected, with the classical prediction for zero-pressure gradient. The latter value, calculated for $\gamma = 1.4$, $Pr = 0.72$, and other conditions pertinent to the experiments, lies some 20 percent above the corresponding zero-order result.

Finally, it should be stressed that the present experimental studies have been made at essentially one Mach number only. In view of the parametric importance of Mach number, further experiments at substantially higher Mach numbers in air are desirable. It is anticipated that further development of the hypersonic shock tunnel will provide the high enthalpies necessary to carry such studies into the Mach number range of 15 to 25 in air. In this range it can be expected that the bluntness-displacement problem will eventually be influenced to a significant degree by complex real-gas phenomena.

References

[1] Lin, S. C., *Cylindrical Shock Wave Produced by Instantaneous Energy Release*, J. Appl. Phys., Vol. 25, No. 1, p. 54, January, 1954.

[2] Lees, L., and Kubota, T., *Inviscid Hypersonic Flow Over Blunt-Nosed Slender Bodies*, Journal of the Aeronautical Sciences, Vol. 24, No. 3, p. 195, March, 1957.

[3] Cheng, H. K., and Pallone, A. J., *Inviscid Leading-Edge Effect in Hypersonic Flow*, Readers' Forum, Journal of the Aeronautical Sciences, Vol. 23, No. 7, p. 700, July, 1956.

[4] Chernyi, G. G., *Hypersonic Flow Past an Airfoil with a Slightly Blunted Leading Edge*, Doklady, Akad. Nauk. USSR, Vol. 114, No. 4, p. 721, 1957; English translation available as C-112, Morris D. Friedman, Inc.

[5] Chernyi, G. G., *Hypersonic Flow Around a Slender Blunt Cone*, Doklady Akad. Nauk. USSR, Vol. 115, No. 4, p. 681, 1957; English translation available as C-113, Morris D. Friedman, Inc.

[6] Bertram, M. H., and Baradell, D. L., *A Note on the Sonic-Wedge Leading-Edge Approximation in Hypersonic Flow*, Readers' Forum, Journal of the Aeronautical Sciences, Vol. 24, No. 8, p. 627, August, 1957.

[7] Guiraud, J. P., *Écoulement Hypersonique d'un Fluide Parfait sur une Plaque Plane Comportant un Bord d'Attaque d'Epaisseur Finie*, Compt. Rend. Acad. Sci., Paris, Vol. 246, p. 2842, 1958.

[8] Mirel, H., and Thornton, P. R., *Effect of Body Perturbations on Hypersonic Flow Over Slender, Power-Law Bodies*, NASA TR R-45, May, 1959.

[9] Hayes, W. D., and Probstein, R. F., *Hypersonic Flow Theory*, Academic Press, New York, 1959.

[10] Moore, F. K., and Cheng, H. K., *The Hypersonic Aerodynamics of Slender and Lifting Configurations*, Presented at the IAS National Meeting at Los Angeles, Calif., Summer, 1959.

[11] Shen, S. F., *An Estimate of Viscosity Effect on Hypersonic Flow Over an Insulated Wedge*, J. Math. & Phys., Vol. 31, p. 192, 1952.

[12] Bertram, M. H., *An Approximate Method for Determining the Displacement Effects and Viscous Drag of Laminar Boundary Layers in Two-Dimensional Hypersonic Flow*, NACA TN 2773, September, 1952.

[13] Lees, L., and Probstein, R. F., *Hypersonic Viscous Flow Over Flat Plate*, Princeton Aeronautical Engineering Lab. Rept. No. 195, 1952.

[14] Shen, S. F., *On the Boundary-Layer Equations in Hypersonic Flow*, Readers' Forum, Journal of the Aeronautical Sciences, Vol. 19, No. 7, p. 500, July, 1952.

[15] Li, T. Y., and Nagamatsu, H., *Shock-Wave Effects on the Laminar Skin Friction of an Insulated Flat Plate at Hypersonic Speed*, Journal of the Aeronautical Sciences, Vol. 20, p. 345, 1953.

[16] Lees, L., *On the Boundary-Layer Equations in Hypersonic Flow and Their Approximate Solutions*, Journal of the Aeronautical Sciences, Vol. 20, p. 143, 1953.

[17] Pai, S. I., *A Note on Hypersonic Flow Over a Flat Plate*, Readers' Forum, Journal of the Aeronautical Sciences, Vol. 20, No. 7, p. 502, July, 1953.

[18] Lees, L., *Hypersonic Viscous Flow Over an Inclined Wedge*, Journal of the Aeronautical Sciences, Vol. 20, No. 11, p. 794, November, 1953.

[19] Stewartson, K., *On the Motion of a Flat Plate at High Speed in a Viscous Compressible Fluid—Pt. II, Steady Motion*, Journal of the Aeronautical Sciences, Vol. 22, No. 5, p. 303, May, 1955.

[20] Pai, S. I., and Shen, S. F., *Hypersonic Viscous Flow Over an Inclined Wedge With Heat Transfer*, 50 Jahre Grenzschichtforschung, ed. by H. Görtler and W. Tollmien, p. 112, F. Vieweg, Braunschweig, 1955.

[21] Kuo, Y. H., *Viscous Flow Along a Flat Plate Moving at High*

Supersonic Speeds, Journal of the Aeronautical Sciences, Vol. 23, No. 2, p. 125, February, 1956.

[22] Pan, L. J., and Kuo, Y. H., *Compressible Viscous Flow Past a Wedge Moving at Hypersonic Speeds*, J. Math. & Phys., Vol. 35, p. 179, 1956.

[23] Lees, L., *Influence of the Leading-Edge Shock Wave on the Laminar Boundary Layer at Hypersonic Speeds*, Journal of the Aeronautical Sciences, Vol. 23, No. 6, p. 594, 1956.

[24] Yasuhara, M., *On the Hypersonic Viscous Flow Past Slender Bodies of Revolution*, J. Phys. Soc. (Japan), Vol. 11, No. 8, p. 878, August, 1956.

[25] Lees, L., *Recent Developments in Hypersonic Flow*, Jet Propulsion, Vol. 27, No. 11, p. 1162, November, 1957.

[26] Oguchi, H., *First-Order Approach to a Strong Interaction Problem in Hypersonic Flow Over an Insulated Flat Plate*, University of Tokyo Aeronautical Research Institute Report No. 330, June, 1958.

[27] Whalen, R. J., *Boundary-Layer Interaction on a Yawed Infinite Wing in Hypersonic Flow*, Readers' Forum, Journal of the Aero/Space Sciences, Vol. 26, No. 12, p. 839, December, 1959.

[28] Busemann, A., *Flüssigleit und Gasbewegung, in Handworterbuch der Naturwissenschaften Auflage*, p. 275; Gustave Fischer, Jena, 1933.

[29] Ivey, H. R., Klunker, E. G., and Bowen, E. N., *A Method for Determining the Aerodynamic Characteristics of Two- and Three-Dimensional Shapes at Hypersonic Speeds*, NACA TN 1613, 1948.

[30] Freeman, N. C., *On the Theory of Hypersonic Flow Past Plane and Axially Symmetric Bluff Bodies*, J. Fluid Mech., Vol. 1, p. 366, October, 1956.

[31] Chester, W., *Supersonic Flow Past a Bluff Body with a Detached Shock: Part I, Two-Dimensional Body*, J. Fluid Mech., Vol. 1, p. 353, October, 1956; *Part II, Axisymmetrical Body*, J. Fluid Mech., Vol. 1, p. 490, November, 1956.

[32] Lighthill, M. J., *Dynamics of a Dissociating Gas—Part I, Equilibrium Flow*, J. Fluid Mech., Vol. 2, January, 1957.

[33] Cole, J. D., *Newtonian Flow Theory for Slender Bodies*, Journal of the Aeronautical Sciences, Vol. 24, June, 1957.

[34] Tsien, H. S., *Similarity Law of Hypersonic Flow*, J. Math. & Phys., Vol. 25, p. 247, 1946.

[35] Hayes, W. D., *On Hypersonic Similitude*, Quart. Appl. Math., Vol. 5, p. 105, 1947.

[36] Van Dyke, M. D., *Application of Hypersonic Small-Disturbance Theory*, Journal of the Aeronautical Sciences, Vol. 21, No. 3, p. 179, March, 1954; also see NACA TR 1194 and NACA TN 3173 by the same author.

[37] Lees, L., *Laminar Heat Transfer Over Blunt-Nosed Bodies at Hypersonic Flight Speeds*, Jet Propulsion, Vol. 26, No. 4, p. 259, April, 1956.

[38] Kemp, N. H., Rose, P. H., and Detra, R. W., *Laminar Heat Transfer Around Blunt Bodies in Dissociated Air*, Journal of the Aero/Space Sciences, Vol. 26, No. 7, p. 421, July, 1959.

[39] Vaglio-Laurin, R., *Turbulent Heat Transfer on Blunt-Nosed Bodies in Two-Dimensional and General Three-Dimensional Hypersonic Flow*, Journal of the Aero/Space Sciences, Vol. 27, No. 1, p. 27, January, 1960.

[40] Chapman, D. R., and Rubesin, M. W., *Temperature and Velocity Profile in Compressible Laminar Boundary Layer With Arbitrary Distribution of Surface Temperatures*, Journal of the Aeronautical Sciences, Vol. 16, p. 547, 1949.

[41] Taylor, G. I., *The Formation of a Blast Wave by a Very Intense Explosion—Pt. I, Theoretical Discussion*, Proc. Roy. Soc. (A), Vol. 201, No. 1065, p. 159, March, 1950.

[42] Sakurai, A., *On the Propagation and Structure of the Blast Wave—Part I*, J. Phys. Soc. (Japan), Vol. 9, No. 2, p. 256, March-April 1954.

[43] Cheng, H. K., *Similitude of Hypersonic Real-Gas Flows Over Slender Bodies With Blunted Noses*, Journal of the Aero/Space Sciences, Vol., 26, No. 9, p. 575, September, 1959.

[44] Hayes, W. D., and Probstein, R. F., *Viscous Hypersonic Similitude*, Journal of the Aero/Space Sciences, Vol. 26, No. 12, p. 815, December, 1959.

[45] Bertram, M. H., *Viscous and Leading-Edge Thickness Effects on the Pressures on the Surface of a Flat Plate in Hypersonic Flow*, Readers' Forum, Journal of the Aeronautical Sciences, Vol. 21, No. 6, p. 430, June, 1954.

[46] Bogdonoff, S. M., and Hammitt, A. G., *The Princeton Helium Hypersonic Tunnel and Preliminary Results above M = 11*, Princeton Aeronautical Engineering Report No. 260, June, 1954; also WADC TN 54-124.

[47] Hammitt, A. G., Vas, I. E., and Bogdonoff, S. M., *Leading-Edge Effects on the Flow Over a Flat Plate at Hypersonic Speeds*, Princeton Aeronautical Engineering Report No. 326, 1955.

[48] Bogdonoff, S. M., and Hammitt, A. G., *Fluid Dynamic Effects at Speeds from M = 11 to 15*, Journal of the Aeronautical Sciences, Vol. 23, No. 2, p. 108, February, 1956.

[49] Hammitt, A. G., and Bogdonoff, S. M., *Leading-Edge Effect on the Flow Over a Flat Plate*, Jet Propulsion, Vol. 26, No. 4, p. 241, May, 1956.

[50] Bertram, M. H., *Tip-Bluntness Effects on Cone Pressure at M = 6.85*, Journal of the Aeronautical Sciences, Readers' Forum Vol. 23, No. 9, p. 898, September, 1956.

[51] Kendall, J. M., Jr., *Experimental Investigation of Leading-Edge Shock Wave–Boundary Layer Interaction at Mach 5.8*, Journal of the Aeronautical Sciences, Vol. 24, No. 1, p. 47, January, 1957.

[52] Vas, I. E., *An Experimental Investigation of the Pressure on a Thin Flat Plate at Hypersonic Speeds*, Princeton Aeronautical Engineering Report No. 377, March, 1957.

[53] Creager, M. O., *Effects of Leading-Edge Blunting on the Local Heat Transfer and Pressure Distributions Over Flat Plates in Supersonic Flow*, NACA TN 4142, December, 1957.

[54] Bertram, M. H., *Boundary-Layer Displacement Effects in Air at Mach Numbers of 6.8 and 9.6*, NACA TN 4133, February, 1958.

[55] Bertram, M. H., and Henderson, A., Jr., *Effects of Boundary-Layer Displacement and Leading-Edge Bluntness on Pressure Distribution, Skin Friction, and Heat Transfer of Bodies at Hypersonic Speeds*, NACA TN 4301, July, 1958.

[56] Creager, M. O., *The Effect of Leading-Edge Sweep and Surface Inclination on the Hypersonic Flow Field Over a Blunt Flat Plate*, NASA Memo 12-26-58 A, January, 1959.

[57] Bertram, M. H., and Feller, W. V., *A Simple Method for Determining Heat Transfer, Skin Friction, and Boundary-Layer Thickness for Hypersonic Laminar Boundary-Layer Flows in a Pressure Gradient*, NASA Memo 5-24-59L, June, 1959.

[58] Henderson, A., Jr., and Johnston, P. J., *Fluid Dynamic Properties of Some Simple Sharp- and Blunt-Nosed Shapes at Mach Numbers from 16 to 24 in Helium Flow*, NASA Memo 5-8-59L, June, 1959.

[59] Wittliff, C. E., Wilson, M. R., and Hertzberg, A., *The Tailored-Interface Hypersonic Shock Tunnel*, Journal of the Aero./Space Sciences, Vol. 26, No. 4, April, 1959.

[60] Wittliff, C. E., and Rudinger, G., *Summary of Instrumentation Development and Aerodynamic Research in a Hypersonic Shock Tunnel*, Cornell Aeronautical Laboratory Report No. AD-917-A-2, WADC TR 58-401 Part I, August, 1958.

[61] Wittliff, C. E., and Wilson, M. R., *Summary of Instrumentation Development and Aerodynamic Research in a Hypersonic Shock Tunnel*, Cornell Aeronautical Laboratory Report No. AD-917-A-3, WADC TR 58-401 Part II, December, 1958.

[62] Vidal, R. J., *Model Instrumentation Techniques for Heat Transfer and Force Measurements in a Hypersonic Shock Tunnel*, Cornell Aeronautical Laboratory Report No. AD-917-A-1, WADC TN 56-315, AD 97238, February, 1956.

[63] Howarth, L., *Modern Developments in Fluid Dynamics*—Vol. 1, High Speed Flow, p. 422; Oxford University Press, London, 1953.

[64] Montroll, E. W., and Shuler, K. E., *Studies in Nonequilibrium Rate Processes: I. The Relaxation of a System of Harmonic Oscillators*, J. Chem. Phys., Vol. 26, No. 3, pp. 454–464, March, 1957.

[65] Cheng, H. K., *Hypersonic Flow With Leading-Edge Bluntness and Boundary-Layer Displacement Effects*, ONR-Sponsored

(*Continued on page 410*)

Transient and Periodic Response of a Loaded Sandwich Panel†

CHIEH C. CHANG* AND BERTRAND T. FANG**
University of Minnesota

Summary

The flexural motion of a rectangular sandwich panel with an orthotropic viscoelastic core is investigated. Differential equations and boundary conditions are derived by taking into account the rotational inertia of the whole panel, and the shearing deformation and viscoelastic damping of the core. The dynamic response of a simply supported rectangular panel to a unit step function is first obtained, and then the general transient and steady-state response of the panel to an arbitrary input function is expressed in terms of the unit response by means of the convolution integral. It is shown that three families of modal shapes of vibration are possible for each nodal pattern of the panel. The frequencies and amplitudes of vibration of these three modes are discussed in detail for the case of an isotropic and elastic sandwich panel. The effects of viscoelastic core and edge compression are also discussed. Two simple physical parameters which represent the effects of shearing deformation and rotational inertia, respectively, are found very essential in the analysis. A number of limiting cases are discussed in detail.

Symbols

A, B, C = amplitudes of vibration
D_0 = $E'h'\bar{h}^2(1+f)^2/(1+K)(1-\mu^2)$, bending stiffness per unit width of sandwich panel
D_Q = $\bar{h}\bar{G}_{xz}(1+f)^2$, shear stiffness per unit width of sandwich panel
E = Young's modulus
f = $(h'+h'')/2\bar{h}$, one half of the ratio of the total facing thickness to the core thickness
g = $\bar{G}_{yz}/\bar{G}_{xz}$, elastic orthotropic index of core
$\bar{G}_{xz}, \bar{G}_{yz}$ = shear modulus of core
$h', h'', \bar{h}$ = thickness of lower facing, upper facing and core
K = $E'h'/E''h''$, stiffness ratio of lower facing to upper facing
L_x, L_y = length and width of panel
$m/2L_x$, $n/2L_y$ = wave numbers
$M_{\alpha\beta}$ = intensity of moments applied at panel edge
n_α = components of outward unit normal vector to boundary
$N_{\alpha\beta}$ = intensity of forces applied at panel edge
q = intensity of time-dependent loading perpendicular to the panel surface
r = $\pi^2 D_0/L_x^2 D_Q$, bending shear stiffness ratio of the panel
s = $\bar{\nu}_{yz}/\bar{\nu}_{xz}$, viscous orthotropic index of core
t = time
u_i(or u, v, w) = displacement in the x_i direction
U, V, W = displacement response to a unit step function
x_1(or x, y, z) = rectangular Cartesian coordinates (see Fig. 1)
α_{mn} = $(N_{xx}^* m^2 + N_{yy}^* n^2\beta^2)\{(1+f)(m^2+n^2\beta^2)^2/(1+K)(1+\eta)\}^{-1}$, ratio of the edge compression to the elastic buckling load of the panel corresponding to the wave pattern m and n
β = L_x/L_y, length-width ratio of panel
δ = variational sign
η = $r(1+f)(m^2+n^2\beta^2)$, shear deformation parameter
μ = Poisson's ratio of facing
$\rho', \rho'', \bar{\rho}$ = mass density of upper facing, lower facing and core
$\bar{\nu}_{xz}, \bar{\nu}_{yz}$ = coefficients of viscosity of the core
ρ_r = $(1+f)(\rho'h'+K^2\rho''h'') + (1/3)(1-K+K^2)\bar{\rho}\bar{h} \simeq (1+K/\bar{h})^2$ times the moment of inertia per unit area of the sandwich panel with respect to an axis parallel to the x_α axis and lying in the neutral surface of the panel
ρ_t = mass per unit area of sandwich element
τ = $\bar{\nu}_{xz}/\bar{G}_{xz}$, retardation time of viscoelastic core
ϕ = $\frac{\pi^2}{L_x^2}(m^2+n^2\beta^2)\frac{\rho_r}{\rho_t}\left(\frac{\bar{h}}{1+K}\right)^2$, rotational inertia parameter
ω = frequency
ω_0 = $(1+K)\sqrt{\bar{G}_{xz}/\bar{h}\rho_r}$, frequency of pure shear vibration of an infinite sandwich panel
ω_c = $(\pi^2/L_x^2)(m^2+n^2\beta^2)\sqrt{D_0/(1+f)\rho_t}$, classical flexural frequency (shear deformation and rotational inertia neglected)

Superscripts

$'$ denotes lower facing
$''$ denotes upper facing
$-$ denotes core
$*$ denotes dimensionless quantity in terms of the new set of units

Subscripts

i, j, k take on the values of 1, 2, and 3
$\alpha, \beta, \gamma, \delta$ take on the values of 1 and 2
$-$ denotes Laplace transform

Introduction

IN THE CLASSICAL ANALYSIS of the flexural vibrations of homogeneous elastic bars and plates, the effects of shearing deformation and rotational inertia are usually neglected. For some time, it has been recognized

Presented at the Aeroelasticity Session, IAS 28th Annual Meeting, N.Y., Jan. 25–27, 1960, under the title, "Flexural Vibrations of a Rectangular Sandwich Panel." Revised and received June 13, 1960.

† This research was supported by the United States Air Force through the Air Force Office of Scientific Research of the Air Research and Development Command, under Contract Number AF 18(603)-112. Reproduction in whole or in part is permitted for any purpose of the United States Government.

* Professor of Fluid Mechanics, Department of Aeronautical Engineering.

** Research Fellow, Department of Aeronautical Engineering.

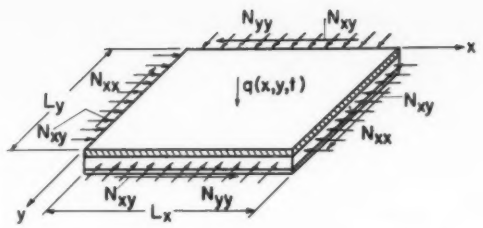

FIG. 1. Sandwich panel under loading (M_{xx}, M_{yy}, M_{xy} and supports are all omitted for clarity).

that this classical theory cannot give satisfactory results for the cases of sharp transients or for the frequencies of vibration of high-order modes. Of particular importance is Mindlin's[1] flexural theory of plates as deduced from the three-dimensional theory of elasticity.

A sandwich panel is a composite structure consisting essentially of a relatively thick, low-density, and low-stiffness core bound between two thin sheets of high-stiffness material. Because of the softness of the core, the shearing deformation in a sandwich panel under bending can be appreciable and because of the heavier concentration of mass at the outer facings which are rather far apart, the rotational inertia of a sandwich panel may well be of considerable importance. It is the purpose of this investigation to study the steady-state and transient vibrations of a sandwich panel taking these factors into account. In addition, the damping of a sandwich panel due to the bonding material between the core and the facings is simulated by assuming that the sandwich core exhibits viscous resistance to shearing deformation.

The problem of the static bending and buckling of a sandwich panel has been treated by the authors in a previous paper.[2] The sandwich construction to be considered here is similar to that of reference 2, i.e., the sandwich panel is rectangular in shape; the two facings are of different thicknesses and the core is orthotropic. The loadings acting on the panel are uniformly distributed time-independent edge forces and moments and arbitrarily distributed time-dependent transverse loads. Fig. 1 shows a sandwich panel under the specified loadings.

Assumptions

(a) The forces in the plane of the panel are taken entirely by the two thin facings of the sandwich panel. Each individual facing acts as a membrane and does not take bending.

(b) The core of the sandwich panel carries the main part of transverse shear loading. The distribution of this transverse shear is approximately constant throughout the thickness of the core. The core behaves like an orthotropic viscoelastic continuum, being characterized by its two shear moduli and two coefficients of viscosity.

(c) The deflections of the panel are small, and are constant across the panel thickness.

(d) The upper facing and the lower facing have the same Poisson's ratio.

Assumptions (a) and (b) regarding the direct stress taken by the facing and the transverse shear taken by the core are widely adopted assumptions based on the relative stiffness of the core and the facings. The assumption that the facings are membranes is equivalent to neglecting quantities of the order of the square of the ratio of facing thickness to core thickness in comparison with unity. The assumption that the transverse shear is constant throughout the thickness of the core is a direct result of assumption (a) that the core does not take forces parallel to the plane of the panel. For homogeneous plates, the transverse shear varies considerably across the thickness of the plate. Some authors[1, 3] introduced a numerical factor in the relationship between the average transverse shear stress and strain to take into consideration this nonuniform distribution of transverse shear. Yu[4] investigated the appropriate value of this numerical factor for sandwich plates from a more general theory and showed that this factor is very close to unity for most common sandwich panels. In assumption (b), the sandwich core is assumed to exhibit viscous resistance to transverse shear. This is to simulate the damping of the bonding material. The assumption of constant deflection across the panel thickness simplifies our analysis. This assumption, however, excludes a possible symmetrical mode of vibration of the panel about its neutral surface. For most structural materials the Poisson's ratios differ by a small amount. By making the last assumption, that the two facings have identical Poisson's ratio, we can show[2] that the lateral displacements in the two facings are related by the simple relationship

$$u''_\alpha = -(E'h'/E''h'')u'_\alpha = -Ku'_\alpha \qquad (1)$$

This simplifies our analysis a great deal.

Analysis

The present problem is different from the static problem of reference 2 in the following respects:

(a) The inertia of the panel, both translational and rotational, is considered.

(b) The sandwich core exhibits a viscous shear stress which is proportional to the time rate of transverse shear strain.

(c) The bending rigidity of each individual facing is neglected.

As in reference 2, the behavior of a sandwich panel can be completely characterized by the displacements u'_α of the middle plane of the lower (or upper) facing of the sandwich panel and the deflection u_3 of the panel. The deflection u_3 is assumed to be constant across the thickness of the panel. The displacement components u_α are assumed to vary with the panel thickness as shown in Fig. 2. It should be emphasized that the u_α

are displacement components associated with the bending of the panel. No coordinate is provided for the displacements due to the direct edge compression and shear. In contrast to the static problem of reference 2, the displacement components u_i are functions not only of the space coordinates but also of time.

The differential equations of motion of the panel in terms of these displacements and their space and time derivatives can be found by considering the equations of motion of a differential element of the panel.* A differential element is shown in Fig. 2 together with the forces acting on it. The law of motion applied to the differential element for the two rotational degrees of freedom in the x_1-x_3 and the x_2-x_3 planes gives the following two equations:

$$\frac{E'h'}{2(1-\mu^2)}(1+f)[2\mu u'_{\gamma,\gamma\alpha}+(1-\mu)(u'_{\alpha,\beta\beta}+u'_{\delta,\alpha\delta})]-\bar{G}_{\alpha 3}\left(\frac{1+K}{\bar{h}}u'_{\alpha}-u_{3,\alpha}\right)-\bar{\nu}_{\alpha 3}\left(\frac{1+K}{\bar{h}}u'_{\alpha,t}-u_{3,\alpha t}\right)=\frac{1}{1+K}\rho_t u'_{\alpha,tt} \quad (2)$$

(No summation on α)

Likewise, the equation of motion in the transverse direction is

$$q-N_{\alpha\beta}u_{3,\alpha\beta}-\bar{h}\bar{G}_{\alpha 3}\left(\frac{1+K}{\bar{h}}u'_{\alpha,\alpha}-u_{3,\alpha\alpha}\right)-\bar{h}\bar{\nu}_{\alpha 3}\left(\frac{1+K}{\bar{h}}u'_{\alpha,\alpha t}-u_{3,\alpha\alpha t}\right)=\rho_t u_{3,tt} \quad (3)$$

Similar to reference 2, the remaining equation of rotation is satisfied identically by the symmetry of stress tensor in the facings and the other two translational equations reduce to Eq. (1) between the lateral dis-

* These equations, together with the boundary conditions, were also obtained from the generalized Hamilton's principle. Because of lack of space the energy integrals are not shown here.

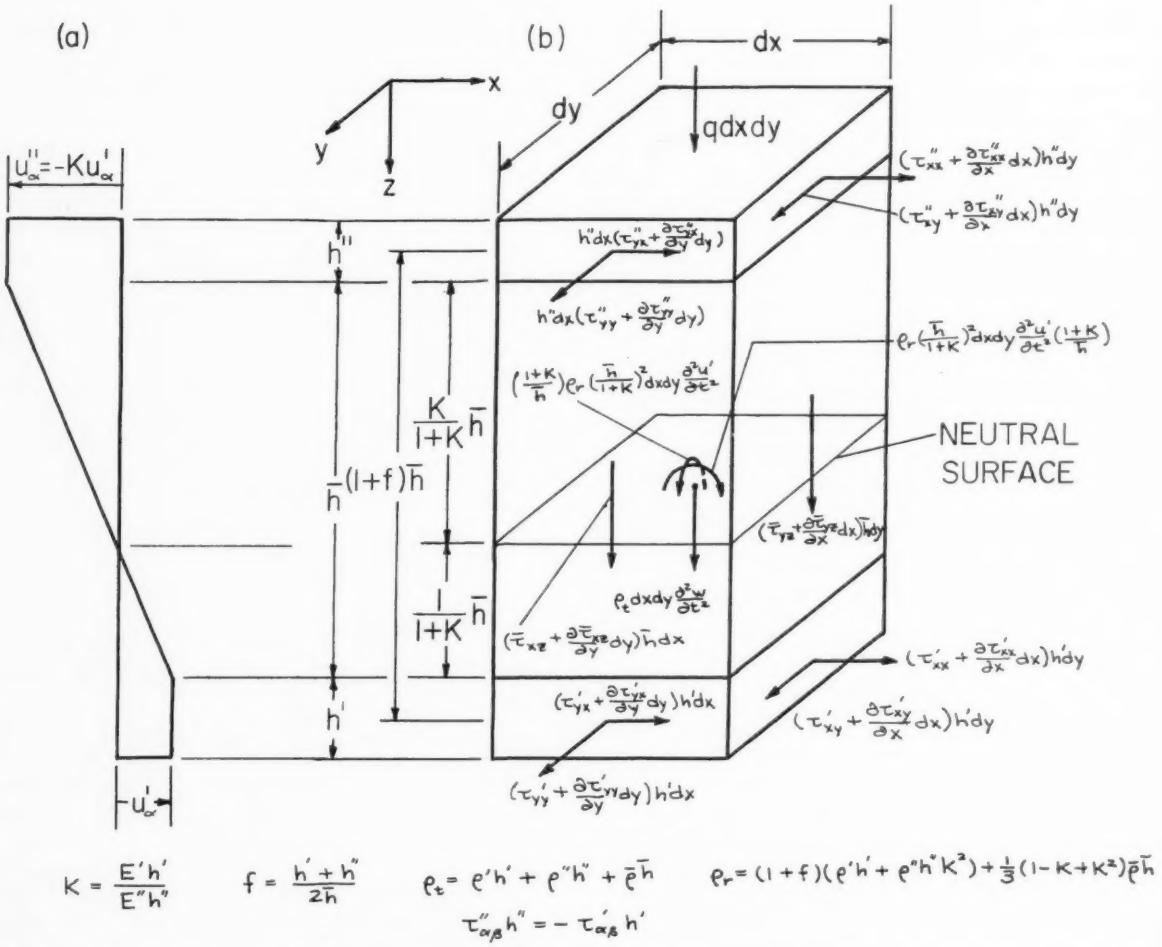

FIG. 2. (a) Variation of displacements u_α across panel thickness (assumed); (b) Inertia and internal forces acting on a sandwich element in flexural motion (forces due to stretching of panel not shown).

placement components in the two facings. In these equations repeated Greek subscripts indicate summation over the range 1 and 2. The notations used are fully described in the section on symbols and are not explained in the text. In deriving the two rotational equations of motion, Eqs. (2), the internal forces in the facings are assumed to be attached to their middle planes. The rotational inertia of the facings is computed as if the mass of the whole facing were concentrated at its middle plane. This is reflected in our writing $\rho_r = (1+f)(\rho' h' + K^2 \rho'' h'') + (1/3)(1 - K + K^2)\bar{\rho}\bar{h}$. Notice that $\rho_r[\bar{h}/(1+K)]$ is approximately equal to the moment of inertia per unit area of the sandwich panel with respect to an axis parallel to the x_α axis and lying in the neutral surface of the panel. The position of the neutral surface is determined by the factor K and is shown in Fig. 2.

The boundary conditions are

$$\{[E'h'/2(1-\mu^2)]\bar{h}(1+f)[2\mu u'_{\gamma,\gamma}\delta_{\alpha\beta} + (1-\mu)(u'_{\alpha,\beta} + u'_{\beta,\alpha})] + M_{\alpha\beta}\} n_\beta = 0 \quad (4)$$

$$\text{or } \delta u'_\alpha n_\beta = 0$$

$$\left\{N_{\alpha\beta} u_{3,\beta} - \bar{h}\bar{G}_{\alpha 3}\left(u_{3,\alpha} - \frac{1+K}{\bar{h}} u'_\alpha\right) - \bar{h}\bar{v}_{\alpha 3}\left(u_{3,\alpha t} - \frac{1+K}{\bar{h}} u'_{\alpha,t}\right)\right\} n_\alpha = 0 \quad (5)$$

$$\text{or } \delta u_3 = 0$$

These boundary conditions correspond to the three boundary conditions necessary for the complete determination of the flexural problem of a plate when shearing deformation is considered.[1, 3] As written in the subscript notation, these boundary conditions are readily applicable to panels of arbitrary shapes.

The dynamic behavior of the flexural motion of a sandwich panel is therefore completely characterized by the three displacement components $u_i(x_1, x_2, t)$ which are solutions of the differential equations (2) and (3) subjected to the boundary conditions (4) and (5).

Simply Supported Rectangular Panel

For a simply supported rectangular sandwich panel, the displacement components u_i can be assumed in the following forms:

$$u' = \sum_{m=1}^{\infty}\sum_{n=1}^{\infty} u_{mn}(t) \cos\frac{m\pi x}{L_x} \sin\frac{n\pi y}{L_y}$$

$$v' = \sum_{m=1}^{\infty}\sum_{n=1}^{\infty} v_{mn}(t) \sin\frac{m\pi x}{L_x} \cos\frac{n\pi y}{L_y}$$

$$w = \sum_{m=1}^{\infty}\sum_{n=1}^{\infty} w_{mn}(t) \sin\frac{m\pi x}{L_x} \sin\frac{n\pi y}{L_y}$$

where $m/2L_x$ and $n/2L_y$ are the wave numbers defining the nodal pattern of the panel and $u_{mn}(t)$, $v_{mn}(t)$, and $w_{mn}(t)$ are the amplitudes of vibration associated with the particular nodal pattern. These displacements satisfy the alternate set of boundary conditions suggested by Hoff[5] for simply supported rectangular sandwich panels.

If we expand the forcing function q in (3) in terms of the eigenfunctions of the region as $q(x, y, t) = \sum_{m=1}^{\infty}\sum_{n=1}^{\infty} q_{mn}(t) \sin\frac{m\pi x}{L_x} \sin\frac{n\pi y}{L_y}$ and substitute this expression together with the displacements given above into the equations of motion (2) and (3), we will obtain three coupled second-order ordinary differential equations for the amplitudes of motion $u_{mn}(t)$, $v_{mn}(t)$, and $w_{mn}(t)$. It is found that these equations can be greatly simplified and made dimensionless by the introduction of certain dimensionless parameters and a set of new characteristic units. The new set of basic units is defined as follows:

Time:	$\dfrac{L_x}{\sqrt{E'/\rho'(1-\mu^2)}}$	= the time for plane elastic wave to travel the length of the lower facing
Length:	$\pi\bar{h}$	= π times the thickness of the core
Mass:	$\rho' h'(\pi\bar{h})^2$	= the mass of a square of lower facing with side length equal to π times the thickness of the core

In terms of these new units and dimensionless parameters the three equations for the amplitudes of motion become

$$\frac{r}{\pi^2}\rho_r^* \frac{d^2 u_{mn}^*}{d_t^{*2}} + \tau^*(1+K)\frac{du_{mn}^*}{d_t^*} + (1+K)\left[r(1+f)\left(m^2 + \frac{1-\mu}{2}n^2\beta^2\right) + 1\right] u_{mn}^* + r(1+f)(1+K)\left(\frac{1+\mu}{2} mn\beta\right) v_{mn}^* - \tau^*\left(\frac{m}{L_x^*}\right)\frac{dw_{mn}^*}{d_t^*} - \left(\frac{m}{L_x^*}\right) w_{mn}^* = 0 \quad (6a)\dagger$$

$$\frac{r}{\pi^2}\rho_r^* \frac{d^2 v_{mn}^*}{d_t^{*2}} + \tau^* s(1+K)\frac{dv_{mn}^*}{d_t^*} + (1+K)\left[r(1+f)\left(n^2\beta^2 + \frac{1-\mu}{2} m^2\right) + g\right] v_{mn}^* + r(1+f)(1+K)\left(\frac{1+\mu}{2} mn\beta\right) u_{mn}^* - \tau^* s\left(\frac{n\beta}{L_x^*}\right)\frac{dw_{mn}^*}{d_t^*} - g\left(\frac{n\beta}{L_x^*}\right) w_{mn}^* = 0 \quad (6b)$$

† Starred quantities are dimensionless quantities in terms of the new set of basic units.

$$\frac{r}{\pi^2}\rho_t^*\frac{d^2w_{mn}^*}{d_t^{*2}}+\frac{\tau^*(m^2+sn^2\beta^2)}{L_x^{*2}(1+K)}\frac{dw_{mn}^*}{d_t^*}+\frac{1}{L_x^{*2}}+\left[\frac{n^2+gn^2\beta^2}{1+K}-r(N_{xx}^*m^2+N_{yy}^*n^2\beta^2)\right]w_{mn}^*-$$

$$\tau^*\left(\frac{m}{L_x^*}\right)\frac{du_{mn}^*}{d_t^*}-\left(\frac{m}{L_x^*}\right)u_{mn}^*-\tau^*s\left(\frac{n\beta}{L_x^*}\right)\frac{dv_{mn}^*}{d_t^*}-g\left(\frac{n\beta}{L_x^*}\right)v_{mn}^*=\frac{r}{\pi^2}q_{mn}^* \quad (6c)$$

Note that in these equations every symbol is dimensionless.

In order to solve these equations for the response $u_{mn}^*(t)$, $v_{mn}^*(t)$, and $w_{mn}^*(t)$ to an arbitrary $q_{mn}^*(t)$ we shall first find the response of the system to a unit step function

$$H_{mn}^*(t)=\begin{cases}0, & t<0\\ 1, & t>0\end{cases} \quad (7)$$

by the method of Laplace transformation. If we designate the response to the unit step function by the upper case alphabet $U_{mn}^*(t)$, $V_{mn}^*(t)$, and $W_{mn}^*(t)$, replace $q_{mn}^*(t)$ by $H_{mn}^*(t)$ in (7), and take the Laplace transformations of Eqs. (6) from the physical t-space to the transformed p-space, the following set of transformed equations is obtained under the condition that the initial displacements and velocities of the panel are zero:

$$\underline{U}_{mn}^*\left\{\frac{r}{\pi^2}\rho_r^*p^2+\tau^*(1+K)p+(1+K)\left[r(1+f)\left(m^2+\frac{1-\mu}{2}n^2\beta^2\right)+1\right]\right\}+$$

$$\underline{V}_{mn}^*\left\{r(1+f)(1+K)\left(\frac{1+\mu}{2}mn\beta\right)\right\}-\underline{W}_{mn}^*\left\{\frac{m}{L_x^*}(\tau^*p+1)\right\}=0 \quad (8a)^{\ddagger}$$

$$\underline{U}_{mn}^*\left\{r(1+f)(1+K)\left(\frac{1+\mu}{2}mn\beta\right)\right\}+\underline{V}_{mn}^*\left\{\frac{r}{\pi^2}\rho_r^*p^2+\tau^*s(1+K)p+\right.$$

$$\left.(1+K)\left[r(1+f)\left(n^2\beta^2+\frac{1-\mu}{2}m^2\right)+g\right]\right\}-\underline{W}_{mn}^*\left\{\frac{n\beta}{L_x^*}(\tau^*sp+g)\right\}=0 \quad (8b)$$

$$-\underline{U}_{mn}^*\left\{\frac{m}{L_x^*}(\tau^*p+1)\right\}-\underline{V}_{mn}^*\left\{\frac{n\beta}{L_x^*}(\tau^*sp+g)\right\}+\underline{W}_{mn}^*\left\{\frac{r}{\pi^2}\rho_t^*\rho^2+\frac{\tau^*(m^2+sn^2\beta^2)}{L_x^*(1+K)}p+\right.$$

$$\left.\frac{1}{L_x^{*2}}\left[\frac{m^2+gn^2\beta^2}{1+K}-r(N_{xx}^*m^2+N_{yy}^*n^2\beta^2)\right]\right\}=\frac{r}{\pi^2}\frac{1}{p} \quad (8c)$$

This set of three linear simultaneous algebraic equations in three unknowns can be solved by the well-known Cramer's rule. The solutions for $\underline{U}_{mn}^*(p)$, $\underline{V}_{mn}^*(p)$, and $\underline{W}_{mn}^*(p)$ in (8) can be expressed as fractions of polynomials in p. The singularities of them are in general simple poles and the inversion of these Laplace transforms to get $U_{mn}^*(t)$, $V_{mn}^*(t)$, and $W_{mn}^*(t)$ can be performed easily when geometrical and elastic details of the sandwich panel are given.

When $U_{mn}^*(t)$, $V_{mn}^*(t)$, and $W_{mn}^*(t)$ are known, the response of the panel in a particular nodal pattern to an arbitrary input $q_{mn}(t)$ which starts at zero at $t=0$, can be expressed by the convolution integral as

$$u_{mn}^*(t)=\int_0^t\frac{dq_{mn}^*(T)}{dT}U_{mn}^*(t-T)dT \quad (9a)$$

$$v_{mn}^*(t)=\int_0^t\frac{dq_{mn}^*(T)}{dT}V_{mn}^*(t-T)dT \quad (9b)$$

$$w_{mn}^*(t)=\int_0^t\frac{dq_{mn}^*(T)}{dT}W_{mn}^*(t-T)dT \quad (9c)$$

By summing up the contributions associated with each nodal pattern we obtain the total response of a sandwich panel to an arbitrary forcing function

$$q^*(x,y,t)=\sum_{m=1}^{\infty}\sum_{n=1}^{\infty}q_{mn}^*(t)\sin\frac{m\pi x}{L_x}\sin\frac{n\pi y}{L_y}$$

‡ A bar under a quantity denotes the Laplace transform of that quantity; e.g., $\underline{U}_{mn}=\underline{U}_{mn}(p)$ is the Laplace transform of $U_{mn}=U_{mn}(t)$.

$$\text{as } u'^* = \sum_{m=1}^{\infty}\sum_{n=1}^{\infty} \cos\frac{m\pi x}{L_x} \sin\frac{n\pi y}{L_y} \int_0^t \frac{dq_{mn}^*(T)}{dT}\, U_{mn}^*(t-T)dT \tag{10a}$$

$$v'^* = \sum_{m=1}^{\infty}\sum_{n=1}^{\infty} \sin\frac{m\pi x}{L_x} \cos\frac{n\pi y}{L_y} \int_0^t \frac{dq_{mn}^*(T)}{dT}\, V_{mn}^*(t-T)dT \tag{10b}$$

$$w^* = \sum_{m=1}^{\infty}\sum_{n=1}^{\infty} \sin\frac{m\pi x}{L_x} \sin\frac{n\pi y}{L_y} \int_0^t \frac{dq_{mn}^*(T)}{dT}\, W_{mn}^*(t-T)dT \tag{10c}$$

Sandwich Panels with Isotropic Core—A Simple Example

When the core of a sandwich panel is isotropic, the system of Eqs. (8) is simplified, and certain general properties of the solution can be obtained and interpreted in terms of the parameters of the panel without having to know the explicit numerical values of the parameters.

Using Cramer's rule, we obtain the solutions to the system of Eqs. (8) as follows:

$$\underline{U}_{mn}^*(p) = \frac{r/\pi^2}{(\rho_t/\rho_r)(1+K)^2}\frac{\Delta_1(p)}{\Delta(p)} \tag{11a}$$

$$\underline{V}_{mn}^*(p) = \frac{r/\pi^2}{(\rho_t/\rho_r)(1+K)^2}\frac{\Delta_2(p)}{\Delta(p)} \tag{11b}$$

$$\underline{W}_{mn}^*(p) = \frac{r/\pi^2}{(\rho_t/\rho_r)(1+K)^2}\frac{\Delta_3(p)}{\Delta(p)} \tag{11c}$$

$$\text{where } \Delta(p) = \psi(p)\left[\left(\frac{p}{\omega_0}\right)^4 + \left(\frac{p}{\omega_0}\right)^3 \tau\omega_0(1+\phi) + \left(\frac{p}{\omega_0}\right)^2\left(1+\eta+\phi-\frac{\eta\phi}{1+\eta}\,\alpha_{mn}\right) + \left(\frac{p}{\omega_0}\right)\tau\omega_0(\eta\phi)\left(1-\frac{1}{1+\eta}\,\alpha_{mn}\right) + \eta\phi(1-\alpha_{mn})\right] \tag{11d}$$

$$\Delta_1(p) = \psi(p)\left(\frac{m}{L_x^*}\right)\left(\frac{\tau p+1}{p}\right) \tag{11e}$$

$$\Delta_2(p) = \psi(p)\left(\frac{n\beta}{L_x^*}\right)\left(\frac{\tau p+1}{p}\right) \tag{11f}$$

$$\Delta_3(p) = \psi(p)\left(\frac{1}{p}\right)\left(\frac{1}{1+K}\right)\left[\left(\frac{p}{\omega_0}\right)^2 + \left(\frac{p}{\omega_0}\right)\tau\omega_0 + (1+\eta)\right] \tag{11g}$$

$$\psi(p) = \left[\left(\frac{p}{\omega_0}\right)^2 + \left(\frac{p}{\omega_0}\right)\tau\omega_0 + \left(1+\frac{1-\mu}{2}\,\eta\right)\right] \tag{11h}$$

$$\omega_0 \doteq (1+K)\sqrt{\frac{\bar{G}_{xz}}{h\rho_r}} \tag{11i}$$

The frequency ω_0 and the nondimensional parameters η, ϕ, and α_{mn} have very important physical interpretations. They are to be discussed in later sections.

The common factor $\psi(p)$, which could have been cancelled from the Δ's, is kept here because it represents a possible pure shear mode of vibration to be discussed later.

The singularities of $\underline{U}_{mn}^*$, $\underline{V}_{mn}^*$ and $\underline{W}_{mn}^*$ are in general simple poles at different values of p,

$$p = 0 \tag{12a}$$

$$p = p_1 = \gamma_1 + i\omega_1 \qquad p = \tilde{p}_1 = \gamma_1 - i\omega_1 \tag{12b}$$

$$p = p_2 = \gamma_2 + i\omega_2 \qquad p = \tilde{p}_2 = \gamma_2 - i\omega_2 \tag{12c}$$

where p_1, $\tilde{p}_1$, p_2, and $\tilde{p}_2$ are roots of the quartic appearing in $\Delta(p)$.

The residues at the pole $p = 0$ are

$$\underline{U}_{mn}^*: \qquad \frac{mL_x^*}{\pi^2(1+f)(m^2+n^2\beta^2)^2(1-\alpha_{mn})} \tag{13a}$$

$$\underline{V_{mn}}^*: \quad \frac{n\beta L_x^*}{\pi^2(1+f)(m^2+n^2\beta^2)^2(1-\alpha_{mn})} \tag{13b}$$

$$\underline{W_{mn}}^*: \quad \frac{L_x^{*2}(1+K)(1+\eta)}{\pi^2(1+f)(m^2+n^2\beta^2)^2(1-\alpha_{mn})} \tag{13c}$$

where

$$\alpha_{mn} = (N_{xx}^* m^2 + N_{yy}^* n^2\beta^2)\left\{\frac{(1+f)(m^2+n^2\beta^2)^2}{(1+K)(1+\eta)}\right\}^{-1}$$

is the ratio of the edge compression to the elastic buckling load of the panel corresponding to the wave pattern m,n. The residues at the other poles are

$$\underline{U_{mn}}^*: \quad \frac{r/\pi^2}{(\rho_t/\rho_r)(1+K)^2}\left(\frac{m}{L_x^*}\right)\left[\tau\omega_0\left(\frac{\underline{p}_\alpha}{\omega_0}\right)+1\right]\left\{4\left(\frac{\underline{p}_\alpha}{\omega_0}\right)^4+3\tau\omega_0(1+\phi)\left(\frac{\underline{p}_\alpha}{\omega_0}\right)^3+ 2\left(1+\eta+\phi-\frac{\eta\phi}{1+\eta}\alpha_{mn}\right)\left(\frac{\underline{p}_\alpha}{\omega_0}\right)^2+(\tau\omega_0)(\eta\phi)\left(1-\frac{\alpha_{mn}}{1+\eta}\right)\left(\frac{\underline{p}_\alpha}{\omega_0}\right)\right\}^{-1} \tag{13d}$$

$$\underline{V_{mn}}^*: \quad \frac{r/\pi^2}{(\rho_t/\rho_r)(1+K)^2}\left(\frac{n\beta}{L_x^*}\right)\left[\tau\omega_0\left(\frac{\underline{p}_\alpha}{\omega_0}\right)+1\right]\left\{4\left(\frac{\underline{p}_\alpha}{\omega_0}\right)^4+3\tau\omega_0(1+\phi)\left(\frac{\underline{p}_\alpha}{\omega_0}\right)^3+ 2\left(1+\eta+\phi-\frac{\eta\phi}{1+\eta}\alpha_{mn}\right)\left(\frac{\underline{p}_\alpha}{\omega_0}\right)^2+(\tau\omega_0)(\eta\phi)\left(1-\frac{\alpha_{mn}}{1+\eta}\right)\left(\frac{\underline{p}_\alpha}{\omega_0}\right)\right\}^{-1} \tag{13e}$$

$$\underline{W_{mn}}^*: \quad \frac{r/\pi^2}{(\rho_t/\rho_r)(1+K)^2}\left[\left(\frac{\underline{p}}{\omega_0}\right)^2+\tau\omega_0\left(\frac{\underline{p}}{\omega_0}\right)+(1+\eta)\right]\left\{4\left(\frac{\underline{p}_\alpha}{\omega_0}\right)^4+3\tau\omega_0(1+\phi)\left(\frac{\underline{p}_\alpha}{\omega_0}\right)^3+ 2\left(1+\eta+\phi-\frac{\eta\phi}{1+\eta}\alpha_{mn}\right)\left(\frac{\underline{p}_\alpha}{\omega_0}\right)^2+(\tau\omega_0)(\eta\phi)\left(1-\frac{\alpha_{mn}}{1+\eta}\right)\left(\frac{\underline{p}_\alpha}{\omega_0}\right)\right\}^{-1} \tag{13f}$$

The inverse transform of $\underline{U_{mn}}^*(p)$, $\underline{V_{mn}}^*(p)$, and $\underline{W_{mn}}^*(p)$ can be expressed in terms of these residues as[6]

$$U_{mn}^*(t) = \text{Residue at } p=0 + \sum(\text{Residue at } p=p_\alpha)e^{p_\alpha t} \tag{14a}$$

$$V_{mn}^*(t) = \text{Residue at } p=0 + \sum(\text{Residue at } p=p_\alpha)e^{p_\alpha t} \tag{14b}$$

$$W_{mn}^*(t) = \text{Residue at } p=0 + \sum(\text{Residue at } p=p_\alpha)e^{p_\alpha t} \tag{14c}$$

$$(p_\alpha = p_1, \tilde{p}_1, p_2, \tilde{p}_2)$$

The first term on the right-hand side of each equation is independent of time and represents the deformation due to a statically applied load of unit intensity. The other members of the equation represent the transient response of the panel owing to the sudden application of the load. The real part γ represents the damping, and the imaginary part ω the damped natural frequency of vibration of the panel.

It is seen that for each nodal pattern of the panel there are two families of modes of vibration represented by the frequencies ω_1 and ω_2. For these modes, the amplitude ratio

$$U_{mn}^{(\alpha)}(t)/V_{mn}^{(\alpha)}t = m/n\beta \quad (\alpha = 1, 2) \tag{15a}$$

is the same for both modes, while

$$\frac{U_{mn}^{(\alpha)}(t)}{W_{mn}^{(\alpha)}(t)} = \frac{(m/L_x^*)[\tau w_0(p_\alpha/\omega_0)+1]}{(1+K)[(p_\alpha/\omega_0)^2+\tau\omega_0(p_\alpha/\omega_0)+(1+\eta)]} \tag{15b}$$

depends on the value of p_α. When damping exists ($\tau \neq 0$), p_α is a complex quantity, and the ratio $U_{mn}(t)/W_{mn}(t)$ as given by (15b) is generally also a complex quantity. This indicates that there is generally phase difference between the displacement components u (or v) and w because of the different amount of damping of these displacements.

There is also another possible mode of vibration which is not excited in an isotropic panel by the loading in a direction perpendicular to the panel surface. It is described by p_3, where

$$\frac{\underline{p}_3}{\omega_0} = \frac{1}{2}\left[-\tau\omega_0 \pm \sqrt{(\tau\omega_0)^2-4\left(1+\frac{1-\mu}{2}\eta\right)}\right] \tag{15c}$$

are the roots of the equation $\psi(p) = 0$. This mode of vibration is characterized by the amplitudes

$$w_{mn}(t) = 0, \qquad u_{mn}(t)/v_{mn}(t) = -n\beta/m \tag{15d}$$

and represents a pure shear vibration without transverse deformation.

The Three Modes of Vibration of an Isotropic and Elastic Sandwich Panel Under No Edge Forces

In the preceding section, we have shown that three different modes of vibration are possible in a simply

supported isotropic and viscoelastic sandwich panel under quite general loading conditions. In this section, we shall give a detailed description of these three modes of vibration for the case in which the sandwich panel is not subjected to any edge forces and the core of the sandwich panel is purely elastic, i.e., there is no damping.

(a) Frequencies of the Three Modes

The frequencies for the three modes of vibration can be obtained from Eqs. (11d), (12b), and (12c). For the present case these frequencies, designated as ω_1, ω_2, and ω_3, for each particular value of m and n, are given in the following:

$$(\omega_1/\omega_0)^2 = (1/2)[(1 + \eta + \phi) - \sqrt{(1 + \eta + \phi)^2 - 4\eta\phi}] \quad (16a)$$

$$(\omega_2/\omega_0)^2 = (1/2)[(1 + \eta + \phi) + \sqrt{(1 + \eta + \phi)^2 - 4\eta\phi}] \quad (16b)$$

$$= \eta\phi/(\omega_1/\omega_0)^2 = (1 + \eta + \phi) - (\omega_1/\omega_0)^2 \quad (16c)$$

$$\left(\frac{\omega_3}{\omega_0}\right)^2 = 1 + \frac{1 - \mu}{2}\eta \quad (16d)$$

where $$\omega_0 = (1 + K)\sqrt{\bar{G}_{xz}/\bar{h}\rho_r}$$

can be interpreted as the frequency of pure shear vibration of an infinite panel.

The three frequencies satisfy the inequalities

$$\omega_2 \geqslant \omega_3 > \omega_1 \quad (17)$$

It is of interest to see that when shearing deformation and rotational inertia are neglected, the only finite frequency as given by Eqs. (16) is

$$(\omega_1)_{\eta=\phi=0} = (\pi^2/L_x^2)(m^2 + n^2\beta^2)\sqrt{D_0/(1 + f)\rho_t} \quad (18a)$$

We shall call this frequency ω_c. It differs from the classical flexural frequency for homogeneous plates only by the appearance of the small parameter f. It can easily be shown that the following relationship exists:

$$\omega_c/\omega_0 = \sqrt{\eta\phi} \quad (18b)$$

$$\omega_c/\omega_1 = \omega_2/\omega_0 \quad (18c)$$

Notice that η and ϕ are functions of m and n which depend on the nodal pattern. Therefore the frequencies ω_1, ω_2, ω_3, and ω_c also depend on the nodal pattern. The formulas for these frequencies in this section are for each particular wave pattern m and n. For all the possible patterns there is a total of triply infinite frequencies.

(b) Amplitudes of the Three Modes

The amplitudes of the motion in a particular nodal pattern excited by a unit step function perpendicular to the panel surface are obtained from Eqs. (13) and (14) as follows:

$$\frac{U_{mn}(t)}{\pi\bar{h}} = \frac{mL_x/\pi\bar{h}}{\pi^2(1 + f)(m^2 + n^2\beta^2)^2} + \sum_\alpha A_{mn}^{(\alpha)} \cos \omega_\alpha t \quad (19a)$$

$$\frac{V_{mn}(t)}{\pi\bar{h}} = \frac{n\beta L_x/\pi\bar{h}}{\pi^2(1 + f)(m^2 + n^2\beta^2)^2} + \sum_\alpha B_{mn}^{(\alpha)} \cos \omega_\alpha t \quad (\alpha = 1, 2) \quad (19b)$$

$$\frac{W_{mn}(t)}{\pi\bar{h}} = \frac{(L_x^2/\pi^2\bar{h}^2)(1 + K)(1 + \eta)}{\pi^2(1 + f)(m^2 + n^2\beta^2)^2} + \sum_\alpha C_{mn}^{(\alpha)} \cos \omega_\alpha t \quad (19c)$$

where

$$A_{mn}^{(\alpha)} = \frac{rm\rho_r/\rho_t}{\pi^2(1 + K)^2 (L_x/\pi\bar{h})[(\omega_\alpha/\omega_0)^4 - \eta\phi]} \quad (19d)$$

$$B_{mn}^{(\alpha)} = \frac{rn\beta\rho_r/\rho_t}{\pi^2(1 + K)^2 (L_x/\pi\bar{h})[(\omega_\alpha/\omega_0)^4 - \eta\phi]} \quad (19e)$$

$$C_{mn}^{(\alpha)} = \frac{r\rho_r/\rho_t[1 + \eta - (\omega_\alpha/\omega_0)^2]}{\pi^2(1 + K)[(\omega_\alpha/\omega_0)^4 - \eta\phi]} \quad (19f)$$

In these equations $A_{mn}^{(1)}$, $B_{mn}^{(1)}$, $C_{mn}^{(1)}$ are the amplitudes of Mode 1, and $A_{mn}^{(2)}$, $B_{mn}^{(2)}$, $C_{mn}^{(2)}$ are the amplitudes of Mode 2. There exist the following simple relationships among these amplitudes:

$$\frac{A_{mn}^{(1)}}{A_{mn}^{(2)}} = \frac{B_{mn}^{(1)}}{B_{mn}^{(2)}} = \frac{(\omega_2/\omega_0)^4 - \eta\phi}{(\omega_1/\omega_0)^4 - \eta\phi} < 0 \quad (20a)$$

$$\frac{A_{mn}^{(1)}}{B_{mn}^{(1)}} = \frac{A_{mn}^{(2)}}{B_{mn}^{(2)}} = \frac{m}{n\beta} > 0 \quad (20b)$$

$$\frac{C_{mn}^{(1)}}{C_{mn}^{(2)}} = \frac{A_{mn}^{(1)}}{A_{mn}^{(2)}} \frac{(\omega_1/\omega_0)^2 - (1 + \eta)}{(\omega_2/\omega_0)^2 - (1 + \eta)} > 0 \quad (20c)$$

$$\frac{A_{mn}^{(1)}}{C_{mn}^{(1)}} = \frac{\pi\bar{h}m/L_x(1 + K)}{(1 + \eta) - (\omega_1/\omega_0)^2} > 0 \quad (20d)$$

$$\frac{A_{mn}^{(2)}}{C_{mn}^{(2)}} = \frac{\pi\bar{h}m/L_x(1 + K)}{(1 + \eta) - (\omega_2/\omega_0)^2} < 0 \quad (20e)$$

Mode 3, which is not excited by loads perpendicular to the panel surface, is characterized by the amplitudes

$$\left.\begin{aligned} w_{mn}(t) &= 0 \\ u_{mn}(t)/v_{mn}(t) &= -n\beta/m < 0 \end{aligned}\right\} \quad (20f)$$

With the above information about the amplitudes and frequencies, these three modes of vibration can be readily described. Fig. 3 illustrates the distinctive features characterizing these three modes. Among the three modes, Mode 1 has the lowest frequency of vibration. The displacement components u, v, and w are in phase, as can be seen from Eqs. (20b) and (20d). It can also be shown from Eq. (20d) that $A_{mn}^{(1)}/C_{mn}^{(1)} \ll 1$, indicating that Mode 1 is predominated by flexural deformation, even though some extent of shearing deformation exists. It is this Mode 1 that corresponds to the classical flexural vibration.

Mode 2 has the highest frequency of vibration. Eqs. (20b) and (20e) show that the displacement components u and v are in phase, while w is out of phase with u and v. It can be shown from Eq. (20e) that $\left| A_{mn}^{(2)}/C_{mn}^{(2)} \right|$ can be quite large for small ϕ, which is generally the case. In other words, the motion of Mode 2 is predominantly shear in the plane of the plate. This type of motion is called thickness shear by Mindlin.[7] Because of this predominance of thickness shear the concave face of the panel is stretched while the convex face is shrunken. This is contrary to Mode 1 and to the classical bending of plates. It can be shown that the shearing deformation of Mode 1 and Mode 2 are in phase, even though the u (or v) displacements of these two modes are out of phase. This is because the shearing deformation of Mode 1 is mainly due to the deflection w, while the shearing deformation of Mode 2 is mainly due to the displacements u and v.

Mode 3 has the intermediate frequency of vibration. The deformation associated with this mode is pure shear in the plane of the plate, as indicated by Eq. (20f) that $w_{mn}(t) = 0$. Eq. (20f) also shows that the two nonvanishing displacement components u and v are out of phase. This shows the distinction between the shearing deformation of Mode 2 and Mode 3—that is, if the shearing deformations of these two modes are in phase in the x-z plane, they are out of phase in the y-z plane, and vice versa. In other words, in Mode 2, if one of the faces of the sandwich panel is stretched, it is stretched in all directions, while in Mode 3, if that face is stretched in the x-direction, it must be shortened in the y-direction. For a simply supported isotropic panel the third mode is not excited by loads perpendicular to the panel surface. For other edge conditions, however, all three modes are coupled together and the third mode will be excited by loads perpendicular to the surface of the panel.

It should be noted that the above description of the three possible modes of vibration holds exactly only for isotropic panels. For orthotropic sandwich panels, Mode 3 is also associated with some extent of flexural deformation and the forces in a direction perpendicular to the panel will excite Mode 3, even though its amplitude is small. These results will be discussed in a later investigation.

The Nondimensional Parameters η, ϕ, and K

We have shown that the frequencies and amplitudes of the flexural vibrations of a sandwich panel can be expressed in a very simple way in terms of two parameters of the panel,

$$\eta = (D_0/D_Q)(1 + f)(\pi^2/L_x^2)(m^2 + n^2\beta^2)$$

and

$$\phi = \frac{\rho_r}{\rho_t}\left(\frac{\bar{h}}{1 + K}\right)^2 \frac{\pi^2}{L_x^2}(m^2 + n^2\beta^2)$$

The factor common to η and ϕ, $(\pi^2/L_x^2)(m^2 + n^2\beta^2)$, is inversely proportional to the square of the wavelength; D_0/D_Q is the ratio of the bending rigidity to the shearing rigidity of the panel; $(\rho_r/\rho_t)[\bar{h}/(1 + K)]^2$ is approximately the ratio of the mass moment of inertia to the mass per unit area of the panel. Therefore the parameter η is directly proportional to the ratio of the bending rigidity to the shearing rigidity of the panel and inversely proportional to the square of the wavelength. The parameter ϕ is directly proportional to the ratio of the mass moment of inertia to the mass per unit area of the panel and inversely proportional to the square of the wavelength. The parameter η measures the relative importance of the bending rigidity to the shearing rigidity of the panel and is designated as the shearing deformation parameter. The parameter ϕ represents the relative importance of the rotational inertia to the translational inertia of the panel and is called the rotational inertia parameter. For the case of the classical analysis of plates, shear deformation and rotational inertia are neglected, and therefore $\eta = \phi = 0$. The greater the values of η and ϕ, the greater are the effects of shear deformation and rotational inertia. Notice that for a particular panel the ratio η/ϕ is fixed, independent of the wavelength. For familiarization with these parameters, numerical values of η and ϕ for a common sandwich panel are given in the following.

Description of panel

Size: 18 × 18 in.
Skins: 0.01 clad 2024-T3 aluminum alloy
Core: 1/8-in. cell size, 0.007 3003-H19 aluminum foil, 0.375 thickness, density 3.1 lbs./ft.

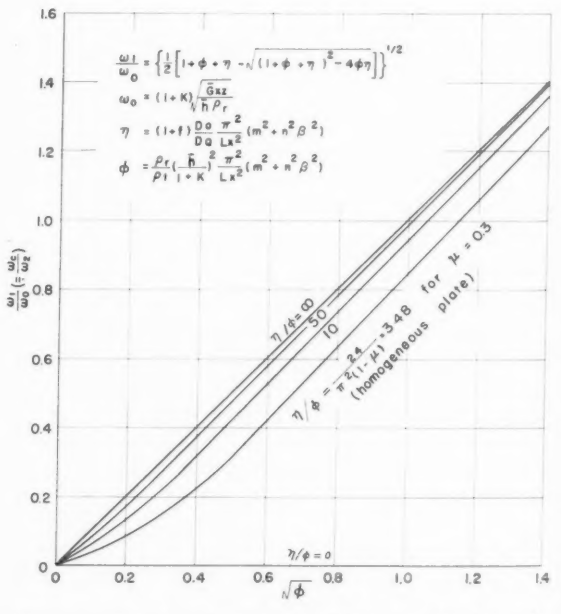

FIG. 3. Normalized frequency of Mode 1, ω_1/ω_0 ($= \omega_r/\omega_2$ vs. $\sqrt{\phi}$ at different η/ϕ or the cases (a) simply supported rectangular sandwich panel and (b) isotropic elastic core.

For this panel

$$\eta = 1.8 \times 10^{-2}\,(m^2 + n^2)$$
$$\phi = 8.4 \times 10^{-4}\,(m^2 + n^2)$$
$$\eta/\phi = 21.4$$

The corresponding fundamental frequencies are

$$\omega_0/\omega_c = 1.29 \times 10^2$$
$$\omega_1/\omega_c = 0.98$$
$$\omega_2/\omega_c = 1.31 \times 10^2$$
$$\omega_3/\omega_c = 1.29 \times 10^2$$

In general η is much greater than ϕ. Notice that the expressions for ω_1/ω_0 (or ω_1/ω_c) and ω_2/ω_0 (or ω_2/ω_c) [Eqs. (16a) and (16b)] are symmetric in η and ϕ. In other words, η and ϕ play the same part in affecting the frequency of Mode 1 and Mode 2. Since for sandwich panels in general $\eta \gg \phi$, it can be concluded that the effect of shearing deformation is much more important than the effect of rotational inertia; in fact, it is more important than in the case of homogeneous plates. Since η and ϕ are inversely proportional to the square of the wavelength, it can be seen that the effects of shearing deformation and rotational inertia are more important for shorter wavelength pulses. This fact is well known.

The introduction of these parameters is very convenient and of practical value. Suppose for a particular panel we want to know whether the bending rigidity of the facings, say D_0', is important. We simply add D_0' to D_0 to obtain a new value of

$$\eta = \frac{D_0 + D_0'}{D_Q}\,(1 + f)\,\frac{\pi^2}{L_x^2}\,(m^2 + n^2\beta^2)$$

and by substituting it into the frequency equations get a very good estimate of the frequencies for which the bending rigidity of the facings is included.* The same procedure can be applied to estimate the effect of the rotational inertia of the facings.

In addition to η and ϕ there is another important parameter, $K = E't'/E''t''$, which is the ratio of the stiffness of the lower facing to the upper facing. K determines the position of the neutral surface of the panel, and takes care of the effect of the difference of thickness and material property between the upper facing and the lower facing. For a symmetrical panel, i.e., a panel with identical upper and lower facing, $K = 1$. For a large class of practically important applications, however, $K \neq 1$; for instance, due to aerodynamic heating, one face of the panel may be weakened considerably ($E' \neq E''$).

Behavior of the Three Frequencies for Limiting Values of the Panel Parameters η and ϕ

(a) $\eta \ll 1$, $\phi \ll 1$—i.e., the panel is very rigid in transverse shear and has very small rotational inertia.

In this case

$$\omega_1/\omega_c \cong 1 - (1/2)(\eta + \phi)$$
$$\omega_2/\omega_c \cong [1 + (1/2)(\eta + \phi)]/\sqrt{\eta\phi}$$
$$\omega_3/\omega_c \cong \left[1 + \frac{1 - \mu}{4}\,\eta\right]/\sqrt{\eta\phi}$$

When $\eta = \phi = 0$,

$$\omega_2,\ \omega_3 \to \infty$$
$$\omega_1 = \omega_c = (\pi^2/L_x^2)(m^2 + n^2\beta^2)\sqrt{D_0/\rho_t(1 + f)}$$

The result that ω_2 and ω_3 go to infinity as η and ϕ go to zero gives us another way of looking at the classical theory. Instead of saying that these two modes of vibration do not exist, it is more appropriate to say that their frequencies of vibration go to infinity when shearing deformation and rotational inertia are neglected.

(b) $\eta \ll 1$—i.e., the panel is very rigid in transverse shear:

$$\omega_1/\omega_c \cong \left(1 - \frac{1}{2}\,\frac{\eta}{1 + \phi}\right)/\sqrt{1 + \phi}$$
$$\omega_2/\omega_c \cong \sqrt{\frac{1 + \phi}{\eta\phi}}\left(1 + \frac{1}{2}\,\frac{\eta}{1 + \phi}\right)$$
$$\omega_3/\omega_c \cong \left[1 + \frac{1 - \mu}{4}\,\eta\right]/\sqrt{\eta\phi}$$

When $\eta = 0$,

$$\omega_1,\ \omega_3 \to \infty$$
$$\omega_1 = \omega_c/\sqrt{1 + \phi}$$

ω_1 differs from the classical flexural frequency only by the factor $1/\sqrt{1 + \phi}$. In general, unless for higher overtones (m,n very large), ϕ is a very small quantity, and ω_1 can be very closely approximated by $\omega_1 \cong \omega_c[1 - (\phi/2)]$. It can be further inferred that the effect of rotational inertia is important only for higher overtones, or what is equivalent, for short-wavelength waves. This fact is well known.

(c) $\phi \ll 1$—i.e., the panel possesses very small rotational inertia:

$$\omega_1/\omega_c \cong \left(1 - \frac{1}{2}\,\frac{\eta}{1 + \phi}\right)/\sqrt{1 + \eta}$$
$$\omega_2/\omega_c \cong \sqrt{\frac{1 + \eta}{\eta\phi}}\left(1 + \frac{1}{2}\,\frac{\phi}{1 + \eta}\right)$$
$$\omega_3/\omega_c = \sqrt{\left(1 + \frac{1 - \mu}{2}\,\eta\right)/\eta\phi}$$

When $\phi = 0$,

$$\omega_2,\ \omega_3 \to \infty$$
$$\omega_1 = \omega_c/\sqrt{1 + \eta}$$

* This does not predict the appearance of additional modes of vibration. See reference 4.

As in case (b), ω_1 differs from the classical flexural frequency ω_2 only by the factor $1/\sqrt{1+\eta}$. Since η is in general a much larger quantity than ϕ, the effect of shearing deformation on the flexural frequency is also much larger than the effect of rotational inertia. Again, it can be seen that the effect of shearing deformation is greater for higher order modes.

(d) $\eta \gg 1$—i.e., the panel is very soft in transverse shear:

$$\omega_1/\omega_c \cong \left[1 - \frac{1}{2}\frac{1}{\eta+\phi}\right]/\sqrt{\eta+\phi}$$

$$\omega_2/\omega_c \cong \left[1 + \frac{1}{2}\frac{1}{\eta+\phi}\right]\sqrt{\frac{\eta+\phi}{\eta\phi}}$$

$$\omega_3/\omega_c \cong \sqrt{\frac{1-\mu}{2\phi}}\left[1 + \frac{1}{\eta(1-\mu)}\right]$$

When $\eta \to \infty$,

$$\omega_1 = 0$$

$$\omega_2 = \omega_c/\sqrt{\phi}$$

$$\omega_3 = \omega_c\sqrt{(1-\mu)/\phi}$$

In the present case, the flexural frequency ω_1 vanishes as $\eta \to \infty$. This is to be expected since in our theory we have neglected the bending rigidity of the individual facings; therefore when the core no longer transmits transverse shear, the bending rigidity of the whole panel vanishes. The two predominantly shear modes, ω_2 and ω_3, do not vanish even though the core no longer carries transverse shear. There is no contradiction in this case, because essentially in these two modes the two facings execute extensional vibrations which result in the shear of the panel as a whole. The following table summarizes the limiting behavior of these frequencies. The other limiting case $\phi \to \infty$ is not considered, since ρ_r/ρ_t does not become very large.

TABLE 1

	ω_0	ω_1	ω_2	ω_3
$\eta \to 0$, $\phi \to 0$	∞	ω_c	∞	∞
$\eta \to 0$	∞	$\omega_c/\sqrt{1+\phi}$	∞	∞
$\phi \to 0$	∞	$\omega_c/\sqrt{1+\eta}$	∞	∞
$\eta \to \infty$	0	0	$\omega_c/\sqrt{\phi}$	$\omega_c\sqrt{(1-\mu)/\phi}$

$\omega_c = (\pi^2/L_x^2)(m^2 + n^2\beta^2)\sqrt{D_0/\rho_t(1+f)}$

Application to Homogeneous Plates

It can be shown that the frequencies obtained in the previous section are applicable not only to sandwich plates but to homogeneous plates as well. For homogeneous and isotropic plates, the physical parameters have the following values:

$$D_0 = Eh^3/12(1-\mu^2), \quad K = 1, \quad f = 0$$

$\rho_r/\rho_t = 1/3$ within the assumption of first-order theory;
$\bar{G}_{xz} = (\pi^2/12)G$ where $\pi^2/12$ is the shear coefficient;
$\eta = [2h^2/L_x^2(1-\mu)](m^2 + n^2\beta^2)$
and $\phi = (\pi^2h^2/12L_x^2)(m^2 + n^2\beta^2) = [\pi^2(1-\mu)/24]\eta$

The three frequencies now become

$$\left(\frac{\omega_1}{\omega_0}\right)^2 = \frac{1}{2}\left\{1 + \frac{h^2}{L_x^2}(m^2+n^2\beta^2)\left(\frac{2}{1-\mu} + \frac{\pi^2}{12}\right) - \sqrt{\left[1 + \frac{h^2}{L_x^2}(m^2+n^2\beta^2)\left(\frac{2}{1-\mu} + \frac{\pi^2}{12}\right)\right]^2 + \frac{\pi^2}{3}\frac{h^2}{L_x^2}(m^2+n^2\beta^2)}\right\} \quad (21a)$$

$$\left(\frac{\omega_2}{\omega_0}\right)^2 = \frac{1}{2}\left\{1 + \frac{h^2}{L_x^2}(m^2+n^2\beta^2)\left(\frac{2}{1-\mu} + \frac{\pi^2}{12}\right) + \sqrt{\left[1 + \frac{h^2}{L_x^2}(m^2+n^2\beta^2\left(\frac{2}{1-\mu} + \frac{\pi^2}{12}\right)\right]^2 + \frac{\pi^2}{3}\frac{h^2}{L_x^2}(m^2+n^2\beta^2)}\right\} \quad (21b)$$

$$\left(\frac{\omega_3}{\omega_0}\right)^2 = 1 + h^2/L_x^2\,(m^2+n^2\beta^2) \quad (21c)$$

where

$$\omega_0 = \pi\sqrt{G/h\rho_t} \quad (21d)$$

With a change of notation, these frequency ratios can be shown to agree exactly with those obtained by Mindlin, Schacknow, and Deresiewicz.[8] It is interesting to note that these frequency ratios depend on only a single parameter, $(h^2/L_x^2)(m^2+n^2\beta^2)$, besides Poisson's ratio. Physically this is quite clear. Since the portion of the plate enclosed by nodal lines behaves exactly like a simply supported plate, the frequency of the overtone corresponding to this nodal pattern would be the same as the fundamental frequency of a plate with geometrical dimensions similar to the portion of the plate bounded by the nodal lines.

Application to Sandwich Beams

The results obtained in the previous sections are for sandwich panels. In the case of sandwich beams the third mode does not exist. Except for this difference, the results obtained for the frequencies and amplitudes of Mode 1

and Mode 2 for sandwich panels are exactly applicable to sandwich beams provided we interpret properly some of the parameters. All we have to do is replace the bending rigidity of the panel by the bending rigidity of the beam [let $\mu = 0$ in $D_0 = E'h'\bar{h}^2(1+f)^2/(1+K)(1-\mu^2)$] and let the wavelength in the y direction go to infinity ($\eta\beta \to 0$).

Effects of Viscoelastic Core and Edge Compression

In the previous sections, the application of our general theory to the flexural vibrations of a simply supported rectangular panel was discussed in detail. For simplicity, the effects of viscoelastic core and edge compression were not considered. In this section we shall consider these effects in the manner of a first-order correction to the previous results. A more exact and more general treatment of these effects will be the subject of a later investigation.

When the effect of viscoelastic core is considered, Eq. (11e), which gives the frequency and damping coefficient of Mode 1 and Mode 2, becomes

$$(p/\omega_0)^4 + (p/\omega_0)^3\tau\omega_0(1+\phi) + (p/\omega_0)^2(1+\eta+\phi) + (p/\omega_0)\tau\omega_0(\eta\phi) + \eta\phi = 0$$

This is a quartic equation which could be solved by the standard method. The result, however, would be cumbersome. We shall find an approximate solution by utilizing the fact that $\tau\omega_0$ is small (small damping) so that we can expand (p/ω_0) as a power series in $\tau\omega_0$—i.e.,

$$(p/\omega_0) = (\gamma + i\omega)/\omega_0 = (p^{(0)}/\omega_0) + (p^{(1)}/\omega_0)(\tau\omega_0) + (p^{(2)}/\omega_0)(\tau\omega_0)^2 + \ldots$$

It can be shown that $p^{(0)}$ is purely imaginary and gives us the frequencies obtained previously; $p^{(1)}$ is real and negative and gives the damping coefficient; $p^{(2)}$ is again purely imaginary and gives the correction to frequency due to the existence of damping.

Correct to $0[(\tau\omega_0)^2]$ the damping coefficient is

$$\gamma^* = (p^{(1)}/\omega_0)\tau\omega_0 \leqslant 0$$

$$= -\frac{\tau^*(1+\phi)}{4}\left[1 \mp \frac{(1+\eta+\phi) - 2\eta\phi/(1+\phi)}{\sqrt{(1+\eta+\phi)^2 - 4\eta\phi}}\right] \qquad \begin{cases} - \text{ Mode 1} \\ + \text{ Mode 2} \end{cases}$$

$$\simeq \begin{cases} -\tau\omega_0(\eta^2\varphi/2) \text{ for } \eta \ll 1 & \text{(Mode 1)} \\ -\tau\omega_0(1+\phi)/2 \text{ for } \phi \ll 1 & \text{(Mode 2)} \end{cases}$$

This shows that Mode 2 will be damped out much faster than Mode 1. This is to be expected since Mode 2 is predominantly shear. The frequency is changed by the amount

$$\frac{p_\alpha^{(2)}}{\omega_0}(\tau\omega_0)^2 = -(\tau\omega_0)^2\frac{p_\alpha^{(1)}}{p_\alpha^{(0)}}\frac{p_\alpha^{(1)}/\omega_0\left[6\,(p_\alpha^{(0)}/\omega_0)^2 + (1+\eta+\phi)\right] + 3(1+\phi)\,(p_\alpha^{(0)}/\omega_0)^2 + \eta\phi}{2\left[2\,(\omega_\alpha^{(0)}/\omega_0)^2 + (1+\eta+\phi)\right]}$$

$$\left(\alpha = \begin{matrix} 1, & \text{Mode 1} \\ 2, & \text{Mode 2} \end{matrix}\right)$$

For $\eta \ll 1$, $\phi \ll 1$ the change in the frequency of Mode 1 is negligible. The nondimensional frequency of Mode 2 is reduced by the amount $(1/8)(\tau\omega_0)^2$.

As to the amplitudes of vibration, it was already pointed out after Eq. (15b) that because of the different amounts of damping, the displacement components u_α in the plane of the panel and the deflection u_3 are not exactly in phase or completely out of phase.

Next we shall consider the effect of edge compression. In this case the equation for the damping coefficient and frequency becomes

$$\left(\frac{p}{\omega_0}\right)^4 + \left(\frac{p}{\omega_0}\right)^3\tau\omega_0(1+\phi) + \left(\frac{p}{\omega_0}\right)^2\left(1+\eta+\phi-\frac{\eta\phi}{1+\eta}\alpha_{mn}\right) + \left(\frac{p}{\omega_0}\right)\tau\omega_0(\eta\phi)$$

$$\times\left(1-\frac{\alpha_{mn}}{1+\eta}\right) + \eta\phi\,(1-\alpha_{mn}) = 0$$

where α_{mn} is the ratio of the edge load to the corresponding buckling load. This quartic equation can be solved approximately by the power-series expansion method used above. The result for the case of $\eta \ll 1$ and $\phi \ll 1$—i.e., for common sandwich panels in their fundamental modes or lower overtones—is summarized as follows:

Damping coefficient

Mode 1: proportional to $(2 - \alpha_{mn})$
Mode 2: almost independent of α_{mn}

Frequency

Mode 1: proportional to $\sqrt{1 - \alpha_{mn}}$

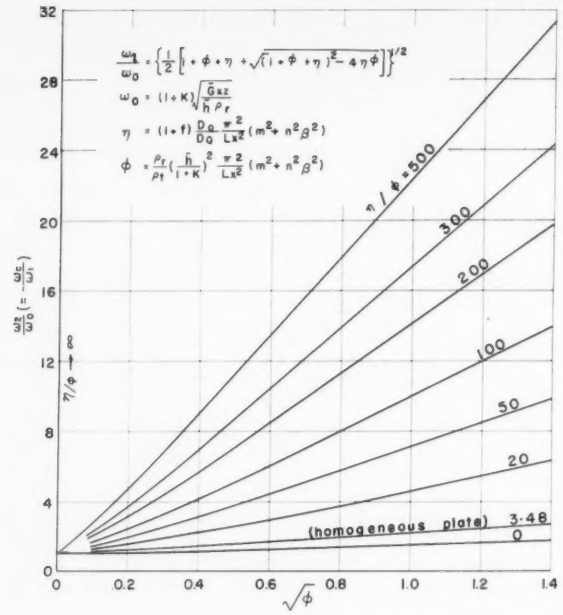

FIG. 4. Normalized frequency of Mode 2, ω_1/ω_0 ($=\omega_c/\omega_2$) vs. $\sqrt{\phi}$ at different η/ϕ for the cases (a) simply supported rectangular sandwich plate and (b) isotropic elastic core.

Mode 2: almost independent of α_{mn}

Therefore the frequency of Mode 1 decreases with the increase of edge compression, a fact to be expected. The result also suggests a method of determining experimentally the elastic buckling load of a sandwich panel by measuring the change of the frequency of Mode 1 with respect to the change of edge compression. Mode 2 is not much changed by the presence of edge compression, again because it is predominantly a shear deformation.

Graphical Presentation of Results

The frequencies for the three modes of the flexural vibration of an elastic and isotropic sandwich panel are computed, and the results are presented in Figs. 3, 4, and 5. The numerical values of the panel parameter range from $\phi = 0$ and $\eta/\phi = 0$ to $\phi = 1.96$ and $\eta/\phi = 500$. In each figure the frequency is normalized by dividing it by $\omega_0 = (1 + K)\sqrt{\bar{G}_{xz}/\bar{h}\rho_t}$, the frequency of pure shear vibration of an infinite panel.

In Fig. 3 the normalized frequency of Mode 1, ω_1/ω_0, is plotted against the rotational inertia parameter $\sqrt{\phi}$ for different values of η/ϕ. For a particular panel this ratio assumes a definite value, in particular $\eta/\phi = 24/[\pi^2(1 - \mu)]$ for a homogeneous plate. Therefore each curve of this figure represents a particular panel. As we move along that curve in the direction of increasing ϕ, we obtain frequencies of higher overtones of that panel ($m^2 + n^2\beta^2$ increases, while the panel parameters remain unchanged). This is the reason that the ratio η/ϕ is used as a parameter instead of η itself. When we want to see the effect of increasing (decreasing) the shearing deformation on the frequency of vibration, we simply pick out a fixed abscissa $\sqrt{\phi}$ and move from a curve of smaller (greater) η/ϕ to a curve of greater (smaller) η/ϕ. In order to see the effect of rotational inertia, we can follow a similar but slightly more tedious procedure. It should be kept in mind, however, that as we vary η and ϕ, the characteristic frequency $\omega_0 = (1 + K)\sqrt{\bar{G}_{xz}/\bar{h}\rho_t}$ also changes. Therefore it may seem to be more significant to use $\omega_c = (\pi^2/L_x^2)(m^2 + n^2\beta^2)\sqrt{D_0/(1 + f)\rho_t}$, the classical flexural frequency, instead of ω_0, the shear frequency, as a basis of comparison. This is done in Fig. 4. However, the plot in Fig. 3 does show certain advantages. It is seen that the curves for different values of the ratio η/ϕ show very small scattering. In fact for $\eta/\phi > 50$ the curves approach the straight line $\eta/\phi = \infty$ ($\omega_1/\omega_0 = \sqrt{\phi}$) very rapidly. For designer's use, this is very convenient. Also favoring the use of ω_0 as a basis of comparison is the fact that ω_0 is fixed for a particular panel and independent of the wave pattern.

Fig. 4 is a plot of the normalized frequency of Mode 2, ω_2/ω_0 against $\sqrt{\phi}$. The numerical values of the parameter η/ϕ range from 0 to 500. Since it has been pointed out that $\omega_2/\omega_0 = \omega_c/\omega_1$, this figure also gives the ratio of the classical flexural frequency, ω_c, to the frequency of Mode 1, ω_1. It can readily be seen from this figure that

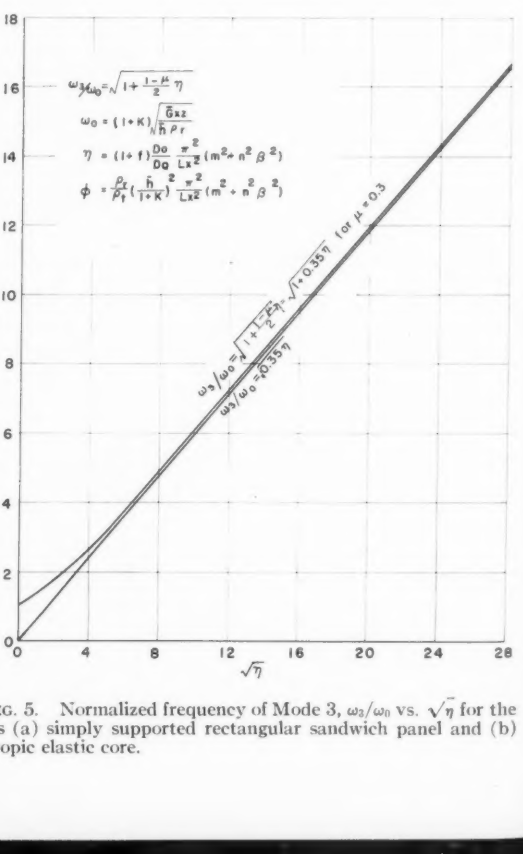

FIG. 5. Normalized frequency of Mode 3, ω_3/ω_0 vs. $\sqrt{\eta}$ for the cases (a) simply supported rectangular sandwich panel and (b) isotropic elastic core.

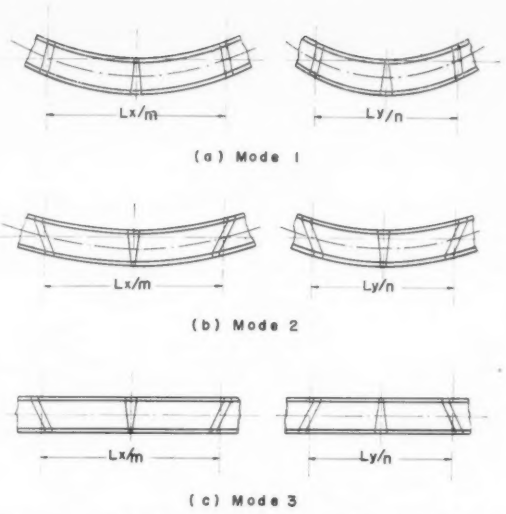

FIG. 6. The modal shapes of the three modes of vibration of a sandwich panel.

(a) $\omega_1 \leqslant \omega_c$.

(b) ω_1/ω_c decreases with the increase of η and ϕ. In other words, the greater the effect of rotational inertia and shearing deformation, and the higher the order of modes, the smaller is the frequency of Mode 1 in comparison with the classical flexural frequency.

(c) For large values of ϕ, $\omega_1/\omega_c \cong 1/\sqrt{\eta\phi}$.

It can be seen by comparing the scale for ω_1/ω_0 and ω_2/ω_0 in Figs. 3 and 4 that ω_1 can be much smaller than ω_2. It should also be pointed out that $\omega_c/\omega_2 = \omega_1/\omega_0$, or the ratio of the classical flexural frequency to the frequency of Mode 2, is also given by the ordinate in Fig. 3. Again this is very convenient for the rapid estimation of the frequency of Mode 2.

Fig. 5 shows the normalized frequency of Mode 3, ω_3/ω_0. In this figure ω_3/ω_0 is plotted against $\sqrt{\eta}$ instead of $\sqrt{\phi}$, because

$$\omega_3/\omega_0 = \sqrt{1 + \frac{1-\mu}{2}\eta}$$

depends on η only. For large values of η the curve approaches the straight line $\omega_3/\omega_0 = \sqrt{(1-\mu)/2}\,\sqrt{\eta}$ asymptotically.

It can also be seen from Figs. 3, 4, and 5 that in contrast with the classical flexural frequency, overtones of ω_1, ω_2, and ω_3 are spaced closer than the order of $(m^2 + n^2\beta^2)$. In fact, for very high overtones $(m,n \gg 1)$ they are approximately proportional to $\sqrt{m^2 + n^2\beta^2}$.

The modal shapes of these three modes of vibration are shown in Fig. 6. The distinction in the deformation associated with each mode is evident, as has been discussed in a previous section.

The ratios of the amplitudes of vibration of Mode 1 and Mode 2 are also computed. The ratios of the displacement components in the y and z directions, $A_{mn}^{(1)}/A_{mn}^{(2)} = B_{mn}^{(1)}/B_{mn}^{(2)}$, are the same and are shown in Fig. 7. For large values of ϕ, this ratio approaches the asymptotic value η/ϕ. The ratios of the deflection in the z direction, $C_{mn}^{(1)}/C_{mn}^{(2)}$, are shown in Fig. 8. These figures seem to indicate that the amplitude of Mode 2 is negligible compared with the amplitude of Mode 1. However, these are the amplitude responses to a unit step function, and it should be understood that Mode 2 cannot be disregarded under general loading conditions. For loading conditions in general, the coefficients of the Fourier expansion of the load form a rapidly decreasing sequence. Therefore, for sustained high-frequency excitation the fundamental vibration of Mode 2 will be more important than the higher overtones of Mode 1.

Conclusion

(a) In this paper the flexural motion of a rectangular sandwich panel with an orthotropic viscoelastic core is treated. It is found that three families of different modes of vibration are possible. The first mode corresponds to the classical flexural vibration. The motion of this mode is dominated by flexural deformation coupled with a small amount of shearing deformation. The second mode is dominated by thickness shear deformation with some extent of flexural deformation. The frequency of the second mode is much higher than that of the first mode. This second mode may become very important under sustained high-frequency excitation, inducing large shear stresses in the core. The third mode is pure shear. For simply supported isotropic panels as treated in the example in

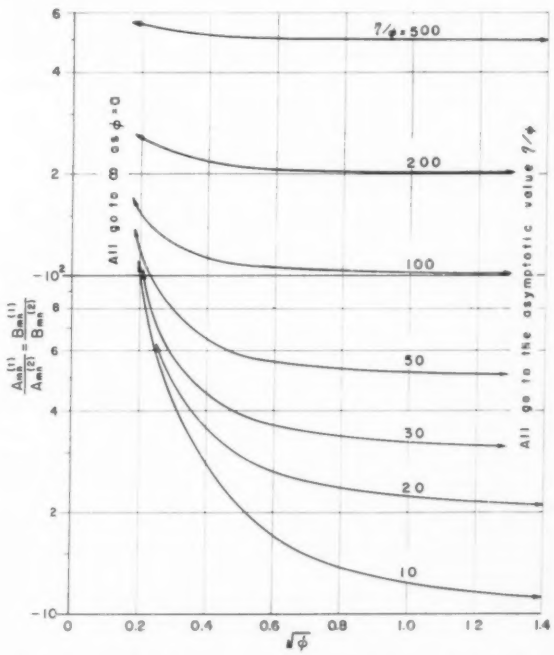

FIG. 7. Ratio of the x and y component of the amplitudes of vibration in Mode 1 and Mode 2, $A_{mn}^{(1)}/A_{mn}^{(2)} = B_{mn}^{(1)}/B_{mn}^{(2)}$ vs. $\sqrt{\phi}$ at different η/ϕ for the cases (a) simply supported sandwich panel and (b) isotropic elastic core.

the preceding sections, this mode is not excited by loads perpendicular to the panel surface. For other boundary conditions, and for orthotropic panels, in general all three modes are coupled together and hence all are excited by loads perpendicular to the surface of the panel.

(b) Two fundamental parameters, η and ϕ, are defined. They represent the relative importance of rotational inertia and shear deformation, respectively. In terms of η and ϕ, the three modes are expressed in simple forms which are convenient for engineering applications. When $\eta, \phi \to 0$ the second and the third modes disappear, and the first mode reduces to that of the classical theory with shear deformation and rotational inertia neglected. The greater the parameters η and ϕ the smaller is the frequency of the first mode as compared with the classical frequency. In conventional sandwich panel, $\eta/\phi \gg 1$.

(c) The theory is applicable to unsymmetrical sandwich panels. The difference in the thickness and the material of the two facings of the panel is very conveniently taken into account by the parameter K, which is the stiffness ratio of the two facings. $K = 1$ for identical facings.

(d) The effect of edge compression and viscous shear in the core are represented by the parameters α_{mn} and τ, respectively. As should be expected, the frequency of the first mode decreases with increase in the edge compression. The damping coefficient is greater for the second mode than for the first because the second mode is essentially a shear motion.

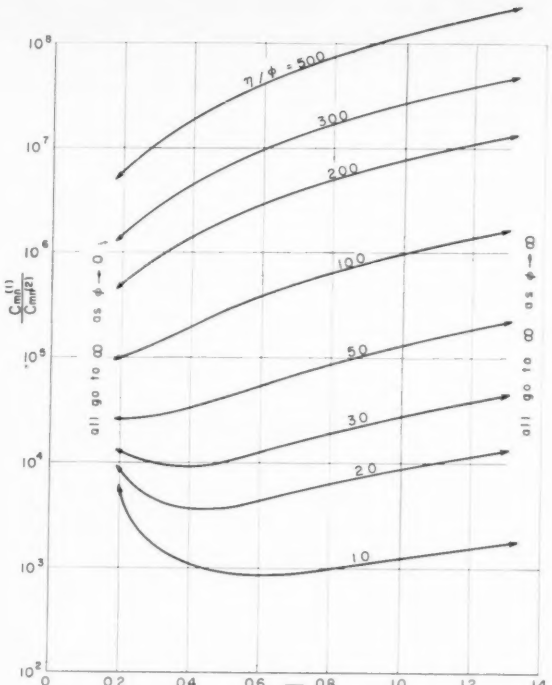

FIG. 8. Ratio of the z component of the amplitudes of vibration in Mode 1 and Mode 2, $C_{mn}^{(1)}/C_{mn}^{(2)}$ vs. $\sqrt{\phi}$ at different η/ϕ for the cases (a) simply supported rectangular sandwich panel and (b) isotropic elastic core.

Remark

After the completion of this paper, some papers by Yu[9,10] on sandwich plates were referred to the authors. In these papers a one-dimensional theory of an infinite symmetrical sandwich plate is developed from the theory of elasticity, taking into account very general core and facing properties. The theory has also been generalized to the two-dimensional case.[11] It is believed that the work of Yu is very important in establishing the limit of validity of the present theory, which is more restrictive but more amenable to engineering applications.

References

[1] Mindlin, R. D., *Influence of Rotatory Inertia and Shear on Flexural Motions of Isotropic, Elastic Plates*, J. Appl. Mech., Vol. 18, No. 1, pp. 31–38, March 1951.

[2] Chang, C. C., and Fang, B. T., *Initially Warped Sandwich Panel Under Combined Loadings*, Journal of the Aerospace Sciences, Vol. 27, No. 10, pp. 779–787, October 1960.

[3] Reissner, E., *The Effect of Transverse Shear Deformation on the Bending of Elastic Plates*, J. Appl. Mech., Vol. 12, No. 2, pp. 69–77, March 1945.

[4] Yu, Y. Y., *Simple Thickness-Shear Modes of Vibration in Infinite Sandwich Plates*, TN No. 2, Department of Mechanical Engineering, Polytechnic Institute of Brooklyn, October 1958.

[5] Hoff, N. J., *Bending and Buckling of Rectangular Sandwich Plates*, NACA TN 225, 1950.

[6] Churchill, R. V., *Modern Operational Mathematics in Engineering*, pp. 167–172; McGraw-Hill Book Co., Inc., New York, 1944.

[7] Mindlin, R. D., *An Introduction to the Mathematical Theory of Vibration of Elastic Plates*, U.S. Army Signal Corps Engineering Laboratories, Fort Monmouth, N.J., 1955.

[8] Mindlin, R. D., Schacknow, A., and Deresiewicz, H., *Flexural Vibrations of Rectangular Plates*, Office of Naval Research Project NR-064-388, Contract Nonr-266(09), TR No. 21, Dept. of Civil Engineering and Engineering Mechanics, Columbia University, June 1955.

[9] Yu, Y. Y., *Flexural Vibrations of Elastic Sandwich Plates*, Journal of the Aerospace Sciences, Vol. 27, No. 4, pp. 272–282, April 1960.

[10] Yu, Y. Y., *Simplified Vibration Analysis of Elastic Sandwich Plates*, AFOSR TN 59-1082, Deptartment of Mechanical Engineering, Polytechnic Institute of Brooklyn, August 1959.

[11] Yu, Y. Y., *A New Theory of Sandwich Plates—General Case*, AFOSR TN 59-1163, Department of Mechanical Engineering, Polytechnic Institute of Brooklyn, November 1959.

Microcards for Volumes 1–5 Available

Microcards for Volumes 3–5 of the JOURNAL are now available (Vols. 1 and 2 were republished in this form earlier). All five volumes are priced at $5.50 each, and are obtainable through:

J. S. Canner & Company, Inc.
Boston, Roxbury 20, Mass.

Some Considerations on the Laminar Stability of Time-Dependent Basic Flows†

S. F. SHEN*

U.S. Naval Ordnance Laboratory

Summary

As a stability criterion for infinitesimal disturbances in an incompressible, parallel but time-dependent basic flow, it is proposed to introduce the concept of "momentary stability," which is said to prevail at the instant if the kinetic energy of the disturbances, as a fraction of the kinetic energy of the basic flow, tends to decrease. The significance of such a criterion is briefly discussed. For special time-dependent basic flows which are described by similar velocity profiles at all times (except for changes in amplitude), *in the inviscid limit* only a change of the time scale is needed to reduce the solution essentially to that for the steady case. The disturbances may be of either the transverse-wave or the longitudinal-vortices type. The result indicates a very strong destabilizing influence of deceleration, which is likely to overshadow that of the velocity profile under normal circumstances. The observations of Fales (on flow over the flat plate) and Coles (on flow between rotating cylinders) are believed to be largely due to the deceleration. At finite Reynolds numbers, the usual procedure of calculating the stability solution on the basis of the instantaneous profile is further shown to be valid only for extremely slow acceleration or deceleration. Even when the solution is acceptable, the condition $c_i = 0$ for neutral stability may not be used without reservation. To calculate momentary stability properly, a procedure for a slowly varying but more general profile is also described.

Symbols

c = wave speed of the disturbance
c_r, c_i = real and imaginary parts, respectively, of the wave speed
t = time
t_0 = time constant of the changing basic flow
u,v = disturbance velocity components in the x- and y-directions, respectively
x,y = Cartesian coordinates along and normal to the basic flow, respectively
y_c = the critical point where $U^* = c$
E = kinetic energy ratio, Eq. (5)
E_0, E_1 = defined in Eq. (42)
G_r = "growth rate" defined as $(1/2E)(dE/dt)$
Re = Reynolds number
Re_{cr} = minimum critical Reynolds number
T = time dependence of the special velocity profile, Eq. (6)
T_1 = time dependence of the velocity profile, Eq. (25)
U = velocity profile of the basic flow
U_m = maximum velocity of the basic flow
$U^*(y)$ = space dependence of the special velocity profile, Eq. (6)
$U_c^{*\prime}$ = velocity gradient of $U^*(y)$ at $y = y_c$
α = wave number of the disturbance
β = time constant parameter for certain special basic flows
δ = thickness of the basic flow in y-direction
ϵ = small parameter for slowly changing profile, Eq. (25)
λ = wavelength of the disturbance
Φ = disturbance mode defined by Eq. (17)
Φ_e = the eigenfunction for the disturbance
Φ_* = defined in Eq. (31)
Ψ = disturbance stream function
Ψ_* = defined in Eq. (29)
ζ = defined by Eq. (19) for Eqs. (20) and (21), or by Eq. (36) for Eqs. (37)–(39)
τ = variable of stretched time scale, Eq. (8)

Superscripts

(0), (1) refer to terms in the expansion Eq. (26)

Introduction

IT IS NOW GENERALLY ACCEPTED that the theory of laminar instability provides the explanation for the initiation of large disturbances which may lead to the transition to turbulent flow when no other causes are present. Heretofore the basic "mean" flow has been assumed to be steady and parallel. Where the basic flow is neither of these, calculations have been made by applying the theory to the instantaneous local velocity distributions—i.e., resorting to a quasi-steady or quasi-parallel treatment. It is reasonable, of course, to assume that such treatment probably gives the right answer when the changes are indeed sufficiently slow with respect to the variable concerned. But likewise the range of validity of this procedure in actual applications—i.e., the maximum permissible time- or space rate of change—is by no means clear. Thus, G. I. Taylor[1] voiced an early criticism regarding the correlation of the laminar stability theory of parallel flows with the transition of the boundary layer, for which there is always a growth in the downstream direction, however small. This objection has been counterbalanced, at least from the experimental side, by the results of Schubauer and Skramstad[2] which confirm in detail the theoretical predictions, based upon the local flow, in the case of the boundary layer over a flat plate.

On the question of unsteady "mean" flow, no systematic investigation seems to exist in the literature. In estimating the transition Reynolds number of the flow between rotating cylinders, Schlichting[3] applied the laminar stability theory for transverse-wave (Tollmien-type) disturbances to the instantaneous profiles

Presented at The Hypersonic Flow Theory Session, IAS 28th Annual Meeting, New York, January 25–27, 1960.

† The work reported was sponsored by the U.S. Bureau of Naval Weapons.

* Consultant, and Professor of Aeronautical Engineering, University of Maryland.

taken when the outer cylinder is suddenly set into motion. The minimum critical Reynolds number based upon the displacement thickness turned out to be about one third of the experimental transition Reynolds number. Since one can usually rely on the stability theory only for qualitative trends of transition, Schlichting regarded the agreement to be as close as might be expected. However, the probable effect of unsteadiness of the mean flow was left completely untouched. More recently, two experimental observations of the generation of the vortices of the transverse-wave type in decelerating flow have come forward. Fales[4] demonstrated this phenomenon by gradually stopping a moving flat plate in a water tank. The slowing down of the laminar boundary layer caused distinct transverse vortices to appear, made visible by coloring the fluid with dye. Coles,[5] in a series of observations of the Taylor stability of the flow between rotating cylinders, included a start-stop operation of the outer cylinder alone. As in the boundary-layer case, after the outer cylinder was stopped, vortices with axes parallel to the circular cylinders were shown to form, to parade and to grow in intensity before eventually bursting into turbulence. The only theoretical attempt to explain this phenomenon of vortex creation by deceleration, to the author's knowledge, was that due to von Kármán and Lin[6] on Fales' experiment. They noted that the instantaneous velocity profile of the boundary layer after the plate was stopped should resemble that of a free-convection boundary layer. The presence of a point of inflection of the velocity profile suggests that the profile should be quite unstable with respect to the transverse-wave disturbances. To support the explanation, a calculation of the critical Reynolds number of such a velocity profile was carried out by use of the standard theory. Under conditions typical of Fales' experiment, the comparison was shown to be qualitatively satisfactory. Still, the emphasis was on the shape of the instantaneous velocity profile alone, so that these authors, like Schlichting, implied the validity of the quasi-steady approach. To be stressed is the fact that thus far no detailed comparisons have been made of the behaviors of the disturbances in an unsteady basic flow with those in a steady basic flow, such as were provided by Schubauer and Skramstad in the case of slightly nonparallel (boundary-layer) flow over a flat plate. A more critical examination of the disturbances in an unsteady basic flow appears to be of fundamental interest, even if from the theoretical viewpoint only.

The present paper represents a step in this direction. In the first place, the criterion for laminar stability of an unsteady basic flow requires some modification from that of the usual steady basic flow. It is proposed to adopt the concept of "momentary stability" in dealing with time-dependent basic flows; such stability is said to prevail when the disturbances tend to become less disturbing at a given instant. The concept of "momentary stability," of course, is a weakened version of the usual concept of stability of a steady mean flow, which requires the distu bances to vanish as $t \to \infty$. The more restrictive definition is necessary since within the period of interest the unsteady basic flow never attains a condition of $t \to \infty$. Furthermore, as the basic flow is changing with time, a disturbance tends to be unstable only if it grows more rapidly than the basic flow. It is proposed to measure the disturbance on the basis of the ratio of the kinetic energy of the perturbations to that of the mean flow, both averaged throughout the boundary-layer thickness and over a wavelength.

The physical model to be investigated is an incompressible, parallel but unsteady basic flow, upon which are superposed two-dimensional infinitesimal perturbations of the transverse-wave type.† The general discussions are centered around a special "similar" basic flow which preserves the velocity profile except for a time-dependent magnitude. The advantage of the special flow is that it permits a transformation of the time scale in the inviscid limit, so that the perturbation equation may be reduced to the same form as for a steady basic flow. Deceleration is found to have an almost overwhelming destabilizing influence regardless of the shape of the velocity profile. Fales' and Coles' experiments should perhaps be explained from this viewpoint rather than on the basis of any quasi-steady consideration.

The quasi-steady method of calculation turns out to be acceptable only for extremely small acceleration or deceleration—the time constant of the basic flow must be much greater than $Re^{1/2}$ times the characteristic time of the disturbances. Even then the quasi-steady "neutral curve" cannot be accepted at face value with regard to its significance for stability.

A formulation of the procedure for calculating the "momentary stability" boundary of slowly changing but otherwise completely arbitrary basic flows is outlined briefly. Essentially, the eigenvalue problem is taken as identical with the quasi-steady approach, but a time-dependent part of the "mode" is determined. With the time-dependent mode, the momentary stability or instability of, say, points corresponding to the quasi-steady neutral curve may be determined.

It should, perhaps, be noted that investigations in this paper are directed only toward the types of disturbances normally considered for steady basic flows. Whether other types of disturbances may not also be of importance for unsteady basic flows is a question that is left completely open.

The Momentary Stability Concept and the Growth Rate Criterion

Let us first recall the classical stability theory for a steady, two-dimensional, parallel basic flow. The fundamental linearized differential equation for two-dimensional disturbances superposed on the steady velocity profile $U(y)$ is

† Needless to say, little basic difference should be encountered in dealing with disturbances of the longitudinal-vortex ("Taylor-Görtler") type.

$$\frac{\partial}{\partial t}\nabla^2\Psi + U\frac{\partial}{\partial x}\nabla^2\Psi - U''\frac{\partial\Psi}{\partial x} = \nu\nabla^2\nabla^2\Psi \qquad (1)$$

Here Ψ is the disturbance stream function such that the disturbance velocity components (u, v) in the x-direction (downstream) and the y-direction (normal to the flow) are given by

$$u = \partial\Psi/\partial y, \qquad v = -\partial\Psi/\partial x$$

The boundary conditions on u and v are homogeneous and apply at the extreme values of y. Thus, the problem is defined independently of the x- and t-coordinates, and one is led to assume the elementary solutions

$$\Psi = e^{i\alpha(x-ct)}\,\Phi(y) \qquad (2)$$

with the constant α real and the constant c possibly complex. The homogeneous boundary conditions now are prescribed for $\Phi(y)$, so that an eigenvalue problem results. The equation for Φ is the well-known Orr-Sommerfeld equation[2]

$$(\Phi'' - \alpha^2\Phi)(U - c) - U''\Phi = (1/i\alpha Re)[\Phi'''' - 2\alpha^2\Phi'' + \alpha^4\Phi] \qquad (3)$$

where Re is the Reynolds number, the reference velocity and the reference length being both taken as unity. For given Reynolds number Re and wave number α, one gets the eigenvalue c. The disturbance will be either amplified without bound as the time $t \to \infty$, or eventually damped out, depending on the sign of the imaginary part of the eigenvalue c.

The above résumé of the usual theory for steady basic flow has been presented in order to draw contrast to the present case of interest. For the unsteady parallel basic flow, the fundamental equation, Eq. (1), remains unchanged even though $U = U(y, t)$. Furthermore, let the boundary conditions remain homogeneous and prescribed at the extreme points of y. While it is still reasonable to assume solutions which are periodic in x, the time-dependence becomes a different matter. In this case the assumed elementary solution, analogous to Eq. (2), is given by:

$$\Psi = e^{i\alpha x}\,\Psi_1(y, t) \qquad (4)$$

so that $u = e^{i\alpha x}(\partial\Psi_1/\partial y)$
$v = -i\alpha e^{i\alpha x}\Psi_1$

For given Re and α, an eigenfunction $\Psi_1(y, t, \alpha, Re)$ is defined. It is necessary, however, to determine which values of α and Re represent a "stable" solution.

One must now reflect on what is meant by "stable" in discussing the possible disturbances represented by a given solution $\Psi_1(y, t, \alpha, Re)$. It is obvious that the asymptotic behavior of the disturbances as $t \to \infty$ is no longer meaningful. In the first place, in considering unsteady basic flow it is already implied that behavior at finite time is of primary interest. In fact, the unsteady basic flow $U(y, t)$ may be described only for finite times. Even if the velocity does have a limiting profile $U(y, \infty)$, the analysis for behavior as $t \to \infty$ would reduce to an examination of the profile $U(y, \infty)$ by the usual formulation for the steady basic flows. The result would be significant, however, only if the prescribed unsteady basic flow is maintained in spite of all the disturbances at all times prior to the establishment of the limiting flow $U(y, \infty)$. Consequently, one must have some idea of how the basic flow is being distorted by the given disturbance $\Psi_1(y, t, \alpha, Re)$ at every instant. As a matter of fact, for unsteady basic flows, the tendency toward stability or instability at any moment is all that can be stated definitely.

As the ultimate goal of the laminar stability theory lies in its possible correlation with the laminar-turbulent transition phenomenon, it is recognized that logically the increase or decrease of a disturbance should be measured only by a comparison with the basic flow itself. If the disturbance is decreasing but the basic flow is decreasing at a faster rate, the disturbance relative to the basic flow would appear amplified at a later instant. Conversely, if the disturbance increases but the basic flow increases even more rapidly, then the disturbance would appear to be decaying. From such elementary considerations a yardstick for measuring the disturbances immediately suggests itself.* First form the ratio of the instantaneous kinetic energy of the disturbance to that of the basic flow, both averaged over one wavelength in the x-direction and throughout the thickness in the y-direction. The time rate of change of this ratio then indicates whether the relative kinetic energy of the disturbance is increasing or decreasing at any instant. The energy ratio is given by

$$E(t) = \int_0^\delta\int_0^\lambda (u^2 + v^2)dxdy \Big/ \lambda\int_0^\delta U_0 dy \qquad (5)$$

Then for convenience one may define a "growth rate"

$$G_r \equiv (1/2E)(dE/dt)$$

and use it as the criterion for the "momentary stability or instability" of the basic flow. If $G_r > 0$, the disturbances are increasing, relatively at the moment, and therefore the flow may be said to be momentarily instable, whereas if $G_r < 0$ the flow may be said to be momentarily stable. The term stability is thus used in a special sense, reflecting only the tendency of the basic flow to become more and more, or less and less, distorted. For the steady case, however, the "growth rate" G_r reduces to the amplification rate of the disturbances in the usual theory.

What must be emphasized here is that the momentary stability defined on the basis of the growth rate carries a more ambiguous significance in its probable correlation with transition than does stability as defined in the usual sense (instability for unbounded disturbance as $t \to \infty$) for the steady basic flow. For the latter, although the mechanism of transition is not yet fully clear, it is quite evident that conditions will change as the disturbance keeps on growing, and that even-

* The same yardstick has been used previously by Lin[3] in discussing the stability of the decaying turbulence spectrum. In a private communication to the author, Prof. Lin suggested that others might have used it under other circumstances. It certainly is a very natural, intuitive choice.

tually turbulent effects must appear. However, for unsteady basic flow, the "growth rate" indicates no more than a tendency. To illustrate, suppose that the "growth rate" is first positive (implying unstable disturbances, according to the definition) and then negative. As the disturbance becomes more and more pronounced during the time interval of "instability," does this mean that turbulence will set in during this interval? If turbulence sets in, it is not certain that the flow may become laminar again at some later time, even if the "growth rate" calculated on the basis of the original laminar basic flow is, say, moderately negative. If turbulence does not set in, then the flow remains laminar in spite of the unstable period, since the disturbance will again be smoothed out in the later stable period. Therefore, in such cases the significance of the "unstable" period is rather uncertain. The question obviously is identical, in a way, with the difficulty of predicting the transition point for a steady basic flow, and can only be answered when the mechanism of transition is more clearly understood. In fact, a quantitative criterion of transition will be needed. When a theory to predict *the* transition point for steady basic flow is established, then and only then will it be possible to calculate the transition for unsteady basic flow according to the concept of "momentary stability" as proposed here. Otherwise one cannot say as much about the unsteady case as about the steady case. Whether transition will or will not follow at a later time can be answered only in special cases by examining the "momentary stability" of the basic flow. However, on the basis of the (momentary) stability criterion as discussed above, it will at least be possible to interpret the solution of Eq. (4) (assuming that a solution can be found) for every given α and Re. The procedure for solution is more tedious than for the steady case in that one must calculate not only the eigenvalue but also the eigenfunction itself, in order to evaluate the "growth rate" from Eq. (5). Then, if the basic flow is "momentarily unstable" for given α, Re, and for all $t > t_1$, the basic flow will be "unstable" for $t > t_1$, although transition will have to come at an even later time. On the other hand, if for $Re < R_{cr}$, G_τ is less than zero for all $\alpha > 0$ and all t, then Re_{cr} will be the minimum critical Reynolds number for the unsteady $U(y, t)$ concerned, in the same sense as for a steady flow. These are two examples for which at least the sufficient condition for stability can be written down by adopting the viewpoint of this paper.

Even before actually determining the solution, one is led to suspect that accelerating flows very probably would have higher critical Reynolds numbers than those estimated on the basis of the instantaneous velocity distribution, and that the reverse would be true for decelerating flows. At least for nearly steady flows, when the time constant of the basic flow is much longer than the period of the wave disturbance, it seems permissible to calculate the disturbance solution on the assumption that the instantaneous basic flow will persist forever. Such was, of course, the procedure used by Schlichting[3] in his calculation of the critical Reynolds number for instantaneous profiles of the flow between rotating cylinders following the sudden start of the outer cylinder. In this case, the reference velocity (that at the outside cylinder wall) is constant, and the disturbance amplitude and hence its kinetic energy would temporarily remain constant along the neutral curve determined by the quasi-steady procedure, while the kinetic energy of the basic flow evidently increases with time. According to the viewpoint of the present paper, these quasi-steady neutral disturbances must actually be regarded as decaying relative to the accelerating basic flow. In fact the argument is even stronger than suggested by the reasoning applied to Schlichting's example. To clarify the point, consider the special basic flow

$$U = T(t/t_0)\,U^*(y) \tag{6}$$

where t_0 is the time constant. The velocity profiles are now identical at different times except for the scale factor T. By the quasi-steady procedure, the instantaneous profile would be $TU^*(y)$ and the neutral disturbances would have amplitudes proportional to T. It would then appear that the energy ratio E, Eq. (5), would be independent of time along the quasi-steady neutral curve. The latter would seem thereby to satisfy the condition for neutral momentary stability regardless of whether T represents an accelerating or decelerating flow. The following closer examination shows, however, that such a conclusion is erroneous—the accelerating flow would actually remain stable for the quasi-steady neutral disturbances.

Analysis of a Special Unsteady Flow

For simplicity, let us first analyze the special unsteady basic flow, Eq. (6). Following the classical theory, we may first adopt the "inviscid" approximation to obtain some information regarding the behavior of the disturbances. Such information is valid as $Re \to \infty$ and often can guide the treatment for finite Reynolds number. To determine the "viscous" solution at finite Reynolds number, however, is rather difficult for the type of profile considered. Nevertheless, the limitations of the quasi-steady approach can be checked without much complication.

(1) *The Inviscid Approximation*

Consider now the abbreviated equation obtained by dropping the viscous terms from Eq. (1):

$$\frac{\partial}{\partial t}\nabla^2\Psi + U\frac{\partial}{\partial x}\nabla^2\Psi - \frac{\partial^2 U}{\partial y^2}\frac{\partial \Psi}{\partial x} = 0 \tag{7}$$

where $U = U(y,t)$. For the special flow

$$U = T(t/t_0)\,U^*(y)$$

the mathematical problem thus defined can be reduced to the classical inviscid equation by a transformation which is essentially a stretching of the time variable. That is, if

$$\tau = t_0 \int T(t/t_0)\, d(t/t_0) \tag{8}$$

then Ψ satisfies

$$\frac{\partial}{\partial \tau}\nabla^2\Psi + U^*(y)\frac{\partial}{\partial x}\nabla^2\Psi - U^{*\prime\prime}(y)\frac{\partial \Psi}{\partial x} = 0 \quad (9)$$

an equation which is identical in appearance to the classical steady case, except that τ replaces t. One can immediately borrow the classical solution for $U^*(y)$ and the corresponding boundary conditions, and write

$$\Psi = e^{i\alpha(x-c\tau)}\,\Phi(y) \quad (10)$$

Therefore the eigenvalue c for a given α as $Re \to \infty$ is the same as that in the classical case with the distribution $U^*(y)$.†

In this special type of the basic flow, the "growth rate" may be defined in a simpler manner, since the time dependence appears only as a separate factor, in both the functions U and Ψ. Thus one may take the energy ratio equivalent to Eq. (5) as

$$E = \text{const.} \times (e^{\alpha c_i \tau}/T)^2 \quad (11)$$

and the growth rate is given by

$$G_\tau = \alpha c_i T - (T'/T)(1/t_0) \quad (12)$$

T' being the derivative of T with respect to t/t_0. Consequently, $G_\tau < 0$ if

$$\alpha c_i < (T'/T^2)(1/t_0) \quad (13)$$

It is seen that for truly "neutral" disturbances, determined by $G_\tau = 0$, αc_i will indeed be proportional to T' (which is positive for accelerating flow and negative for decelerating flow) and inversely proportional to the time constant of the basic flow. (It is trivial to show that the same time-scale stretching, Eq. (8), works also for the inviscid case in the stability of disturbances of the Taylor-Görtler type for flows over a curved surface.) Since for the basic flow [Eq. (6)]

$$(1/U)(\partial U/\partial t) = (T'/T)(1/t_0) \quad (14)$$

a more explicit form of Eq. (13) is

$$\alpha\,\tilde{c}_i < (1/U)(\partial U/\partial t) \quad (15)$$

where $\tilde{c}_i = c_i T$. The quantity $\alpha\tilde{c}_i$ clearly represents the amplification rate as computed by the quasi-steady procedure, the factor T entering here because of the change of the reference velocity with time. In other words, for the special profile Eq. (6), one may in the inviscid limit *calculate* the eigenvalue c for a given α by the quasi-steady procedure, but the "momentary stability" is *not* given by the neutral disturbances so obtained. The acceleration or deceleration has a very profound effect. With accelerating flow, c_i can be positive and the disturbance will remain "momentarily stable." With decelerating flow, c_i has to be sufficiently negative to maintain such stability.

The experience with available computed results for steady parallel flows suggests that generally the quantity αc_i in the unstable region of the stability diagram

† Note that the quasi-steady procedure is obviously inapplicable in this special case, since, by Eq. (10), the disturbance amplitudes are *not* proportional to T.

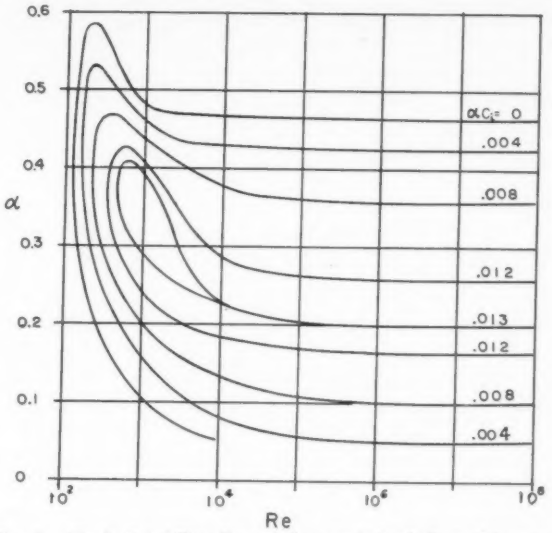

FIG. 1. Typical stability diagram for steady basic flow with pressure gradient.

is rather small, say, of the order of 10^{-3}. Thus, as a rule of thumb, when the time constant of the changing basic flow is much shorter than $10^3 \times$ (reference length/reference velocity of the basic flow), an accelerating flow will probably be always momentarily stable and a decelerating flow (if the Reynolds number is not too small) always momentarily unstable—whatever the velocity distribution may be.

To illustrate this point further, a typical stability diagram including contours of constant amplification rates, as calculated by Pretsch,[9] is presented as Fig. 1. The velocity distribution corresponds to one of the Falkner-Skan profiles with adverse pressure gradient. Suppose now in an unsteady basic flow one has the same spatial velocity distribution but a time dependence of

$$T = e^{\beta t}$$

The condition for neutral momentary stability, in the inviscid limit, is then

$$\alpha c_i = \beta e^{-\beta t}$$

An accelerating flow will have $\beta > 0$, and the time constant t_0 will be simply $1/\beta$. An examination of the asymptotic behavior (at large Reynolds numbers) in Fig. 1 shows that up to the time $\beta t \sim 0(1)$ no disturbance is unstable enough to be disruptive if $\beta \geq 0.013$. Up to such a time, therefore the basic flow would be completely stable.† The case of decelerating flows may be discussed in a similar fashion; the conclusion is naturally in the opposite direction. Although these results are derived strictly only for the special flow of Eq. (6), the criterion in the form of Eq. (15) might be of qualitative significance even for more general flows.

A corollary may also be drawn regarding the pro-

† Of course, inviscid consideration will not determine whether at finite Reynolds numbers there might not be an imbedded instable region, according to the concept of momentary stability.

file shape $U^*(y)$: The existence of a point of inflection in $U^*(y)$ is much less significant for the stability, at infinite Reynolds number, of accelerating or decelerating flows. In the accelerating case, the inflection point is necessary for instability but not sufficient, whereas in the deceleration case it is sufficient for instability but not necessary.

(2) *A Critical Examination of the Quasi-Steady Approach*

To determine the minimum critical Reynolds number according to the concept of "momentary stability," the full Eq. (1), including the kinematic viscosity ν, must be considered. It seems clear right from the beginning that the special case

$$U = T(t/t_0)U^*(y)$$

which permits a stretching of the time scale to reduce the inviscid differential equation to the classical form, no longer has the same advantage at finite Reynolds numbers. However, it is convenient to use it as an example to demonstrate the restrictions of the quasi-steady approach. Consider the complete viscous form of Eq. (9):

$$(\partial/\partial\tau)\nabla^2\Psi + U^*(y)(\partial/\partial x)\nabla^2\Psi - U^{*\prime\prime}(\partial\Psi/\partial x) = (\nu/T)\nabla^2\nabla^2\Psi \quad (16)$$

One sees qualitatively, besides the time-stretching (with τ replacing t), that the *effective* Reynolds number with

$$\nu_{\text{eff.}} = \nu/T$$

will vary with time. Now let us follow the steps of a quasi-steady approach. Guided by the inviscid solutions for Eq. (9), we may postulate the solution of Eq. (16) in the form:

$$\Psi = e^{i\alpha(x-c\tau)}\,\Phi(y, \tau) \quad (17)$$

The equation for Φ reads

$$(\partial/\partial\tau)\nabla^2\Phi + i\alpha[(U^* - c)\nabla^2\Phi - U^{*\prime\prime}\Phi] = (\nu/T)\nabla^2\nabla^2\Phi \quad (18)$$

with $\nabla^2 \equiv (\partial^2/\partial y^2) - \alpha^2$. Now for the viscous solutions, we may use the same classical arguments, focusing attention near the critical layer $y = y_c$ where $U^* - c = 0$ (see reference 7), thus Eq. (18) is simplified to

$$(\partial/\partial\tau)\nabla^2\Phi + i\alpha(U^* - c)\nabla^2\Phi \cong (\nu/T)\nabla^2\nabla^2\Phi$$

In the neighborhood of the critical layer, however, a transformation may be used to magnify the y-direction in the standard manner:

$$\zeta = (y - y_c)(\alpha U_c^{*\prime}/\nu_{\text{eff.}})^{1/3} \quad (19)$$

Hence the differential equation becomes

$$\nu_{\text{eff.}}{}^{-1/3}(\alpha U_c^{*\prime})^{-2/3}(\partial/\partial\tau)\nabla^2\Phi + i\zeta\nabla^2\Phi = (\partial^2/\partial\zeta^2)\nabla^2\Phi \quad (20)$$

If the term in $\partial/\partial\tau$ on the left-hand side is omitted, the solutions are known to be

$$\nabla^2\Phi = \sqrt{\zeta}\,H_{1/3}^{(1),\,(2)}[2/3(i\zeta)^{3/2}] + 0(\nu_{\text{eff.}}/\alpha U_0^{*\prime})^{1/3} \quad (21)$$

as long as c_i is small. From Eq. (21) an estimate of $(\partial/\partial\tau)\nabla^2\Phi$ may be made:

$$\frac{\partial}{\partial\tau}\nabla^2\Phi = \frac{\partial \ln \zeta}{\partial\tau}\left[\zeta\frac{\partial}{\partial\zeta}\nabla^2\Phi\right]$$

But

$$\frac{\partial}{\partial\tau}\ln\zeta = {}^1/_3\,\frac{1}{T}\frac{dT}{d\tau} = {}^1/_3\,\frac{dT}{dt}\frac{1}{T^2}$$

so that the first term of Eq. (20) is negligible only if

$$\frac{1}{3}\frac{T'}{T^{5/3}}\frac{1}{t_0} \ll \nu^{1/3}(\alpha U_0^{*\prime})^{2/3} \quad (22)$$

Again, since in this special case

$$\frac{1}{U}\frac{\partial U}{\partial t} = \frac{T'}{T}\frac{1}{t_0}$$

Eq. (22) may be rewritten in *dimensional* form as

$$\frac{1}{U}\frac{\partial U}{\partial t} \ll 3\nu^{1/3}\left(\alpha\,\frac{\partial U_c}{\partial y}\right)^{2/3} \quad (23)$$

Now let

U_m = maximum value of the instantaneous velocity distribution

Re = Reynolds number based upon the instantaneous value U_m and the thickness δ

Then a more convenient version of Eq. (23) is

$$(U_m t_0/\delta)^{-1} \ll (\alpha\delta)^{2/3}\,Re^{-1/3} \quad (24)$$

as long as $(\partial U_c/\partial y) \sim 0(U_m/\delta)$. Physically, the left-hand side represents the ratio of the characteristic time δ/U_m for the disturbances to the characteristic time t_0 of the basic flow. If we calculate the neutral curve by the quasi-steady procedure, we find that $\alpha\delta \sim 0(1)$ near the minimum critical Reynolds number, and that the ratio $\delta/U_m t_0$ has to be less than $0(Re^{-1/3})$ to justify the *solution*. In addition, it may be recalled that ordinarily the amplification rate αc_i in the unstable region of the quasi-steady stability diagram is, very roughly speaking, smaller than $0(Re^{-1/3})$ near the minimum critical Reynolds number (e.g., see Fig. 1). The disturbances calculated by the quasi-steady procedure thus would amplify or decay at a rate probably comparable to the rate of change of the basic flow that satisfies Eq. (23). From this consideration, even if Eq. (23) is satisfied one still cannot justify the use of the quasi-steady procedure alone to predict the minimum critical Reynolds number for momentary stability. The "growth rate" remains the criterion for such purposes. Even the neutral curve derived from the quasi-steady procedure seems to be of very limited significance in dealing with unsteady basic flows.

Analysis of the Momentary Stability of Slowly Varying Profiles

While illuminating, the special profile $U = T(t/t_0)U^*(y)$ is too restrictive for most actual applica-

tions. Furthermore, the stretching of the time scale, by Eq. (8), is no longer helpful when finite Reynolds numbers must be considered. Therefore, a slowly varying general profile will now be examined:

$$U(y, t) = U^{(0)}(y) + \epsilon T_1(t/t_0)U^{(1)}(y) + \ldots \quad (25)$$

ϵ being a small constant parameter. The solution Ψ will be developed in ascending powers of ϵ,

$$\Psi = \Psi^{(0)}(x, y, t) + \epsilon\Psi^{(1)}(x, y, t) + \ldots \quad (26)$$

It is then necessary to solve for the perturbation $\Psi^{(1)}$ for given α, Re, noting that $\Psi^{(0)}$ should be the classical solution for $U^{(0)}(y)$. Upon substituting Eq. (25) into Eq. (1) and equating terms of order ϵ, there results

$$\frac{\partial}{\partial t}\nabla^2\Psi^{(1)} + U^{(0)}\frac{\partial}{\partial x}\nabla^2\Psi^{(1)} - U^{(0)\prime\prime}\frac{\partial\Psi^{(1)}}{\partial x} - \nu\nabla^2\nabla^2\Psi^{(1)} = -T_1\left[U^{(1)}\frac{\partial}{\partial x}\nabla^2\Psi^{(0)} - U^{(1)\prime\prime}\frac{\partial}{\partial x}\Psi^{(0)}\right] \quad (27)$$

A particular $T_1\,(t/t_0)$ convenient for treatment is

$$T_1 = e^{\beta t} \quad (28)$$

for which it is possible to take

$$\Psi^{(1)} = e^{\beta t}\Psi_*{}^{(1)}(x, y, t) \quad (29)$$

The equation for $\Psi_*{}^{(1)}$ becomes, upon substitution of Eqs. (28) and (29) into Eq. (27),

$$\left(\beta + \frac{\partial}{\partial t}\right)\nabla^2\Psi_*{}^{(1)} + U^{(0)}\frac{\partial}{\partial x}\nabla^2\Psi_*{}^{(1)} - U^{(0)\prime\prime}\frac{\partial\Psi_*{}^{(1)}}{\partial x} - \nu\nabla^2\nabla^2\Psi^{(1)} = -U^{(1)}\frac{\partial}{\partial x}\nabla^2\Psi^{(0)} + U^{(1)\prime\prime}\frac{\partial}{\partial x}\Psi^{(0)} \quad (30)$$

Let $\Psi^{(0)} = e^{i\alpha(x-ct)}\,\Phi^{(0)}(y)$

Then one may take

$$\Psi_*{}^{(1)} = e^{i\alpha(x-ct)}\,\Phi_*{}^{(1)}(y) \quad (31)$$

so that Eq. (30) reduces to

$$\left[U^{(0)} - \left(c + i\frac{\beta}{\alpha}\right)\right]\left[\frac{d^2}{dy^2} - \alpha^2\right]\Phi_*{}^{(1)} - U^{(0)\prime\prime}\Phi_*{}^{(1)} - \frac{\nu}{i\alpha}\left[\frac{d^2}{dy^2} - \alpha^2\right]^2\Phi_*{}^{(1)} = -U^{(1)}\left[\frac{d^2}{dy^2} - \alpha^2\right]\Phi^{(0)} + U^{(1)\prime\prime}\Phi^{(0)} \quad (32)$$

One recognizes the left-hand side of Eq. (32) as identical with the equation which determines the classical solution $\Phi^{(0)}$ for $U^{(0)}(y)$, except for the term $i(\beta/\alpha)$ added to the wave velocity c. In addition, there are the inhomogeneous terms on the right-hand side depending on $U^{(1)}$ and $\Phi^{(0)}$. Let the boundary conditions on $\Phi_*{}^{(1)}$ remain homogeneous and independent of time t.† Then the solution of $\Phi_*{}^{(1)}$ from Eq. (32) follows the classical procedure for the solution $\Phi^{(0)}$, the inhomogeneous terms on the right-hand side introducing a particular solution obtainable by quadrature.

Little need be said about the inviscid approximation (obtained by dropping the viscous term). As a particular example, suppose $U^{(1)} = U^{(0)}$, i.e.,

$$U = (1 + \epsilon e^{\beta t})U^{(0)}(y)$$

hence the time-stretching transformation [Eq. (8)] may be used as a check. It is easily verified that the inviscid solution for Eq. (32), if the boundary conditions permit, is simply

$$\Phi_*{}^{(1)} = -ic(\alpha/\beta)\Phi^{(0)} \quad (33)$$

One has, therefore, to $0(\epsilon)$,

$$\Psi = e^{i\alpha(x-ct)}\,[1 + \epsilon(i\alpha c/\beta)e^{\beta t}]\Phi^{(0)} \quad (34)$$

On the other hand, the earlier method gives

$$\Psi = e^{i\alpha(x-c\tau)}\,\Phi^{(0)}$$

with

$$\tau = t_0\int(1 + \epsilon e^{\beta t})d(t/t_0) = t + \frac{\epsilon}{\beta}e^{\beta t}$$

Developing $e^{-i\alpha c\tau}$ for small ϵ, one obtains again Eq. (34).

For the viscous solution, as long as β/α is small (of order $\nu^{1/3}$), one may focus attention near the critical point $y = y_c$ in the usual manner. Eq. (32) is thus reduced to

$$\left[U^{(0)} - \left(c + i\frac{\beta}{\alpha}\right)\right]\frac{d^2\Phi_*{}^{(1)}}{dy^2} - \frac{\nu}{i\alpha}\frac{d^4\Phi_*{}^{(1)}}{dy^4} \cong -U^{(1)}\frac{d^2\Phi^{(0)}}{dy^2} \quad (35)$$

where $\Phi^{(0)}$ is the viscous solution for the profile $U^{(0)}(y)$ by the classical theory. For points near the quasi-steady neutral curve pertaining to $U^{(0)}(y)$,

$$\Phi^{(0)} = \Phi^{(0)}(\zeta), \quad \zeta = (y - y_c)(\alpha U_c{}^{(0)\prime}/\nu)^{1/3} \quad (36)$$

The perturbation $\Phi_*{}^{(1)}$ in such cases may be solved from

$$(d^2/d\zeta^2)\Phi_*{}^{(1)\prime\prime} - i(\zeta - \zeta_1)\Phi_*{}^{(1)\prime\prime} \cong i[(\alpha U_c{}^{(0)\prime}/\nu)^{1/3} \times U_c{}^{(1)}/U_c{}^{(0)\prime} + \zeta(U_c{}^{(1)\prime}/U_c{}^{(0)\prime})]\Phi^{(6)\prime\prime} \quad (37)$$

where $\zeta_1 = i(\beta/\nu)(\alpha U_c{}^{(0)\prime}/\nu)^{-2/3}$

$U_c{}^{(0)\prime}$, $U_c{}^{(1)}$, $U_c{}^{(1)\prime}$ are values of $dU^{(0)}/dy$, $U^{(1)}$, $dU^{(1)}/dy$, respectively, at $y = y_c$ and the primes indicate differentiation with respect to y. The solution $\Phi_*{}^{(1)\prime\prime}$, and hence $\Phi_*{}^{(1)}$, are thus obtainable by quadrature. In fact, if one puts

$$\Phi_*{}^{(1)\prime\prime} = -iU_c{}^{(1)}(\alpha/\beta)\Phi^{(6)\prime\prime} + \nabla\Phi_*{}^{(1)\prime\prime} \quad (38)$$

then $\Delta\Phi_*{}^{(1)\prime\prime}$ satisfies the following:

$$(d^2/d\zeta^2)\Delta\Phi_*{}^{(1)\prime\prime} - i(\zeta - \zeta_1)\Delta\Phi_*{}^{(1)\prime\prime} = i\zeta(U_c{}^{(1)\prime}/U_c{}^{(0)\prime}\Phi^{(6)\prime} \quad (39)$$

Hence even for $U^{(1)} = U^{(0)}$—i.e., for similar profiles described by Eq. (6)—there remains the solution $\Delta\Phi_*{}^{(1)}$ which cannot be absorbed by the scale-stretching transformation. It may be recalled that the viscous

† Thus the boundary itself must also be independent of time so that the conclusion following would not be applicable to boundary layers with rapidly changing thickness.

solutions are important for flows with a solid boundary which usually lies at a finite value of ζ from the critical point. The influence of $\Delta\Phi_*^{(1)}$ under these circumstances is not likely to be trivial.

The procedure for the solution of the disturbance may now be summarized as follows. First, the two inviscid and two viscous solutions of $\Phi^{(0)}$ are the classical ones for the prescribed $U^{(0)}(y)$. Given α, Re, and the boundary conditions, the eigenvalue c and the eigenfunction $\Phi_e^{(0)}$ are then determined. These are to be put into Eq. (32) together with the given β and $U^{(1)}$, and the solution $\Phi_e^{(1)}$ is now uniquely determined by the boundary conditions. In practice one may again prefer to handle the calculation by splitting it into the inviscid and viscous solutions as discussed above. At any rate, the disturbance

$$\Psi = e^{i\alpha(x-ct)}[\Phi_e^{(0)} + \epsilon^{\beta t}\Phi_e^{(1)}]$$

is thus completely determined except for the amplitude which is arbitrary in the linear theory.

To assess the momentary stability at various times, the growth rate must be calculated. By definition,

$$\left.\begin{aligned} u &= \partial\Psi/\partial y = \text{Real}\{e^{i\alpha(x-ct)}(\partial\Phi_e/\partial y)\} \\ v &= \partial\Psi/\partial y = \text{Real}\{-i\alpha e^{i\alpha(x-ct)}\Phi_e\} \end{aligned}\right\} \quad (40)$$

where $\Phi_e = \Phi_e^{(0)} + \epsilon e^{\beta t}\Phi_e^{(1)}$ is the eigenfunction. Thus, with subscripts R and I denoting real and imaginary parts, respectively,

$$u^2 = (e^{-i\alpha ct}\Phi_e')\big|_R^2 \cos^2\alpha x - (e^{-i\alpha ct}\Phi_e')_R (e^{-i\alpha ct}\Phi_e')_I \cdot \sin 2\alpha x + (e^{-i\alpha ct}\Phi_e')_I^2 \sin^2\alpha x$$

Hence, since the integration is to be taken over one wavelength,

$$\iint u^2 dx\,dy = \frac{\lambda}{2} e^{2\alpha c_i t}\int |\Phi_e'|^2\,dy$$

where c_i is the imaginary part of c. In a similar way one can evaluate

$$\iint v^2 dx\,dy$$

Finally,

$$E = (e^{2\alpha c_i t}/2)\int[|\Phi_e'|^2 + \alpha^2|\Phi_e|^2]dy \Big/ \int[U^{(0)} + \epsilon T_1 U^{(1)}]^2 dy = (e^{2\alpha c_i t}/2)E_0(1 + 2\epsilon E_1 T_1) + 0(\epsilon^2) \quad (41)$$

where

$$E_0 = \int[|\Phi_e^{(0)\prime}|^2 + \alpha^2|\Phi_e^{(0)}|^2]dy \Big/ \int (U^{(0)})^2 dy$$

$$E_1 = \text{Real}\left\{\frac{\int[\Phi_e^{(0)\prime}\Phi_e^{(1)\prime} + \alpha^2\Phi_e^{(0)}\Phi_e^{(1)}]dy}{\int[|\Phi_e^{(0)\prime}|^2 + \alpha^2|\Phi_e^{(0)}|^2]dy} - \frac{\int U^{(0)}U^{(1)}dy}{(U^{(0)})^2 dy}\right\} \quad (42)$$

Differentiating, one gets

$$G_r \equiv (1/2E)(dE/dt) \cong \alpha c_i + \epsilon\beta T_1 E_1 \quad (43)$$

Thus

$$G_r \gtreqless 0 \text{ as } \alpha c_i \gtreqless -\epsilon\beta T_1 E_1 \quad (44)$$

For the special case $U^{(1)} = U^{(0)}$ and in the inviscid limit, Eq. (24) holds. The function E_1 turns out to be

$$E_1 = k - 1 \quad (45)$$

with $k = -\alpha c_i/\beta$. It is easy to verify that the criterion Eq. (44) is identical to the previous one, Eq. (13), when both are applicable.

Concluding Remarks

(1) In extending the usual stability theory for infinitesimal disturbances to time-dependent basic flows, one must modify the criterion of stability. It is proposed to introduce a concept of "momentary stability," which is said to prevail at the instant if the kinetic energy of the disturbances, as a fraction of the kinetic energy of the basic flow, tends to decrease. The time rate of change of the kinetic energy ratio is essentially what is termed the "growth rate" in this paper. The "growth rate" is so defined that it coincides with the amplification rate in the case of steady flows.

(2) It is more difficult to correlate the time history of the momentary stability of a time-dependent basic flow to the laminar-turbulent transition phenomenon. For instance, the significance of an interim period of momentary instability, followed by momentary stability, is rather obscure. Only if the flow turns out to be always momentarily unstable after a certain instant, may one infer that transition to turbulence must occur sooner or later after that instant. Likewise, a minimum critical Reynolds number can be defined if the basic flow is always momentarily stable, for disturbances of any wavelength, below the particular Reynolds number.

(3) The Orr-Sommerfeld equation for disturbances in an incompressible, parallel but time-dependent basic flow is examined. In the inviscid limit and for basic flows of the type

$$U(y, t) = T(t/t_0)U^*(y)$$

the disturbance equation is reduced to a form identical with that for the usual steady flow, after a stretching of the time scale. The conclusion is that momentary stability will prevail if

$$\alpha\tilde{c}_i < (1/U)(\partial U/\partial t)$$

where $\alpha\tilde{c}_i$ is the amplification rate calculated for the instantaneous profile of the changing basic flow. From examining typical stability calculations, one is led to predict that when the time constant of the basic flow is much shorter than $10^3\times$ (the time constant of the disturbances of the instantaneous profile), accelerating flows are likely to be always momentarily stable and decelerating flows always momentarily unstable—for the type of disturbance considered. The shape of the velocity distribution loses much of its importance. It is believed that Fales' and Coles' experimental observations are largely if not predominantly attributable to the effect of deceleration revealed in this paper.

(*Continued on page 417*)

Influence of Transverse Shear on Nonlinear Vibrations of Sandwich Beams With Honeycomb Cores

HU-NAN CHU*
The Martin Company

Summary

In this paper are derived the nonlinear equations of motion for a honeycomb-core sandwich beam. The nonlinearity comes from the moderately large deflections—the linear stress-strain law is still assumed. The derivation utilizes the variational principle and takes into account the effect of transverse shear deformation. Solution of nonlinear periods is determined for a beam with hinged, immovable ends.

Three numerical examples are worked out for sandwiches with aluminum-alloy facings and aluminum-foil honeycomb core. The cores have transverse-shear moduli ranging from 22,000 to 150,000 psi. The thickness-length ratios used are one tenth (1/10) and one twentieth (1/20).

The conclusion is that in nonlinear vibration analyses of honeycomb sandwich constructions commonly used in flight structures, the influence of transverse shear deformation can, as a rule, be neglected.

(I) Introduction

NONLINEAR VIBRATIONS OF HOMOGENEOUS BEAMS have been investigated by A. C. Eringen,[1] while H. Chu and G. Herrmann[2] have considered nonlinear vibrations of homogeneous flat plates, and E. Reissner[3] has reported on nonlinear vibrations of homogeneous cylindrical shells.

In these few examples from the available literature, "The nonlinearity of the problem," to quote V. V. Novozhilov,[4] "arises from the geometry."

To be more specific, the rotations of the cross sections are sufficiently large to be of consequence in such strain-displacement relations as

$$\epsilon_x = (\partial u/\partial x) + (1/2)(\partial w/\partial x)^2$$

where ϵ_x is the lengthwise strain; u and w are the displacements in the directions of length and thickness respectively; and x is the lengthwise coordinate. Terms such as $(1/2)(\partial w/\partial x)^2$ arise from large rotations which are absent in the linear theories. Note that the results of references 1, 2, and 3 apply only to wavelengths large compared with the thicknesses—i.e., the effect of transverse shear deformation has been neglected.

Received March 21, 1960. Revised and received June 20, 1960.

* Structures Research Staff.

In sandwich constructions, owing to the weaker core, transverse shear deformation affects a much wider range of wavelengths[5] than in the corresponding homogeneous cases. The wavelengths in question usually include those for which finite-amplitude vibration analyses are of interest. Therefore, it is necessary to determine the possible influence of the transverse shear deformation on the period of nonlinear vibrations. This is done here by analyzing the finite-amplitude vibrations of a honeycomb-sandwich beam, and including transverse shear deformation in the strain-displacement relations. First a linear distribution of

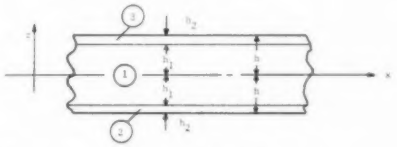

FIG 1. Cross section of a sandwich beam.

the displacements across the thickness is assumed, and then the equations of motion are derived, with the use of the principle of minimum potential energy. A form of solution is then assumed and periods are found which are then compared with periods found by neglecting transverse shear deformation.

(II) Equations of Motion

(a) *Strains and Displacements*

The three-dimensional strain expressions for moderately large rotations are given, for example, in Novozhilov's book.[4] When applied to the sandwich beams, the three-dimensional strain expressions reduce to the following:

$$\left.\begin{aligned} \epsilon_{xzi} &= e_{xzi} + (1/2)(e_{xzi} - \omega_{yi})^2 \\ \epsilon_{zzi} &= e_{zzi} \end{aligned}\right\} \qquad (1)$$

where $e_{xzi} = \partial u_{xi}/\partial x$, $2e_{zzi} = (\partial u_{xi}/\partial z) + (\partial u_{zi}/\partial x)$, $2\omega_{yi} = (\partial u_{xi}/\partial z) - (\partial u_{zi}/\partial x)$ $\qquad (2)$

The subscript i takes on the values 1, 2, and 3 denoting the various layers, as shown in Fig. 1. The letter e refers to the strain expressions in the linear theory, while ω_y is the rotation.

Eqs. (1) are only approximately correct, in that ϵ_{yyi} and ϵ_{zzi} are not considered. Accordingly, this discussion must be limited to frequencies that are sufficiently low to render ϵ_{yyi} and ϵ_{zzi} unimportant. It should also be noted that the strains in Eqs. (1) are not necessarily small compared with the rotations.

The displacements are then assumed to be as follows:

$$\left.\begin{aligned} u_{x1}(x, z, t) &= u(x, t) + z\psi(x, t) \\ u_{x2}(x, z, t) &= u - h_1(w' + \psi) - zw' \\ u_{x3}(x, z, t) &= u + h_1(w' + \psi) - zw' \\ u_{zi}(x, z, t) &= w(x, t) \end{aligned}\right\} \tag{3}$$

where the prime notation ($'$) indicates differentiation with respect to x, the lengthwise coordinate of the beam. ψ may be called the shear angle of the core. Transverse shear deformation of the faces has been neglected, since the faces are assumed to be thin as compared with the core.

The strain-displacement relations are then determined by use of Eqs. (1), (2), and (3):

$$\left.\begin{aligned} \epsilon_{xx1} &= u' + (1/2)w'^2 + z\psi' \\ \epsilon_{xx2} &= u' - h_1(w'' + \psi') + (1/2)w'^2 - zw'' \\ \epsilon_{xx3} &= u' + h_1(w'' + \psi') + (1/2)w'^2 - zw'' \\ \epsilon_{xz1} &= (1/2)(\psi + w') \end{aligned}\right\} \tag{4}$$

(b) *Stress Equations of Motion*

To derive the equations of motion, we shall use what is most commonly known as the principle of minimum potential energy, in which variation is performed only on the displacements. To save space, however, the details of the derivation will be omitted. For these details, interested readers may consult a research report of the same title and by the same author as the present article, issued by The Martin Company, Denver Division, March 1960. The procedure is outlined as follows.

First, the total strain energy W is calculated with the use of Eqs. (4), and the total kinetic energy T and the total work done W_e by the external forces are found with the aid of Eqs. (3). Then the variational principle states that for all arbitrary time intervals $(t_2 - t_1)$ the true state of stress corresponds to that in which

$$\delta \int_{t_1}^{t_2} (T - W + W_e)\, dt = 0 \tag{5}$$

The result is the following set of stress equations of motion:

$$\left.\begin{aligned} &\frac{\partial}{\partial x}(N_{x2} + N_{x3}) + F_x = 2(h_1\rho_1 + h_2\rho_2)\ddot{u} \\ &\frac{\partial}{\partial x}[M_{x1} + h_1(N_{x3} - N_{x2})] - Q_{x1} + \frac{h_1}{h} m_x = \\ &\qquad \frac{2}{3}\rho_1 h_1^3\ddot{\psi} + h_1h_2\rho_2\left[2h_1\ddot{\psi} - h_2\frac{\partial\ddot{w}}{\partial x}\right] \\ &\frac{\partial^2}{\partial x^2}[(M_{x2} + M_{x3}) - h_1(N_{x3} - N_{x2})] + \\ &\frac{\partial}{\partial x}\left[(N_{x2} + N_{x3})\frac{\partial w}{\partial x} + Q_{x1}\right] + q + \frac{h_2}{h}\frac{\partial m_x}{\partial x} = \\ &\qquad 2(h_1\rho_1 + h_2\rho_2)\ddot{w} + h_1h_2^2\rho_2\frac{\partial\ddot{\psi}}{\partial x} - \frac{2}{3}\rho_2 h_2^3\frac{\partial^2\ddot{w}}{\partial x^2} \end{aligned}\right\} \tag{6}$$

where

$$\left.\begin{aligned} N_{x2} &= \int_{-h}^{-h_1} \sigma_{xx2}dz, & N_{x3} &= \int_{h_1}^{h} \sigma_{xx3}dz \\ Q_{x1} &= \int_{-h_1}^{h_1} \sigma_{xz1}\, dz, & M_{x1} &= \int_{-h_1}^{h_1} \sigma_{xz1}\, z\, dz \\ M_{x2} &= \int_{h}^{-h_1} \sigma_{xx2}\, z\, dz, & M_{x3} &= \int_{h_1}^{h} \sigma_{xx3}\, z\, dz \end{aligned}\right\} \tag{7}$$

$$F_x = f_x\big]_{z=-h}^{z=h} \qquad m_x = f_x z\big]_{z=-h}^{z=h} \qquad q = f_z\big]_{z=-h}^{z=h} \tag{8}$$

and dots ($\dot{u}$, $\ddot{w}$, $\dot{\psi}$, etc.) indicate differentiation with respect to time. In Eqs. (7), the letter σ denotes stress, while in Eqs. (8) f_x and f_z are the components of surface traction in the x- and the z-directions respectively.

In deriving Eqs. (6), the fact has been utilized that resistance of the honeycomb cores perpendicular to the honeycomb flutes is small compared to that of the faces.

The appropriate initial conditions are the specifications for initial displacement and initial velocities. The appropriate end conditions are the specifications for one member of each of the following products:

$$(N_{x2} + N_{x3})u, \qquad [M_{x1} + h_1(N_{x3} - N_{x2})]\psi$$

$$[h_1(N_{x3} - N_{x2}) - (M_{x2} + M_{x3})](\partial w/\partial x)$$

$$[Q_{x1} + Q_{x2} + Q_{x3} - (h_2/h)m_x]w$$

where $\quad Q_{x2} = \int_{-h}^{-h_1} f_z\, dz, \qquad Q_{x3} = \int_{h_1}^{h} f_z\, dz$

However, these conditions do not insure that the solution will be unique; they merely establish that energy will be conserved[6] within the approximations imposed earlier in this paper.

For vanishing cores, $h_1 \to 0$. Eqs. (6) reduce to

$$(\partial N_x/\partial x) + F_x = 2h_2\rho_2\ddot{u}$$

$$(\partial^2 M_x/\partial x^2) + (\partial/\partial x)(N_x\partial w/\partial x) + q + (\partial m_x/\partial x) = 2h_2\rho_2\ddot{w} - (2/3)\rho_2 h_2^3(\partial^2\ddot{w}/\partial x^2)$$

where $\qquad N_x = N_{x2} + N_{x3}$

and $\qquad M_x = M_{x1} + M_{x2} + M_{x3}$

These equations are the same as those shown in refer-

ence 6, except that here the notation $2h_2$ replaces h and ρ_2 is ρ.

(c) *Stress-Displacement Relations*

There are six three-dimensional stress-strain relations for the orthotropic, transversely isotropic[7] core. ϵ_{yy1} and ϵ_{zz1} can be eliminated algebraically among the six, while ϵ_{xy1} and ϵ_{yz1} are zero when applied to a beam. Thus, this reduces the number from six to two for this case, namely:

$$\left.\begin{aligned}\sigma_{xx1} &= E_1\epsilon_{xx1} + \nu_1\sigma_{yy1} + (E_1/E_{z1})\nu_{z1}\sigma_{zz1}\\ \sigma_{xz1} &= 2G_{z1}\epsilon_{xz1}\end{aligned}\right\} \quad (9a)$$

where the subscript z indicates quantities associated with the z-axis, the axis of elastic symmetry. Thus ν_1 is the isotropic Poisson's ratio in the transverse plane (the x, y-plane), while ν_{z1} is Poisson's ratio associated with orthotropy. E_1 and E_{z1}, and G_1 and G_{z1}, are related similarly.

Likewise, for the two identical isotropic faces, we have

$$\left.\begin{aligned}\sigma_{xx2} &= E_2\epsilon_{xx2} + \nu_2\sigma_{yy2} + \nu_2\sigma_{zz2}\\ \sigma_{xz2} &= 2G_2\epsilon_{xz2}\\ \sigma_{xx3} &= E_2\epsilon_{xx3} + \nu_2\sigma_{yy3} + \nu_2\sigma_{zz3}\\ \sigma_{xz3} &= 2G_2\epsilon_{xz3}\end{aligned}\right\} \quad (9b)$$

Next we integrate Eqs. (9a) and (9b) according to Eqs. (7), employing the strain-displacement relations of Eqs. (4). In carrying out the integration, the following are observed:

Integrals containing σ_{xz2} and σ_{xz3} are zero because the transverse shear deformation of the faces has been neglected. This is justified if the faces are both thin and heavy as compared with the core.

Integrals containing σ_{yy1} and σ_{zz1} are neglected, which will necessarily limit our computations to frequencies somewhat below those of the thickness-stretch and width-stretch modes. This is justified because we are concerned primarily with the interaction of transverse shear and large amplitudes on frequencies of the first branch which describes primarily the flexural modes. The lowest thickness-stretch mode, for example, is associated with the extensional mode. Although, in nonlinear vibrations, the extensional and flexural motions are coupled through the nonlinear terms,[6] both the extensional mode and the thickness-stretch mode have frequencies much higher than the first-branch flexural mode.[8] Incidentally, this would furnish a justification for the neglect of the longitudinal inertia. However, this neglect will be justified by reasons that appear later in the paper. On the other hand, it is easily seen that the width-stretch modes have frequencies still higher than that of the thickness-stretch modes.

The result is the following set of stress-displacement relations:

$$\left.\begin{aligned}N_{x2} &= h_2E_2[u' - h_1(w'' + \psi') + (1/2)w'^2 + (1/2)(h + h_1)w'']\\ N_{x3} &= h_2E_2[u' + h_1(w'' + \psi') + (1/2)w'^2 - (1/2)(h + h_1)w'']\\ M_{x1} &= (2/3)E_1h_1^3\psi', \qquad Q_{x1} = 2h_1G_{z1}(\psi + w')\\ M_{x2} &= -(E_2/2)h_2(h + h_1)[u' - h_1(w'' + \psi') + (1/2)w'^2] - (E_2/3)(h^3 - h_1^3)w''\\ M_{x3} &= (E_2/2)h_2(h + h_1)[u' + h_1(w'' + \psi') + (1/2)w'^2] - (E_2/3)(h^3 - h_1^3)w''\end{aligned}\right\} \quad (10)$$

Ordinarily, a shear coefficient κ should be associated with the expression for Q_{x1}. However, since the scope of this paper is limited to sandwiches with thin and heavy faces, and since κ is nearly unity for this type of sandwich,[5] Eqs. (10) will remain unmodified.

(d) *Displacement Equations of Motion*

If we substitute Eqs. (10) into Eqs. (6) we obtain

$$\left.\begin{aligned}&2h_2E_2(u'' + w'w'') + F_x = 2(h_1\rho_1 + h_2\rho_2)\ddot{u}\\ &(^2/_3E_1h_1^3 + 2h_1^2h_2E_2)\psi'' - h_1h_2^2E^2w''' - 2h_1G_{z1}(\psi + w') + (h_1/h)m_x = (^2/_3\rho_1h_1^3 + 2\rho_2h_1^2h_2)\ddot{\psi} - h_1h_2^2\rho_2(\partial\ddot{w}/\partial x)\\ &[-^2/_3(h^3 - h_1^3) + h_1h_2^2]E_2(\partial^4w/\partial x^4) - 2h_1^2h_2E_2\psi''' + (\partial/\partial x)[2h_2E_2w'(u' + {}^1/_2w'^2)] + 2h_1G_{z1}(\psi + w') + q + (h_2/h)(\partial m_x/\partial x) = 2(h_1\rho_1 + h_2\rho_2)\ddot{w} + h_1h_2^2\rho_2(\partial\ddot{\psi}/\partial x - {}^2/_3\rho_2h_2^3(\partial^2\ddot{w}/\partial x^2)\end{aligned}\right\} \quad (11)$$

If flexure of the core is to be neglected, then the term $^2/_3E_1h_1^3\psi''$ in Eqs. (11) must be put to zero.

Next, if the nonlinear terms are put to zero in Eqs. (11), then the longitudinal motions will become uncoupled from the flexural motions, while the last two equations of (11) will describe two branches of flexural motions. The first (lower) branch, which is the one presently of interest, has in-phase relationships between ψ and $-w'$ in free vibrations. The second (higher) branch has out-of-phase relationships between ψ and $-w'$. The situation is somewhat analogous to a double pendulum.

(III) Solution for Free Vibrations

In free vibrations, F_x, m_x, and q of Eqs. (11) are zero. Also, for primarily flexural vibrations, the longitudinal inertia term is small to a higher order than other terms and can therefore be neglected. This is made clear by perturbation procedures in reference 2. We may therefore write, to a first approximation, the first equation of (11) as

$$2h_2E_2\,(u'' + w'w'') = 0 \tag{12a}$$

The remaining two equations of (11) are written

$$(^2/_3E_1h_1^3 + 2h_1^2h_2E_2)\psi'' - h_1h_2^2E_2w''' - 2h_1G_{z1}(\psi + w') = (^2/_3\rho_1h_1^3 + 2\rho_2h_1^2h_2)\ddot{\psi} - h_1h_2^2\rho_2(\partial\ddot{w}/\partial x) \tag{12b}$$

$$[-^2/_3(h^3 - h_1^3) + h_1h_2^2]E_2(\partial^4w/\partial x^4) - 2h_1^2h_2E_2\psi''' + (\partial/\partial x)[2h_2E_2w'(u' + {}^1/_2w'^2)] + 2h_1G_{z1}(\psi + w') = 2(h_1\rho_1 + h_2\rho_2)\ddot{w} + h_1h_2^2\rho_2(\partial\ddot{\psi}/\partial x) - {}^2/_3\rho_2h_2^3(\partial^2\ddot{w}/\partial x^2) \tag{12c}$$

If we impose the boundary condition that $u = 0$ at $x = 0$ and $x = l$, then Eq. (12a) can be integrated as follows:

$$u' = \frac{1}{2}\left[\frac{1}{l}\int_0^l w'^2\,dx - w'^2\right] \tag{13}$$

where l is the length of the beam. If Eq. (12b) is differentiated with respect to x and then added to Eq. (12c), the following is obtained:

$$[-^2/_3E_2(h^3 - h_1^3)](\partial^4w/\partial x^4) + {}^2/_3E_1h_1^3\psi''' + (\partial/\partial x)[2h_2E_2w'(u' + {}^1/_2w'^2)] = 2(h_1\rho_1 + h_2\rho_2)\ddot{w} + (^2/_3\rho_1h_1^3 + 2\rho_2h_1^2h_2 + h_1h_2^2\rho_2)(\partial\ddot{\psi}/\partial x) - (^2/_3\rho_2h_2^3 + h_1h_2^2\rho_2)(\partial^2\ddot{w}/\partial x^2) \tag{14}$$

If ψ is set equal to $-w'$ in Eq. (14), then the transverse shear is totally neglected, and we have

$$-^2/_3[E_1h_1^3 + E_2(h^3 - h_1^3)](\partial^4w/\partial x^4) + \left[h_2E_2\,\frac{1}{l}\int_0^l w'^2\,dx\right](\partial^2w/\partial x^2) = 2(h_1\rho_1 + h_2\rho_2)\ddot{w} - {}^2/_3[\rho_1h_1^3 + \rho_2(h^3 - h_1^3)](\partial^2\ddot{w}/\partial x^2) \tag{15}$$

which makes use of Eq. (13). If, on the other nand, the transverse shear of the core is considered, Eqs. (14) and (12c) become, by virtue of Eq. (13),

$$-^2/_3E_2(h^3 - h_1^3)(\partial^4w/\partial x^4) + {}^2/_3E_1h_1^3\psi''' + \left[\frac{h_2E_2}{l}\int_0^l w'^2\,dx\right](\partial^2w/\partial x^2) = 2(h_1\rho_1 + h_2\rho_2)\ddot{w} + (^2/_3\rho_1h_1^3 + 2\rho_2h_1^2h_2 + h_1h_2^2\rho_2)(\partial\ddot{\psi}/\partial x) - (^2/_3\rho_2h_2^3 + h_1h_2^2\rho_2)(\partial^2\ddot{w}/\partial x^2) \tag{16a}$$

$$[-^2/_3(h^3 - h_1^3) + h_1h_2^2]\,E_2(\partial^4w/\partial x^4) - 2h_1^2h_2E_2\psi''' + \left[\frac{h_2E_2}{l}\int_0^l w'^2\,dx\right](\partial^2w/\partial x^2) + 2h_1G_{z1}(\psi + w') = 2(h_1\rho_1 + h_2\rho_2)\ddot{w} + h_1h_2^2\rho_2(\partial\ddot{\psi}/\partial x) - {}^2/_3\rho_2h_2^3(\partial^2\ddot{w}/\partial x^2) \tag{16b}$$

The form of the nonlinear term suggests that we should do well to begin with an assumed solution for w. If we assume that

$$w = AT(t)\,\sin\,(\pi x/l) \tag{17}$$

The nonlinear term is then

$$\frac{h_2E_2}{l}\int_0^l w'^2\,dx = 2h_2E_2\left(\frac{\pi AT}{2l}\right)^2$$

If we also assume a solution for ψ and require that the time function in ψ be the same as $T(t)$ in w, then ψ takes the form

$$\psi = BT(t)\,\cos\,(\pi x/l) \tag{18}$$

from Eq. (12b). Furthermore, $T(t)$ would have to be simple harmonic in t. To explain this inconsistency, we observe that for very small nonlinearities, Eqs. (12b) and (12c) describe two modes, one of which is ψ-motion, primarily, and the other primarily w-motion. We see that Eq. (12b) describes primarily the ψ-motion. Since Eq. (12b) is linear, the influence of large amplitudes is therefore essentially on the lower branch, i.e., primarily on the w-motions. Therefore, we turn to Eqs. (16a) and (16b) which describe primarily w-motions while taking into account the influence of ψ-motions.

If we substitute Eqs. (17) and (18) into Eqs. (16a) and (16b), we obtain

$$\ddot{T} + p_1^2T + p_1^2\left[\frac{3(h_2/h)}{k(E_1/E_2)(h_1/h)^3 + 1 - (h_1/h)^3}\right]\beta^2T^3 = 0 \tag{19}$$

$$\ddot{T} + p_1^2T + p_1^2\left[\frac{(h_2/h)r_E\delta^2}{(2/\pi)^2(h_1/h)(1-k) + r_E\{(1/3)[1 - (h_1/h)^3] - (h_1/h)(h_2/h)[(h_1/h)k + (h_2/2h)]\}\delta^2}\right]\beta^2T^3 = 0 \tag{20}$$

where

$$p_1^2 = \frac{(\pi^2/3)\delta^2 r_E C_{S1}[1 - (h_1/h)^3]}{(\pi^2/3)\delta^2\{(h_1/h)^3 + r_\rho[1 - (h_1/h)^3] - 3(1 - k)r_\rho(h_1/h)(h_2/h)[(h_1/h) + (h_2/2h)]\} + 4(h_1/h)(1 + r_h r_\rho)}$$

$$= \frac{8(1 - k)(h_1/h)C_{S1}^2 + r_E C_{S1}^2\{(2/3)[1 - (h_1/h)^3] - (h_1/h)(h_2/h)[2(h_1/h)k + (h_2/h)]\}\pi^2\delta^2}{(8h_1/h)(1 + r_h r_\rho) + r_\rho(h_2/h)^2[(h_1/h)k + (2/3)(h_2/h)]\pi^2\delta^2} \tag{21}$$

and

$$\left.\begin{aligned} \beta = A/2h, \quad \delta = 2h/l, \quad r_h = h_2/h_1, \quad r_E = E_2/G_{z1} \\ r_\rho = \rho_2/\rho_1, \quad C_{S1}^2 = G_{z1}/\rho_1, \quad k = -Bl/A\pi \end{aligned}\right\} \tag{22}$$

Eq. (21) serves to determine k. We hope that for most practical purposes k as determined by (21) will not differ perceptibly from the k found by equating the coefficients of T^3 from Eqs. (19) and (20). If the difference is appreciable, then new solutions for w and ψ must be assumed to eliminate the over-determinacy in k. For example, if w and ψ can be expanded into series of product of functions of t and x, then the new solutions may be had by taking more terms in the series, instead of the one-term approximations of Eqs. (17) and (18). The examples in the next section, however, will show that Eq. (21) is adequate.

On the other hand, if transverse shear deformation is completely neglected, we then have, from Eq. (15),

$$\ddot{T} + p_0^2 T + p_0^2\left[\frac{3(h_2/h)}{(E_1/E_2)(h_1/h)^3 + 1 - (h_1/h)^3}\right]\beta^2 T^3 = 0 \tag{23}$$

where

$$p_0^2 = \frac{(\pi^2/3)\delta^2 r_E C_{S1}[1 - (h_1/h)^3]}{(\pi^2/3)\delta^2\{(h_1/h)^3 + r_\rho[1 - (h_1/h)^3]\} + 4(h_1/h)(1 + r_h r_\rho)} \tag{24}$$

For most honeycomb sandwich constructions, E_1/E_2 is of the order of 10^{-4} to 10^{-5}. Eqs. (19) and (23) will therefore have the same form:

$$\ddot{T} + p^2 T + p^2 F(\beta) T^3 = 0 \tag{25}$$

where $F(\beta) = \dfrac{3(h_2/h)\beta^2}{1 - (h_1/h)^3}$ (approximately) (26)

From this we can immediately write down

$$\frac{T_1^*}{T_1} = \frac{2K(\bar{k})}{\pi}\frac{p_1}{p_1^*} \quad \text{and,} \quad \frac{T_0^*}{T_0} = \frac{2K(\bar{k})}{\pi}\frac{p_0}{p_0^*} \tag{27}$$

where

T_1^* is the nonlinear period, transverse shear considered;

T_1 is the linear period, transverse shear considered;

T_0^* is the nonlinear period, transverse shear not considered;

T_0 is the linear period, transverse shear not considered;

$K(\bar{k})$ is the complete elliptic integral of the first kind;

$\bar{k} = \sqrt{F(\beta)/2[1 + F(\beta)]}$

and $p_1/p_1^* = p_0/p_0^* = 1/\sqrt{1 + F(\beta)}$

$$= \frac{\text{linear frequency}}{\text{nonlinear frequency}}$$

In other words, $T_1^*/T_1 = T_0^*/T_0$, and hence the conclusion: The effect of transverse shear deformation on the nonlinear vibrations is negligible if it is negligible for the corresponding linear vibrations.

(IV) Numerical Examples

The data in Table 1 are averages from references 9 and 10 for aluminum honeycomb cores.

TABLE 1

	Core 1 (weak)	Core 2 (intermediate)	Core 3 (strong)
G_{z1}	2.2×10^4 psi	6×10^4 psi	15×10^4 psi
E_{z1}	10×10^4 psi	25×10^4 psi	50×10^4 psi
E_1	80 psi	200 psi	500 psi
$\rho_1 g$	2.7 lb./cu. ft.	6 lb./cu. ft.	9 lb./cu. ft.

The faces are made of aluminum alloy with $E_2 = 10^7$ psi and $\rho_2 g = 172.8$ lb./cu. ft. The thickness ratio $r_h = 2/23$ is assumed for all three cases—that is, the core accounts for 92 percent of the total thickness of the beam. The k values in Table 2 were obtained by use of Eq. (21).

TABLE 2

k	Core 1	Core 2	Core 3
($\delta = 1/10$)	0.9218 (0.9204)	0.9698 (0.9693)	0.9877 (0.9875)
($\delta = 1/20$)	0.9790 (0.9789)	0.9922 (0.9922)	0.9969 (0.9969)

The values in parentheses are obtained by equating the coefficients of the nonlinear terms of Eqs. (19) and (20). This shows that the transverse shear effect does increase with the amplitudes, since the values in the parentheses are generally smaller. The increases, however, are negligible over the ranges usually of

interest. Therefore the method of approximation and the manner of determining k are adequate for most practical purposes. Thus, the importance of transverse shear deformation is determined entirely by the corresponding linear vibrations.

The influence of transverse shear on the linear periods can be seen from

$$\frac{T_1}{T_0} = \frac{p_0}{p_1} = \sqrt{1 - \frac{\pi^2(1-k) r_\rho \frac{h_1}{h}\frac{h_2}{h}\left(\frac{h_1}{h} + \frac{h_2}{2h}\right)\delta^2}{\frac{\pi^2}{3}\left[\left(\frac{h_1}{h}\right)^3 + r_\rho\left(1 - \frac{h_1^3}{h^3}\right)\right]\delta^2 + 4\left(\frac{h_1}{h}\right)(1 + r_h\, r_\rho)}} \tag{28}$$

The data in Table 3 were calculated from Eq. (28). If we take the case of Core 1 where $\delta = 1/10$ and the transverse shear is about 8 percent of the rotation of the cross section, we see that the transverse shear influence is less than 0.1 percent with regard to the frequency. However, it must be realized that metal honeycomb cores

TABLE 3

	Core 1	Core 2	Core 3
T_1/T_0 ($\delta = 1/10$)	0.999286	0.999766	0.999917
T_1/T_0 ($\delta = 1/20$)	0.999952	0.999985	0.999995

are generally stronger than many other types of cores. For example, cores made of cellular cellulose acetate are generally less than one tenth as strong as the average aluminum honeycomb cores. Therefore, the effect of transverse shear in cellular cellulose acetate-core sandwiches can become considerably important.

In designing honeycomb sandwich constructions for flight structures, a rule-of-thumb assumption would be a core about 10 times as thick as the total faces and accounting for only one third of the total weight, approximately. Of our examples, therefore, Core 3 would seem most appropriate, with its density of 9 lb./ft.^{3} Therefore, in nonlinear vibration analyses of honeycomb sandwich constructions used in flight structures, the influence of transverse shear deformation can, as a rule, be neglected.

References

[1] Eringen, A. C., *On the Nonlinear Vibration of Elastic Bars*, Quart. Appl. Math., Vol. 10, p. 361, 1952.

[2] Chu, Hu-Nan, and Herrmann, G., *Influence of Large Amplitudes on Free Flexural Vibrations of Rectangular Elastic Plates*, J. Appl. Mech., pp. 532–540, December 1956.

[3] Reissner, E., *Nonlinear Effects in Vibrations of Cylindrical Shells*, Ramo-Wooldridge Corp. Report No. AM5-6, September 1955.

[4] Novozhilov, V. V., *Foundations of the Nonlinear Theory of Elasticity*, Graylock Press, Rochester, N. Y., 1953.

[5] Yu, Yi-Yuan, *Flexural Vibrations of Elastic Sandwich Plates*, Technical Note No. 3, Air Force Office of Scientific Research Contract AF49(638)-453, March 1959.

[6] Herrmann, G., *Influence of Large Amplitudes on Flexural Motions of Elastic Plates*, NACA TN 3578, May 1956.

[7] Hildebrand, F. B., Reissner, E., and Thomas, G. B., *Notes on the Foundations of the Theory of Small Displacements of Orthotropic Shells*, NACA TN 1833, March 1949.

[8] Mindlin, R. D., *An Introduction to the Mathematical Theory of Vibrations of Elastic Plates*, monograph prepared for U. S. Army Signal Corps Engineering Laboratories, Fort Monmouth, N.J., 1955.

[9] Kuenzi, E. W., *Mechanical Properties of Aluminum Honeycomb Cores*, U.S. Department of Agriculture, Forest Products Laboratory, Report No. 1849, September 1955.

[10] *Sandwich Construction for Aircraft*, A bulletin issued by the ANC-23 Panel on Sandwich Construction, Departments of Defense and Commerce, U.S.A., May 1951.

✦ ✦ ✦

Boundary-Layer Displacement (*Continued from page 381*)

Cornell Aeronautical Laboratory Report No. AF 1285-A-4, August, 1960.

[66] Guiraud, J. P., *Écoulement Hypersonique d'un Fluide Parfait sur une aile Mince Comportant un Bord d'Attaque Émousse*, Compt. Rend. Acad. Sci., Vol. 248, p. 3524, June, 1959.

[67] Wittliff, C. E., and Wilson, M. R., *An Investigation of Heat Transfer to Slender Yawed Cones in the Hypersonic Shock Tunnel*, Cornell Aeronautical Laboratory Report No. AF-1270-A-2 (to be published).

[68] Hall, J. G., and Russo, A. L., *Studies of Chemical Nonequilibrium in Hypersonic Nozzle Flows*, Cornell Aeronautical Laboratory Report No. AD-1118-A-6, AFOSR TN 59-1090, November 1959; also Proceedings Combustion Institute Meeting, Los Angeles, Calif., Nov. 2–5, 1959, Butterworths Scientific Publications, London.

[69] Boyer, D., Eschenroeder, A., and Russo, A., *Approximate Solutions for Nonequilibrium Airflow in Hypersonic Nozzles*, Cornell Aeronautical Laboratory Report No. AD-1345-W-1 (to be published).

[70] Skinner, G. T., *Analog Network to Convert Surface Temperature to Heat Flux*, J. Amer. Rocket Soc., Vol. 30, No. 6, p. 569, June, 1960.

[71] Hall, J. G., and Golian, T. C., *Shock-Tunnel Studies of Hypersonic Flat-Plate Airflows*, Cornell Aeronautical Laboratory Report (to be published).

A Study of Cotangential, Elliptical Transfer Orbits in Space Flight†

WILLIAM LI-SHU WEN*
Ryan Aeronautical Company

Summary

The purpose of this paper is to determine suitable cotangential, elliptical transfer orbits between a given pair of coplanar terminal orbits in space flight. The condition of tangency of two noncoaxial, confocal conics is established first. This condition is then used to determine the possible cotangential transfer ellipses between two coplanar, noncoaxial, confocal conic orbits of practical importance. These terminal orbits may both be ellipses or one may be an ellipse and the other a hyperbola. They may intersect with each other or make no contact. Whatever the case may be, it is found that there are many such transfer ellipses possible between a given pair of terminal orbits. The locus of the centers of these transfer orbits can be described by an auxiliary conic completely defined by the initial conditions of the problem. By use of the coordinates of this auxiliary conic, r_0 and η_0, as parameters, the variations of the transfer-orbit elements (semimajor axis a and linear eccentricity c) with its orientation angle l can be determined by either analytical or geometrical methods. Once the functions $a(l)$ and $c(l)$ are determined it is easy to calculate, with reference to orbit orientation l, such functions of a and c as the variations of points of departure and arrival, as well as transfer energy and transfer time. With this information available, the transfer-orbit optimization (or the selection of a suitable orbit to meet a specific requirement) can be easily made.

Symbols

A = apoapsis
a = semimajor axis
b = semiminor axis
c = linear eccentricity
E = eccentric anomaly
e = numerical eccentricity
F = common focus of conics
G = universal constant of gravitation
l = orientation angle (Fig. 3)
M = central of mass
M = mean anomaly
m = mass of the moving body
O = center of conic
P = periapsis
p = parameter of conic orbit
r = radial distance from center of attraction
r_A = apodistance
r_P = peridistance
S = separation of centers of two Confocal conics
τ = period of orbit
t = time
V = velocity in flight path
γ = angle between major axes (Fig. 1)
Δ = discriminant
η = true anomaly
φ = angle between major axis and line connecting orbit centers (Fig. 3)

Subscripts

1 pertaining to or associated with terminal orbit No. 1
2 pertaining to or associated with terminal orbit No. 2
0 pertaining to auxiliary conic

Received February 15, 1960. Revised and received November 15, 1960.

† A detailed version of this paper was written in 1958 while the author was with The Dynamics Group, Convair, San Diego.

* Senior staff scientist, Astronics Dept., Aerospace Division.

(I) Introduction

The problem of cotangential elliptical transfer between two coplanar, noncoaxial, terminal ellipses was first investigated by D. F. Lawden.[1] From purely geometrical argument, Lawden established the relationship between the elements of the transfer orbit and those of the terminal orbits, and found that between a given pair of terminal ellipses there are an infinite number of possible cotangential transfer ellipses. To find the optimum transfer orbit (with respect to energy or time), he proposed a geometrical-graphical method because, in general, closed-form solution is not feasible. In treating the problem of interception via tangential ellipses for confocal elliptic orbits, Gedeon[2] has derived some analytical expressions which can be used for digital computer computation of the polar coordinates of the intercept point and the characteristics of the transfer orbit when the coordinates of the release point are given.

In this article, we treat the whole problem by an alternative approach. At the same time, the scope of discussion is expanded to cover more general cases, i.e., ellipse–ellipse–ellipse transfer and hyperbola–ellipse–ellipse transfer.

By analytical reasoning, we first establish the conditions of tangency, intersection, and noncontact between two coplanar confocal conic orbits in terms of the orbit elements a (semimajor axis), c (linear eccentricity), and l (orientation angle). The conditions so formulated express more clearly the physical situations and the geometrical relationships of the problem. These conditions are then used to determine the elements (a, c, l) of the cotangential transfer ellipses between two terminal orbits. Both analytical and geometrical methods of solution are formulated. Other important items during transfer maneuver (such as points of transfer, transfer energy requirement, and transfer time) are then determined from a and c as functions of transfer orbit orientation l. Thus, all the information needed for transfer orbit selection is available.

(II) The Geometrical Relation Between Two Coplanar, Confocal, Noncoaxial Orbits

Consider two coplanar, confocal, noncoaxial orbits 1 and 2, orientated as shown in Fig. 1 where F is their common focus, O_1 and O_2 are their centers, and γ is the angle between the major axes, always measured counterclockwise at periapsis end. If these two orbits have a point r in common, then it can be expressed by the polar equation of either orbit as

$$r = \frac{p_1}{1 + e_1 \cos \eta_1} = \frac{p_2}{1 + e_2 \cos \eta_2} = \frac{p_2}{1 + e_2 \cos (\eta_1 - \gamma)} \tag{II-1}$$

Eqs. (II-1) yield a quadratic equation in $\cos \eta_1$

$$(B^2 + C^2) \cos^2 \eta_1 + 2AB \cos \eta_1 + (A^2 - C^2) = 0$$

and its solution is

$$\left.\begin{aligned} \cos \eta_1 &= \frac{-AB \pm C\sqrt{(B^2 + C^2) - A^2}}{(B^2 + C^2)} \\ \text{where} \quad A &= \frac{1}{p_1} - \frac{1}{p_2}, \quad B = \frac{e_1}{p_1} - \frac{e_2}{p_2} \cos \gamma \\ C &= (e^2/p_2) \sin \gamma \end{aligned}\right\} \tag{II-2}$$

The geometrical relation between two confocal orbits is then expressed by the following conditions:

$$\begin{aligned} \Delta &= (B^2 + C^2) - A^2 \\ &= \left(\frac{e_1}{p_1}\right)^2 - \frac{2e_1e_2 \cos \gamma}{p_1p_2} + \left(\frac{e_2}{p_2}\right)^2 - \left(\frac{1}{p_1} - \frac{1}{p_2}\right)^2 \\ &= \frac{e_1^2 - 1}{p_1^2} + \frac{e_2^2 - 1}{p_2^2} + \frac{2}{p_1p_2}(1 - e_1e_2 \cos \gamma) \end{aligned}$$

$$\left.\begin{aligned} &> 0 \quad \text{two conics intersecting at two and only two points} \\ &= 0 \quad \text{two conics tangential at only one point} \\ &< 0 \quad \text{two noncontacting conics} \end{aligned}\right\} \tag{II-3}$$

From the relations

$$b^2 = a^2(1 - e^2) = a^2 - c^2$$

and

$$p = a(1 - e^2) = b^2/a$$

we have

$$\Delta = \frac{1}{b_1^2b_2^2}[c_1^2 - 2c_1c_2 \cos \gamma + c_2^2 - (a_1 - a_2)^2]$$

Since b^2 is positive for ellipses and negative for hyperbolas, the conditions (II-3) can be reduced to the following two cases (see Fig. 2):

(i) If the two conics are of same kind, we have

$$S^2 = c_1^2 - 2c_1c_2 \cos \gamma + c_2^2 \gtreqless (a_1 - a_2)^2$$

$$\text{for} \begin{cases} \text{intersecting} \\ \text{tangential} \\ \text{noncontacting} \end{cases} \tag{II-4a}$$

(ii) If the two conics are of different kinds, we have

$$S^2 = c_1^2 + 2c_1c_2 \cos \gamma + c_2^2 \lesseqgtr (a_1 + a_2)^2$$

$$\text{for} \begin{cases} \text{intersecting} \\ \text{tangential} \\ \text{noncontacting} \end{cases} \tag{II-4b}$$

where a and c are positive for ellipses and negative for hyperbolas, while S, being the separation of orbit centers, is always positive. The conditions for the special cases of one or both orbits being circular ($e = 0$) or parabolic ($e = 1$) can easily be derived from Eqs. (II-3) and (II-4).

From Eq. (II-3) the condition of tangency is $B^2 + C^2 = A^2$. Then from Eq. (II-4) the true anomalies of the point of tangency are

$$\left.\begin{aligned} \cos \eta_1 &= -\frac{B}{A} = \frac{(e_2/p_2) \cos \gamma - (e_1/p_1)}{(1/p_1) - (1/p_2)} \\ \text{or} \quad \cos \eta_2 &= \cos (\eta_1 - \gamma) = \\ &\frac{(e_2/p_2) - (e_1/p_1) \cos \gamma}{(1/p_1) - (1/p_2)} \end{aligned}\right\} \tag{II-5}$$

The radial distance r to the point of tangency may be obtained by substituting the first equation in (II-5) into Eq. (II-1); by virtue of Eq. (II-3), we have

$$r = 2\frac{(1/p_1) - (1/p_2)}{[(1 - e_1^2)/p_1^2] - [(1 - e_2^2)/p_2^2]} \tag{II-6}$$

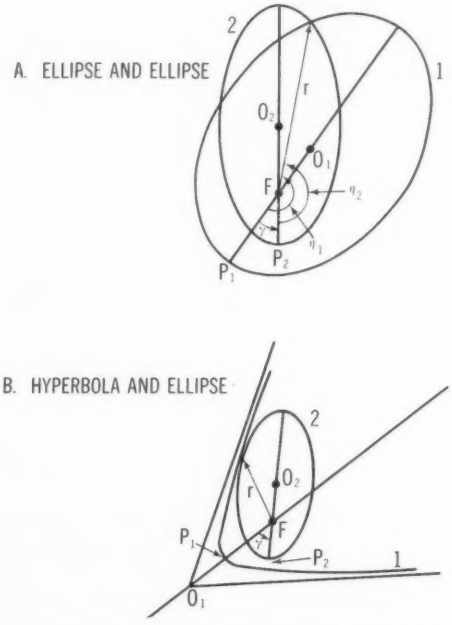

FIG. 1. Orientation of two coplanar, confocal, noncoaxial conics.

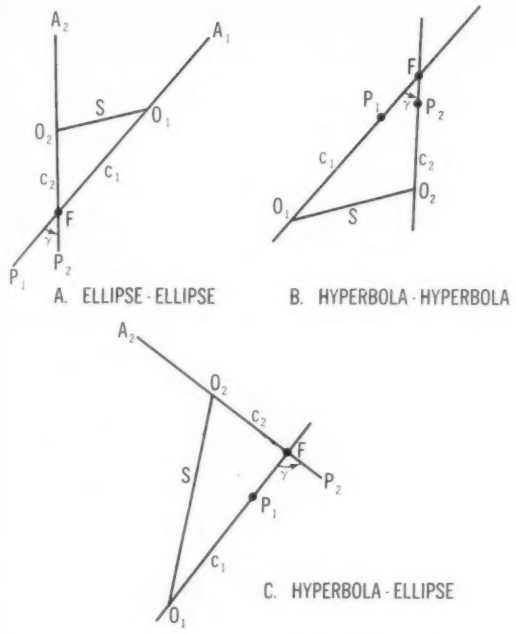

FIG. 2. Geometrical representation of two confocal conics.

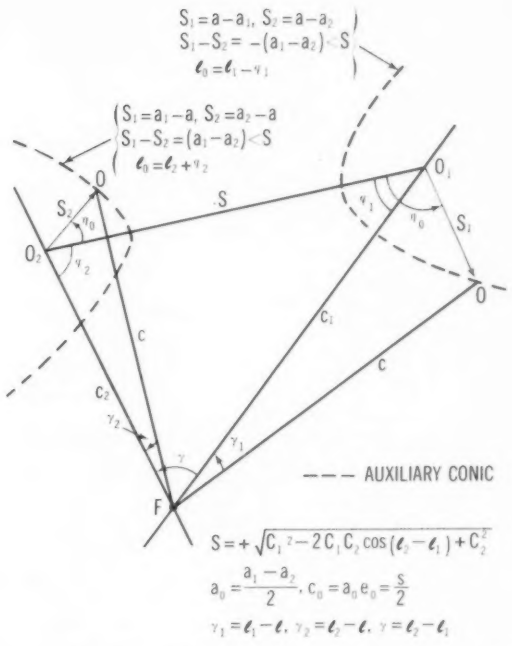

FIG. 4. Linear eccentricity and orientation angle of transfer ellipse between two intersecting ellipses.

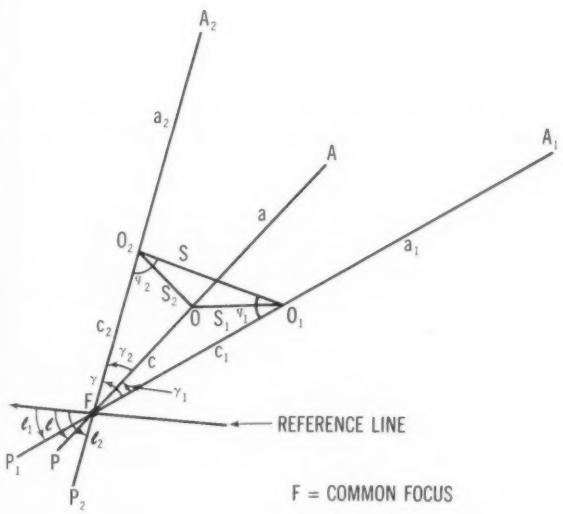

FIG. 3. Geometrical representation of a cotangential transfer ellipse between two terminal ellipses.

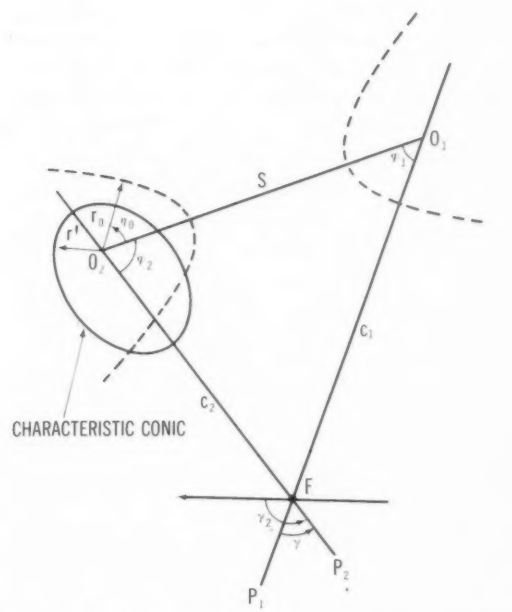

FIG. 5. Characteristic conics of two intersecting terminal ellipses.

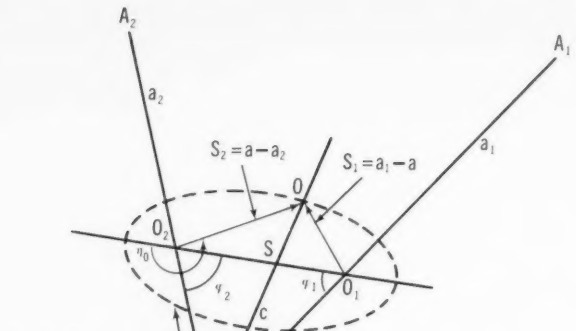

FIG. 6. Auxiliary conics of noncontacting terminal ellipses.

It is to be noted that the second expression in Eqs. (II-3) is the same as that derived by Lawden[1] through geometrical argument, whereas Gedeon,[3] using a different analytical approach, has derived the intersecting condition which is equivalent to the third expression of Eqs. (II-3).

(III) Cotangential Transfer Between Two Coplanar Orbits

For a given pair of coplanar, confocal terminal orbits characterized by the parameters (a_1, c_1, l_1) and (a_2, c_2, l_2) (see Fig. 3) that may both be elliptical or hyperbolic, or one elliptical and the other hyperbolic; let (a, c, l) be a transfer orbit sharing a focus with the terminal orbits and tangential to both. Applying condition (II-4), we have the cotangential conditions:

$$\left.\begin{aligned} S_1 &= +\sqrt{c_1^2 - 2c_1c\cos(l - l_1) + c^2} = \pm(a_1 - a) \\ S_2 &= +\sqrt{c_2^2 - 2c_2c\cos(l_2 - l) + c^2} = \pm(a_2 - a) \end{aligned}\right\} \quad \text{(III-1)}$$

We also have

$$S = \pm\sqrt{c_1^2 - 2c_1c_2\cos(l_2 - l_1) + c_2^2} \gtreqless \pm(a_1 - a_2) \quad \text{(III-2)}$$

depending upon the nature of and the relation between two terminal orbits. Bearing in mind the trigonometric relations in Fig. 3, we obtain from the cotangential conditions (III-1) the expressions

$$\begin{aligned} &S_1 - S_2 = \pm(a_1 - a_2) < S \\ \text{or} \quad &S_1 + S_2 = \pm(a_1 - a_2) > S \end{aligned} \quad \text{(III-3)}$$

It is noted that the second part of Eqs. (III-3) specifies the relation between terminal orbits according to (III-2), while the first part of Eqs. (III-3) says that the locus of the centers (O) of all cotangential transfer orbits is a conic with terminal orbit centers (O_1 and O_2) as loci. For briefness, we shall refer this locus as the *auxiliary conic* (a_0, c_0, l_0) with

$$\left.\begin{aligned} &2|a_0| = |a_1 - a_2|, \qquad 2|c_0| = 2|a_0|e_0 = S \\ &l_0 = l_i \pm \varphi_i \quad \text{or} \quad l_i \pm \varphi_i \pm \pi \quad (i = 1, 2) \end{aligned}\right\} \quad \text{(III-4a)}$$

$$\left.\begin{aligned} &\frac{\sin\varphi_1}{c_2} = \frac{\sin\varphi_2}{c_1} = \frac{\sin|l_2 - l_1|}{S} \\ &S_i = r_0 = \frac{a_0(1 - e_0^2)}{1 + e_0\cos\eta_0} \end{aligned}\right\} \quad \text{(III-4b)}$$

r_0 = radial distance of O from O_i,
η_0 is measured from l_0

The cotangential transfer orbit (a, c, l) is obtained as

$$\left.\begin{aligned} a &= a_i \pm S_i \\ c^2 &= c_i^2 \pm 2c_iS_i\cos(\eta_0 \pm \varphi_i) + S_i^2 \\ c\cos(l_i - l) &= c_i \pm S_i\cos(\eta_0 \pm \varphi_i) \end{aligned}\right\} \quad \text{(III-5)}$$

The type of the transfer orbit is determined by the following criteria:

$$\begin{aligned} a^2 - c^2 = a_i^2 - c_i^2 \pm 2a_iS_i[1 \pm e_i\cos(\eta_0 \pm \varphi_i)] \\ > 0 \quad \text{elliptic} \\ = 0 \quad \text{parabola} \\ < 0 \quad \text{hyperbola} \end{aligned} \quad \text{(III-6)}$$

It is easy to apply the general criterion (III-1) to (III-6) to the specific cases as follows.

(1) Ellipse–Ellipse–Ellipse Cotangential Transfer

In this case let us assume $a > c > 0$, $a_2 > c_2 > 0$, $a_1 > a_2$. Then from Eqs. (III-1), (III-3), and (II-4a), we see that:

(A) When terminal orbits are intersecting, the auxiliary conic is a hyperbola with two branches (see Fig. 4).

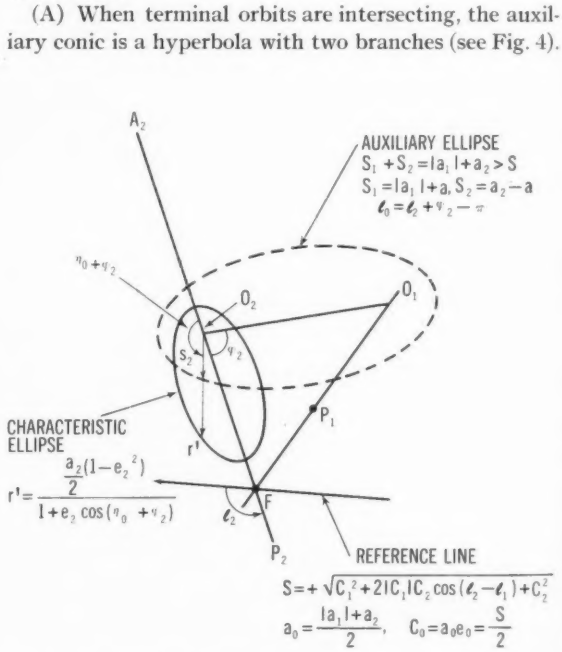

FIG. 7. Characteristic conic of intersecting terminal hyperbola and ellipse.

For the branch focused at O_1, the associated transfer orbits are specified by

$$\left.\begin{aligned} &a = a_1 + S_1 > a \\ &c^2 = c_1^2 - 2c_1S_1\cos(\eta_0 - \varphi_1) + S_1^2 \\ &c\cos(l_1 - l) = c_1 - S_1\cos(\eta_0 - \varphi_1) \\ &a^2 - c^2 = a_1^2 - c_1^2 + \\ &\qquad 2a_1S_1[1 + e_1\cos(\eta_0 - \varphi_1)] \end{aligned}\right\} \quad \text{(III-7)}$$

Since $a^2 - c^2 > 0$ for all values of η_0, this whole branch represents the locus of the centers of a group of exterior cotangential transfer ellipses with $a > a_1$.

For the branch focused at O_2, the associated transfer orbits are specified by

$$\left.\begin{aligned} &a = a_2 - S_2 < a_2 \\ &c^2 = c_2^2 - 2c_2S_2\cos(\eta_0 + \varphi_2) + S_2^2 \\ &c\cos(l_2 - l) = c_2 - S_2\cos(\eta_0 + \varphi_2) \\ &a^2 - c^2 = a_2^2 - c_2^2 - \\ &\qquad 2a_2S_2[1 - e_2\cos(\eta_0 + \varphi_2)] \end{aligned}\right\} \quad \text{(III-8)}$$

The type of the transfer orbit is determined by the following conditions:

$$S_2 \lessgtr \frac{(a_2/2)(1 - e_2^2)}{1 + e_2\cos(\pi + \eta_0 + \varphi_2)} \quad \text{for} \begin{cases} \text{cotangential ellipse} \\ \text{cotangential parabola} \\ \text{cotangential hyperbola} \end{cases} \quad \text{(III-9)}$$

The right-hand side of Eq. (III-9) represents an ellipse (γ', η') focused at O_2 with

$$a' = a_2/2, \quad c' = c_2/2,$$

$$l' = l_2 + \pi, \quad \eta' = \pi + \eta_0 + \varphi_2$$

We shall call this ellipse the characteristic ellipse (or conic). By applying condition (II-b) we see that in the present case the auxiliary hyperbola and the characteristic ellipse are intersecting. Therefore *only that part of the auxiliary hyperbola which is enclosed by the characteristic ellipse Eq. (III-9)* is the locus of the center of a group of interior cotangential transfer ellipses with $a < a_2$ (see Fig. 5).

(B) When terminal orbits are noncontacting the auxiliary conic is an ellipse with O_2 as focus (see Fig. 6). The transfer orbits are given by

$$\left.\begin{aligned} &a = a_2 + S_2 = a_1 - S_1 \\ &c^2 = c_2^2 + 2c_2S_2\cos(\eta_0 + \rho_2) + S_2^2 \\ &c\cos(l_2 - l) = c_2 + S_2\cos(\eta_0 + \varphi_2) \\ &a^2 - c^2 = a_2^2 - c_2^2 + \\ &\qquad 2a_2S_2[1 - e_2\cos(\eta_0 + \varphi_2)] \end{aligned}\right\} \quad \text{(III-10)}$$

Since $a^2 - c^2 > 0$ for all values of η_0, all the possible cotangential transfer orbits are elliptical.

(2) *Hyperbola–Ellipse–Hyperbola Cotangential Transfer*

In this case let $a_1 < c_1 < 0$, $a_2 > c_2 > 0$. From Eqs. (III-1), (III-3), and (II-4b) we see that:

(A) When the terminal orbits intersect, the auxil-

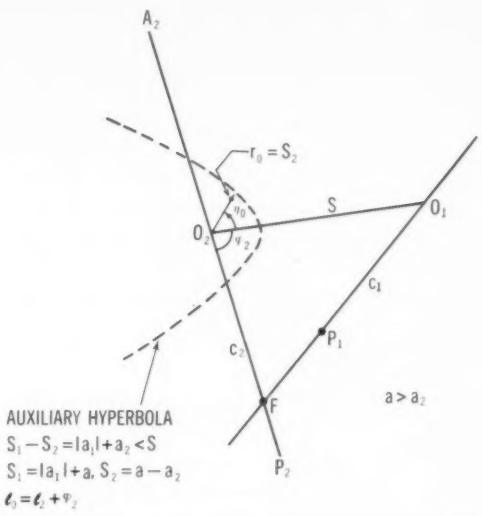

FIG. 8. Auxiliary conic of noncontacting terminal hyperbola and ellipse.

TABLE 1

Geometrical Determination of Cotangential, Elliptical Transfer Orbit

Terminal Orbits		Auxiliary Conic (r_0, η_0)	Characteristic Conic (r', η')	a
ellipse-ellipse	intersecting	hyperbola: $\left(\frac{a_1 - a_2}{2}, \frac{S}{2}, \ell_1 - \varphi_1, O_1\right)$	none	$a_1 + S_1$
$a_1 > c_1$	$S > a_1 - a_2$			
$a_2 > c_2$		hyperbola: $\left(\frac{a_1 - a_2}{2}, \frac{S}{2}, \ell_2 + \varphi_2, O_2\right)$	ellipse: $\left(\frac{a_2}{2}, \frac{c_2}{2}, \ell_2 + \varphi_2, O_2\right)$	$a_2 - S_2$ $(r_0 < r')$
assuming:				
$a_1 > a_2$	non-contacting	ellipse: $\left(\frac{a_1 - a_2}{2}, \frac{S}{2}, \ell_2 + \varphi_2 - \pi, O_2\right)$	none	$a_2 + S_2$
	$S < a_1 - a_2$			
hyperbola-ellipse	intersecting	ellipse: $\left(\frac{\lvert a_1\rvert + a_2}{2}, \frac{S}{2}, \ell_2 + \varphi_2 - \pi, O_2\right)$	ellipse: $\left(\frac{a_2}{2}, \frac{c_2}{2}, \ell_2 + \pi, O_2\right)$	$a_2 - S_2$ $(r_0 < r')$
$a_1 < c_1$	$S < \lvert a_1\rvert + a_2$			
$a_2 > c_2$	non-contacting	hyperbola: $\left(\frac{\lvert a_1\rvert + a_2}{2}, \frac{S}{2}, \ell_2 + \varphi_2, O_2\right)$	none	$a_2 + S_2$
	$S > \lvert a_1\rvert + a_2$			

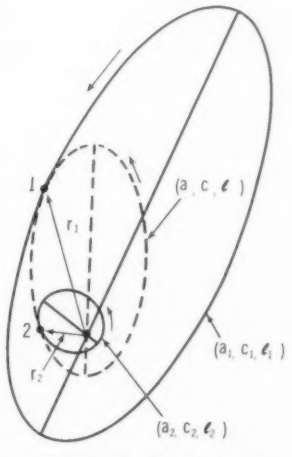

FIG. 9. Points of orbital transfer.

iary ellipse and the characteristic ellipse are as shown in Fig. 7. The transfer ellipse elements are $a = a_2 - S_2$; c^2 and l are given as before by the expressions in Eq. (III-10).

(B) When the terminal orbits are noncontacting, the auxiliary hyperbola is as shown in Fig. 8. The transfer orbit is specified by $a = a_2 + S_2$; c and l are given as before by the expressions in Eq. (III-8).

Since $$a^2 - c^2 = a_2^2 - c_2^2 + 2a_2S_2\,[1 + e_2 \cos(\eta_0 + \varphi_2)] > 0$$

for all values of η_0, all the possible contangential transfer orbits are elliptical.

(3) *Circular Cotangential Transfer Orbit*

It is easy to show that the necessary and sufficient condition for the existence of a cotangent transfer circle ($c = 0$) is as follows:

(A) Ellipse–Circle–Ellipse Transfer: $a_1 > a_2 > 0$

Intersecting terminal orbits:

$$a = r_{1A} = r_{2A} \quad \text{or} \quad a = r_{1P} = r_{2P}$$

Noncontacting terminal orbits:

$$a = r_{1P} = r_{2A}$$

(B) Hyperbola–Circle–Ellipse Transfer: $a_1 < 0$, $a_2 > 0$

Intersecting terminal orbits:

$$a = r_{1P} = r_{2P}$$

Noncontacting terminal orbits:

$$a = r_{1P} = r_{2A}$$

In all cases the center of the transfer circle is at the common focus F.

(IV) Computation of Transfer Ellipse Elements

From the above analysis the transfer ellipse elements a, c, and l are expressible as known functions of the true anomaly (η_0) of the auxiliary conic. Then the variations of a and c with l can be calculated by means of digital computer according to the formulas derived in the previous two sections. In this way, the calculation procedure becomes purely analytical.

If a high degree of accuracy is not required, as in a preliminary study, the geometrical method proposed in Table 1 may be used conveniently to obtain quick results.

In Table 1 we specify a given conic by a set of four parameters (a, c, l, F), where the parameters a, c, l are as previously defined. F signifies the location of the focus. Referring to Fig. 3, we are given, for the two terminal orbits, (a_1, c_1, l_1, F), center point O_1, and (a_2, c_2, l_2, F), center point O_2; (a, c, l, F) and center point O for the transfer orbit are to be determined. The procedure for geometrical solution is as follows:

(1) Draw the major axes of the terminal orbits through the common focus F according to their orientations, and measure S, φ_1, and φ_2.

(2) Construct the auxiliary conic (r_0, η_0) and the characteristic conic (r', η') according to Table 1.

(3) Measure c, l, r_0 for different applicable values of η_0.

(4) Calculate a according to the formulas in the table.

(V) Points of Transfer, Transfer Energy, and Transfer Time

The points of transfer (points of cotangency), the energy required for orbit change at transfer points, and the transfer time can all be expressed in terms of the transfer orbit elements a and c. Therefore, they are also functions of transfer orbit orientation l, and can be determined easily once $a(l)$ and $c(l)$ are obtained. The desired expressions for these important items will be derived in this section.

(1) *Points of Transfer*

Referring to Fig. 9, let

(r_1,η_1) = point of tangency between (a_1, c_1, l_1) and (a, c, l), where η_1 is referred to terminal orbit (a_1, c_1, l_1);

(r_2,η_2) = point of tangency between (a_2, c_2, l_2) and (a, c, l), where η_2 is referred to terminal orbit (a_2, c_2, l_2).

Applying Eqs. (II-5) and (II-6), we have, letting $i = 1, 2$,

$$r_i = 2\,\frac{ab_i^2 - a_ib^2}{b_i^2 - b^2}, \qquad \cos\eta_i = \frac{c_ib^2 - cb_i^2\cos(l_i - l)}{ab_i^2 - a_ib^2} \tag{V-1}$$

Thus when a, c, and hence b are known, the coordinates of points of transfer can be calculated by above equations. Conversely, if (r_1,η_1) and (r_2,η_2) are given, the required transfer orbit can be determined from the following expressions:

$$\left.\begin{aligned} a &= \frac{r_2k_1 - r_1k_2}{2(k_1 - k_2)} \quad \text{and} \quad c^2 = a^2 - \frac{r_2 - r_1}{k_1 - k_2} \\ \tan l &= -\frac{n_2\cos l_1 - n_1\cos l_2}{n_2\sin l_1 - n_1\sin l_2} \end{aligned}\right\} \tag{V-2}$$

where $$k_i = (2a_i - r_i)/b_i^2$$

and $$n_i = \left(\frac{a_i}{b_i^2} - \frac{a}{b^2}\right)\cos\eta_i + \frac{c_i}{b_i^2}$$

(2) *Transfer Energy Requirement*

From the standard expression of orbital velocity, the orbital velocity changes (energy changes) at r_i are

$$\Delta V_i = \sqrt{GM}\left|\left(\frac{2}{r_i} - \frac{1}{a_i}\right)^{1/2} - \left(\frac{2}{r_i} - \frac{1}{a}\right)^{1/2}\right| \tag{V-3}$$

The total energy required to complete the transfer is

$$\Delta V = \Delta V_1 + \Delta V_2 \qquad \text{(V-4)}$$

(3) Transfer Time

The flight time required in going from r_1 to r_2 along the transfer ellipse is obtained by applying Kepler's equation and Kepler's third law, which yield

$$\Delta t = \sqrt{a^3/GM}\,[E_2 - E_1 - e(\sin E_2 - \sin E_1)] \qquad \text{(V-5)}$$

with $\cos E_i = (a - r_i)/c$

References

[1] Lawden, D. F., *Orbital Transfer via Tangential Ellipses*, Journal of the British Interplanetary Society, Vol. II, No. 6, pp. 278–289, November 1952.

[2] Gedeon, Geza S., *Orbital Mechanics of Satellites*, in *Advances in Astronautical Sciences*, Vol. 3, pp. 19-1 to 19-33; Plenum Press, Inc., New York, 1958.

[3] Gedeon, Geza S., *The Intersection of Coplanar, Confocal Conic Sections*, The Journal of the Astronautical Science, Vol. VII, No. 2, pp. 45–46, Summer 1960.

✦ ✦ ✦

Laminar Stability (*Continued from page 404*)

(4) At finite Reynolds numbers, the quasi-steady solution, based upon the instantaneous profile, may be justified only if the time constant of the basic flow is much greater than $Re^{1/2} \times$ (the time constant of the disturbances of the instantaneous profile), Re being the instantaneous Reynolds number. Furthermore, it is still necessary to compute the "growth rate" to arrive at a statement about the stability of the basic flows, even if the quasi-steady solution itself is acceptable. The quasi-steady "neutral curve" provides little information regarding the stability of time-dependent basic flows.

(5) For slowly varying but otherwise arbitrary velocity profiles, the procedure of analysis (with certain restrictions) is outlined briefly. For points along, say, the quasi-steady neutral curve, both the inviscid and viscous solutions for the time-dependent basic flow may be thus constructed. On the basis of these solutions it will be possible to establish contours of constant growth rate similar to the contours for constant amplification or decay in the steady case.

References

[1] Taylor, G. I., *Some Recent Developments in the Study of Turbulence*, Proc. 5th Congress Appl. Mech., Cambridge, Mass., pp. 294–310, 1938.

[2] Schubauer, G. B., and Skramstad, H. K., *Laminar Boundary Layer Oscillations and Transition on a Flat Plate*, Journal of the Aeronautical Sciences, Vol. 14, pp. 69–78, 1947.

[3] Schlichting, H., *Über die Entstehung der Turbulenz in einem rotierenden Zylinder*, Nachr. Ges. Wiss. Goettingen, Math.-Physik Kl., pp. 160–198, 1932.

[4] Fales, E. N., *A New Laboratory Technique for Investigation of the Origin of Fluid Turbulence*, J. Franklin Inst., Vol. 259, pp. 491–414, 1955.

[5] Coles, D., *Motion Picture on Circular Couette Flow*, submitted to Nat. Sci. Foundation under Grant G-3494, April 1958.

[6] von Kármán, Th., and Lin, C. C., *Theoretical Comments on Paper by Mr. E. N. Fales*, J. Franklin Inst., Vol. 259, pp. 517–518, 1955.

[7] Lin, C. C., *The Theory of Hydrodynamic Stability*, Cambridge University Press, 1955.

[8] Lin, C. C., *A Critical Discussion of Similarity Concepts in Isotropic Turbulence*, Proc. Symp. Appl. Math. (Amer. Math. Soc.), Vol. 4, pp. 19–27, 1951.

[9] Pretsch, J., *Die Anfachung instabiler Störungen in einer laminaren Reibungsschicht*, Jahrbuch der deutschen Luftfahrtforschung, pp. 154–71, 1942.

✦ ✦ ✦

Change of Address

Since the Post Office Department does not as a rule forward magazines to forwarding addresses, it is important that the Institute be notified of changes in address 30 days in advance of publishing date to ensure receipt of every issue of the JOURNAL and AEROSPACE ENGINEERING. Notices should be printed legibly and sent to:

Circulation Department
Institute of the Aerospace Sciences, Inc.
2 East 64th Street, New York 21, N.Y.

Readers' Forum

BRIEF REPORTS of investigations in the aerospace sciences and discussions of papers published in the JOURNAL are presented in this special department. Entries must be restricted to a maximum of 1,300 words or the equivalent of one JOURNAL page including formulas and illustrations. Publication is completed as soon as possible after receipt of the material. The Editorial Committee does not hold itself responsible for the opinions expressed by the correspondents.

Contents

Further Comments on "Standing Detonation Waves in a Combustion Tunnel" ..... THOMAS C. ADAMSON, JR. 418

Transit Angle for Low-Thrust Spacecraft ..... FRANK M. PERKINS 419

Generalized Spectral Representation in Aeroelasticity: Part II ..... ARTHUR K. CROSS 420

A Drag Hypothesis for Jet-Flapped Wings ..... G. K. KORBACHER 421

Author's Reply ..... ELLIOTT G. REID 422

On a Generalized Solution to a Torsion Problem in Linear Elasticity ..... HOWARD E. BRANDT 422

The Torsion of Prismatic Bars of Regular Polygonal Cross Section ..... F. W. NIEDENFUHR and A. W. LEISSA 424

A Note on the Motion of a Spinning Rocket With Eccentric Thrust ..... A. G. BENNETT 426

On the Rolling Motion of Low-Aspect Ratio Delta Wings ..... PETER J. MANTLE 427

Higher Order Theory of Curved Shock ..... REUBEN R. CHOW AND LU TING 428

Note on Three-Dimensional Free-Mixing ..... MARTIN H. BLOOM 430

Losses in Subsonic and Transonic Axial-Flow Compressors at Optimum Conditions ..... GAETANO E. PROVENZALE 431

Some Comments on the Inversion of Certain Large Matrices ..... BERTRAM KLEIN 432

Further Comments on "Standing Detonation Waves in a Combustion Tunnel"

Thomas C. Adamson, Jr.
Associate Professor, Aeronautical and Astronautical Engineering Department, The University of Michigan, Ann Arbor, Mich.

February 3, 1961

RECENTLY, Kovitz[1] attempted to explain the anomalous results obtained by Gross and Chinitz[2] in a supersonic combustion tunnel. Specifically, he presented a gross method to explain the movement of a standing detonation wave to a new location as the amount of hydrogen injected was changed, along with speculation as to whether this same method might be of value in explaining the so-called hysteresis effect (persistence of the detonation wave, once formed, even after the incoming temperature has been reduced below the value necessary to start the reaction). In this method it was assumed that all upstream flow properties other than fuel flow remained constant, and that any reaction occurring at the injector was negligible.

There are many possible explanations for the results obtained by Gross and Chinitz. One of these includes the possibility that the above-mentioned wave movement and hysteresis simply do not exist under constant upstream conditions and that, in fact, in the Gross-Chinitz tunnel, an unknown amount of reaction occurred at the fuel injector. Keeping in mind the constant incoming Mach number and the structure of the detonation wave, this explanation makes the most physical sense. Additional validity is ascribed to this explanation by the fact that Nicholls[3] was unable to reproduce these anomalous results in his facility. However, decisive proof has been given by Rhodes.[4] Using the Gross-Chinitz combustion tunnel, which has been moved to the Arnold Engineering Development Center, Rhodes reports the following results,[4]: "the phenomena observed at Fairchild, in which the position of the normal shock is a function

Contributors Please Note

Readers' Forum items must be confined to the equivalent of one page in the *Journal*. Contributions that exceed this limit will be returned to the authors for condensation and rewrite. To avoid inconvenience and delay, please adhere to the following specifications:

(1) Five, double-spaced, typewritten, manuscript pages (8½ by 11 in.), including wide margins, equations, and headings, equal one printed page.

(2) For every illustration, deduct at least one-half or as much as one manuscript page, depending on the size of the illustration.

of the fuel flow and the wave is stable at a much lower temperature than that required to ignite it, was duplicated. Under these conditions, a flame near the tip of the hydrogen injector and a sodium emission upstream of the normal shock were seen. The hydrogen injector was modified to inject fuel at the throat of the tunnel. Under these conditions, no flame at the injector and no evidence of reaction upstream of the shock were seen. Also, although there was a temperature rise in the test section upon the addition of hydrogen from the injector, there was no movement of shock. No evidence of reaction was seen in the test section when the inlet temperature was reduced below the ignition point."

It seems clear that (1) the varying shock position and hysteresis phenomena do not exist with constant upstream conditions, and thus (2) Kovitz' analysis is not relevant.

References

[1] Kovitz, A. A., *Some Comments on Standing Detonation Waves*, Journal of the Aerospace Sciences, Readers' Forum, Vol. 28, No. 1, pp. 75–76, January 1961.

[2] Gross, R. A., and Chinitz, W., *A Study of Supersonic Combustion*, Journal of the Aero/Space Sciences, Vol. 27, No. 7, pp. 517–524, July 1960.

[3] Nicholls, J. A., and Dabora, E. K., *Recent Results on Standing Detonation Waves*, AFOSR TN-60-441, May 1960. Presented at the Eighth International Symposium on Combustion held at California Institute of Technology, August 29–September 2, 1960.

[4] Rhodes, R. P., *Standing Detonation Wave*, Proceedings of Fourth Contractor's Meeting on Airbreathing Combustion, AFOSR TN-60-1253, p. 5, October 1960.

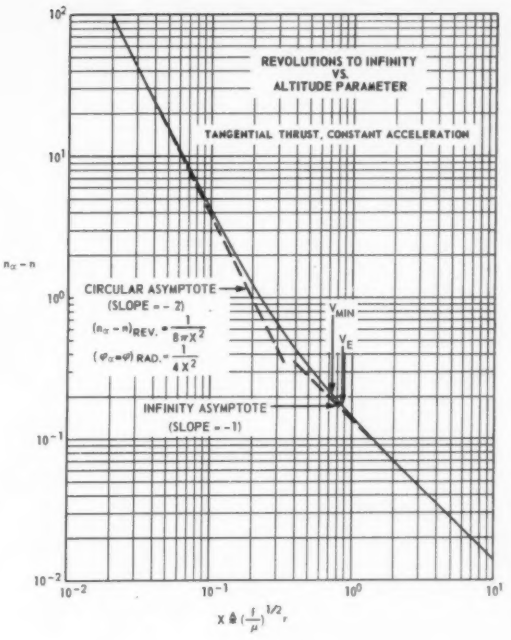

FIG. 1.

Transit Angle for Low-Thrust Spacecraft

Frank M. Perkins
Staff Systems Analyst, Engineering, Convair, A Division of General Dynamics Corporation, San Diego, Calif.

September 30, 1960

THE COMPLETELY GENERALIZED SOLUTION for trajectory prediction of low-thrust spacecraft employing a tangentially directed, constant-thrust acceleration and operating in a single gravity field is presented in reference 1. The relations between altitude, velocity, flight-path inclination, and time are presented in parametric form as single-valued solitary curves applicable for flight all the way from an initial circular orbit on out to infinity. These curves apply to all tangential, constant-acceleration, low-thrust flight paths starting in circular orbit at any altitude about any planet.

Reference 1 omitted the solution for the angle subtended at the center of the gravity source by the travel of the spacecraft (range or transit angle). This solution is presented in Fig. 1 as a number of revolutions, starting at any point on the trajectory and ending as the spacecraft approaches infinity, versus the altitude parameter X. To determine the revolutions traversed between any two points on the trajectory, it is merely necessary to take the difference between the two points on Fig. 1. The altitude parameter X is defined in reference 1 as follows:

$$X = a^{1/2}(r/r_0) = (f/\mu)^{1/2} r \tag{1}$$

where r = distance from center of planet
f = thrust acceleration = force/mass
μ = gravity constant (distance^3/time^2) = $r^2 g$
g = gravity acceleration (at any altitude)
a = dimensionless thrust acceleration = $f/(\mu/r_0^2)$

and where subscript 0 denotes the initial circular orbit.

The equation for the circular asymptote of Fig. 1 is obtained by putting Eq. (14) of reference 1 into local differential form, substituting the circular velocity relationship from Eq. (20) into this, and integrating to infinity. Of course, circular flight does not apply all the way to infinity, but for the purpose of obtaining the circular asymptote, it may be assumed to apply in the mathematical sense.

The slope of the infinity asymptote of Fig. 1 may be derived as follows. By definition, the rate of change of the transit or range angle φ and radius distance r with time are,

$$\dot{\varphi} = (V \cos \theta)/r \tag{2}$$

$$\dot{r} = V \sin \theta \tag{3}$$

where θ is the flight-path angle measured above local horizontal.

At α $$\sin \theta \to 1.0 \tag{4}$$

Dividing Eq. (2) by Eq. (3) and bearing in mind that Eq. (4) yields

$$d\varphi/dr = \cos \theta/r \tag{5}$$

Multiplying both sides by $r/(\varphi_\alpha - \varphi)$ and then putting r in terms of the altitude parameter X results in the following:

$$\frac{d \ln (\varphi_\alpha - \varphi)}{d \ln X} = \frac{-\cos \theta}{\varphi_\alpha - \varphi} = -\frac{\to 0}{\to 0} \tag{6}$$

Since both the numerator and denominator of the right-hand side of Eq. (6) approach zero, the value of this fraction is equal to the ratio of the time differentials of the numerator and denominator at infinity. Performing the differentiation and substituting Eq. (4) into the numerator yields

$$\frac{d \ln (\varphi_\alpha - \varphi)}{d \ln X} = \frac{\dot{\theta}}{-\dot{\varphi}} \tag{7}$$

As the vehicle approaches infinity, the gravity which had caused the flight path to turn becomes negligible compared to the thrust acceleration, and the flight path approaches a straight line. Under these conditions, the rates of change of both flight-path angle $\dot{\theta}$ and transit angle $\dot{\varphi}$ approach $V \cos \theta/r$. Therefore,

$$\dot{\theta} = \dot{\varphi} \tag{8}$$

and the logarithmic slope of Eq. (7) becomes minus one:

$$\frac{d \ln (\varphi_\alpha - \varphi)}{d \ln X} = -1.0 \tag{9}$$

It is interesting to note that although the flight-path angle changes from 39.2° at the parabolic escape point to approach

90° at infinity (reference 1), the vehicle completes only about 0.17 revolutions during this phase of the trajectory.

The same type of parametric generalization used for tangential thrust in reference 1 is applicable to the case of horizontal thrust as well. The parametric curves are omitted here to conserve space. There is very little difference in the trajectories up to the parabolic escape point, although the difference then becomes marked because of the high flight-path angle. There may be some navigational simplicity in maintaining horizontal thrust when an horizon scanner is used to determine local vertical. When the flight-path angle becomes appreciable, however, the energy gained by the vehicle per unit of propellant expended is much higher by directing the thrust along the local velocity vector.

References

[1] Perkins, Frank M., *Flight Mechanics of Low-Thrust Spacecraft*, Journal of Aero/Space Sciences, Vol. 26, No. 5, pp. 291–297, May 1959.

Generalized Spectral Representation in Aeroelasticity: Part II

Arthur K. Cross
Norair Division, Northrop Corporation, Los Angeles, Calif.
September 28, 1960

In a previous note,[1] a formalism was developed by which measured modal information can be converted into stiffness information. These dynamically measured stiffness data show in detail any defects present in theoretical stiffness data or in stiffness data determined by static testing procedures. Examples for highly idealized wings with elastic axes were then outlined. It is proposed in the present note to apply the method to a general unrestrained, statically indeterminate structure with the aid of a greatly simplified formulation of Eqs. (8) to (12) of reference 1.

In terms of the notation of reference 1, the equations of motion for unrestrained vibration are

$$\mathbf{H} \equiv H - L_0 q_0 = \omega^2 CMH \tag{1}$$

$$-L_0{}^t MH = L_1 q_0 = -L_2 L_3 H \tag{2}$$

Operating on Eq. (1) with $-L_0{}^t M$ yields

$$-L_0{}^t MH + L_0{}^t ML_0 q_0 = -\omega^2 L_0{}^t MCMH \tag{3}$$

After elimination of $-L_0{}^t MH$ between Eqs. (2) and (3), there results

$$-\omega^2 L_0{}^t MCMH = (L_1 + L_0{}^t ML_0) q_0 \tag{4}$$

Consequently q_0 can be eliminated between Eq. (1) and Eq. (4) so that

$$H = \omega^2 [I - L_0(L_1 + L_0{}^t ML_0)^{-1} L_0{}^t M] CMH = \omega^2 KCMH \tag{5}$$

Alternatively, K may be calculated by eliminating q_0 between Eqs. (1) and (2) with the result that

$$K = (I + L_0 L_1{}^{-1} L_0{}^t M)^{-1} \tag{6}$$

Then the spectral representation for C is

$$C = K^{-1} \sum_{i=1}^{3m} \omega_i{}^{-2} H_i \mathbf{H}_i{}^t / \mathbf{H}_i{}^t M H_i \tag{7}$$

The above formulation is somewhat awkward, since it requires separate handling of the mode shapes at the reference station (the q_0 matrix) and the mode shapes at the other stations (the H matrix). The following reformulation of Eqs. (1) to (6) is based on a straightforward coordinate transformation.

Consider a general unrestrained structure having $6m$ elastic degrees of freedom and 6 rigid degrees for which a $[6(m+1) \times 1]$ mode-shape matrix is denoted by Y where

$$Y^t = [H^t, q_0{}^t] \tag{8}$$

Then $\mathbf{H}$ and Y are related as follows:

$$\mathbf{H} = UY \quad \text{where} \quad U \equiv [I, -L_0] \tag{9}$$

[where I denotes a $(6m \times 6m)$ unit matrix and L_0 is a $(6m \times 6)$ generalization of the rigid-body mode-shape matrix L_0 defined in reference 1].

The representations of the stiffness and mass matrices relative to the new coordinates Y are denoted by the symbols χ and μ, respectively, and are determined by the condition that the strain energy V and the kinetic energy T be invariant:

$$V = (1/2)\mathbf{H}^t C^{-1} \mathbf{H} = (1/2) Y^t [U^t C^{-1} U] Y \equiv (1/2) Y^t \chi Y \tag{10}$$

$$T = (1/2)\dot{\mathbf{H}}^t M \dot{\mathbf{H}} \equiv (1/2)\dot{Y}^t \mu \dot{Y} \tag{11}$$

Thus the $[6(m+1) \times 6(m+1)]$ matrices χ and μ are defined as follows:

$$\chi \equiv U^t C^{-1} U, \qquad \mu \equiv \begin{bmatrix} M & O \\ O & L_1 \end{bmatrix} \tag{12}$$

The equations of motion in the new coordinates are found by varying the energy $\mathbf{E}$, which is expressed in the new coordinates as follows:

$$\mathbf{E} = T + V = (1/2)[Y^t \chi Y - \omega^2 Y^t \mu Y] \tag{13}$$

Then

$$\delta \mathbf{E} = O = \delta Y^t (\chi Y - \omega^2 \mu Y) \tag{14}$$

Since the variations δY are independent,

$$\chi Y = \omega^2 \mu Y \tag{15}$$

For a system acted on by motion dependent or other forces described by the $[6(m+1) \times 1]$ matrix $F(t)$, the variational condition (14) is replaced by a condition involving the generalized work $W = Y^t F(t)$:

$$\delta \int_{t_1}^{t_2} [L + W] dt = 0 = -\int_{t_1}^{t_2} \delta Y^t [\mu \ddot{Y} + \chi Y - F(t)] dt \tag{16}$$

The independence of the variations δY then implies that

$$\mu \ddot{Y} + \chi Y = F(t) \tag{17}$$

The above representation is particularly advantageous when it is desired to reduce the size of the matrices involved by converting to a modal description. Then, if the coordinate transformation

$$Y(t) = SC(t) \tag{18}$$

is carried out, where S represents a $[6(m+1) \times p]$ matrix of expansion functions and $C(t)$ is a $(p \times 1)$ matrix of generalized modal coordinates, the following variational condition results from the substitution of Eq. (18) into Eq. (16):

$$\delta \int_{t_1}^{t_2} [L + W] dt = -\int_{t_1}^{t_2} \delta C^t(t) [M_g \ddot{C}(t) + K_g C(t) - S^t F(t)] dt \tag{19}$$

Hence the equations of motion for the forced system have the following form in the new coordinates:

$$M_g \ddot{C}(t) + K_g C(t) = F_g(t) \tag{20}$$

where

$$M_g \equiv S^t \mu S, \quad K_g \equiv S^t \chi S, \quad \text{and} \quad F_g(t) \equiv S^t F(t) \tag{21}$$

are the generalized mass, stiffness, and force matrices, respectively.

The application of the coordinate transformation (9) to the construction of the spectral representation of the flexibility matrix of an unrestrained redundant structure is outlined below. It is assumed that n external loads described by an $(n \times 1)$ matrix E are applied to the structure under consideration. These loads produce n statically determinate loads and r redundant loads which are described, respectively, by an $(n \times 1)$ matrix D and an $(r \times 1)$ matrix R. In practice, the equality of the number of external loads and statically determinate loads must be achieved by a judicious choice of lumped-mass locations so that using the same number of lumped masses (i.e., the

number of "external" or inertia loads) and statically determinate loads does not result in singular matrices **T** and **V** where the latter are matrices of the coefficients of the relations between the applied, statically determinate, and redundant loads. That is,

$$D = \mathbf{T}R + \mathbf{V}E \tag{22}$$

(The restriction does not apply to **T** for cases where $r \neq n$, for then **T** is rectangular.) In terms of the local flexibility-property matrix B and the statically determinate loads matrix D as given by Eq. (22), the strain energy may be expressed as

$$V = (1/2)D^tBD \tag{23}$$

The variational principle (16) implies in the present case that

$$\delta(V - W) = \delta[(1/2)D^tBD - E^tY] = 0 \tag{24}$$

Substitution of Eq. (22) into Eq. (24) and explicit evaluation of the variation yields

$$\delta R^t[(\mathbf{T}^tB\mathbf{V})E + (\mathbf{T}^tB\mathbf{T})R] + \delta E^t[(\mathbf{V}^tB\mathbf{T})R + (\mathbf{V}^tB\mathbf{V})\mathbf{E} - Y] = 0 \tag{25}$$

Since the variations δR and δE are independent, R may be eliminated between the two resulting equations with the well-known result that

$$Y = [\mathbf{V}^tB\mathbf{V} - (\mathbf{V}^tB\mathbf{T})(\mathbf{T}^tB\mathbf{T})^{-1}(\mathbf{T}^tB\mathbf{V})]\mathbf{E} = C\mathbf{E} \tag{26}$$

According to Eq. (15) above and Eq. (7b) of reference 1, χ can be determined from experimental modes Y_i by the following expansion:

$$\chi = \sum_{i=1}^{6m} \omega_i^2 \mu Y_i Y_i^t \mu / Y_i^t \mu Y_i \qquad (6m \equiv n) \tag{27}$$

The basic flexibility-data matrix B is determined from the empirically determined χ^{-1} matrix by noting that Eqs. (9) and (12) imply that the upper left $(6m \times 6m)$ submatrix of χ is C^{-1}. Inspection of Eq. (26) shows that B can be determined by iteration—i.e., if B_0 is taken to be the theoretically determined basic flexibility-data matrix,

$$B_{n+1} = (\mathbf{V}^t)^{-1}[\mathbf{C} + (\mathbf{V}^tB_n\mathbf{T})(\mathbf{T}^tB_n\mathbf{T})^{-1}(\mathbf{T}^tB_n\mathbf{V})]\mathbf{V}^{-1} \tag{28}$$

Examination of the elements of the empirical B matrix thus determined reveals any defects present in either the idealization of the actual structure or the static measurement of the geometric data or elastic constants. If a flutter model is constructed with internal structure corresponding to that of the actual airplane, comparison of the dynamically measured B matrices of each can suggest structural changes in the model to improve the simulation of the airplane-stiffness properties.

References

[1] Cross, A. K., *Generalized Spectral Representation in Aeroelasticity*, Journal of the Aero/Space Sciences, Readers' Forum, Vol. 26, No. 11, pp. 766–767, November 1959.

A Drag Hypothesis for Jet-Flapped Wings

G. K. Korbacher
Assistant Professor of Aeronautical Engineering, Institute of Aerophysics, University of Toronto, Toronto, Ontario, Canada
June 28, 1960

UNDER THE HEADING "Jet-Flap Thrust Recovery," Foley and Reid[1] recently announced the "significant finding that substantially complete thrust recovery has been obtained in two-dimensional-flow tests on a jet-flap wing." This finding is based on experimental results (Figs. 3 and 4 of reference 1). The constant slope of the lines in Fig. 3 of reference 1, which is the same as the slope 0.94 in Fig. 4 of reference 1, represents a thrust-recovery factor of 0.94. This finding is substantiated by test results of NGTE[2, 3] and ONERA[4] as shown in reference 5.

A value of 0.0243 for the slope dc_D/dc_L^2 is used in reference 1 in the transformation of the experimental values of Fig. 3 to those of Fig. 4. The choice of this value does not affect the slope 0.94 of the "experiment" line in Fig. 4 (reference 1), but it changes its intercept with the vertical axis. As this point of intercept can be obtained from the test results of Fig. 2 (reference 1) at $c_\mu = 0$—at least as an average value—the value by which c_L^2 has to be multiplied is indirectly fixed.

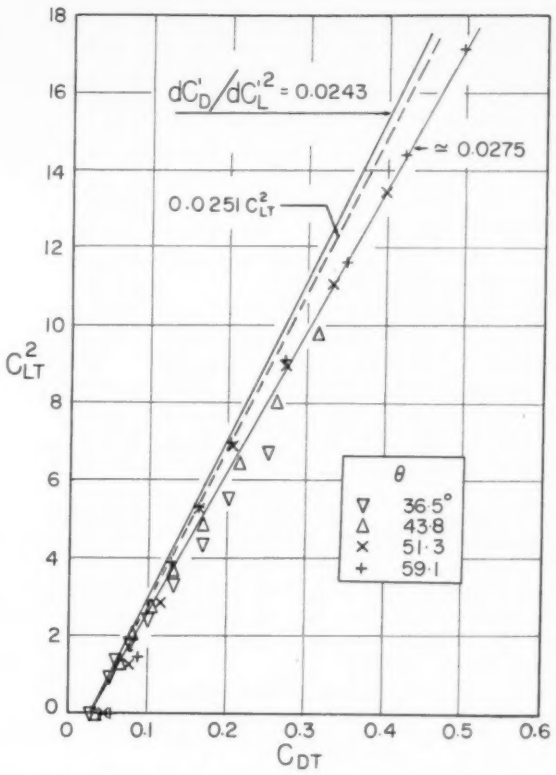

FIG. 1. Total drag vs. total lift squared (test results of reference 1).

According to reference 1, the value 0.0243 was established by measuring wing forces at various angles of attack with the slot sealed ($c_\mu = 0$) and flap undeflected. One would prefer, however, the use of the dc_{DT}/dc_{LT}^2 of the jet-flapped wing ($c_\mu \neq 0$), where the subscript T designates total values. The use of $(dc_D/dc_L^2)_{c_\mu=0}$ instead implies the "drag hypothesis" (formerly suggested in reference 4) as

$$(dc_D/dc_L^2)_{c_\mu=0} = dc_{DT}/dc_{LT}^2 = 0.0243 \tag{1}$$

No doubt, this relationship would be of great significance if it could be proved to be true. It seems, however, that the test results of reference 1 leave some doubt about the validity of this hypothesis. Additional information about $(dc_D/dc_L^2)_{c_\mu=0}$ is required from researchers who work with two-dimensional jet-flap wings, in order to prove or disprove Eq. (1) for jet-flap wings in general.

If one plots the crucial graph of the total drag vs. the total lift-squared from the test results of reference 1, Fig. 1 is obtained. It shows that the drag hypothesis can be considered only as an approximation.

Next, if all two-dimensional jet-flap test results[2–4] are consulted in order to establish whether dc_{DT}/dc_{LT}^2 is a constant or may be approximated by a constant over a limited c_μ-range ($c_\mu \leq 1$), one still does not obtain a unique answer.[5]

Finally, if established empirical relationships and theoretical predictions are used, the following relationship is derived[6]

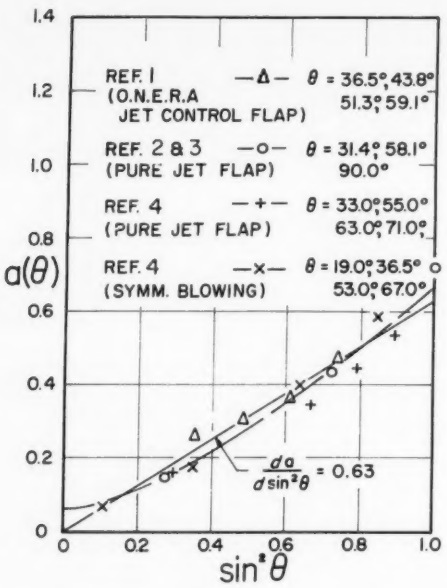

FIG. 2. Plot of a (θ) vs. $\sin^2\theta$ for all available two-dimensional jet-flap results.

$$dc_{DT}/dc_{LT}{}^2 = 0.63/K^2 \tag{2}$$

Here K^2 is a specific constant for each particular jet-flap wing and can be obtained from[4, 6]

$$c_{LT} = K\, c^{1/2} \sin\theta \tag{3}$$

where θ is the jet deflection angle. The constant 0.63 follows from[2]

$$c_{DT} = (c_D)_{c_\mu=0} + a(\theta)\, c_\mu \tag{4}$$

which after differentiation with respect to c_μ produces $a(\theta)$. Now if from all available two-dimensional jet-flap tests results $a(\theta)$ is plotted vs. $\sin^2\theta$, Fig. 2 is obtained[5] and the result is

$$d\, a(\theta)/d\, \sin^2\theta = \text{const.} = 0.63 \tag{5}$$

Eq. (2) suggests that $dc_{DT}/dc_{LT}{}^2$ is a constant as long as K is a constant or can be approximated by a constant over at least a limited range of c_μ-values. It was found[6] that for $c_\mu \leq 1$, K can be considered a constant, but that for $c_\mu \geq 3$, this no longer seems to be the case.

Spence[7] has derived an expression from which it follows that K is a constant only for small values of c_μ; for higher c_μ = values, K becomes a function of c_μ and increases with c_μ. Fortunately, the average c_μ-value for jet-engine-powered aircraft at the moment of take-off is as low as 0.5. A preliminary study[8] of how their take-off characteristics can be improved with a jet-flapped wing indicated jet coefficients at take-off still below 2.5. This suggests that the practical range of jet coefficients coincides well with that for which the above relationships are applicable.

Finally, the predictions of Eq. (2) may be compared with those of Maskell's and Spence's theory[9] for three-dimensional jet-flapped wings. Since Eq. (2) was derived from quasi-two-dimensional test results, this comparison can only be qualitative. From theory[9] follows

$$dc_{DT}/dc_{LT}{}^2 = 1/(\pi AR + 2c_\mu) \tag{6}$$

This equation, for $\pi AR \gg 2c_\mu$ reduces to

$$dc_{DT}/dc_{LT}{}^2 \simeq 1/\pi AR = (dc_D/dc_L{}^2)_{c_\mu=0} \tag{7}$$

This brings out the limitation of the drag hypothesis. Further, Eq. (6) predicts a decrease in slope with increasing c_μ. Thus, the predictions of Eqs. (2) and (6) agree in principle.

REFERENCES

[1] Foley, W. M., and Reid, E. G., *Jet Flap Thrust Recovery*, Journal of the Aero/Space Sciences, Vol. 26, No. 6, pp. 385–387, June, 1959.

[2] Dimmock, N. A., *An Experimental Introduction to the Jet Flap*, NGTE, Rept. No. R175, July, 1955.

[3] Dimmock, N. A., *Some Further Jet Flap Experiments*, NGTE, Memo No. M255, 1956.

[4] Malavard, L., Poisson-Quinton, Ph., and Jousserandot, P., *Theoretical and Experimental Investigations of Circulation Control*, ONERA TN No. 37, June, 1956.

[5] Korbacher, G. K., and Sridhar, K., *A Note on the Total Drag of Jet Flapped Wings*, UTIA Rept. No. 64, May, 1960.

[6] Dimmock, N. A., *Some Early Jet Flap Experiments*, Aero. Quart., Vol. 8, Part 4, November, 1957.

[7] Spence, D. A., *A Treatment of Jet Flap by Thin Aerofoil Theory*, RAE Rept. Aero–2568, November, 1955; also, *The Lift Coefficient of a Thin Jet-Flapped Wing*, Royal Soc. Proc. Ser. (A) 238, 46–68, 1956.

[8] Korbacher, G. K., *The Jet Flap and STOL*, Decennial Symposium at UTIA, October, 1959.

[9] Maskell, E. C., and Spence, D. A., *A Theory of the Jet Flap in Three Dimensions*, RAE Rept. Aero–2612, September, 1958; also Royal Soc. Proc. Ser. (A) 251, 407–425, 1959.

Author's Reply

Elliott G. Reid
Stanford University, Department of Aeronautical Engineering, Stanford, Calif.
June 28, 1960

THE SUBJECT OF THIS COMMENT is the final sentence of Professor Korbacher's first paragraph; the statement therein that Foley's finding "is substantiated" by earlier British and French work is incorrect.

The fact is that the results of the cited experiments are so conspicuously inconclusive in their failure to demonstrate anything approaching complete thrust recovery that they actually provided the principal impetus for the Standford investigation—which was directed specifically toward "verification or disproval of the jet-flap thrust recovery theorem."

Foley's work resulted in the demonstration of thrust recovery in excess of 90 percent at jet deflection angles as large as 59.1 deg. This is hardly "substantiated" by the recovery of only 64 percent of the jet reaction at a slightly smaller deflection (58.1 deg.) in the NGTE work—the results of which are summarized in Fig. 4 of Korbacher's reference 6. Dimmock's comment on this point (p. 335, reference 6) is significant; he says, "The existence of a pressure thrust is undeniable, but its magnitude relative to the full jet reaction was initially rather disappointing."

To the best of the writer's knowledge, Foley's finding was unique when published and has been substantiated only by the results of subsequent Stanford work—of which no account has as yet been published.

On a Generalized Solution to a Torsion Problem in Linear Elasticity

Howard E. Brandt
Physics Student, Massachusetts Institute of Technology, Cambridge, Mass.
August 10, 1960

RECENTLY, Stanišić[1–3] with his students at Purdue University published a number of excellent papers concerning the torsion of prismatical bars with various cross sections. In each of these papers the application of the Galerkin method has been dexterously illustrated. The advantages of this method have been shown by Krylov and Kantorovich,[4] Stanišić,[5] Sokolnikoff,[6] and innumerable other scientists in the field of mathematical physics. Stanišić has developed the problem

for the torsion of a prismatical bar with hexagonal cross section.[3] However, this problem can be generalized, and the stress and displacement fields can be obtained for any N-sided polygonal cross section, using a transform technique illustrated in this paper. This generalization is a result of the topological character of the stress function in the Prandtl sense and is associated with the properties of the Laplacian operator. Moreover, this problem has wide application in the design of transport jet engines. Hence, in that which follows, a technique will be developed in order to find the stress, displacement, and torsional rigidity for any prismatical bar of N-sided regular polygonal cross section. Stanišić's solution then becomes a special case of this study.

Mathematical Formulation of the Problem and its Solution

The solution to the problem will be found by use of the Prandtl stress function, applying the Galerkin method. This method for determining stress and displacement fields has been outlined by Stanišić and Shirely.[2] Therefore, only the mathematical analysis peculiar to the immediate problem will be presented in this paper.

The stress function is assumed in the Prandtl sense,

$$\psi(x, y) = \sum_{m=1}^{n} A_m \eta_m(x, y), \qquad (m = 1, 2, 3, \ldots, n) \tag{1}$$

and the Galerkin form of the stated problem becomes

$$\iint_S \nabla^2[\psi(x, y) + 2]\eta_r(x, y)dS = 0, \quad (r = 1, 2, 3, \ldots, n) \tag{2}$$

where $\eta_r(x, y)$ are coordinate functions which must be found, such that the boundary condition $\psi(\Gamma) = 0$ is satisfied on the boundary Γ of the N-sided polygon; A_m are constants satisfying Eq. (2); and S is the domain of integration.

We first find a function, $\psi(x, y)$, which satisfies the boundary condition $\psi(\Gamma) = 0$. For this purpose refer to Fig. 1. The regular polygonal cross section has N sides which divide the polygon into N-congruent isosceles triangular surfaces, S_1, S_2, ..., S_{N-1}, S_N. The base vertices of S_m, $m = 1, 2, \ldots, N-1, N$, are the points, $P_{m-1}(x_{m-1}, y_{m-1})$ and $P_m(x_m, y_m)$. A function $\psi(x, y)$ defined on the polygonal surface must be found such that the boundary condition is satisfied along the lines, L_m, passing through the points, P_m and P_{m-1}. It is readily shown that

$$L_m \equiv x \cos(\pi/N)(2m - 1) + y \sin(\pi/N)(2m - 1) - R = 0 \qquad (m = 1, 2, 3, \ldots, N) \tag{3}$$

Hence $\psi(x, y)$ will be of the following form

$$\psi(x, y) = A_1 \prod_{n=1}^{N}\left[x \cos\frac{\pi}{N}(2n - 1) + y \sin\frac{\pi}{N}(2n - 1) - R\right] \tag{4}$$

where A_1 is a constant of first approximation to be determined later and $\prod$ denotes the product of expressions with indicated index. Hence Eq. (2) becomes

$$\iint_S [A_1\nabla^2\eta_1(x, y) + 2]\eta_1(x, y)dS = 0 \tag{5}$$

where

$$\eta_1(x, y) = \prod_{n=1}^{N}\left[x \cos\frac{\pi}{N}(2n - 1) + y \sin\frac{\pi}{N}(2n - 1) - R\right] \tag{6}$$

Solving for A_1 yields

$$A_1 = -2\,\frac{\sum_{m=1}^{N}\iint_{S_m}\prod_{n=1}^{N}\phi_n(x, y)dS}{\sum_{m=1}^{N}\iint_{S_m}\left\{\nabla^2\prod_{n=1}^{N}\phi_n(x, y)\right\}\prod_{n=1}^{N}\phi_n(x, y)dS} \tag{7}$$

where the integrals are evaluated over the respective triangles, S_m, and

$$\phi_n(x, y) = x \cos(\pi/N)(2n - 1) + y \sin(\pi/N)(2n - 1) - R \tag{8}$$

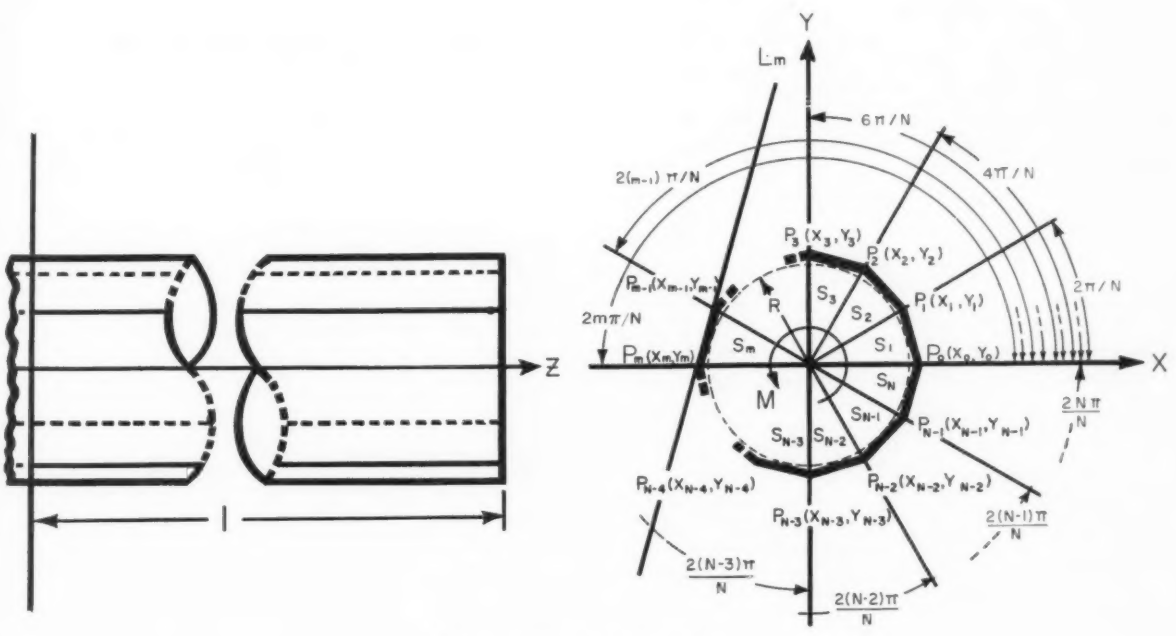

Fig. 1. Geometry of the section.

But it is readily shown that

$$\nabla^2 \prod_{n=1}^{N} \phi_n(x, y) = \prod_{n=1}^{N} \phi_n(x, y) \left\{ \nabla^2 \sum_{n=1}^{N} \log_e \phi_n(x, y) + \left[\frac{\partial}{\partial x} \sum_{n=1}^{N} \log_e \phi_n(x, y) \right]^2 + \left[\frac{\partial}{\partial y} \sum_{n=1}^{N} \log_e \phi_n(x, y) \right]^2 \right\}$$

$$= \prod_{n=1}^{N} \phi_n(x, y) \left\{ - \sum_{n=1}^{N} \phi_n^{-2}(x, y) + \left[\sum_{n=1}^{N} \frac{\cos (2n - 1)\pi/N}{\phi_n(x, y)} \right]^2 + \left[\sum_{n=1}^{N} \frac{\sin (2n - 1)\pi/N}{\phi_n(x, y)} \right]^2 \right\}$$

or

$$\nabla^2 \prod_{n=1}^{N} \phi_n(x, y) = - \prod_{n=1}^{N} \phi_n(x, y) \sum_{k=1}^{N} \left\{ \phi_k^{-2}(x, y) - \sum_{n=1}^{N} \frac{\cos 2(n - K)\pi/N}{\phi_k(x, y)\phi_n(x, y)} \right\} \tag{9}$$

The limits of integration must now be determined for S_m, $m = 1, 2, \ldots, N - 1, N$. For such purpose we most conveniently change to polar coordinates. The lower limit with respect to r for each S_m is clearly $r_{mL} = 0$. The upper limit with respect to r for S_m is readily obtained from Eq. (3), letting $x = R \cos \theta$ and $y = r \sin \theta$, and employing a common trigonometric identity. Hence $r_{m_u} = R \sec [\theta - (2m - 1)\pi/N]$. The lower and upper limits of integration with respect to θ are seen from Fig. 1 to be respectively $\theta_{mL} = (2m - 1)\pi/N$ and $\theta_{m_u} = 2\pi m/N$. Eq. (8) in polar coordinates becomes

$$\phi_n(\theta, r) = r \cos [\theta - (2n - 1)\pi/N] - R \tag{10}$$

Hence Eqs. (7) to (11) imply

$$A_1 = \frac{2 \sum_{m=1}^{n} \int_{2(m-1)\pi/N}^{2m\pi/N} \int_{0}^{R \sec [\theta-(2m-1)\pi/N]} r \prod_{n=1}^{n} \phi_n(\theta, r) dr d\theta}{\sum_{m=1}^{N} \int_{2(m-1)\pi N}^{2m\pi/N} \int_{0}^{R \sec [\theta-(2m-1)\pi/N]} r \left\{ \prod_{n=1}^{N} \phi_n(\theta, r) \right\}^2 \sum_{k=1}^{N} \left\{ \phi_k^{-2}(r, \Theta) - \sum_{n=1}^{N} \frac{\cos 2(n - k)\pi/N}{\phi_k(r, \theta)\phi_n(r, \theta)} \right\} dr d\theta} \tag{11}$$

Therefore,

$$\psi(x, y) = \frac{2 \prod_{n=1}^{N} \phi_n(x, y) \sum_{m=1}^{N} \int_{(2m-1)\pi/N}^{2m\pi/N} \int_{0}^{R \sec [\theta-(2m-1)\pi/N]} r \prod_{n=1}^{N} \phi_n(\theta, r) dr d\theta}{\sum_{m=1}^{N} \int_{(2m-1)\pi/N}^{2m\pi/N} \int_{0}^{R \sec [\theta-(2m-1)\pi/N]} r \left\{ \prod_{n=1}^{N} \phi_n(\theta, r) \right\}^2 \sum_{k=1}^{N} \left\{ \phi_k^{-2}(r, \theta) - \sum_{n=1}^{N} \frac{\cos 2(n - k)\pi/N}{\phi_k(r, \theta)\phi_n(r, \theta)} \right\} dr d\theta} \tag{12}$$

The torsional rigidity is given by

$$D = 2G \sum_{j=1}^{N} \int_{2(j-1)\pi/N}^{2j\pi/N} \int_{0}^{R \sec [\theta-(2j-1)\pi/N]} r\psi(r, \theta) dr d\theta, \tag{13}$$

where $\psi(r, \theta)$ is obtained from Eq. (12) by substituting $x = r \cos \theta$ and $y = r \sin \theta$, and G is the shear modulus.

The stress tensor is given by

$$[\tau_{ij}] = \begin{bmatrix} 0 & 0 & G\alpha\psi_y(x, y) \\ 0 & 0 & -G\alpha\psi_x(x, y) \\ G\alpha\psi_y(x, y) & -G\alpha\psi_x(x, y) & 0 \end{bmatrix} \tag{14}$$

where α is the twist per unit length and the subscripts x, y denote the corresponding derivatives with respect to x and y. The displacement field is given by

$$[u_i] = \begin{bmatrix} -\alpha yz \\ \alpha xz \\ \alpha F(x, y) \end{bmatrix} \tag{15}$$

where $$F(x, y) = \int_{P_0(x_0, y_0)}^{P(x,y)} \left\{ \frac{\partial f(x, y)}{\partial y} dx - \frac{\partial f(x, y)}{\partial x} dy \right\} \tag{16}$$

and $$f(x, y) = \psi(x, y) + (1/2)(x^2 + y^2) \tag{17}$$

Using the generalized method here presented, it can be easily shown that Stanišić's solution previously developed in the literature for particular N appears as a special case of this theory.

References

[1] Shirely, L. K., and Stanišić, M. M., *On the Torsion of Cylindrical Beam Having a Trapezoidal Cross Section*, Journal of the Aero/Space Sciences, Readers' Forum, Vol. 26, No. 7, pp. 462–464, July 1959.

[2] Stanišić, M. M., and Sherwood, B. A., *Torsion of an Elliptical Shaft With Diametrically Opposite Flat Sides*, Journal of the Aero/Space Sciences, Readers' Forum, Vol. 27, No. 6, pp. 462–463, June 1960.

[3] Stanišić, M. M., Hauck, C. A., and Mathias, R. A., *Concerning the Torsion of Prismatic Bars Having a Hexagonal Cross-Section*, Journal of Aerospace Sciences, Readers' Forum, Vol. 27, No. 8, pp. 631–633, August 1960.

[4] Kantorovich, L. V., and Krylov, V. I., *Approximate Methods of Higher Analysis*, Interscience Publishers, Inc., New York, 1958.

[5] Stanišić, M. M., *Free Vibration of a Rectangular Plate With Damping Considered*, Quart. Appl. Math., Vol. 12, No. 4, pp. 361–367, January 1955.

[6] Sokolnikoff, I. S., *Mathematical Theory of Elasticity*, McGraw-Hill Book Co., Inc., New York, 1956.

The Torsion of Prismatic Bars of Regular Polygonal Cross Section

F. W. Niedenfuhr and A. W. Leissa

Associate Professor and Assistant Professor, Respectively, Department of Engineering Mechanics, The Ohio State University; also, Consultants, North American Aviation, Columbus, Ohio

August 22, 1960

THE DIFFERENTIAL EQUATION[1] to be solved is

$$\nabla^2\psi = -2G\beta \tag{1}$$

subject to the boundary condition

$$\psi = 0, \quad \text{on} \quad B \tag{2}$$

where ψ is the torsional stress function, G is the shear modulus, β is the angle of twist per unit length of the bar, B is the boundary of the cross section, and ∇^2 is the Laplacian operator in two dimensions. An obvious solution of Eq. (1) is

$$\psi = -G\beta r^2/2 + \sum_{n=0,1,2,\ldots} A_{nN} r^{nN} \cos nN\theta \tag{3}$$

where r and θ are polar coordinates and N is the number of sides of the polygon. Eq. (3) expresses the N-fold symmetry of the problem.

Fig. 1 shows the coordinate system used, and the orientation of a typical side of the boundary polygon. The complete polygon is to be formed by combining N elements of the type

shown in the figure. The centroid of the polygon will coincide with the coordinate origin.

The N-fold symmetry of Eq. (3) makes it possible to satisfy the boundary condition at all points of B by analytically satisfying Eq. (2) only along that part of the boundary which lies in the range $0 \leqq \theta \leqq \pi/N$. This means, for instance, if a circle is viewed as a polygon with $N = \infty$, it is only necessary to satisfy the boundary condition at the single point $r = a$, $\theta = 0$. This can be done by terminating the series of Eq. (3) after the first term. One then obtains

$$\psi = -G\beta r^2/2 + A_0$$

Satisfying the boundary condition at $r=a$ then yields

$$A_0 = G\beta a^2/2$$

The resulting stress function for the circular boundary is the exact solution to the stated boundary-value problem.

An approximation[2] to the solution for regular polygons with a finite number of sides can be obtained as follows: Using the series of Eq. (3) truncated to contain k, say, terms, impress the boundary condition (2) at k points of the boundary.

The lowest order case to consider is that of the equilateral triangle, $N = 3$. In this case an exact solution can be obtained by matching the boundary condition at two points only—viz., at $\theta = 0$, $r = a \cos(\pi/3)$, and $\theta = \pi/3$, $r = a$, for in this case the true torsion function is expressible in the form

$$\psi = -G\beta r^2/2 + A_0 + A_3 r^3 \cos 3\theta$$

This problem accordingly holds no further interest since its solution in closed form is well known.[1]

Higher polygons require a larger number of terms in the torsion function to approach the exact solution, but surprisingly accurate results can be obtained by again using only two terms of the series in Eq. (3). In the general case, therefore, write

$$\psi = -G\beta r^2/2 + A_0 + A_N r^N \cos N\theta \tag{4}$$

and set $\psi = 0$ at the center of a side and at a vertex of the polygon. At the center of a side we obtain the condition

$$0 = -(G\beta/2)[a \cos(\pi/N)]^2 + A_0 + A_N[a \cos(\pi/N)]^N \tag{5}$$

while at the vertex we obtain

$$0 = -G\beta a^2/2 + A_0 - A_N a^N \tag{6}$$

Solving Eqs. (5) and (6) for A_0 and A_N we find

$$A_N = \frac{-G\beta}{2a^{N-2}} \cdot \frac{\sin^2(\pi/N)}{1 + \cos^N(\pi/N)}$$

$$A_0 = \frac{G\beta a^2}{2}\left[1 - \frac{\sin^2(\pi/N)}{1 + \cos^N(\pi/N)}\right] \tag{7}$$

The maximum shearing stress in the bar is at the center of a side of the polygon, and is obtained from the formula

$$\tau_{max} = \left.\frac{\partial \psi}{\partial r}\right|_{\substack{r = a\cos\pi/N \\ \theta = 0}} \tag{8}$$

According to Eqs. (4) and (7) then, the maximum stress in the bar is given by

$$\tau_{max} = -G\beta a \cos(\pi/N)\left[1 + \frac{N}{2}\frac{\sin^2(\pi/N)\cos^{N-2}(\pi/N)}{1 + \cos^N(\pi/N)}\right] \tag{9}$$

Some results of calculation with Eq. (9) are shown in Table 1.

The case $N = 6$, the regular hexagon, is of some interest here as the stress values in the Table show that the recently published results obtained by Stanišić, Hauck, and Mathias[3] are in considerable error, being of the order of 30 percent too low. The particular formulation of Galerkin's method used by those authors appears to be excessively tedious as well as inaccurate when compared with the present analysis.

The reference values of $(\tau_{max}/G\beta a)$ given in Table 1 were computed by keeping five terms in the series of Eq. (3) and satisfying the boundary condition at five points of the boundary segment $0 \leqq \theta \leqq \pi/N$. Convergence studies of this method have shown that these reference values are accurate to within less than one tenth of one percent.

TABLE 1

N	$(\tau_{max}/G\beta a)_{\text{Eq. (9)}}$	$(\tau_{max}/G\beta a)_{\text{reference}}$	% Error
3	0.7500	0.7500 (exact)	0
4	0.9898	0.9549 (exact)	4
5	1.0838	1.0309	5
6	1.1230	1.0623	6
7	1.1388	1.0753	6
8	1.1437	1.0801	6
9	1.1433	1.0808	6
10	1.1404	1.0796	5
∞	1	1 (exact)	0

The torque carried by the bar can always be obtained from the well-known formula

$$T = 2\int \psi dA \tag{10}$$

where the integration is carried out over the region of the cross section, but it is simpler in the case of a regular polygon to use an approximation. It is easy to show[4] in this case that if we write

$$T = KG\beta a^4 \tag{11}$$

where a is the radius of the circumscribing circle, that the functional K is bounded above and below by

$$\frac{N}{8}\sin\frac{2\pi}{N}\left(1 + \cos\frac{2\pi}{N}\right) \leqq K \leqq \frac{N^2}{8\pi}\sin^2\left(\frac{2\pi}{N}\right) \tag{12}$$

Table 2 shows values of these bounds and accurate reference values of K for the first few polygons. From this table we see that there is little point in making further calculations for the stiffness of the higher polygons, since the difference in the upper and lower bounds on K is less than seven percent for $N \geqq 7$. The reference value of K for $N = 5$ was obtained by truncating

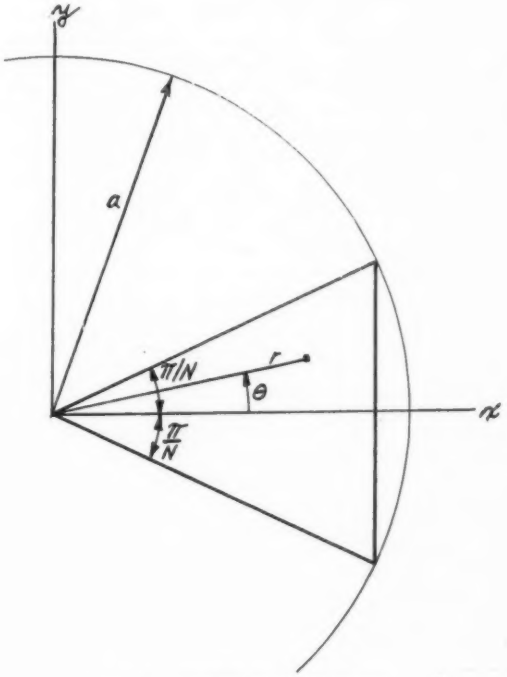

FIG. 1. Typical polygonal sector.

TABLE 2

N	$K_{\text{lower bound}}$	$K_{\text{reference}}$	$K_{\text{upper bound}}$
3	0.162	0.1949 (exact)	0.268
4	0.500	0.5624 (exact)	0.636
5	0.777	0.8461	0.896
6	0.976	1.0359	1.076
7	1.110		1.189
8	1.205		1.271
9	1.275		1.327
10	1.330		1.380
∞	$\pi/2$	$\pi/2$ (exact)	$\pi/2$

the series of Eq. (3) at five terms, matching the boundary condition at five points, and then carrying out the integration indicated in Eq. (10). The reference value for $N = 6$ was taken from reference 4. Note that the value of K for a hexagon given in reference 3 is incorrect.

REFERENCES

[1] Timoshenko, S., and Goodier, J. N., *Theory of Elasticity*, McGraw-Hill Book Co., Inc., New York, 1951.

[2] Conway, H. D., *The Approximate Analysis of Certain Boundary Value Problems*, J. Appl. Mech., Vol. 27, pp. 275–277, June 1960.

[3] Stanišič, M. M., Hauck, C. A., and Mathias, R. A., *Concerning the Torsion of Prismatic Bars Having a Hexagonal Cross-Section*, Journal of the Aerospace Sciences, Vol. 27, No. 8, pp. 631–633, August 1960.

[4] Pólya, G., and Szegö, G., *Isoperimetric Inequalities in Mathematical Physics*, Chapt. I, Princeton University Press, Princeton, N.J., 1951.

A Note on the Motion of a Spinning Rocket With Eccentric Thrust

A. G. Bennett*
Instructor, Division of Engineering Sciences, Purdue University, Lafayette, Ind.
September 1, 1960

THIS is an approximate analysis of the deviation of the axis of a spinning rocket due to a transverse moment arising from an eccentric thrust that rotates with the rocket. It is assumed that there is symmetry about the spin axis, no aerodynamic force, constant mass, and that the deviation of the spin axis is small enough to allow a certain linearization in the equations of motion. The apex (a point on the spin-axis unit distance from the mass center) traces an overall circular path with superimposed lobes (nutations), the details of which depend upon the ratio of spin-axis moment of inertia to transverse moment of inertia. When this inertia ratio is unity, the gyroscopic terms in the equations of motion cancel and the apex moves in an unbounded spiral path. If the transverse moment is suddenly removed, the apex moves in a circular path tangent to the direction of motion at the instant the moment was removed. The diameter of this circular path can be as much as twice the average diameter of the path with the moment acting. A most interesting result is that there is an optimum ratio of inertias which minimizes the maximum deviation.

The equations of motion are set in body-fixed axes x, y, z with origin at the mass center and with x along the spin axis of the rocket. The angular position of x, y, z with respect to nonrotating axes x_0, y_0, z_0 is specified by the three Euler angles ϑ the deviation of the spin axis, ψ the procession of the line of nodes, and φ the angle between the line of nodes and the y axis. Quantities A, B, C are the mass moments of inertia about x, y, z, respectively. The moment M due to eccentric thrust is applied about the body-fixed y axis. With this and the assumption of symmetry so that $B = C$, the spin velocity about the x axis is a constant, Ω. Defining the inertia ratio $a = A/B$ and with ω_y and ω_z representing the rotation about the y and z axes, the equations of motion are

$$\dot{\omega}_y - (1 - a)\Omega\omega_z = M/B, \qquad \dot{\omega}_z + (1 - a)\Omega\omega_y = 0$$

With $y = z = 0$ at $t = 0$ and assuming M is constant, the solution of these equations is

$$\omega_y = [M/(1 - a)\Omega B] \sin (1 - a)\Omega t$$

$$\omega_z = [M/(1 - a)\Omega B][\cos (1 - a)\Omega t - 1]$$

From the coordinate geometry it is known that

$$\Omega = \dot{\psi} \cos \vartheta + \dot{\varphi}$$

$$\omega_y = \dot{\psi} \sin \vartheta \sin \varphi + \dot{\vartheta} \cos \varphi$$

$$\omega_z = \dot{\psi} \sin \vartheta \cos \varphi - \dot{\vartheta} \sin \varphi$$

Together with the solution for the ω's above, these equations phrase the problem for the determination of the orientation of the rocket. It is here, as in other fixed-point motion problems, that difficulties appear. The complicated and unmanageable nature of the equations reflects the basic fact that finite angles do not add as vectors. Since infinitesimal angles do, we are led to look for some sort of a linearization. One may not presume ψ or φ to be small. They must be allowed to increase indefinitely. We first eliminate $\dot{\psi}$ and find

$$\omega_y = \Omega \tan \vartheta \sin \varphi + [\dot{\vartheta} \cos \varphi - \dot{\varphi} \tan \vartheta \sin \varphi]$$

$$\omega_z = \Omega \tan \vartheta \cos \varphi - [\dot{\vartheta} \sin \varphi + \dot{\varphi} \tan \vartheta \cos \varphi]$$

With the assumption that ϑ is small so that $\tan \vartheta \cong \vartheta$, the terms in the square brackets become perfect differentials. Defining new variables $\alpha = \vartheta \sin \varphi$ and $\gamma = \vartheta \cos \varphi$, we have

$$\omega_y = \Omega\alpha + \dot{\gamma}, \qquad \omega_z = \Omega\gamma - \dot{\alpha}$$

Taking $\vartheta = \varphi = 0$ at $t = 0$, the initial conditions for these equations are $\alpha = \gamma = 0$ at $t = 0$. With $m = M/A\Omega^2$ the solution may be written

$$\alpha/m = [\sin(1 - a)\Omega t]/(1 - a) - \sin \Omega t$$

$$\gamma/m = [\cos (1 - a)\Omega t]/(1 - a) - \cos \Omega t - [a/(1 - a)]$$

To investigate the solution, it is convenient to transfer back to the nonrotating coordinates x_0, y_0, z_0. Omitting the geometric details

$$\vartheta_{y_0}/m = \frac{\cos a\Omega t}{1 - a} - \frac{a \cos \Omega t}{1 - a} - 1, \quad \vartheta_{z_0}/m = \frac{\sin a\Omega t}{1 - a} - \frac{a \sin \Omega t}{1 - a}$$

The angles ϑ_{y_0} and ϑ_{z_0} are the components of ϑ about the x_0 and y_0 axes. For small ϑ, the angle ϑ is approximately equal to the linear displacement of the apex. That is, ϑ_{z_0} corresponds to y_0 of the apex and ϑ_{y_0} to negative z_0 of the apex. With this interpretation, we see that the path of the apex is an epicycloid with center at $z_0/m = 1$. This path may be generated by rolling on a cylinder of unit radius, a cylinder of radius

$b = a/(1 - a)$ for $0 < a < 1$ or

$b = 1/(a - 1)$ for $1 < a < 2$

Other details of the motion may be obtained from the familiar geometry of an epicycloid. Note that the number of lobes (nutations) in the overall rotation about the point $z_0/m = 1$ is just the reciprocal of b. If we denote the distance from this same point to the apex by r/m, we have

$$r_{min}/m = 1, \qquad r_{max}/m = \left|\frac{1 + a}{1 - a}\right|$$

Note that r_{max}/m is unbounded as the inertia ratio approaches unity. This is the situation in the nonlinearized solution as well. When $A = B = C$ the gyroscopic terms cancel and the motion is a simple acceleration under the action of the applied moment. The solution for this case shows the path of the apex is an unbounded spiral. This fact leads one to believe that there may be an optimum value of inertia ratio for minimum deviation. Such is the case if we set the question appropriately. We will determine the minimum of the maximum deviation as a function of inertia ratio for a given mass of rocket, given rotational speed,

* Presently Summer Faculty Associate, Boeing Airplane Company.

and given transverse moment. The maximum deviation determined previously may be written in the form

$$\frac{\Omega^2 r_{max}}{m} = \frac{1}{A}\left|\frac{1+a}{1-a}\right|$$

For a general body of revolution A may be written as a function of the inertia ratio alone. We find that the minimum of the maximum deviation occurs for an inertia ratio

$$a = (3 - \sqrt{7})/2 \cong 0.177$$

This value of inertia ratio corresponds to $l/d = 2.78$ for a right circular cylinder. This optimum of inertia ratio may have useful practical application.

Now consider the rocket with no external moment but with an initial transverse rotational velocity. This corresponds to the situation when the moment is suddenly removed. The solution can be carried out as previously. It is found that the apex traces a circular path tangent to the direction of motion when the moment as removed. The radius of this motion is

$$r/m = \left|\frac{2}{1-a}\sin {}^1\!/_2(1-a)\Omega t^*\right|$$

where t^* is the time at which the moment is removed. If the moment is removed precisely at the cusp of the epicycloid, r/m is zero and motion of the apex stops. If the moment is removed at the center of a lobe of the epicycloid, the radius of the remaining motion is $2/(1 - a)$, twice the average deviation under the influence of the constant moment.

The results of the analysis are self-explanatory and little comment is necessary. The main point of the analysis is the method of linearization which allows the simple solution. The linearization is not objectionable for some problems. In the case of the spinning rocket, large deviations eliminate the problem—perhaps the rocket.

In reference 1, an analysis similar to that presented here is made. By utilizing automatic computing equipment it was possible to obtain particular solutions including the nonlinearities of the basic equations such as varying moments of inertia. However, the numerical solution does not lend itself to an easy interpretation of the general nature of the motion. It is quite correctly pointed out in this reference that in a rocket the mass may vary rapidly and this fact must be taken into account. Variable mass causes an obvious difficulty with the idea of optimum inertia ratio. However, we know that the laws of motion apply instantaneously to a system of varying mass (if the forces due to expulsion of mass are included). At each instant we have just a new initial value problem with the same basic equations. The nature of the motion is not grossly different. We expect that maintaining the inertia ratio in the vicinity of the optimum for fixed mass would insure minimum deviation.

Reference

[1] Jarmolow, K., *Dynamics of a Spinning Rocket with Varying Inertia and Applied Moment*, J. Applied Physics, Vol. 20, No. 3, pp. 308–313, March 1957.

On the Rolling Motion of Low-Aspect-Ratio Delta Wings

Peter J. Mantle*
Research Engineer, Canadian Armament Research and Development Establishment, Valcartier, P.Q., Canada
September 6, 1960

SOME PRELIMINARY RESULTS obtained from free-flight tests on low-aspect-ratio delta wings are presented. These results are experimental evidence of the damping in roll (C_{l_p}) and nonlinear sideslip[1] ($C_{l_{\alpha\beta}}$) obtained in an aeroballistics range at supersonic speeds ($1.20 < M < 2.50$) and with aspect ratios 0.50, 1.0, and 2.0. These Mach numbers and aspect ratios permitted the flight conditions to cover the region bounded by near-normal shock and nearly supersonic leading edges.

* Now at the Guggenheim Aeronautical Laboratory, California Institute of Technology, Pasadena, Calif.

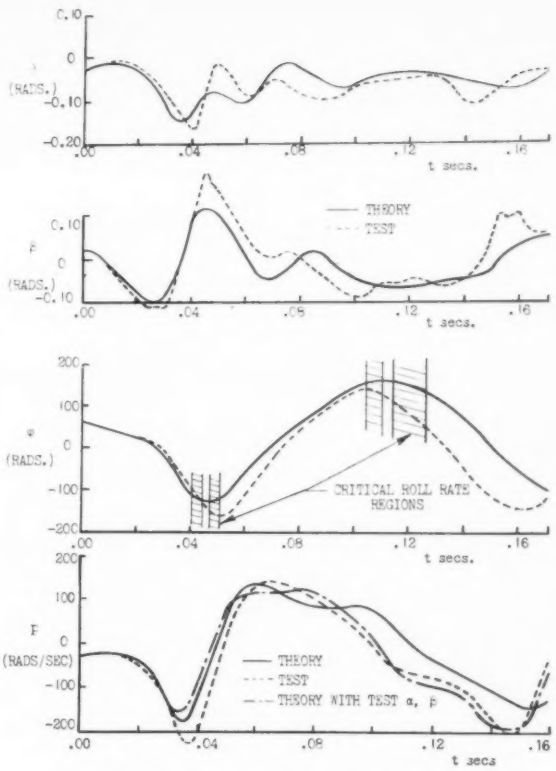

FIG. 1. Comparison of theory and test.

The application of the aeroballistics range (as a complementary tool to the wind tunnel) in dynamic stability analysis of free-flight test data has already been discussed in reference 2.

From some analog simulations and theoretical studies[3] based on slender-body-theory predictions, it was found that the equation of rolling motion which best fitted the experimental trajectories could be written

$$\ddot{\phi} - \left(\frac{\rho\, USl^2}{2I_{xx}}\right) C_{l_p}\,\dot{\phi} - \frac{\rho\, U^2 Sl}{2I_{xx}}\, C_{l_{\alpha\beta}}\,\alpha\beta = 0 \qquad (1)$$

where

- ϕ = angle of bank (rad.)
- α = pitch incidence (rad.)
- β = sideslip angle (rad.)
- ρ = air density (slugs/cu.ft.)
- U = wing forward velocity (ft./sec.)
- S = wing-planform area (sq.ft.)
- l = reference length (G.M.C.) (ft.)
- I_{xx} = moment of inertia in roll (slugs.ft^2)
- C_l = rolling moment/$^1\!/_2\rho U^2 Sl$

and

$$C_{l_p} = \frac{\partial C_l}{\partial(pl/U)}, \qquad C_{l_{\alpha\beta}} = \frac{\partial^2 C_l}{\partial\alpha\partial\beta}$$

To indicate the validity of Eq. (1) to represent the rolling motion of delta wings, comparison is made between test and analog-simulated trajectories for a typical case in Fig. 1.

It is to be noted that this particular wing experienced roll rates equal to the natural frequencies in pitch and yaw,[4] but that any expected resonance was not experienced due to the high rates of acceleration in roll through these critical values.

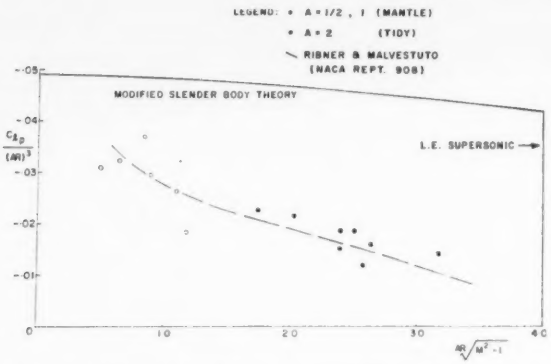

FIG. 2. Damping in roll of low-aspect-ratio delta wings.

Replacing Eq. (1) by its equivalent finite-difference form and applying the method of least squares to minimize experimental errors solutions were found both by hand and on an IBM 650 digital computer. Five-point differentiation on parabolically smoothed data was used to achieve the necessary accuracy. In a certain number of cases, however, certain mathematical difficulties were incurred by a weighting in the matrices of some elements. This weighting depended upon the relative magnitudes of the amplitudes in pitch, roll, and yaw. These difficulties were discussed in reference 1 and reference 5 but only the finalized results are presented here.

The values of damping in roll and the nonlinear sideslip have been normalized for generality in Figs. 2 and 3. These curves cover the range for a given aspect ratio from normal shock to supersonic leading edges. It is seen that only for very low-aspect ratios (slender wings) do the theoretical estimates approach the present test values.

Ribner and Malvestuto[6] modified the slender-body-theory results to account for the effect of the proximity of the Mach cone to the leading edges of the wing; but this effect has been seriously underestimated.

A probable cause of this marked disagreement is the neglect in the theory of the effect of the spanwise variation in Mach number due to yawing and also, of more importance, the assumption of the wrong edge condition by ignoring the leading-edge vortex flow.

As the Mach cone approaches the wing leading edge ($AR\sqrt{M^2-1} \to 4.0$), both the damping in roll and nonlinear sideslip reduce to very small values. This may be explained by consideration of the case of just-supersonic leading edges ($AR\sqrt{M^2-1} = 4.0$). For the wing in this condition, if it sideslips to port, the effect of sweepback will be to induce a negative roll rate while the now-supersonic starboard leading edge with its lower pressure will induce a positive roll rate. These two counteracting effects will thus yield either a zero or small residual value of $C_{l_{\alpha\beta}}$.

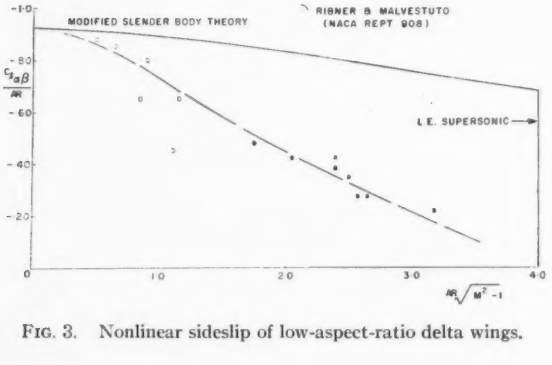

FIG. 3. Nonlinear sideslip of low-aspect-ratio delta wings.

REFERENCES

[1] Mantle, P. J., *Some Free Flight Results of the Lift Curve Slope and Rolling Derivatives of Low Aspect Ratio Delta Wings*, CARDE TM AB-67, 1960.

[2] Bull, G. V., *Aeronautical Studies in the Aeroballistics Range*, Jahrbuch, 1957, der WGL p. 247, or CARDE Rept 302/57.

[3] Mantle, P. J., *Some Dynamic Stability Characteristics of Low Aspect Radio Delta Wings*, CARDE TM AB-34, 1959.

[4] Phillips, W. H., *Effect of Steady Rolling on Longitudinal and Directional Stability*, NACA TN 1627, 1947.

[5] Mantle, P. J., *On the Analysis of Large Scale Linear Equations as Applied to Free Flight Data Reduction*, CARDE TM AB-66, 1960.

[6] Ribner, H. S., and Malverstuto, F. S., *Stability Derivatives of Triangular Wings at Supersonic Speeds*, NACA Rept. No. 908, 1948.

Higher Order Theory of Curved Shock*

Reuben R. Chow and Lu Ting
Research Assistant and Research Associated Professor, respectively, Aerodynamics Laboratory, Polytechnic Institute of Brooklyn, Freeport, N.Y.

September 1, 1960

BASED ON THE ASSUMPTION that the Navier-Stokes equations hold inside the shock layer, the stretching or boundary-layer technique proposed by R. von Mises[1] and G. Ludford[2] serves for a systematic approach in the analysis of the shock structure. The usual Rankine-Hugoniot shock conditions associated with zero shock thickness appears consistently in the analysis as the Reynolds number approaches infinity.

For moderately high Reynolds number, L. I. Sedov, M. P. Michailova, and G. G. Chernyi[3] proposed a theory for the corrections of Rankine-Hugoniot shock conditions taking into account the effect of viscosity, heat conduction, and the shock curvature behind a curved strong shock. The effect of shock structure was neglected in the theory presented. Probstein[4] has attempted to improve Sedov's solution by taking into account the effect of shock structure. In his analysis it is necessary to introduce an arbitrary shock thickness and approximate the velocity profile by a linear distribution. In the present note, it will be shown that this arbitrariness and approximation can be avoided by the systematic expansion scheme of references 1 and 2 which has also been developed for the boundary-layer theory[5] and the mixing problem.[6]

It is well known that the zero-order shock-structure analysis involves only the local slope of the shock surface, and the shock conditions remain the same if the shock surface is replaced locally by an oblique shock with the same inclination, because the shock conditions involve only the local quantities before and behind the shock but not their derivatives. In the next-order shock condition the first derivatives of the local quantities will appear while the normal derivatives can always be related to the derivative along the shock. To preserve the same local first derivative along the shock, the two-dimensional shock surface can be replaced by an equivalent circular shock with the same local curvature and slope. It is, therefore, necessary to develop the next-order shock relationships for a circular shock only.

Similarly, the next-order shock conditions across an axially symmetric shock are locally equivalent to those across a spherical

* This contract is administered by the Aeronautical Research Laboratory of the Air Research and Development Command and partially supported by the Air Force Ballistic Missile Division, Contract No. AF 33(616)-6118, Project No. 7064, Task No. 70169.

The authors wish to express their sincere thanks to Professor Antonio Ferri for his supervision and suggestions, and to Roberto Vaglio-Laurin for his stimulating discussions.

shock. The higher order shock relationships for a spherical shock will be reported later.

In order to demonstrate the technique of stretching of coordinates, the matching conditions, and how to obtain the higher order shock relationships, we discuss in detail the circumferential component v. With the radius of the circular shock equal to unity, and subscripts 1 and 2 designating the quantities before and behind the shock, the velocity component v can be expressed as

$$v_1 = v_1^{(0)} = U \sin \vartheta \tag{1}$$

$$v_2(r, \vartheta, \epsilon) = v_2^{(0)}(r, \vartheta) + \epsilon v_2^{(1)}(r, \vartheta) + 0(\epsilon) \tag{2}$$

where ϵ is the reciprocal of the Reynolds number, defined as: $\epsilon = \mu_\infty/\rho_\infty U$. The symbols without subscripts 1 or 2 indicate the quantities inside the shock. The coordinate r normal to the shock will be stretched to s by the factor $1/\epsilon$, i.e., $r - 1 = \epsilon s$. The velocity component inside the shock can be expressed as:

$$v(s, \vartheta, \epsilon) = v^{(0)}(s, \vartheta) + \epsilon v^{(1)}(s, \vartheta) + 0(\epsilon) \tag{3}$$

The matching conditions on the boundary of the shock layer for the zero-order and the first-order solutions are, respectively,

$$\lim_{s \to \infty} v^{(0)}(s, \vartheta) = v_1^{(0)}(1^+, \vartheta) = U \sin \vartheta; \quad \lim_{s \to -\infty} v^{(0)} = v_2^{(0)}(1^-, \vartheta) \tag{4}$$

$$\lim_{s \to \infty} v^{(1)}(s, \vartheta) = 0, \quad \lim_{s \to -\infty} v^{(1)}(s, \vartheta) = v_2^{(1)}(1^-, \vartheta) + (\partial/\partial r) v_2^{(0)}(1^-, \vartheta) s \tag{5}$$

If $\partial v_2^{(0)}/\partial r$ does not vanish behind the shock, $v^{(1)}(s, \vartheta)$ cannot be finite, as $s \to -\infty$ while $v_2^{(1)}$ at the shock is given by the equation

$$v_2^{(1)}(1^-, \vartheta) = \lim_{s \to -\infty} [v^{(1)}(s, \vartheta) - s(\partial/\partial r) v_2^{(0)}(1^-, \vartheta)]$$

In Sichel's analysis[7] for a weak normal shock $v^{(1)}(s, \vartheta)$ is finite as $s \to -\infty$ because behind a normal shock $v_2^{(0)}$ vanishes.

For other quantities before, behind, and inside the shock layer, expansion schemes corresponding to Eqs. (1), (2), and (3) are introduced. The matching conditions are equivalent to Eqs. (4) and (5). The normal coordinate inside the shock is stretched so that the derivatives of a quantity with respect to s or ϑ will not change its order of magnitude. After the substitution of Eq. (3) and its equivalent into the Navier-Stokes equations, terms of like orders of ϵ are collected and equated to zero. From the tangential component of the equation of motion, the zero-order differential equation is $\partial v^{(0)}/\partial s = 0$; hence $v^{(0)} = U \sin \vartheta = v_2^{(0)}(1^-, \vartheta)$ from Eq. (4). The zero-order shock condition can be obtained directly by integrating the differential equation from $s = -\infty$ to $+\infty$. Similarly, the next-order shock condition can be obtained by integrating the next-order differential equation and applying Eq. (5) without solving for $v^{(1)}$. The result is

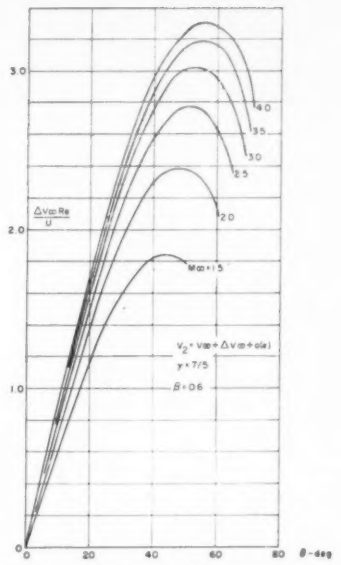

FIG. 1. The first-order tangential component of velocity.

$$R_0 \rho^{(0)} u^{(0)} v_2^{(1)} = R_0 \frac{\mu}{\epsilon} \frac{\partial v_2^{(0)}}{\partial r} + \int_{-\infty}^{0} \left[\frac{\partial}{\partial \vartheta}(p^{(0)} - p_2^{(0)})\right] \partial s + \int_{0}^{+\infty} \left[\frac{\partial}{\partial \vartheta}(p^{(0)} - p_\infty)\right] \partial s + v_\infty \frac{\partial v_1^{(0)}}{\partial \vartheta} \left[\int_{-\infty}^{0} (\rho^{(0)} - \rho_2^{(0)}) \partial s + \int_{0}^{+\infty} (\rho^{(0)} - \rho_\infty) \partial s\right] - \left[\frac{(\mu_v - 2/3\mu)}{\epsilon} + \frac{\mu}{\epsilon}\right] \frac{\partial}{\partial \vartheta}(u_1^{(0)} - u_2^{(0)}) \tag{6}$$

The integral terms on the right-hand side of Eq. (6) are associated with the zero-order shock structure. They can be evaluated either analytically or numerically with the help of the zero-order structure solution. A compact form is obtained for $P_r = 3/4$ where we can perform the transformation from the physical coordinate, s, to the velocity coordinate $u^{(0)}$ when evaluating the integrals:

$$\frac{v_2^{(1)}}{U} = v_2^{(1)*} = \left(\frac{1}{1+\beta}\right) \tan \vartheta \left\{\left(\frac{\gamma+3}{\gamma+1}\right) - \left(\frac{2}{\gamma+1}\right) \frac{1}{M_\infty^2 \cos^2 \vartheta} - \frac{(\gamma+1) M_\infty^2 \cos^2 \vartheta}{(\gamma-1) M_\infty^2 \cos^2 \vartheta + 2}\right\} - \left\{\frac{32}{3}\left[\frac{\gamma}{(1+\gamma)^2}\right](1 - \log_e 2)\right\} \sin \vartheta + \left\{\left[\frac{8}{3}\left(\frac{\gamma}{1+\gamma}\right) \log_e 2\right]\left[1 + \left(\frac{\gamma+1}{\gamma-1}\right) \frac{M_\infty^2 \cos^2 \vartheta}{M_\infty^2 \cos^2 \vartheta + 2}\right]\right\} \sin \vartheta$$

$$\beta = (3/4)(\mu_e/\mu) \tag{7}$$

The result is shown in Fig. 1. Following the same procedure, the first-order variations in the normal component of impulse, mass flux, and stagnation enthalpy have been obtained from the next-order equations of the normal component of equation of motion, the continuity equation, and the energy equation in Reference 8.

In the derivation of Eq. (7), it has been assumed that $u^{(0)}$ at $s = 0$ takes the mean value u^* of those before and behind the shock. Therefore, the body shape should be modified by an amount of order ϵ to be compatible with the first-order solutions $u_2^{(1)}$ and $v_2^{(1)}$. On the other hand, if the body shape is defined, the location of $u^{(0)} = u^*$ in $s - \vartheta$ plane is defined by the compatibility condition of the first-order solution behind the shock.

REFERENCES

[1] Von Mises, Richard, *Mathematical Theory of Compressible Fluid Flow*; Academic Press, Inc., New York, 1958.

[2] Ludford, G. S. S., *The Boundary Layer Nature of Shock Transition in a Real Fluid*, Quart. Appl. Math., Vol. 10, No. 1, April 1952.

[3] Sedov, L. I., Michailova, M. P., and Chernyi, G. G., *Ob'iyanii Vyazkosti i Teploprovodnosti na Techenie Gaza za Silno Iskrivlennoi Udarnoi Volnoi*, Vestnik Moskovskovo Universiteta, No. 3, pp. 95–100, 1953. (English translation by R. F. Probstein, WADC TN-59-349.)

[4] Probstein, R. F., and Kemp, N. H., *Viscous Aerodynamic Characteristics in Hypersonic Rarefied Gas Flow*, Journal of the Aero/Space Sciences, Vol. 27, No. 3, pp. 174–192, March 1960.

[5] Freidrichs, K. O., *Special Topics in Fluid Dynamics*; Lecture Notes, New York University, 1952–1953.

[6] Ting, L., *On the Mixing of Two Parallel Streams*, J. Math. Phys., Vol. 38, No. 3, pp. 153–165, October 1959.

[7] Sichel, M., *Higher-Order Corrections to Taylor's Solution for Weak, Normal, Shock Waves*, Journal of the Aerospace Sciences, Vol. 27, No. 8, pp. 635–636, August 1960.

[8] Chow, R., and Ting, L., *Higher Order Theory of Curved Shock*, Polytechnic Institute of Brooklyn, PIBAL Report No. 609, August 1960.

Note on Three-Dimensional Free-Mixing†

Martin H. Bloom
Professor of Aeronautical Engineering,
Polytechnic Institute of Brooklyn, Freeport, N.Y.
September 13, 1960

THIS NOTE describes some quasi-two-dimensional properties of three-dimensional viscous free-mixing more fully discussed in reference 1.

The following equations of boundary-layer type can be used to describe three-dimensional free-mixing flows (the notation of reference 2 is used):

continuity:

$$\frac{\partial R}{\partial t} + \frac{1}{e_1 e_2 e_3}\left\{\frac{\partial}{\partial x_1}[e_2 e_3 R V_1] + \frac{\partial}{\partial x_2}[e_1 e_2 R V_2] + \frac{\partial}{\partial x_3}[e_1 e_2 (R V_3 + \overline{\rho v_3})]\right\} = 0 \quad (1)$$

x_1 *momentum (neglecting body forces):*

$$R\left[\frac{\partial V_1}{\partial t} + V_1\frac{\partial V_1}{e_1\partial x_1} + V_2\frac{\partial V_1}{e_2\partial x_2} + \left(V_3 + \frac{\overline{\rho v_3}}{R}\right)\frac{\partial V_1}{e_3\partial x_3} + \frac{V_1 V_2}{e_1 e_2}\frac{\partial e_1}{\partial x_2} - \frac{V_2^2}{e_1 e_2}\frac{\partial e_2}{\partial x_1}\right] = -\frac{\partial P}{e_1\partial x_1} + \frac{1}{e_1^2 e_2 e_3}\frac{\partial}{\partial x_3}\left[e_1^2 e_2\left(\mu\frac{e_1\partial(V_1/e_1)}{e_3\partial x_3} - \frac{R}{e_1}\overline{v_1 v_3}\right)\right] + \frac{1}{e_1^2 e_2 e_3}\frac{\partial}{\partial x_2}\left[e_1^2 e_3\mu\frac{e_1(V_1/e_1)}{e_2\partial x_2}\right] \quad (2)$$

x_2 *momentum:*

$$R\left[\frac{\partial V_2}{\partial t} + V_1\frac{\partial V_2}{e_1\partial x_1} + V_2\frac{\partial V_2}{e_2\partial x_2} + \left(V_3 + \frac{\overline{\rho v_3}}{R}\right)\frac{\partial V_2}{e_3\partial x_3} + \frac{V_2 V_3}{e_2 e_3}\frac{\partial e_2}{\partial x_3} + \frac{V_1 V_2}{e_1 e_2}\frac{\partial e_2}{\partial x_1} - \frac{V_1^2}{e_1 e_2}\frac{\partial e_1}{\partial x_2}\right] = -\frac{\partial P}{e_2\partial x_2} + \frac{1}{e_1 e_2^2 e_3}\frac{\partial}{\partial x_3}\left[e_1 e_2^2\left(\mu\frac{e_2\partial(V_2/e_2)}{e_3\partial x_3} + \mu\frac{e_2}{e_2}\frac{\partial}{\partial x_2}\left(\frac{V_3}{e_3}\right) - R\overline{v_2 v_3}\right)\right] + \frac{1}{e_1 e_2^2 e_3}\frac{\partial}{\partial x_1}\left[e_2^2 e_3\mu\frac{e_1}{e_2}\frac{\partial}{\partial x_2}\left(\frac{V_1}{e_1}\right)\right] \quad (3)$$

x_3 *momentum:*

$$P = P_e + 0(\delta) \quad (4)$$

energy equation:

$$R\left[\frac{\partial H}{\partial t} + V_1\frac{\partial H}{e_1\partial x_1} + V_2\frac{\partial H}{e_2\partial x_2} + \left(V_3 + \frac{\overline{\rho v_3}}{R}\right)\frac{\partial H}{e_3\partial x_3}\right] = \frac{1}{e_1 e_2 e_3}\frac{\partial}{\partial x_3}\left\{e_1 e_2\left[\mu\frac{\partial H}{e_3\partial x_3} + \frac{1-Pr}{Pr}\frac{\partial h}{e_3\partial x_3}\right] - Ru_3 H\right\} \quad (5)$$

and in the inviscid flow:

$$V_{1e}(\partial V_{1e}/e_1\partial x_1) = -(1/R_e)(\partial P_e/e_1\partial x_1) \quad (6a)$$

$$(V_{1e}^2/e_1 e_2)(\partial e_1/\partial x_2) = (1/R_e)(\partial P_e/e_2\partial x_2) \quad (6b)$$

An orthogonal (within the boundary-layer approximations) curvilinear coordinate system for this problem can be set up as follows: A reference streamline S within the viscous core, preferably near the "center" is selected. Coordinate surfaces x_2 = constant are defined to contain various inviscid streamlines at the outer edge of the viscous layer and S as well. Quasi-cylindrical surfaces x_3 = constant enclosing S form the second coordinate family, while surfaces x_1 = constant approximately normal to S complete the system. For the special case in which the outer streamlines are straight and parallel, the familiar cylindrical coordinates can be used ($x_1 = x$, $x_2 = \vartheta$, $x_3 = r$, $e_1 = 1$, $e_2 = r$, $e_3 = 1$).

Considerations identical to those presented in reference 2* show that if $\kappa \equiv (1/e_1 e_2)(\partial e_1/\partial x_2) \to 0$, where κ is the component of outer streamline curvature in the plane tangent to the outermost surface x_3 = constant, the momentum equations exhibit homogeneity and admit the solution $V_2 = \overline{v_2 v_3} = 0$. This is also a consequence of the homogeneity of the boundary conditions which in turbulent flow is based on the assumption $\overline{v_2 v_3} = 0$ in the neighborhood of S, where $V_2 = V_3 = 0$. That is, at $x_3 = 0$ and $x_3 \to \infty$, $V_2 = \overline{v_2 v_3} = 0$. Of course, the initial conditions (at $x_1 = 0$) must be consistent with these conditions. Therefore, initially swirling flows for which $V_2 \neq 0$ (for instance), are excluded; for example, see reference 5.

The two-dimensionality will hold within varying degrees of approximation when the term $[(V_1/V_{1e})^2 - (R_e/R)]\kappa$, which appears in Eq. (3) is negligible. This term need not be small if $\kappa \neq 0$ and the inviscid Mach numbers are high.

When cross-flow components are not zero but are small compared to V_1, the approach used by Carrier[3] in dealing with flow along a corner can be attempted. This involves solving the x_1 momentum equation together with the continuity equation which is arbitrarily divided into two equations. This provides three equations for the velocity components, the other two momentum equations being neglected in a first approximation.

The determination of the absolute orientation of the three-dimensional free-mixing region depends upon the establishment of a third boundary condition from which the additive functions of the cross-flow components V_2 and V_3 can be determined. This well-known situation has been discussed most recently by Ting[4] for the two-dimensional mixing of two semi-infinite uniform streams. Except in special cases the additional boundary condition stems from the requirement that the pressure across the mixing region is constant to orders higher than zero. Hence, the first-order self-induced pressures due to displacement in each of the two streams must be the same. This requirement provides the condition by which the first-order cross-flow is determined absolutely.

An analogous but more complicated condition holds for three-dimensional mixing. In this case, it develops that the two cross-flow components at the reference axis must be adjusted so as to minimize the mean deviation from the mean of the self-induced pressure increments at a given streamwise station. When the flow is symmetric about one plane, only one velocity component can be adjusted to minimize the pressure deviations. For flows symmetric about two planes, the determining condition ($V_2 = V_3 = 0$ at $x_3 = 0$) is evident and higher order solutions need not be considered for this purpose.

It is noted that the coordinate system used to derive the cross-flow conditions is not quite the same as that previously described, which postulates that $x_3 = 0$, coincides with a streamline S. The reference line S_a in the latter instance must be an absolute one fixed to the inviscid flow. Since V_2 and V_3 are not necessarily zero on S_a, the position of S is finally measured with respect to S_a.

References

[1] Bloom, M. H., *On Three-Dimensional Free-Mixing*, PIBAL Report No. 474, AFOSR TN 60-986, August 1960.

[2] Vaglio-Laurin, R., *Turbulent Heat Transfer on Blunt-Nosed Bodies in Two-Dimensional and General Three-Dimensional Hypersonic Flow*, WADC

† This work was done in connection with AFOSR, Contract AF 49(638)-217, AFOSR TN 60-986.

* But with the further restriction that R and μ are constant and $e_1 e_2 e_3$ is independent of x_2.

TN 58-301, ASTIA 206 050, September 1958; also Journal of Aero/Space Sciences, Vol. 27, No. 1, pp. 27–36, January 1960. (The JAS version does not include Appendix A of the WADC note which is pertinent here.)

[3] Carrier, G., *The Boundary Layer in a Corner*, Quart. Appl. Math., Vol. IV, No. 4, p. 367, January 1947.

[4] Ting, L., *On the Mixing of Two Parallel Streams*, J. Math. & Phys., Vol. 38, No. 3, p. 153, October 1959.

[5] Bloom, M. H., and and Steiger, M. H., *Axially Symmetric Free-Mixing With Swirl*, WADC, ARL TN 60-163, PIBAL Rept. 628, November 1960.

Losses in Subsonic and Transonic Axial-Flow Compressors at Optimum Conditions

Gaetano E. Provenzale
Head, Compressor and Turbine Section, Curtiss-Wright Corp., Wright Aeronautical Div., Wood-Ridge, N.J.
September 23, 1960

NASA[1] has designed and tested a considerable number of axial-flow compressor cascades, as well as subsonic and transonic single stages. While the losses of the rotor mean and hub radial sections and of the whole span of the stator blades have been correlated reasonably well by the two-dimensional cascade loss parameter $\bar{\omega} \cos \alpha_2/2\sigma$ and a loading factor called "diffusion factor," the rotor-tip radial section correlation is obviously unsatisfactory.[1]

Presented and discussed are the results of an analytical investigation based on test data at minimum-loss conditions of numerous NASA[2–14] and Curtiss-Wright single stages. The results, shown in Figs. 1 and 2, indicate an average improvement in the correlation of the rotor-tip test data of about 60 percent over the NASA correlation.[1] Figs. 1 and 2 permit a better prediction of the relative total-pressure-loss coefficient at minimum-loss angle of incidence for flow through subsonic and supersonic axial-compressor rotor tips having 65-(A_{10}) or double circular-arc airfoils. The main conclusion of this paper is that higher values of solidity than those employed in most of the existing compressor rotors are necessary to obtain higher rotor-tip efficiency, especially at supersonic Mach numbers.

The loss parameter $\bar{\omega} \cos \alpha_2/2\sigma$ was developed theoretically by Lieblein and Roudebush and was shown to correlate well the two-dimensional cascade test data as a function of diffusion factor.[15] The test data for the rotor mean and hub sections, and the stator tip, mean and hub sections were correlated reasonably well by the same loss parameter and diffusion factor,[1] probably because the flow at these blade sections is closer to a two-dimensional type of flow, while the rotor-tip section experiences various flow phenomena of a predominantly three-dimensional type. Test results of some NASA[4,6] and WAD transonic rotors, and later analyses[16–18] had indicated that the scatter of the tip loss parameter could be related to local shock losses arising from increased blade-surface Mach numbers.

The writer initiated an investigation in order to rationalize the tip flow phenomena and improve the rotor-blade design and loss prediction in the tip region. The test data of subsonic flow were separated from the test data of supersonic flow. The subsonic Mach number range available (0.3 to 0.97) covers typical values of hub and mean section Mach numbers. This separation of the test data should have reduced the scatter of the tip loss parameter, but it did not. Fig. 3 shows the still very high degree of scatter. All this indicated that the shock losses were not the main reason for the scatter. The idea of a continuous tip-loss function of Mach number was developed, and the loss coefficient became a power function of solidity in terms of an exponent n function of Mach number. Values of $n = 1.0$ for $M = 1.0$ and $n = 2.0$ for $M = 1.1$ correlate the test data satisfactorily as shown in Figs. 1 and 2. The nature of the n function should be determined, as more test data become available at Mach numbers greater than 1.1.

The various flow phenomena present at the tip, such as thickening of boundary layer due to radial secondary flows, radial clearance, etc., may explain why the tip behaves differently

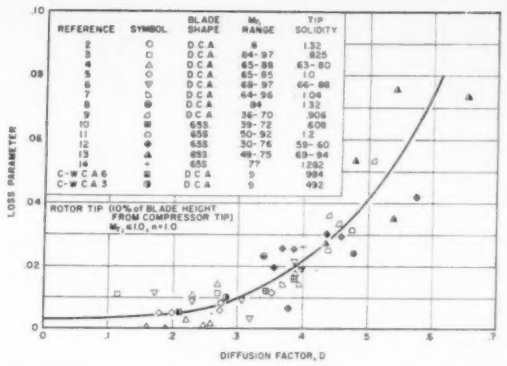
REFERENCE
SYMBOL
BLADE SHAPE
M_r RANGE
TIP SOLIDITY
2 O D.C.A. .6 1.32
3 □ D.C.A. .64-.97 .825
4 △ D.C.A. .65-.88 .63-.80
5 ◇ D.C.A. .65-.85 1.0
6 ▽ D.C.A. .68-.97 .66-.88
7 ▷ D.C.A. .64-.96 1.04
8 ● D.C.A. .84 1.32
9 ◁ D.C.A. .36-.70 .906
10 ■ 65S. .39-.72 .608
11 ○ 65S. .50-.92 1.2
12 ◆ 65S. .30-.76 .59-.60
13 ▲ 65S. .49-.75 .69-.94
14 + 65S. .77 1.282
C-W C A 6 ▣ D C A 9 .984
C-W C A 3 ◑ D C A 9 .492
ROTOR TIP (10% of BLADE HEIGHT FROM COMPRESSOR TIP)
$M_{r_1} \leq 1.0$, $n = 1.0$
LOSS PARAMETER
DIFFUSION FACTOR, D

FIG. 1. Total-pressure-loss parameter $(\bar{\omega}\sigma^n \cos \alpha_2)/2$ vs. diffusion factor D.

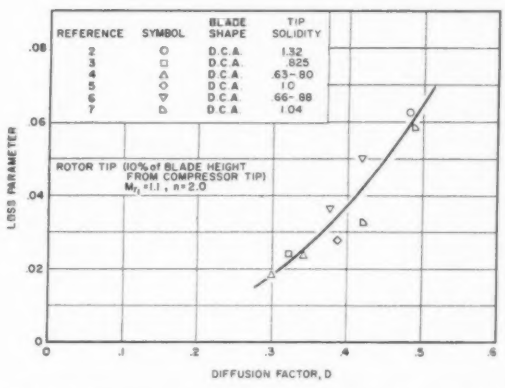

FIG. 2. Total-pressure-loss parameter $(\bar{\omega}\sigma^n \cos \alpha_2)/2$ vs. diffusion factor D.

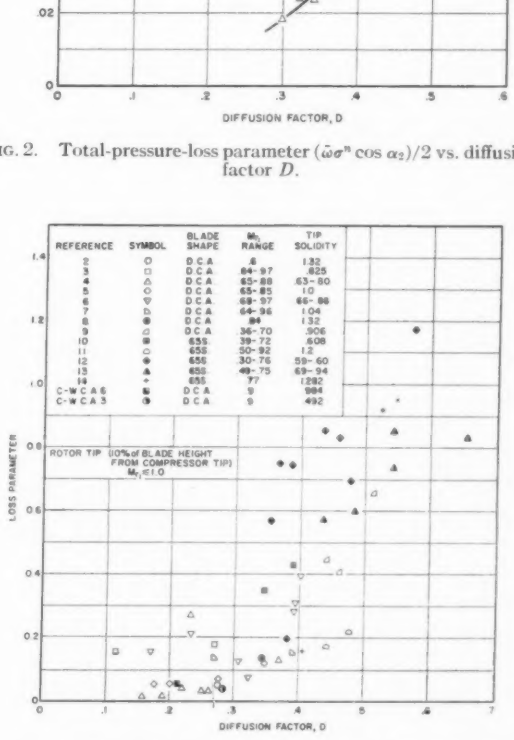
REFERENCE
SYMBOL
BLADE SHAPE
M_r RANGE
TIP SOLIDITY
2 O D.C.A. .6 1.32
3 □ D.C.A. .64-.97 .825
4 △ D.C.A. .65-.88 .63-.80
5 ◇ D.C.A. .65-.85 1.0
6 ▽ D.C.A. .68-.97 .66-.88
7 ▷ D.C.A. .64-.96 1.04
8 ● D.C.A. .84 1.32
9 ◁ D.C.A. .36-.70 .906
10 ■ 65S. .39-.72 .608
11 ○ 65S. .50-.92 1.2
12 ◆ 65S. .30-.76 .59-.60
13 ▲ 65S. .49-.75 .69-.94
14 + 65S. .77 1.282
C-W C A 6 ▣ D C A 9 .984
C-W C A 3 ◑ D C A 9 .492
ROTOR TIP (10% of BLADE HEIGHT FROM COMPRESSOR TIP)
$M_{r_1} \leq 1.0$
LOSS PARAMETER
DIFFUSION FACTOR, D

FIG. 3. Total-pressure-loss-parameter $(\bar{\omega} \cos \alpha_2)/2\sigma$ vs. diffusion factor D.

than the mean and hub sections at subsonic flow. High values of solidity apparently reduce the negative effects of these flow phenomena mostly by providing a better flow guidance. Limited available test data indicate that the same effect of Mach number on loss coefficient exists over the whole blade at supersonic speeds. Wright Aeronautical is engaged in a program of high-

work, high-solidity single-stage tests to determine the upper limit of rotor-tip solidity above which the frictional losses become predominant.

Concluding, the writer hopes to provide an improved method for predicting rotor-tip losses and designing better rotors, and also to provide material that would stimulate further the interest in the development of a general theory of compressor aerodynamics.

References

[1] Members, Compressor and Turbine Research Division, *Aerodynamic Design of Axial-Flow Compressors*, Vol. II, NACA RM E56B03a, pp. 97–156, August 1956.

[2] Sandercock, D. M., Lieblein, S., and Schwenk, F. C., *Experimental Investigation of an Axial-Flow Compressor Inlet Stage Operating at Transonic Relative Inlet Mach Numbers.* (IV)—*Stage and Blade-Row Performance of Stage with Axial-Discharge Stators*, NACA RM E54C26, 1954.

[3] Robbins, W. H., and Glaser, F. W., *Investigation of an Axial-Flow Compressor Rotor with Circular-Arc Blades Operating Up to a Rotor-Inlet Relative Mach Number of 1.22*, NACA RM E53D24, 1953.

[4] Tysl, E. R., and Schwenk, F. C., *Experimental Investigation of a Transonic Compressor Rotor with a 1.5 Inch Chord Length and an Aspect Ratio of 3.0.* (III)—*Blade-Element and Overall Performance at Three-Solidity Levels*, NACA RM E56D06, 1956. (2 Rotors.)

[5] Schwenk, F. C., and Tysl, E. R., *Experimental Investigation of a Transonic Compressor Rotor with a 1.5 Inch Chord Length and an Aspect Ratio 3.0.* (II)—*Blade-Element Performance*, NACA RM E55F10, 1955.

[6] Schwenk, F. C., and Lewis, G. W., Jr., *Experimental Investigation of a Transonic Axial-Flow Compressor Rotor with Double-Circular-Arc Airfoil Blade Sections.* (III)—*Comparison of Blade-Element Performance with Three Levels of Solidity*, NACA RM E55F01, 1955. (2 Rotors.)

[7] Lewis, G. W., Jr., and Schwenk, F. C., *Experimental Investigation of a Transonic Axial-Flow Compressor Rotor with Double-Circular-Arc Airfoil Blade Section.* (II)—*Blade-Element Performance*, NACA RM E54J08, 1955.

[8] Schwenk, F. C., Lieblein, S., and Lewis, G. W., Jr., *Experimental Investigation of an Axial-Flow Compressor Inlet Stage Operating at Transonic Relative Inlet Mach Numbers.* (III)—*Blade-Row Performance of Stage with Transonic Rotor and Subsonic Stator at Corrected Tip Speeds of 800 and 1000 Feet Per Second*, NACA RM E53G17, 1953.

[9] Mahoney, J. J., Duga, P. D., Budinger, R. E., and Goelzer, H. F., *Investigation of Blade-Row Flow Distributions in Axial-Flow Compressor Stage Consisting of Guide Vanes and Rotor-Blade Row*, NACA RM E50G12 1950.

[10] Jackson, R. J., *Analysis of Performance of Four Symmetrical-Diagram-Type Subsonic Inlet-Stage Axial-Flow Compressors*, NACA RM E53K03, 1954.

[11] Moses, J. J., and Serovy, G. K., *Some Effects of Blade Trailing-Edge Thickness on Performance of a Single-Stage Axial Flow Compressor*, NACA RM E51F28, 1951.

[12] Jackson, R. J., *Effects on the Weight-Flow Range and Efficiency of a Typical Axial-Flow Compressor Inlet Stage That Result from the Use of a Decreased Blade Camber or Decreased Guide-Vane Turning*, NACA RM E52G02, 1952. (3 Rotors.)

[13] Standahar, R. M., and Serovy, G. K., *Some Effects of Changing Solidity by Varying the Number of Blades on Performance of an Axial Flow Compressor Stage*, NACA RM E52A31, 1952. (2 Rotors.)

[14] Wright, L. C., and Wilcox, W. W., *Investigation of Two-Stage Counter-rotating Compressor.* (II)—*First Rotor Blade-Element Performance*, NACA RM E56G09, 1956.

[15] Lieblein, S., Schwenk, F. C., and Broderick, R. L., *Diffusion Factor for Estimating Losses and Limiting Blade Loading in Axial-Flow Compressor Blade Elements*, NACA RM E53D01, 1953.

[16] Schwenk, F. C., Lewis, G. W., and Hartmann, M. J., *A Preliminary Analysis of the Magnitude of Shock Losses in Transonic Compressors*, NACA RM E57A30, 1957.

[17] Miller, G. R., and Hartmann, M. J., *Experimental Shock Configurations and Shock Losses in a Transonic-Compressor Rotor at Design Speed*, NACA RM E58A146, 1958.

[18] Lewis, G. W., Tysl, E. R., and Fessler, T. E., *Analysis of Transonic Rotor-Blade Passage Loss with Hot-Wire Anemoters*, NACA RM E58C04, 1958.

Some Comments on the Inversion of Certain Large Matrices

Bertram Klein
Convair, A Division of General Dynamics Corp., San Diego, Calif.

September 20, 1960

THE SUBJECT of matric structural analysis has been treated in two recently published papers in the JOURNAL.[1,2] The authors of these papers have made a number of statements about the inversion of certain large matrices. It is the purpose of this note to bring to the attention of the reader certain facts that shed new light on this important problem. It is shown here that the situation is not as hopeless as the above-mentioned authors intimate.

In general, the time necessary to invert a large, sparse matrix of the type encountered in the method of matric structural analysis advocated by the writer[3–7] is a function of several things as follows in order of importance:

(1) The machine, method, and program used.

(2) The number of redundants in the system, say R.

(3) The number of nonzero elements present in the matrix, say N.

(4) The order of the matrix, say M.

Notice first that the size of the matrix itself is the least important item. This premise may be surprising. The simple example which follows may illustrate this point. Suppose we have two systems of equations in which R and N are the same but M is different. Then, actually the inversion time can be longer for the system with the smaller M, contrary to customary thinking. It appears from such reasoning that N/M may be a parameter of significance.

Notice next that the type of machine available is the prime factor. Naturally, no problem would exist if we had at our disposal a very fast machine with very large, high-speed, storage space. Present-day machines are limited in high-speed storage space. Therefore, one has to resort to auxiliary lower speed storage that affects inversion time. The method and program we use is important. It is believed that the method presented in references 8 and 9 can be made highly efficient because it isolates very nicely the redundant part of the solution. The size of this subsystem R is an important factor in inversion time. Really, the degree of difficulty of an inversion is closely related to the size of the redundant matrix. This matrix size is the number of equations that cannot be put into a pretriangularized form. It represents the number of redundants in the system in the structural sense. Notice that this number is determined automatically in the program.[8,9]

Naturally the smaller the number of nonzero elements in the matrix, the less shuffling that has to be done.

In conclusion, we say that the time for inversion may be a complicated function,

$$T = T(R, N, M)$$

and one cannot draw any conclusions on the basis of M alone.

References

[1] Crichlow, W. J., and Haggenmacher, G. W., *The Analysis of Redundant Structures by the Use of High-Speed Digital Computers*, Journal of the Aerospace Sciences, Vol. 27, No. 8, pp. 595–606, 614, August 1960.

[2] Samson, C. H., Jr., and Bergmann, H. W., *Analysis of Low-Aspect-Ratio Aircraft Structures*, Journal of the Aerospace Sciences, Vol. 27, No. 9, pp. 679–693, 711, September 1960.

[3] Klein, B., *A Simple Method of Matric Structural Analysis*, Journal of the Aeronautical Sciences, Vol. 24, No. 1, pp. 39–46, January 1957.

[4] Klein, B., *A Simple Method of Matric Structural Analysis: Part II—Effects of Taper and Consideration of Curvature*, Journal of the Aeronautical Sciences, Vol. 24, No. 11, pp. 813–820, November 1957.

[5] Klein, B., *Simple Method of Matric Structural Analysis: Part III—Analysis of Flexible Frames and Stiffened Cylindrical Shells*, Journal of the Aeronautical Sciences, Vol. 25, No. 6, pp. 385–394, June 1958.

[6] Klein, B., *A Simple Method of Matric Structural Analysis: Part IV—Nonlinear Problems*, Journal of the Aero/Space Sciences, Vol. 26, No. 6, pp. 351–359, June 1959.

[7] Klein, B., *A Simple Method of Matric Structural Analysis: Part V—Structures Containing Plate Elements of Arbitrary Shape and Thickness*, Journal of the Aerospace Sciences, Vol. 27, No. 11, pp. 859–866, November 1960.

[8] Klein, B., *Application of the Wille Rearranging Technique to a Typical Structural Matrix*, Journal of the Aeronautical Sciences, Readers' Forum, Vol. 25, No. 5, pp. 342–343, May 1958.

[9] Klein, B., *New Methods in Matric Structural Analysis*, Proceedings of the Second Electronic Computer Conference, Pittsburgh, Pa., Sept. 1960.

REQUIREMENTS *for* CONTRIBUTIONS
to the publications of the
INSTITUTE *of the* AEROSPACE SCIENCES

The Institute of the Aerospace Sciences invites both members and nonmembers from any country to submit papers for publication in the JOURNAL OF THE AEROSPACE SCIENCES and AEROSPACE ENGINEERING. The Institute, following the practice of other societies, does not pay for contributions.

The following directions for the preparation of papers, if followed by authors, will save correspondence, avoid the return of papers for changes, minimize the work of preparation for the printer, and save the expense due to the charges made for "author's corrections."

MANUSCRIPTS: The original typewritten copy of the paper is desired. **To expedite review, an additional copy of both the manuscript and figures should be submitted.** The manuscript must be double or triple spaced on one side of white paper sheets, consecutively numbered. There should be wide margins to allow for the marking of directions to the printer. Correcting, changing, or adding to papers after they are in type is costly. It is, therefore, imperative that papers submitted be in final form. Typographical errors may be corrected on proofs, but if authors wish to add material, they may do so at their own expense. In mailing, drawings may be rolled, but manuscripts should be sent flat. Send by first-class mail (register if you wish for your own protection) to the Editorial Office, Institute of the Aerospace Sciences, 2 East 64th Street, New York 21, N.Y. All manuscripts will be examined by the Editorial Committee and by the Editor. Authors will be advised as promptly as possible whether the paper is acceptable for publication.

TITLES: The title of the paper should be brief. The name and initials of the author should be written as he prefers. The use of the full name of an author is advocated because of the frequent duplication of initials and surnames which sometimes makes it difficult to establish the identity of the author. This is particularly important for large annual indexing and abstracting services. All titles and degrees or honors are omitted. The name of the organization with which the author is associated should be placed after his name on a separate line. The date on which the paper is received will be inserted by the Editor. The author's title or position should be indicated in a footnote.

SUMMARIES OR ABSTRACTS: An abstract to be printed at the beginning should accompany each article. It should be adequate as an *index* and as a *summary*. It should contain a statement of major conclusions reached, since summaries in many cases constitute the only source of information used in compiling scientific reference indexes. Abstracts printed in other journals, especially foreign, in most cases consist of summaries from printed papers. The summary should explain as adequately as possible the major conclusions to a nonspecialist in the subject and should contain from 100 to 300 words, depending on the length of the paper.

SUBHEADINGS: Subheadings should be inserted by the author at frequent intervals. The work of editorial preparation will be simplified by the author's provision of many subheadings.

MATTER USUALLY DELETED: Photographs or illustrations of little technical interest and not showing advances in general practice. Too detailed tabular matter (general results of such tables may be included in the text). Lengthy descriptions of materials or processes or of preliminary experiments or theories that preceded final results; salient features only are of interest.

REFERENCES: References should be numbered consecutively and grouped together at the end of the manuscript, with only the corresponding number being mentioned in the text. The arrangement should be as follows. For books: [1]Durand, W. F., *Aerodynamic Theory*, 1st Ed., Vol. 1, p. 23; Julius Springer, Berlin, 1934. For magazines: [1]England, C. R., Crawford, A. B., and Mumford, W. W., *Some Results of a Study of Ultra-Short-Wave Transmission Phenomenon*, Proc. IRE, Vol. 20, No. 12, pp. 481–482, March, 1933. Please give author, title, edition, volume, number, page, publisher, and place and date of publication as indicated. Omission of one required fact causes much extra editorial work and possible inaccuracies.

ILLUSTRATIONS: Illustrations should accompany manuscripts, and each should always be referred to in the text by number. Drawings or graphs should not be larger than 12 × 16 inches, and must be made with jet black India ink on white paper or tracing cloth, the latter being preferred. *Do not use typewriter for lettering.* The smallest lettering on 8 × 10 inch figures should be no less than $^1/_4$ inch high. Cross-section paper (white with black lines) may be used, but it should not have more than 4 lines per inch. If finer ruled paper is used, the major division lines should be drawn in with black ink, omitting the finer divisions. In the case of finely ruled paper, only blue-lined paper can be accepted. *Tracing paper and blueprints* are not acceptable. Lettering and all markings must be large enough to be readable after reduction to single-column width ($3^1/_{16}$ in.). Mail rolled or flat; never fold. Drawings that cannot be reproduced (including pencil drawings) will be returned to the author for redrawing, thus delaying publication of the paper. Photographs should be distinct and show clear black and white contrasts. They must be on glossy white paper. Avoid round or oval photographs.

CAPTIONS AND LEGENDS: Legends or captions must accompany each drawing or photograph submitted. If written on the drawing or photograph they should be placed below and well outside the part to be reproduced. Each table should have a caption such as Table 1, Table 2, Table 3, etc. Captions should be complete in themselves so as to make the data intelligible to the reader without reference to the text. A duplicate list of captions for figures should be included as the last page of the manuscript. Use "Fig. 1" (not Figure 1), "Figs. 3 and 4," etc., in both the text and the numbering of illustrations. In the text, "Eq. (1)" or "Eqs. (1) and (2)" is used, not "Equation (1)." In captions, legends, and in table headings, write all words in full; do not abbreviate, except for "Fig." and "Eq."

MATHEMATICAL WORK: Formulas may be typewritten or carefully written in pen and ink, the writing to be large enough so that it can be marked for the printer. Considerable space for marking should be allowed above and below all equations. All complicated equations should be repeated on separate sheets with adequate space left for marking. The solidus should be used for simple fractions appearing within the text. Make all expressions clear to the typesetter. Greek letters used in formulas should be clearly designated by name in the margin of the manuscript. The difference between capital and lower-case letters should be clearly distinguished and care taken to avoid confusion between zero (0) and the letter (o), between the numerical (one) and the letter (ell) and the prime (′), between alpha and a, kappa and k, u and mu, v and nu, n and eta. All subscripts and exponents should be clearly distinguished. Avoid complicated exponents and subscripts. Dots and bars over letters or mathematical expressions should also be avoided. When it is necessary to repeat a complicated expression, it should be represented by some convenient symbol.

SYMBOLS AND ABBREVIATIONS: The symbols recommended in the American Standard Association "Letter Symbols for Aeronautical Sciences," ASA Y10.7—1954, should be used wherever practicable. All symbols should be clearly written and carefully checked. Standard abbreviations should be used, and it should be noted that most abbreviations are lower case.

CORPORATE MEMBERS

OF THE

INSTITUTE OF THE AEROSPACE SCIENCES

AC SPARK PLUG DIVISION, GENERAL MOTORS CORPORATION

ACADEMY OF AERONAUTICS

AEROJET-GENERAL CORPORATION

AERONCA MANUFACTURING CORPORATION

AERONUTRONIC, DIVISION OF FORD MOTOR COMPANY

AEROSPACE CORPORATION

AGAWAM AIRCRAFT PRODUCTS, INC.

ALLIED RESEARCH ASSOCIATES, INC.

ALLISON DIVISION, GENERAL MOTORS CORPORATION

AMERICAN AIRLINES, INC.

AMERICAN BOSCH ARMA CORPORATION

AMERICAN OIL COMPANY

AMOCO CHEMICALS CORPORATION

ARDE ASSOCIATES

ASTRO-ELECTRONIC PRODUCTS DIVISION, RADIO CORPORATION OF AMERICA

AVCO-EVERETT RESEARCH LABORATORY

AVIEN, INC.

BEECH AIRCRAFT CORPORATION

BELL AEROSPACE CORPORATION

THE BENDIX CORPORATION

BOEING AIRPLANE COMPANY

BOOZ, ALLEN APPLIED RESEARCH, INC.

BULOVA RESEARCH AND DEVELOPMENT LABORATORIES, INC.

CANADAIR, LTD.

CHANCE VOUGHT CORPORATION

THE CHASE MANHATTAN BANK

CHICAGO AERIAL INDUSTRIES INC.

CONTINENTAL MOTORS CORPORATION

CORNELL AERONAUTICAL LABORATORY, INC.

COX & COMPANY, INC.

CURTISS-WRIGHT CORPORATION

DANIEL, MANN, JOHNSON, & MENDENHALL

THE DECKER CORPORATION

DEFENSE ELECTRONIC PRODUCTS DIVISION, RADIO CORPORATION OF AMERICA

DEFENSE SYSTEMS DIVISION, GENERAL MOTORS CORPORATION

DEL MAR ENGINEERING LABORATORIES

DELCO-RADIO DIVISION, GENERAL MOTORS CORPORATION

DELCO-REMY DIVISION, GENERAL MOTORS CORPORATION

DOAK AIRCRAFT COMPANY, INC.

DOUGLAS AIRCRAFT COMPANY, INC.

DZUS FASTENER COMPANY, INC.

EASTERN AIR LINES, INC.

EATON MANUFACTURING COMPANY

EDO CORPORATION

ELASTIC STOP NUT CORPORATION OF AMERICA

ENGINEERING SUPERVISION COMPANY

FAIRCHILD CAMERA AND INSTRUMENT CORPORATION

FAIRCHILD ENGINE AND AIRPLANE CORPORATION

THE GARRETT CORPORATION

GENERAL APPLIED SCIENCE LABORATORIES, INC.

GENERAL DYNAMICS CORPORATION

GENERAL ELECTRIC COMPANY

GENERAL PRECISION, INC.

THE B. F. GOODRICH COMPANY

GOODYEAR AIRCRAFT CORPORATION

GRUMMAN AIRCRAFT ENGINEERING CORPORATION

HOFFMANN AIRCRAFT COMPANY

HUGHES AIRCRAFT COMPANY

INSURANCE COMPANY OF NORTH AMERICA COMPANIES

INTERNATIONAL BUSINESS MACHINES CORPORATION FEDERAL SYSTEMS DIVISION

THE INTERNATIONAL NICKEL COMPANY, INC.

ITT FEDERAL LABORATORIES, A DIVISION OF INTERNATIONAL TELEPHONE AND TELEGRAPH CORPORATION

JANITROL AIRCRAFT DIVISION, MIDLAND-ROSS CORPORATION

JOHNS-MANVILLE SALES CORPORATION

KOLLSMAN INSTRUMENT CORPORATION

LAVELLE AIRCRAFT CORPORATION

LEAR, INCORPORATED

C. W. LEMMERMAN, INC.

THE LIQUIDOMETER CORPORATION

ARTHUR D. LITTLE, INC.

LOCKHEED AIRCRAFT CORPORATION

THE MARQUARDT CORPORATION

THE MARTIN COMPANY

McDONNELL AIRCRAFT CORPORATION

MELETRON CORPORATION

MINNEAPOLIS-HONEYWELL REGULATOR COMPANY

MOBIL OIL COMPANY

NATIONAL CREDIT OFFICE, INC.

NORTH AMERICAN AVIATION, INC.

NORTHROP CORPORATION

PAN AMERICAN WORLD AIRWAYS, INC.

THE RALPH M. PARSONS COMPANY

PIASECKI AIRCRAFT CORPORATION

POLY INDUSTRIES, INC.

REPUBLIC AVIATION CORPORATION

ROHR AIRCRAFT CORPORATION

RYAN AERONAUTICAL COMPANY

SHELL OIL COMPANY

SIMMONDS PRECISION PRODUCTS, INC.

SOLAR AIRCRAFT COMPANY

SOUTHWEST PRODUCTS COMPANY

SPACE TECHNOLOGY LABORATORIES, INC.

R. DIXON SPEAS ASSOCIATES

SPERRY GYROSCOPE COMPANY, DIVISION OF SPERRY RAND CORPORATION

STANDARD-THOMSON CORPORATION

STANLEY AVIATION CORPORATION

THERM, INCORPORATED

THIOKOL CHEMICAL CORPORATION

THOMPSON RAMO WOOLDRIDGE INC.

TRANS WORLD AIRLINES, INC.

UNION CARBIDE METALS COMPANY, DIVISION OF UNION CARBIDE CORPORATION

UNITED AIR LINES, INC.

UNITED AIRCRAFT CORPORATION

UNITED STATES AVIATION UNDERWRITERS, INC.

VEHICLE RESEARCH CORPORATION

WESTERN GEAR CORPORATION

WESTINGHOUSE ELECTRIC CORPORATION